AD NUMBER: ADB024969
LIMITATION CHANGES
TO: Approved for public release; distribution is unlimited.
FROM: Distribution authorized to U.S. Government agencies only; Test and Evaluation; Apr 1977. Other requests shall be referred to Naval Air Systems Command, Washington, DC 20361.
AUTHORITY
USNEPRF ltr dtd 23 Jul 1979

AD NUMBER

AD-B024 969

NEW LIMITATION CHANGE

TO **DISTRIBUTION STATEMENT - A**
Approved for public release;
distribution is unlimited

LIMITATION CODE: 1

FROM **DISTRIBUTION STATEMENT - B**
Distribution authorized to U.S.
Gov't. agencies only.

LIMITATION CODE: 3

AUTHORITY

USNEPRF; JUL 23, 1979

NAVY TACTICAL APPLICATIONS GUIDE

VOLUME 1

TECHNIQUES AND APPLICATIONS OF IMAGE ANALYSIS

DEFENSE METEOROLOGICAL SATELLITE PROGRAM (DMSP)

Prepared under the direction of

Robert W. Fett

TACTICAL APPLICATIONS DEPARTMENT

Naval Environmental Prediction Research Facility

Monterey, California 93940

1977

THE WALTER A. BOHAN COMPANY

8088 DAYTON STREET, PARK RIDGE, ILLINOIS 60068

PROGRAMS IN SATELLITE METEOROLOGY / APPLIED RESEARCH AND VISUAL COMMUNICATIONS

UNCLASSIFIED

SECURITY CLASSIFICATION OF THIS PAGE (When Data Entered)

REPORT DOCUMENTATION PAGE

READ INSTRUCTIONS BEFORE COMPLETING FORM

1. REPORT NUMBER: NAVENVIRPREDRSCHFAC Applications Report CR 77-03
2. GOVT ACCESSION NO.
3. RECIPIENT'S CATALOG NUMBER

4. TITLE (and Subtitle): Navy Tactical Applications Guide. Volume I. Techniques and Applications of Image Analysis
5. TYPE OF REPORT & PERIOD COVERED
6. PERFORMING ORG. REPORT NUMBER

7. AUTHOR(s): Robert W. Fett and Walter F. Mitchell
8. CONTRACT OR GRANT NUMBER(s): The Walter A. Bohan Company N00228-76-C-3025 and Amendment P00002

9. PERFORMING ORGANIZATION NAME AND ADDRESS: The Walter A. Bohan Company, 2026 Oakton Street, Park Ridge, Illinois 60068
10. PROGRAM ELEMENT, PROJECT, TASK AREA & WORK UNIT NUMBERS: A 370370C/076B/5F52551700; TA WF52-551-716; NEPRF WU: 055:2-9

11. CONTROLLING OFFICE NAME AND ADDRESS: Naval Air Systems Command (AIR-370), Department of the Navy, Washington, D.C. 20361
12. REPORT DATE: January 1977
13. NUMBER OF PAGES: 110

14. MONITORING AGENCY NAME & ADDRESS (if different from Controlling Office): Naval Environmental Prediction Research Facility, Monterey, California 93940
15. SECURITY CLASS. (of this report): Unclassified
15a. DECLASSIFICATION/DOWNGRADING SCHEDULE

16. DISTRIBUTION STATEMENT (of this Report): Distribution limited to U.S. Gov't. agencies only; Test and Evaluation; April 1977. Other requests for this document must be referred to

17. DISTRIBUTION STATEMENT (of the abstract entered in Block 20, if different from Report)

18. SUPPLEMENTARY NOTES

19. KEY WORDS (Continue on reverse side if necessary and identify by block number)

Defense Meteorological Satellite Program (DMSP)
Sunglint
Anomalous Gray Shades
Barrier Effects
Ocean Waves and Swell
Atmospheric Moisture
Upwelling
Eddies

20. ABSTRACT (Continue on reverse side if necessary and identify by block number)

Background on the Defense Meteorological Satellite Program (DMSP) is provided, updated for the Navy system and the Block 5-D spacecraft.

Geometrical aspects of sunglint are described with nomograms for determining the distance from the subsatellite track to the Primary Specular Point (PSP). Various aspects of sunglint patterns with implications vis a vis determining sea state and —> next p.

DD FORM 1 JAN 73 1473 EDITION OF 1 NOV 65 IS OBSOLETE S/N 0102-LF-014-6601

UNCLASSIFIED

SECURITY CLASSIFICATION OF THIS PAGE (When Data Entered)

051910 LB

20. Abstract (continued)

low-level wind direction are illustrated and described.

The meaning of anomalous gray shade patterns appearing in DMSP Very High Resolution (VHR) visual data is thoroughly explored with examples of each specific cause and suggestions for tactical use.

Island and land barrier effects on sea state and atmospheric moisture are illustrated in a variety of different sunglint relationships.

Sections in Volume I may be expanded at a later date with additional case studies developed through on-going research and contract efforts.

Foreword

In 1971 USS CONSTELLATION (CV-64) was deployed to the Western Pacific with prototype equipment which gave "CONNIE" the unique on board capacity to read-out and process high resolution imagery directly from the Defense Meteorological Satellite Program (DMSP) satellites; thus providing a new dimension to meteorological support of tactical operations. Since 1971, and based on the success of the CONSTELLATION system, a considerable investment has been made, and is being made, to provide similar capabilities aboard key Navy ships and selected sites ashore. Maximum benefit from the DMSP data now being made available to the Navy, however, requires sophisticated approaches to image interpretation.

The DMSP has advanced the state-of-the-art in meteorological satellite picture resolution, quality, and automatic rectification. At the same time ambiguities have been introduced for the unprepared system user. The DMSP visible mode sensor samples a broader range of the spectrum than other satellite systems, and gives a peak response in near-infrared wavelengths as opposed to the normal peak response in the visible spectrum range. Anomalous gray shade patterns become evident which are generally not detected or well delineated by other systems. It is one of the major purposes of Volume I of the Navy Tactical Applications Guide to describe these anomalies, and to discuss their implications and applications in the Navy tactical environment. Volume II, now in preparation, shifts the emphasis from basic image analysis to a detailed description of significant environmental phenomena and effects, and includes an important section devoted to oceanographic phenomena and air-sea interactions.

This volume is based on the research efforts of Mr. Robert W. Fett, Head, Tactical Applications Department, NEPRF. A contribution was also made by LCDR Walter F. Mitchell, Fleet Weather Facility, Suitland, Maryland (Section 1A and 1C).

The following publications may be referred to for basic information on meteorological satellite data interpretation: (1) Guide for Interpretation of Satellite Photography and Nephanalysis, Project FAMOS Research Report (4-67), August 1967, (2) Guide for Observing the Environment with Satellite Infrared Imagery, Project FAMOS Research Report (NWRF F-0970-158), and (3) Application of Meteorological Satellite Data in Analysis and Forecasting, ESSA Technical Report NESC 51, March 1974.

This guide has been prepared to fulfill the needs of Navy meteorologists' for DMSP data interpretation techniques for Fleet operational applications. Comments on this Guide are solicited for consideration in future volumes in this series.

P.A. PETIT
Captain, U.S. Navy
Commanding Officer

Acknowledgements

Special thanks are extended to AGC Robert H. Whritner and personnel of the Navy Satellite Van Division, Naval Weather Service Facility, San Diego, who provided many of the DMSP transparencies used in this Guide, and to Russell Chambers and AG2 Christopher Reith, NEPRF, who developed the documentation for the case studies. Appreciation is also extended to personnel at Fleet Weather Central, Rota, Spain, to those at Keesler Air Force Base, and aboard the aircraft carriers USS CONSTELLATION and USS JOHN F. KENNEDY, who gathered DMSP data for NEPRF use.

The format for this guide was designed and developed by Walter A. Bohan and Lido A. Andreoni of The Walter A. Bohan Company. Their contributions, technical review, and editorial assistance is also gratefully acknowledged.

Contents

Introduction

The participation of the U.S. Navy in the Joint Services Defense Meteorological Satellite Program (DMSP), formerly known as the Data Acquisition and Processing Program (DAPP), has ushered in new opportunities for the use of satellite data to support tactical operations. The timeliness, resolution, and quality of these data coupled with unique display capabilities constitutes a significant advancement in the "state-of-the-art" of meteorological satellites.

Forecasters of the U.S. Navy must be prepared to optimize their use of data from this system. Previous manuals, notably Project FAMOS' Guide for Interpretation of Satellite Photography and Nephanalysis (August 1967) and Guide for Observing the Environment with Satellite Infrared Imagery (September 1970) stressed cloud pattern recognition as an aid in synoptic or large-scale analysis. This guide features new techniques of image analysis based on interpretations of sunglint and anomalous gray-shade patterns uniquely depicted in DMSP data.

The Navy Tactical Applications Guide is intended to be a practical guide for the shipboard forecaster and for forecasters in Forecast Centers possessing a DMSP capability. The Guide will be a continuing series of volumes with loose-leaf sections. Sections will be published individually and distributed immediately upon completion for rapid dissemination of new DMSP imagery interpretation concepts. Some sections will be supplemented by 16mm sound films to emphasize evolving qualities of weather situations as viewed by geosynchronous satellites in comparison to the polar-orbiting satellites.

As the DMSP system is incorporated on board ships and in Forecast Centers of the U.S. Navy, it is recognized that individual forecasters will find documentation for many of the unusual phenomena occurring in various areas of the world. It is desired to incorporate as many of these as are useful within the Guide for the benefit of Navy meteorologists in years to come. Forecasters and Forecast Centers are encouraged to submit their contributions to the Tactical Applications Department, Naval Environmental Prediction Research Facility, Monterey, California 93940. For significant contributions, proper recognition will be given to the individual, or individuals, and stations concerned.

Fig. 1. ESSA 3 Mosaic. Passes 618 and 619. 20 November 1966.

Fig. 1 is an example of an ESSA 3 mosaic used to illustrate a jet stream over the Atlantic and the eastern United States in the Project FAMOS' Guide of 1967. The current NOAA/GOES series of meteorological satellites provide improved resolution and contrast in comparison to this example. Note that the contrast between land and water in this picture is very poor. Coastal region outlines are not visible. Only the presence of the superimposed grid showing geographical outlines permits one to deduce approximate land-water coastal boundaries.

Fig. 2 shows a DMSP visible mode product (0.3 nm resolution) over the same area. Land-water contrast, made possible by an enlarged spectral interval (0.4 - 1.1 μm) extending into the near infrared, is excellent. Lakes, bays, streams, tributaries, etc., are all readily visible making possible precise gridding and landmark identification. Fig. 3 illustrates the type of enlargement capabilities built into the display which facilitates the determination of location and the interpretation of data, down to very small cumulus cloud elements. Accompanying infrared imagery for the same area and to the same scale, available in a variety of modes, permits deduction of cloud height and surface temperatures of the land and of the sea.

Fig. 2. FTV-28. DMSP Visible Data: VHR. Normal Enhancement Mode. 1709 GMT. 31 May '973.

Fig. 3. DMSP Visible Data: VHR. Enlargement of Gulf o Mexico-Florida Area.

Fig. 3 also illustrates some additional qualities of DMSP data which provide information that may be of value to the tactical forecaster. Note the appearance of dark gray-shade areas over the open water in the Gulf of Mexico and alternate dark/light gray-shade areas off the east Florida coast. How are these to be interpreted? Do they represent changes of sea state? Are some of the gray shades produced by patches of small unresolved clouds? Are they representative of changes in water-vapor content of the atmosphere? Major sections of the Navy Tactical Applications Guide will be devoted to discussions of these anomalous gray-shade patterns and their use in image analysis. Other volumes will use this material as basic background for the development of regional meteorology and air-sea interaction studies for tactical operations.

Section 1

The DMSP System

1A Satellite Sensors

1B Data Modes for Image Analysis

1C Data Accuracy

Acknowledgments

Gratitude is extended to Air Weather Service (MAC), United States Air Force for their approval to use portions of the Defense Meteorological Satellite Program (DMSP) User's Guide (AWS-TR-74-25) in the preparation of the Navy Tactical Application Guide. Some information contained in this section has been extracted in whole or in part from the Air Weather Service Guide. Other information was obtained from the Harris Corporation, Electronic Systems Division, Engineering Bulletin, entitled Data Display System and the AN/SMQ-10 User's Manual series NAVAIR 50-30 SMQ-10.

1A Satellite Sensors

Primary Sensors. Block 5C

The primary sensors used to obtain DMSP Data are contained in a sensor package. The sensor package is mounted on the DMSP so that with nominal spacecraft attitude control the sensors are always oriented toward the earth. These sensors are scanning radiometers which respond to radiation within specific spectral ranges. Two types of data are obtained: visible mode data, which is a measure of reflected solar radiation; and infrared mode data, which is a measure of emitted earth and cloud radiation.

The spectral interval used for obtaining visible data is 0.4 - 1.1 micrometers (μm). Fig. 1A-1 depicts the sensor's normalized response curve for this spectral range. It shows that the sensor responds as though there were minus violet, blue and green filters blocking most of the energy in the shorter wave length portion of the spectral range. This minimizes the blue light backscattering of the atmosphere and allows good contrast between dark objects in the earth scene, such as terrain and water boundaries.

The response at the other end of the spectral range is a result of the type of detector used. A silicon detector is used in order to sense small amounts of radiation in the visible spectrum. Its natural response provides sensing into the near infrared. However, the radiation sensed primarily is still reflected solar radiation. Two benefits are derived from this response. First, vegetation is more reflective at wave lengths longer than 0.7 μm than it is for shorter visible wavelengths, which provides good vegetation, soil, or water contrasts. Second, it allows good sensor response to lunar illumination. The lunar radiation curve approximates the emission from a 4000K blackbody. This emission peaks inside the sensor's response range. The earth scene under lunar illumination is therefore more perceptible than it would be for a sensor whose response approximates the human's eye. The sensor's half-power response points are at 0.57 μm and 0.97 μm.

In order to sense infrared radiation, a thermistor bolometer, combined with filtering, is used to respond in the 8 - 13 μm spectral range. The sensor response curve approximates that in Fig. 1A-1 except the abscissa would be labelled 8 - 14 μm rather than 0.4 - 1.2 μm. The 8 - 13 μm range is used primarily because it contains the peak radiations emitted by the earth and its atmosphere. The broad spectral range was selected so that the field of view of the detector could be narrowed to obtain good spatial resolution while still maintaining a good signal-to-noise ratio at the detector. A fortunate by-product of this spectral interval is that nearly all cirrus, even that just barely visible to a ground based observer, is detected by the sensor.

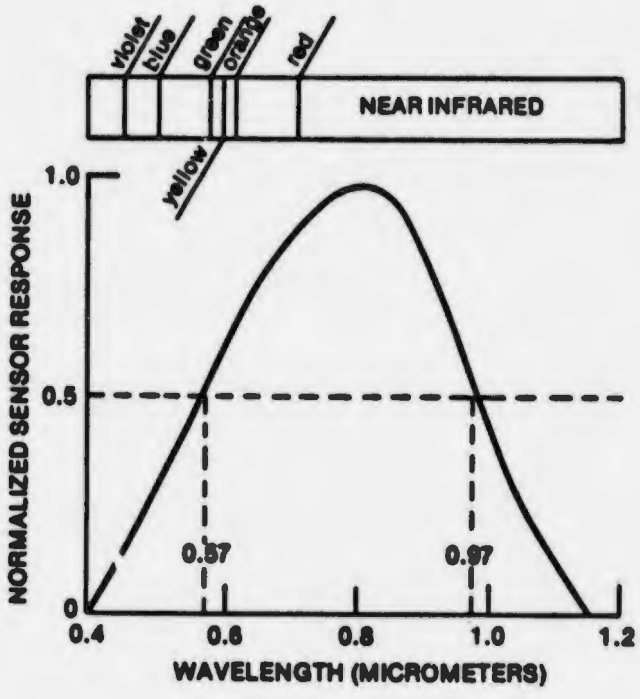

1A-1. Normalized sensor response for a simulated solar radiation source.

The sensor package consists of two scanning radiometers. One is a two-channel scanner for high resolution (HR) visible and infrared (MI) data; the other scanner is a two-channel device for very high resolution visible (VHR) and very high resolution infrared (WHR) data. Each radiometer consists of a mirror mounted on a shaft which rotates such that the mirror (which is mounted 45° to the direction of motion) scans the earth scene from horizon to horizon (Fig. 1A-2). The VHR/WHR shaft revolves at 5.34 Hertz (Hz). The mirror on the shaft is double-faced so that for each shaft revolution two scans are made of the earth scene. This scan rate combined with a 0.766 milliradian field of view from 450 nm, gives a spatial resolution of 0.33 nm at subpoint.

The HR/MI scanner is driven by a 3:1 reduction gear from the VHR/WHR shaft and revolves at 1.78 Hz. Since this mirror is single-faced and rotates at one-third the speed of the VHR/WHR mirror, only one-sixth the number of scan lines are produced. This scan rate, combined with a 4.56 milliradian field of view, provides 2.0 nm resolution visible data at subpoint. The MI detector has a 5.33 milliradian field of view which yields 2.4 nm resolution infrared data. For either radiometer the incoming scene radiation is reflected from the scanning mirror to a parabolic mirror which, in turn, focuses that radiation onto a dichroic beam splitter. The beam splitter allows visible spectrum radiation to pass without reflection, while at the same time reflecting infrared radiation. The visible radiation is collected at the respective HR and VHR detectors, and the infrared radiation is collected at the MI and WHR detectors.

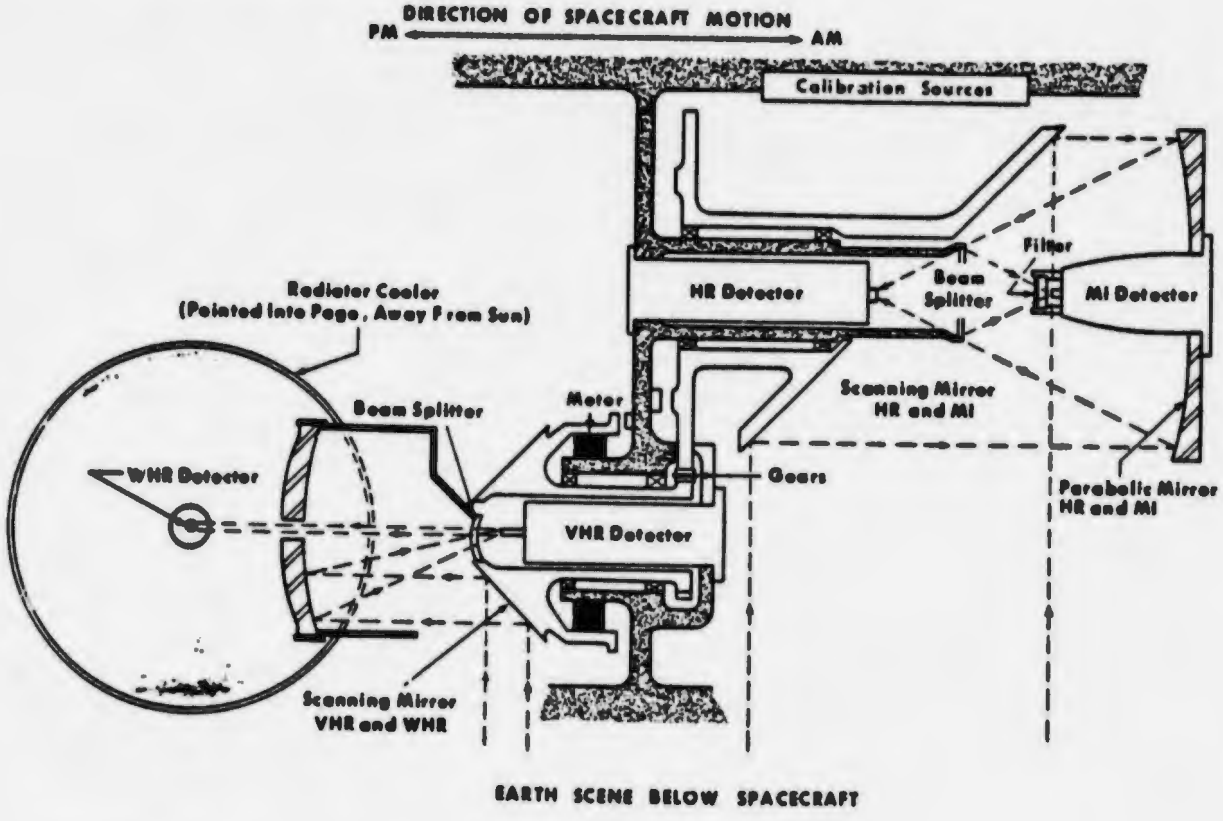

1A-2. DMSP Scanning Radiometer Optics.

In order to obtain the proper spatial resolution the detectors for VHR and WHR are physically smaller than their counterparts for HR and MI radiation. Consequently, for visible radiation, the VHR data are only available during the daytime where there is sufficient reflected solar illumination of the earth scene to provide an adequate signal-to-noise ratio at the detector. (The light level under full sunlight is between five and six orders of magnitude greater than full moonlight). For infrared data there is little difference between the total amount of radiation emitted from the earth during day or night. However, due to the fact that a different type of detector is used and that the WHR detector area is approximately 1/36th that of the MI detector, a greater signal-to-noise ratio problem exists than with the other sensors. In order to accurately discern the small amounts of infrared energy available to the WHR detector, it is passively cooled using a radiational cooling patch so that the thermal noise of the detector is reduced and does not obscure the scene radiation.

Fig. 1A-3 is a photograph of the Defense Meteorological Satellite Program (DMSP), Block 5C, satellite with the sensors mounted near the bottom of the spacecraft (right). The white face on the spacecraft is earth oriented and therefore the sensors on the right are earth oriented. The top of the spacecraft (left) always is oriented toward the sun. The panels on the left form a sun shade which shields the sensor package when the spacecraft is in an early morning orbit. In this orbit, near the poleward portion of each revolution, there is a possibility of direct sunlight impinging on the sensors.

The shiny box-like structure in the lower right contains the radiative cooler for the WHR detector. The cooler is pointed to the right, away from the sun. Above the cooler is a narrow aperture in which the VHR/WHR wedge-shaped mirror rotates. Just above the narrow aperture is the larger opening for the HR/MI scanning mirror. Of interest is the fact that these mirrors are precisely weighted and rotate in opposite directions so that there is no net momentum transfer to the spacecraft from their operation. The circular area on the white face to the left of the sensors, contains the antenna for the data transmitter.

Not seen in the picture, but extremely important to data production, is a unique feature in this system. A zero-resolution, super hemispheric radiometer is mounted 180° away from the sensor package nadir. This radiometer measures the amount of sunlight incident on the spacecraft, and, with the earth-oriented sensor system, essentially measures the solar illumination of the earth scene at the data subpoint (Fig. 1A-4). The output from this radiometer, in conjunction with a programmable gain memory unit, controls the signal level output for the visible data. In other words, the visible data received at tactical sites are normalized on the spacecraft for solar illumination. The data appear to have the same brightness whether from near the solar subpoint or near the terminator. Crossing the terminator, however, causes additional problems.

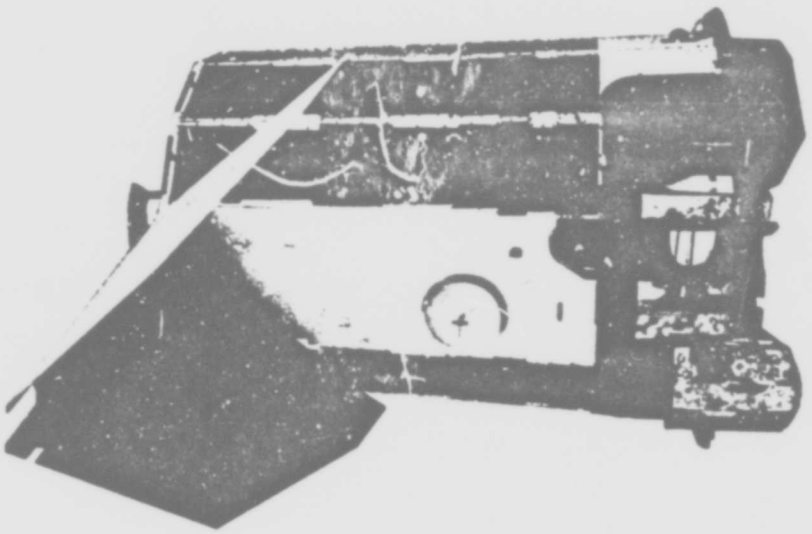

1A-3. Defense Meteorological Satellite Program (DMSP), Block 5C, satellite and sensors.

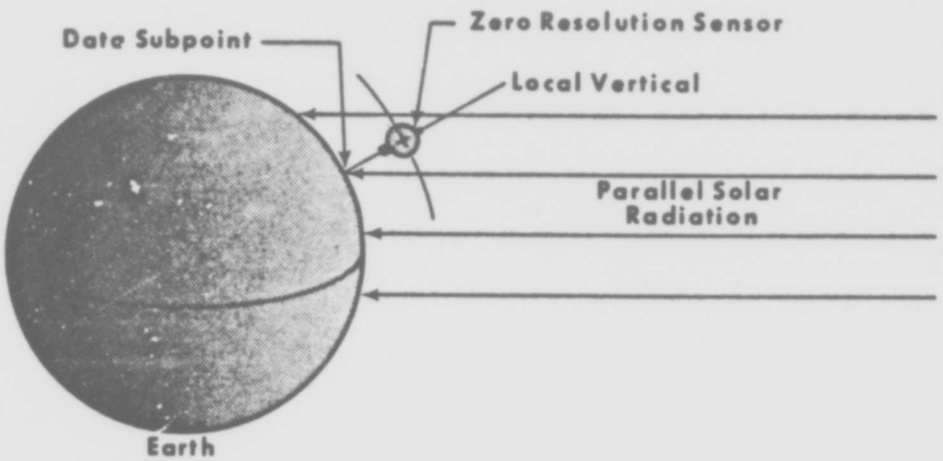

1A-4. Relationship between zero-resolution sensor and data subpoint. Incident solar radiation at each place is essentially identical.

Fig. 1A-5 shows the orientation of a sun-synchronous orbit to the terminator for an 0600 equator crossing at equinox. Notice how the sensor will have to scan from horizon to horizon through full brightness in the Southern Hemisphere progressing to full darkness in the Northern Hemisphere. Once the spacecraft reaches line AA' (Fig. 1A-6) the scene on the left begins to get progressively darker and the area of darkness expands. When the data subpoint reaches the terminator, half of the sensor scan is in the dark area and half in the light. At this point, scanning from horizon to horizon, the brightness change from far left to far right is spread over 26.8° of longitude at the equator. This is a brightness change of six orders of magnitude. In order to receive meaningful data across the terminator, one must have more than the along-track gain control provided by the zero-resolution sensor, one must also have along-scan gain control. In other words, as the sensor (HR) scans from dark to light, the gain for each scan line must change as the scanner moves into increasing brightness. As the spacecraft moves further into darkness, the along-scan gain must occur at a different location along the scan line. This compensation also will occur as the spacecraft leaves darkness on the other side of the earth. Additionally, the along-scan gain control must vary seasonally as the orientation of the terminator to the orbit changes.

There are four supplementary sensors which go on the DMSP spacecraft. Normally each DMSP carries two supplementary sensors, the exact complement differing according to the time period the orbit is planned for, and the condition of the various supplementary sensors on older spacecraft.

Supplementary Sensor E (SSE) is a vertical temperature profile radiometer. It is an eight channel instrument with six channels (668.5, 677, 695, 708, 725, and 747 cm^{-1}) in the carbon dioxide 15 μm absorption region; one channel (535 cm^{-1}) in a water vapor absorption band; and one channel (835 cm^{-1}) in the 11 μm atmospheric window. A scanning mirror steps across the subtrack of the satellite, allowing the SSE to view 25 separate columns of the atmosphere every 32 seconds over a cross-track ground swath of 100 nm. While the scanning mirror is stopped at a scene station, the channel filters are rotated through the

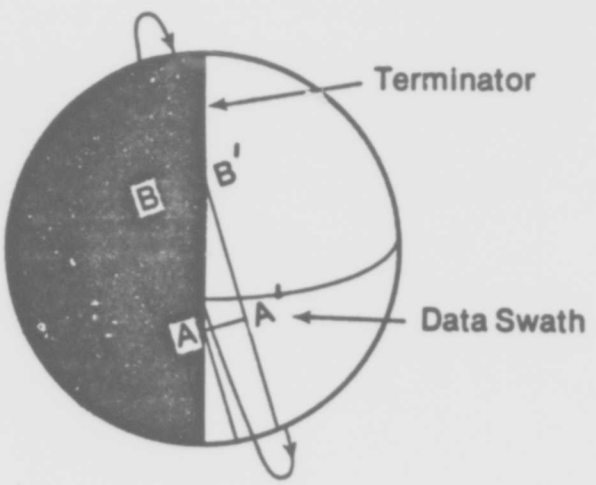

1A-5. Orientation of orbit terminator for a 0600 sun-synchronous orbit at equinox.

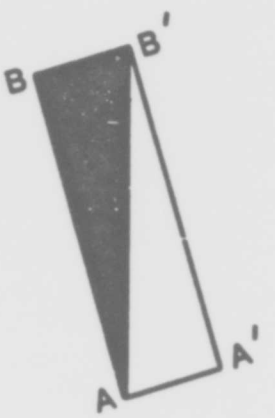

1A-6. Data swath across the terminator from AA' to BB' in Fig. 1A-5.

field-of-view. The detected radiation is measured by a tri-glycine, pyro-electric detector. Surface resolution at nadir for the SSE half-power points is approximately 20 nm.

Supplementary Sensor J (SSJ) is an electron spectrograph with one fixed channel and one stepping channel. The channels detect energetic electrons over ranges of energies associated with visible aurora. The fixed channel is 6 KeV and the stepping channel cycles through eight energy thresholds: 54, 98, 219, 600, 1400, 3540, 8200, and 1970 eV. The data sample is taken approximately every second. The field-of-view is 3 degrees by 12 degrees.

SSJ has been improved. The second generation is called SSJ/2. It consists of a single stepping channel with six energy ranges. Nominal energy steps are 0.3, 0.68, 1.6, 3.5, 7.9, and 18 KeV. The sampling rate is 0.0922 seconds per energy step and the field-of-view is a 30 degree anti-earth cone.

Supplementary Sensor L (SSL) is a lightning detector. It operates only at night to detect lightning flashes in the 0.4 - 1.1 μm range. Peak response is near 0.8 μm. Twelve silicon photodiodes are used to detect the flashes, each photodiode viewing a different nominal 400 x 400 nm field on the earth's surface. The photodiodes are aligned in a 3 x 4 array such that the SSL's field-of-view is 1200 x 1600 nm. The SSL stores the value of the largest pulse observed by each photodiode during a one second sampling interval. The peak pulse and total number of counts per second for each detector makes up the information in the SSL data stream.

The data from all supplementary sensors are low volume, on the order of 100 bits per second. The data are multiplexed into the primary sensor data stream and recorded on board the spacecraft. No real-time readout is made to tactical sites since some computer processing is necessary for all supplementary sensor data.

Primary Sensors. Block 5D

The Block 5D satellite is illustrated in Fig. 1A-7. The Operational Linescan System (OLS) is the primary data acquisition system on the Block 5D satellite and is the system of primary importance to Navy tactical sites. The system is designed to gather and output in real-time or store multi-orbit day and night, visible and infrared spectrum data from earth scenes, and provide such data, together with appropriate calibration, indexing, and other auxiliary signals, to the spacecraft for transmission to ground stations. The data is collected, stored and transmitted in fine (F-data) or smoothed (S-data) resolution.

The OLS provides a near-constant image resolution system with optical compensation for image motion. On-board preprocessing of the data provides for the various modes of data output. Global coverage is provided, including complete terminator coverage in both visible (L-data) and thermal (T-data) modes.

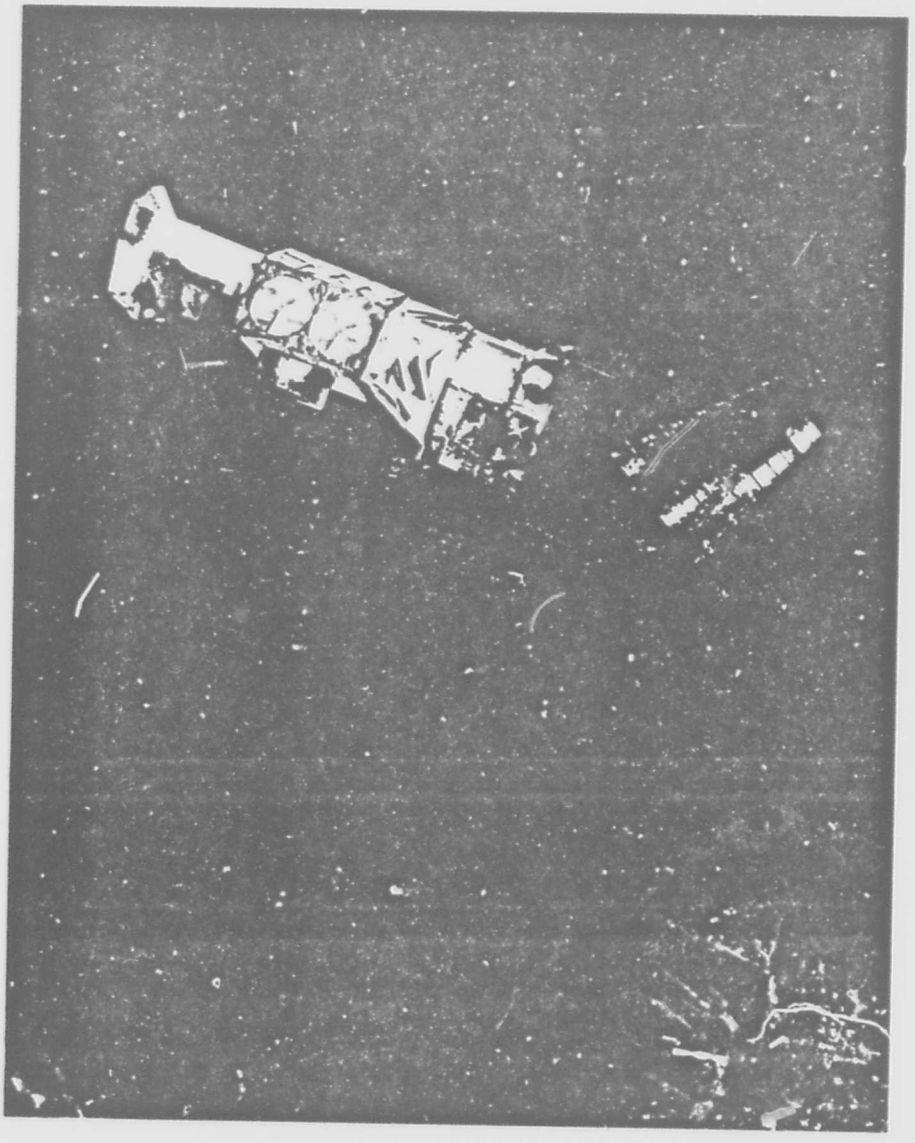

1A-7. Block 5D Satellite.

Fine resolution data is collected continuously, day and night, by the segmented infrared detector (TF-data), and continuously during daytime only by the segmented, silicon diode detector (LF-data). Fine resolution data has a nominal linear resolution of 0.3 nm. Tape recorder storage capacity and transmission constraints limit the quantity of fine resolution data which can be provided to a total of 40 minutes of data per ground station readout.

Data smoothing permits global coverage in both the infrared (TS) and visible (LS) spectrum to be stored on the tape recorders. Smoothing is accomplished by electrically reducing the sensor resolution to 1.5 nm in the along-scan direction, then digitally averaging five such 0.3 x 1.5 nm samples in the along-track direction. A nominal linear resolution of 1.5 nm results. 400 minutes of LS and TS data may be transmitted in a single ground station readout.

Additionally, a photomultiplier tube allows collection of visible (LS) data under quarter-moon or brighter nighttime conditions at 1.5 nm nominal linear resolution.

A combination of one type of fine resolution data and the complementary smoothed resolution data (LF and TS or TF and LS) is available in the real-time data transmission (RTD) mode. Either encrypted or clear data can be transmitted simultaneously with two channels of stored data. In addition, the OLS can simultaneously transmit two channels of RTD data, with each channel having encrypted or clear selectivity.

The OLS data processing subsystem provides the data management functions to process, record, and output data for as many as six special sensors.

The OLS utilizes a scanning optical telescope driven in a sinusoidal motion by counter-reacting coiled springs and a pulsed motor. This motion moves the instantaneous field-of-view of the detectors across the satellite subtrack, with a maximum scanning velocity at nadir. The scanning velocity slows as the telescope goes to edge of scan (active data swath) and reverses direction during the overscan period. The aperture size is dynamically changed to reduce angular instantaneous field-of-view as it nears the edge of scan, thereby maintaining an approximately constant scan spot on the earth. The swath width is 1600 nm from a nominal altitude of 450 nm.

The optics consist of a Cassegrainian telescope whose elements are common to both visible and infrared imagery, and a set of relay optics that separates the wavelengths and fields-of-view for the different detectors.

In the fine mode visible (LF) channel, a three-segment silicon diode detector is switched at ± 400 nm from subtrack, using either of two segments from that point to end of scan. All three segments are used and summed together within 400 nm of subpoint. Detector geometry and segment switching compensate for the optical rotation of the field-of-view, as a function of scan angle. A mirror in the telescope assembly is dynamically driven to accomplish image motion compensation by removing the satellite's along-track motion component from the motion of the instantaneous field-of-view to preserve scan line contiguity.

In the photomultiplier tube (PMT), electro-magnetic deflection of the electron beam over an aperture mask changes the angular instantaneous field-of-view to provide approximate constant resolution and image derotation.

The infrared detector, consisting of two segments, is switched at nadir to provide approximately constant ground scan-spot size and image derotation.

The frequency of oscillation of the scanning optics of fine resolution visible data is designed to provide 0.3 nm x 0.3 nm resolution.

The visible daytime response of the OLS is in the spectral range of 0.4 - 1.0 μm, chosen so as to provide maximum contrast between earth, sea and cloud elements of the image field. The visible fine mode is available for day scenes only.

The smooth resolution visible (LS) data channel (1.5 nm x 1.5 nm) provides visible data across a dynamic range from full sunlight (10^{-2} w/cm^2 sr) to quarter-moonlight (10^{-9} w/cm^2 sr). The smooth resolution visible data at night is provided from a photomultiplier tube operated in the same spectral range. For full terminator coverage, the photomultiplier tube is energized automatically as the radiance decreases. In response to various gain controls for the photomultiplier tube, visible data in the terminator region are collected with minimal light-level variations. In daytime, smooth resolution data is derived from the fine mode visible data by analog and digital data processing in the OLS. Five fine mode resolution cells are averaged along a scan line to produce a single intermediate resolution (0.3 nm x 1.5 nm) cell. Five such cells are digitally averaged along track to produce a single smooth mode cell. The smoothed mode data maintains the constant resolution of the fine mode data. The averaging of visible data to lower resolution allows storage on each OLS primary recorder of up to four orbits of both visible and infrared data.

Fine resolution infrared (TF) data are provided by the OLS infrared detector, a segmented tri-metal (HgCdTe) detector operating at approximately 105 K. The OLS infrared spectral response of 8.0 - 13.0 μm was chosen to optimize detection of both water and ice crystal clouds. The sensor output is normalized in terms of the equivalent blackbody temperature of the radiating object; that is, a shaping network is employed to change the fourth-power-of-temperature response of the detector, such that sensor output voltage is a simple, linear function of scene temperature. This detector is passively cooled by a radiative cooler viewing free space. The tri-metal detector is accurate within 1 K rms across the (equivalent blackbody) temperature range 210 K to 310 K. The noise equivalent temperature difference of the infrared system is 1 K across the same range.

The smooth resolution infrared (TS) data is obtained by on-board processing of the fine mode infrared data, as described for the visible channels. It should be noted that fine mode visible and infrared data are gathered through the same (coherent) optics and are digitally identified. Thus, corresponding visible and infrared data cells maintain their unique one-to-one location correspondence throughout the data processing chain.

The OLS on-board data processing subsystem performs command, control, data manipulation, storage, and management functions. Commands are received from the ground through the spacecraft command system, stored, and processed according to time codes. The OLS data processing subsystem also executes commands, accomplishes the smoothing of fine resolution data, derives gain commands from orbital parameters for normalization of visible data and dynamic signal control, and outputs the data to the spacecraft communications system. All data are processed, stored and transmitted in digital format.

The OLS data processing subsystem also accepts data from the special sensors, and inputs this data into the smooth data stored format for transmission.

S-band transmitters are provided on the Block 5D spacecraft for data transmission. Two of these may be operated simultaneously for stored data playback. A third S-band transmitter is used for direct digital transmission (DDT) to tactical sites around the world.

DDT consists of either LF and TS or LS and TF data, transmitted in digital format at 1.024 Mbps. DDT data will normally be encrypted.

There are five special sensors on the Block 5D spacecraft.

Special Sensor D (SSD) is the Atmospheric Density Sensor which will provide a measure of major atmospheric constituents (Nitrogen, Oxygen, and Ozone) in the earth's thermosphere (100 - 250 km in altitude) by making earth-limb observations of the ultraviolet radiation from this atmospheric region. The SSD is currently under development. The sensor will measure the radiation emitted in the ultraviolet spectral region from excitation of molecular nitrogen by impinging solar radiation. The intensity of the emitted radiation is proportional to the excitation rate and the number of molecules at any given altitude. Funneltrons and a photomultiplier tube will detect the radiation after it passes through a collimator which provides a 0.1 x 4.0 degree field-of-view. The SSD will be mechanically driven to scan vertically through the earth's limb in about 30 seconds. The instrument will provide approximately 50 sets of density profiles on the daylight portion of each orbit.

Special Sensor J (SSJ) is the Precipitating Electron Spectrometer. A small, lightweight (3 lb) sensor, the SSJ counts ambient electrons with energies ranging from 50 eV - 20 KeV. Utilizing a time-sequenced variable electrostatic field to deflect the particles toward a channeltron detector, the sensor determines the number of electrons having energies within certain sub-ranges of the 60 eV - 20 KeV spectrum.

Special Sensor H (SSH) is the Temperature/Water Vapor/Ozone Radiometer. The SSH, a scanning infrared radiometer, will provide global data which yields vertical temperature profiles, vertical water vapor profiles, and total ozone concentration.

Special Sensor B (SSB) is a gamma radiation measurement sensor provided to DMSP by an Air Force Agency (AFTAC).

Special Sensor M (SSM), the passive microwave temperature sounder, will be a 7-channel scanning radiometer which will measure radiation in the 5 - 6 mm wavelength region (50 - 60 GHz) to provide data for profiling on a global basis atmospheric temperatures from the earth's surface to altitudes above 30 km. It is being designed to scan in synchronization with the infrared temperature and water vapor sounder (SSH) already developed. The microwave sounder complements the infrared sounder by providing temperature soundings over previously inaccessible cloudy regions of the globe and at higher altitudes than are attainable with the infrared sensor. The SSM will occupy the SSB location on selected satellites.

1B Data Modes for Image Analysis

System Description

Hardcopy (film transparency) output is a product of the data display system (DDS). The function of this system is to accurately reproduce the image scenes as recorded by the spacecraft's primary sensors. The Navy system uses an integrated hardware/software concept combining the flexibilities of a minicomputer with automatic functions of a hardcopy generator, permitting several varieties of data output to meet the needs of the user. For example, data enhancement and infrared "slicing" techniques are computer controlled as opposed to being "hard-wired" thereby permitting a wide range of variations in the output imagery. The system also permits copy annotation which may include full documentation for important parameters of each specific pass, in addition to a gray scale for the particular visible enhancement or infrared enhancement mode selected.

The DDS consists of three basic units, the data processor, the computer, and the hardcopy generator. A teletype unit and a digital magnetic tape unit are associated as peripheral units. A typical shipboard unit, is illustrated in Fig. 1B-1.

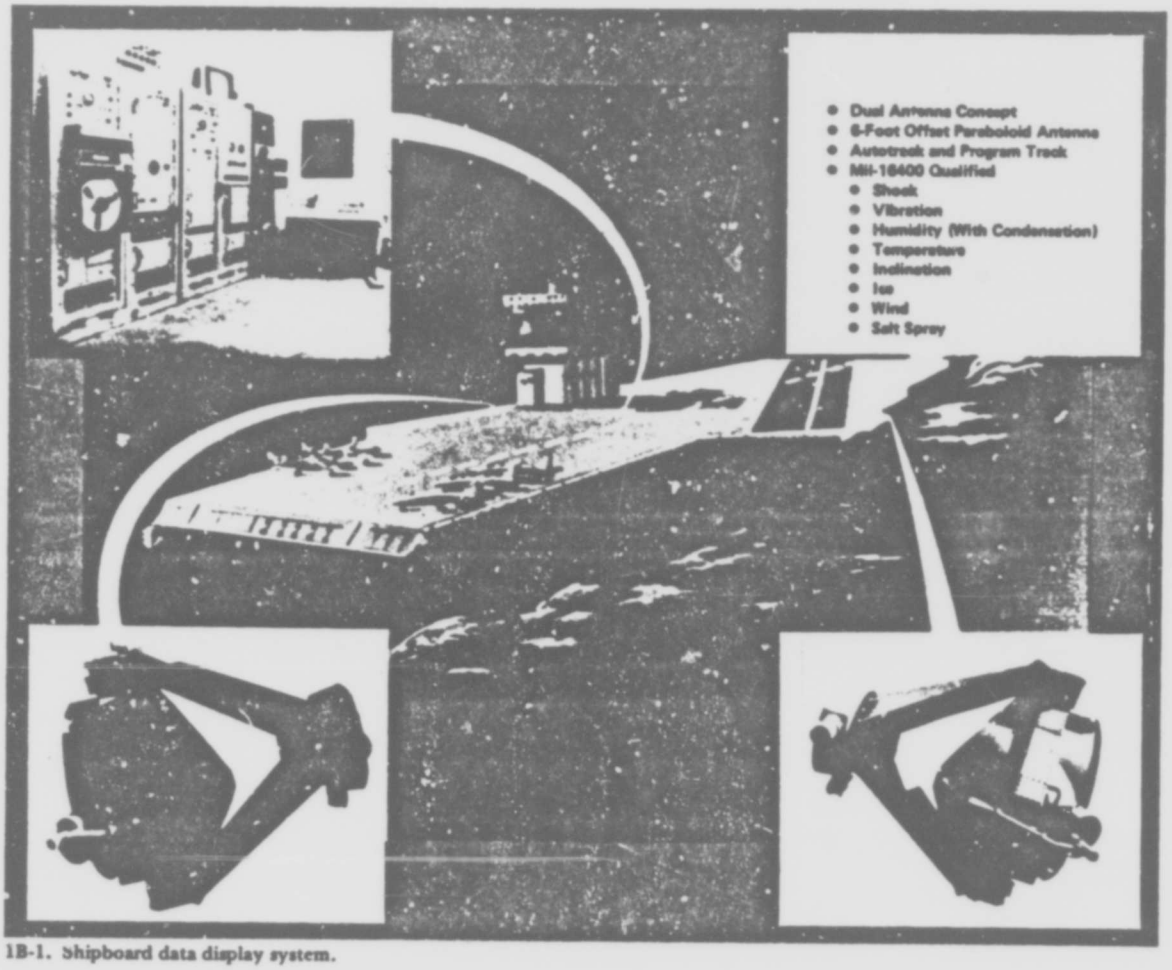

1B-1. Shipboard data display system.

The data processor subsystem includes a decommutator, a time-code reader, and a computer interface.

The data processing hardware and software synchronizes and decommutates the input pulse-code modulated (PCM) data, makes necessary parameter corrections/manipulations, and converts the resultant to digital picture information.

The decommutator provides frame and line synchronization for downlink data and transfers video, calibration, and Greenwich Meridian Time (GMT) data into the computer core memory via the computer interface unit. The time-code reader (housed in the decommutator chassis) converts the timing pulse to a computer code so that the GMT annotation of selected scan lines is included in the hardcopy output along the edge of the imagery.

Premission parameter-option selection for the DDS is accomplished by operator communications through the teletype unit with the software. Premission, real-time, and postmission software programs for processing data are permanently stored in the computer mainframe and expansion memories. These programs are initially loaded from recorded tape cassettes during system setup. A digital magnetic tape unit is contained as an integral part of the data processing subsystem. Because it is a cassette unit, operator handling is held to a minimum, and tape storage requires very little space.

Data processing subsystem functions can be summarized as follows:

- Decommutate and synchronize input imagery data.
- Correlate GMT to imagery data.
- Digitally correct, calibrate, and project the imagery data.
- Format modified imagery data for hardcopy generator transfer.
- Store/verify satellite parameter files.
- Provide operator - central processing unit (CPU) communications.
  - Accept premission input data.
  - Generate system setup checklist.
  - Provide output data option selections.
  - Generate postmission summary.
- Generate output imagery copy annotations.
- Format and print out special teletype messages.
- Handle power and equipment interrupts.

The hardcopy generator (HCG) accepts the modified, conditioned computer generated imagery data in increments of a single line. The display buffer (DB) provides temporary storage for this information in random-access, solid-state memories. The DB also provides the control to the computer output channel. Upon the receipt of a complete line of data, the DB unloads its memory into a demultiplexer, which divides the 24-bit computer words into four discrete 6-bit bytes. The resulting data are input to the display control logic (DCL). The 6-bit words are then used to access any one of 64 discrete one-shot multivibrator circuits. The pulse-width duration of the one-shot outputs increases with respect to increasing gray-shade levels. This information is then transferred in a serial format to the cathode ray tube (CRT) modulation circuits. CRT sweep and retrace are synchronized to the beginning and end of each line of data. The resulting light output from the CRT travels through a folded optical assembly and is focused onto photographic film which is stepped sequentially as each new scan line is added.

When data transmission is completed, the computer issues a command to the HCG, which causes the film to be cut and transferred

to the processor. Once there, it is automatically routed through the developer, fix and wash tanks, dried in the film dryer, and deposited in a film catch box.

The total HCG operation is controlled by a modularized microprocessor contained within the DCL. The microprocessor controls the incoming data, the film positioning, monitors possible HCG malfunctions, and identifies problem conditions to the computer. This feature provides maximum flexibility for interface redefinition in the event that the HCG should be used in a different system.

A visual light emitting diode (LED) display is provided at the DCL for operator convenience to verify the status of the internal HCG operation.

In summary, these are the functions of the HCG:

- Decode CPU data and communications.
- Control all CRT and film processing functions.
- Convert imagery data to CRT beam pulse-width modulation.
- Generate film images from line scan CRT.
- Provide back-to-back imaging.
- Develop, fix, and dry the output film image.
- Test pattern generation for self-test function.
- Provide control panel and CPU status of HCG functions.

Included in the DDS software is a 24-bit word central processing unit (CPU) with 64K of memory to establish a centralized operator control point and to allow maximum flexibility in the data processing algorithms via software.

During the equipment setup phase, the operator establishes display requirements for the image. The CPU converts operator requests into device commands to the system hardware components. All system devices have been designed to be programmable from the CPU to allow a centralized control point of operation.

The software approach to the implementation of the data processing algorithms allows for sophisticated data processing techniques with maximum flexibility for custom-tailored changes to meet specialized requirements.

The system software allows operator selection from a set of fixed data enhancement curves in addition to the general capability for the operator to define any data modification mapping corresponding to his imaging requirements. The set of fixed mapping curves is readily expandable through software and any data enhancement function can be implemented. Currently provided are low, high, normal, and logarithmic enhancement for visible data. Temperature expansion and thresholding techniques are provided for infrared data.

The system software uses a Transverse Mercator Projection in the across-track dimension to accurately map input data samples for imaging. This technique eliminates the undesirable visual effects created by the earth's curvature (foreshortening) on the product.

The software approach allows virtually unlimited flexibility in the selection of map scales and selection of smaller segments of the input data set for scale expansion. For scale expansion, the operator may select any point in the image as the center point by specifying its location in two dimensions. The CPU then produces an expanded image about the operator-specified center point. The current software

provides a normal (X1) (1:15M scale), a double (X2) (1:7.5M scale), and quadruple (X4) (1:3.75M scale) expansion capability.

The system software provides character annotation in the margins of the imaged data. (The data time is tagged with a GMT annotation in real-time in the right margin.) All information pertinent to the image is annotated on the top margin. This information includes date, satellite, orbit, direction (NE or SW) of upper, right corner of data, and display variables such as satellite identification number, rise time, fade time, altitude, roll, data type, data enhancement, image center point, and scale. An additional capability is provided for the operator to transmit lines of annotation, containing any information, from the operator communications device to the image via the central processing unit software.

DMSP Data Types and Enhancement Curves

Four types of data are produced by the spacecraft's primary sensors; however, it is not possible for a tactical readout site to receive all of them. The DMSP transmitter operates at 512 kilobits per second (kbs) (5C) or 1024 kilobits per second (5D). This allows transmission of a multiplexed data stream consisting of HR, MI and either VHR or WHR for the Block 5C spacecraft and LF/TS or LS/TF in the case of the Block 5D spacecraft. The data rates of VHR (LF) and WHR (TF) are so massive that both cannot fit into a 512 kbs data stream. The normal operating mode is for VHR (LF) transmission on the ascending portion of an orbit and WHR (TF) on the descending orbit. Both HR and MI data are transmitted to all receiving sites for Block 5C while either LS or TS data are transmitted for Block 5D. If the spacecraft is placed in an early morning ascending (early evening descending) orbit where there is an earth terminator problem in the visible scene, the VHR (LF) data are transmitted on the ascending portion of the orbit near the equator where there is sufficient daylight illumination for visible imagery (along-scan automatic gain control for visible imagery through the terminator region exists only for the HR (LS) sensor). When the spacecraft progresses poleward far enough so that the edge of the VHR (LF) scan line enters the terminator, the transmission is switched to WHR (TS).

The two types of visible data, VHR and HR for Block 5C spacecraft, complement each other for several meteorological applications. The VHR and equivalent LF are designed to examine weather systems in detail, with a 0.3 nm resolution, such that not only is the overall synoptic pattern readily identifiable, but the details of the cloud patterns and their structure are observed. As such, VHR and LF are the primary visible products used for direct readout during daylight. These are supplemented by the 2.4 nm MI and 1.5 nm TS infrared data for thermal comparisons. The HR (2 nm resolution) is used as a backup to the VHR during daytime operations at direct readout locations. At nighttime the low-light capabilities of the HR and LS sensors provide useful products of 2 nm resolution and 1.5 nm respectively (under quarter-moon conditions) which greatly improves the analyst's capability to correctly interpret nighttime infrared data in modes WHR for Block 5C and TF for the Block 5D spacecraft.

. Sensor resolution for both Block 5C and Block 5D degrades somewhat as distance from the satellite subpoint increases toward the eastern and western horizons. Fig. 1B-2 is a graphical illustration which summarizes surface resolution dependence on distance from satellite subpoint for each of the Block 5D sensors.

Contrast enhancement is used to vary the distribution of gray shades in these data. Fig. 1B-3 illustrates the set of 4 fixed mapping curves (Mods 0 through 3) devised for the system. Mod 5 is a special enhancement devised by the San Diego site location using the expandable software capability of the Navy System.

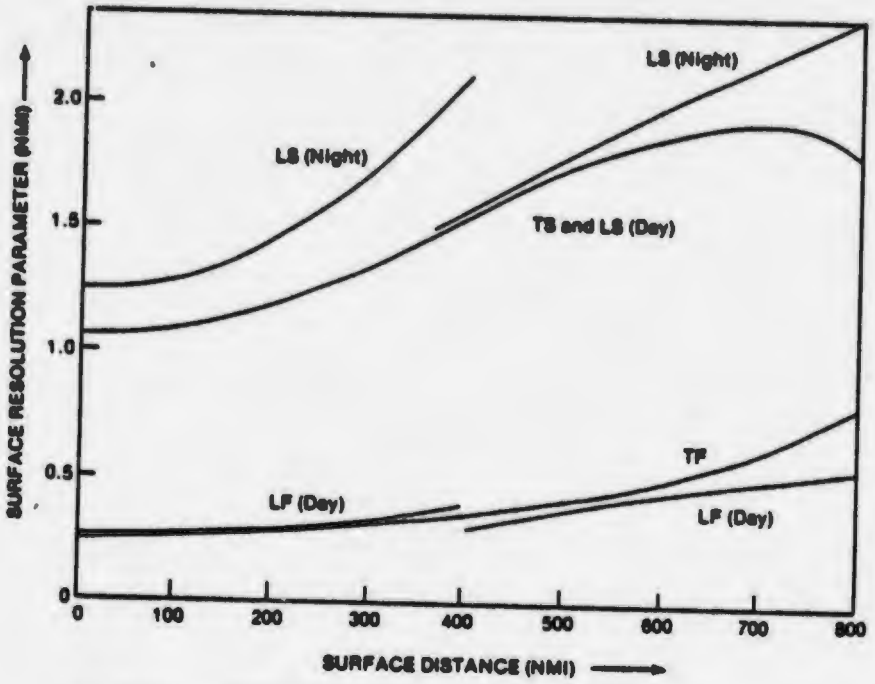

1B-2. Surface Resolution Parameter. (Courtesy "Block 5D Compilation," Hq. USAF SAMSO, July 1975).

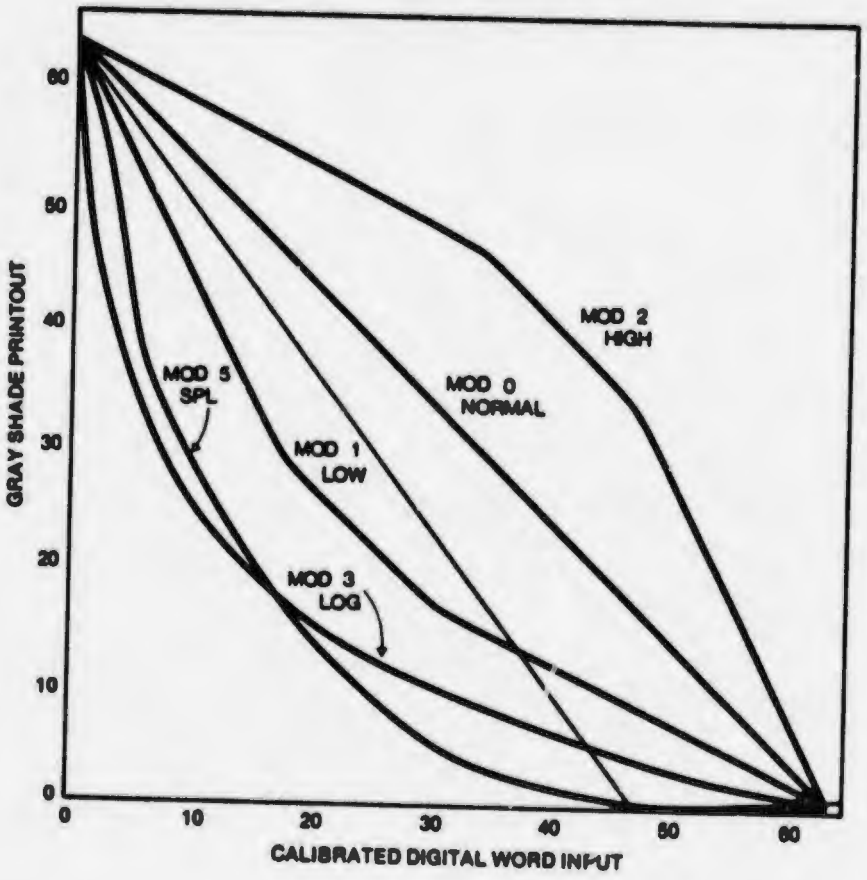

1B-3. Mapping Curves Mods 0 through 3.

Visible Mode Data: VHR[1]
Mod O. Normal Enhancement Mode

Fig. 1B-4 is an example (78% of original size) of VHR (very high resolution, 0.5 nm) data in the Mod O, or normal enhancement mode, and normal map scale (1:15 million). In this mode the data are presented using a linear scale of gray shades, from dark tones to light tones, over the signal range (see gray scale at top of figure). Note that terrain features (dark tones/low reflectivity) are somewhat subdued and normally bright cloud masses (light tones/higher reflectivity) are also somewhat subdued in appearance. This presentation is characteristic of the linear gray-scale mode.

The best separation (contrast) between gray shades steps is apparent in the mid-scale range. The mid-scale gray shades (middle tones/average reflectivity) are excellent for bringing out the structural details of cloud systems of great vertical development such as thunderstorms and squall lines. Although contrast in low-level (and less reflective) cloud forms, such as stratus and stratocumulus, and lesser developed convective cloudiness over land areas is not optimum, it is adequate.

1. All DMSP data shown in this section are from the Block 5C system. Block 5D data are expected to be similar in appearance. Enhancement mode capabilities are identical for both systems with the Navy processing and display equipment.

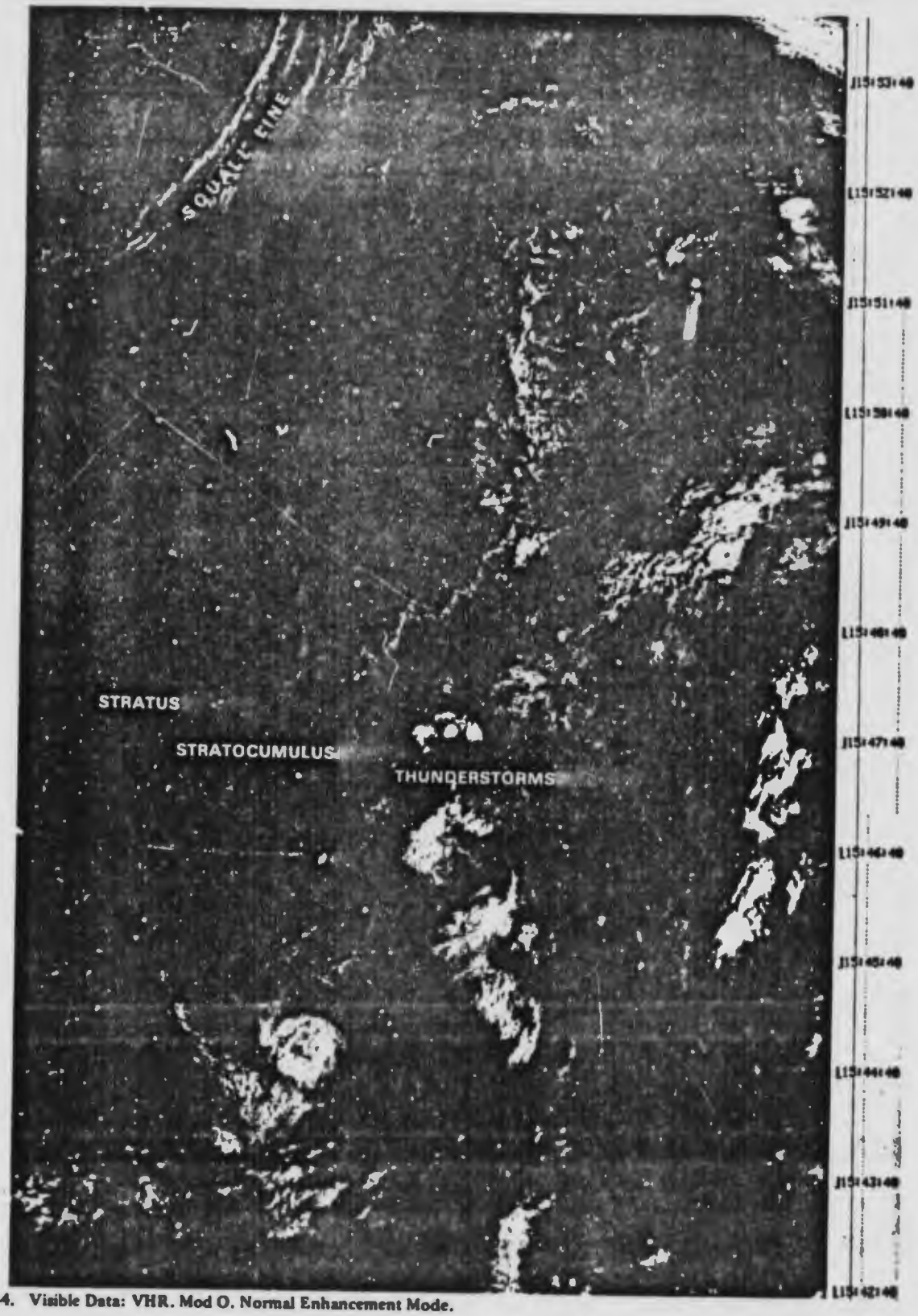

1B-4. Visible Data: VHR. Mod O. Normal Enhancement Mode.

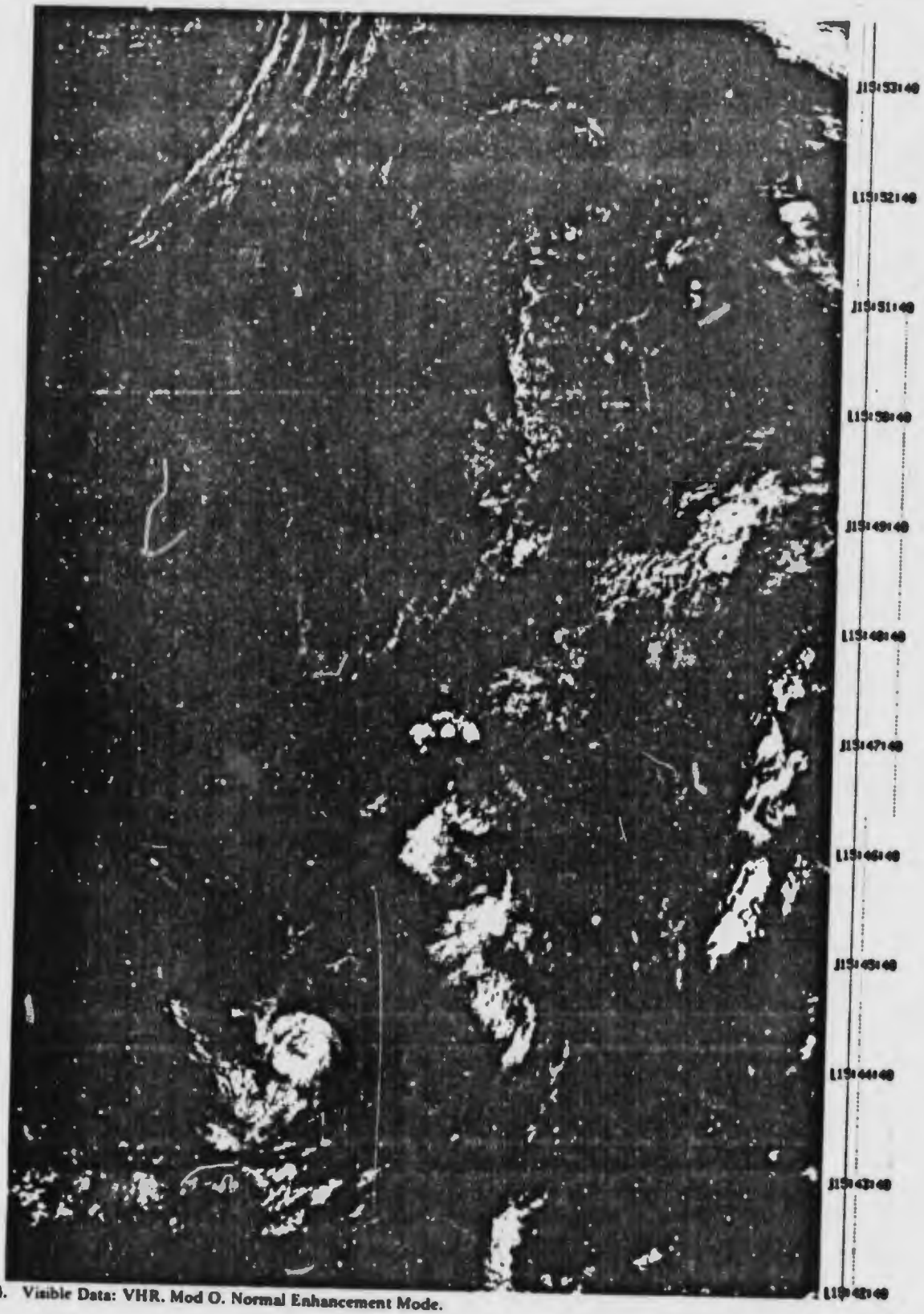

1B4. Visible Data: VHR. Mod O. Normal Enhancement Mode.

1B-5. Visible Data: VHR. Mod 1. Low Enhancement Mode.

Visible Mode Data: VHR
Mod 1. Low Enhancement Mode

In order to provide more definition in the dark tone areas of the imagery, Mod 1, a low enhancement mode was devised (Fig. 1B-5, right figure). The gray-shade scale in this mode shows a distinct separation in the tonal steps at the low end of the scale, in comparison to the Mod 0 mode. This provides for better definition in the darker tone areas of the imagery. An improvement in terrain detail is apparent in Fig. 1B-5 when compared to Fig. 1B-4 (left figure). More detail can be observed not only over land but also over water areas (as gray-shade patterns not identifiable as cloud forms), such as in the sunglint area south of Mexico and in the stratocumulus cloudiness area west of Baja. These gray-shade patterns are often important indicators of sea state, low-level wind direction, aerosols and atmospheric moisture, and other parameters, as will be discussed in later sections of the Guide.

Note, however, that the details (middle tones) in the bright cloud masses are degraded in comparison to the normal enhancement mode (Fig. 1B-4). In particular, compare the lack of cloud detail in Hurricane Jewel, south of Baja, in the low enhancement and the normal enhancement modes. On the other hand, observe how small, low-level cloud elements in the cloud pattern surrounding Hurricane Jewel are emphasized in the low enhancement mode. These cloud forms appear with better definition in this presentation than in any other enhancement mode. The low enhancement mode is therefore well suited for deriving low-level winds based on cloud alignment.

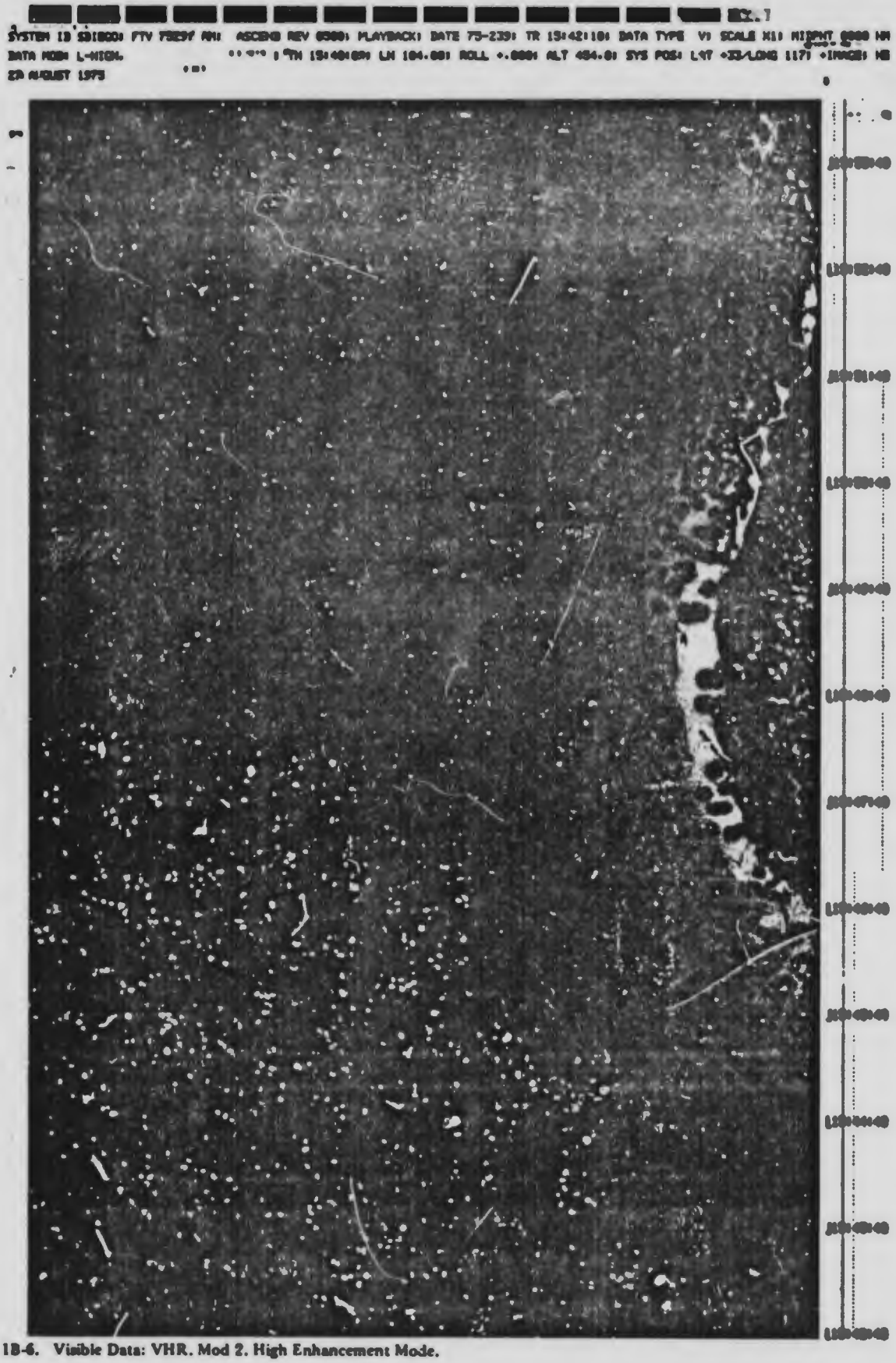

1B-6. Visible Data: VHR. Mod 2. High Enhancement Mode.

Visible Mode Data: VHR
Mod 3. Log Enhancement Mode

Mod 3, the log enhancement mode, is illustrated in Fig. 1B-7. In this mode, the contrast between gray-shade steps in areas of lower reflectivity is increased at a sacrifice of contrast in the average and high reflective areas. In the dark tone area of the gray scale above the legend, note that there is a distinct difference (contrast) between adjacent gray-shade steps. The log enhancement mode is the only mode that provides such sharp contrast steps between gray shades at the low end of the gray scale. Something remarkable comes out of this as can be seen by referring to the area to the south of Hurricane Jewel. Note the dark area appearing between Hurricane Jewel and the strong convective cloud band to the southeast. This anomalous gray-shade area occurs in an area of anticyclonically turning low-level cloud lines, suggesting high pressure and subsidence in advance of an approaching storm, Tropical Storm Katrina (off the picture to the southeast of the bright convective cloud band). The VHR sensor, as will be discussed in following sections, is sensitive to changes in reflectivity due to atmospheric scattering. The evaporation of haze droplets in an area due to subsidence results in less light being reflected to the spacecraft sensor from the area in comparison to that reflected from a surrounding more moist area. Hence measured brightness would be reduced. The log mode presentation emphasizes such differences in reflectivity. Similar appearing dark areas which may be related to dry conditions can be observed off the west coast of Baja.

1B-7. Visible Data: VHR. Mod 3. Log Enhancement Mode.

Visible Mode Data: VHR
Mod 5. Special Enhancement Mode

A final enhancement mode, called MOD 5 SPL, was developed at the San Diego site location. This mode increases contrast in the middle gray-shade tones at mid-scale, as shown in Fig. 1B-8. It will be noted that this mode delineates more clearly, than many of the others, the complete range of cloud details; from the squall line embedded in the frontal system; to details in the mid-lautude field of stratocumulus; to delineation of thunderstorm structure; and, finally, in enhancing details of hurricane and convective cloud band structure.

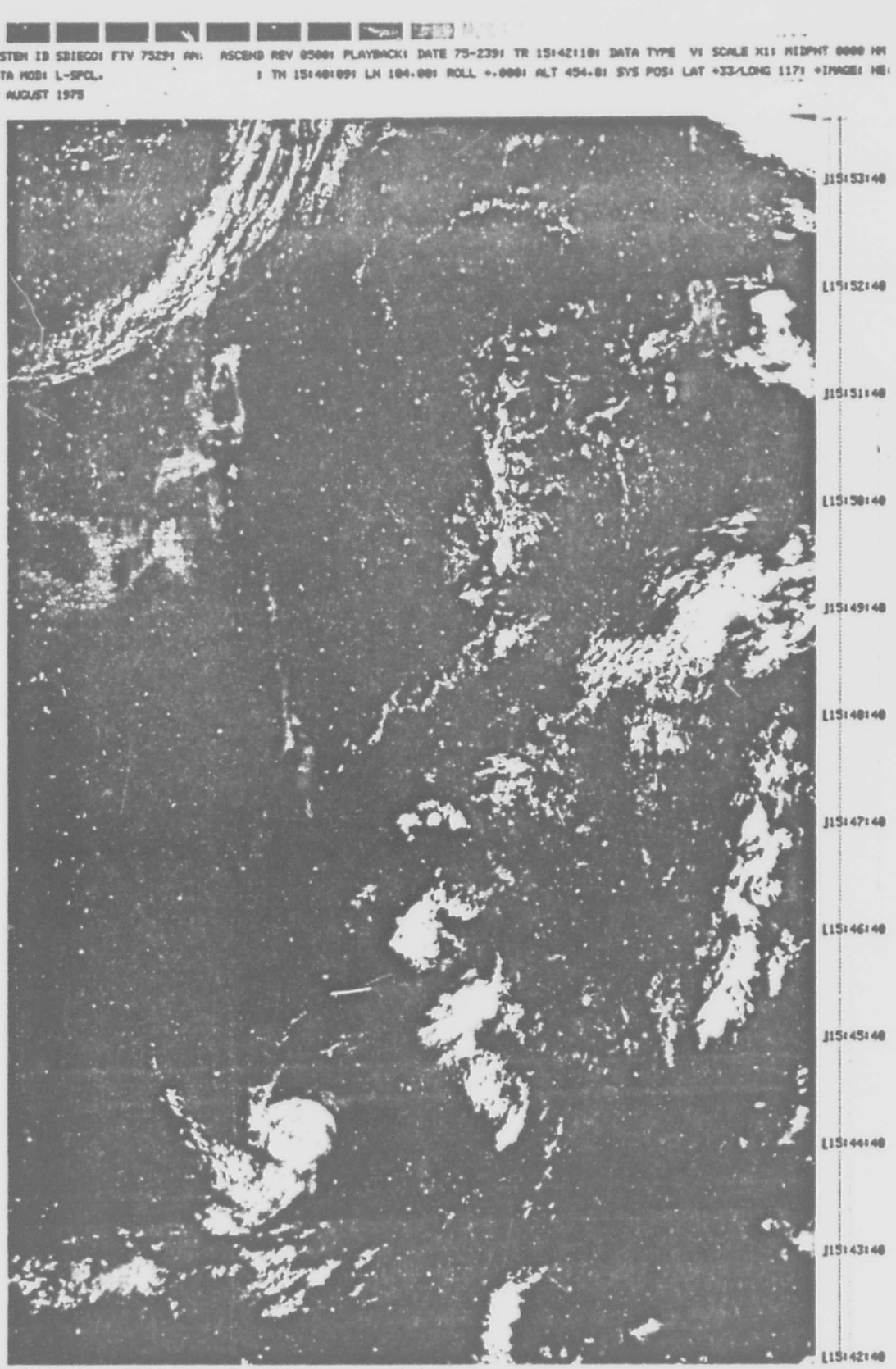

1B-8. Visible Data: VHR. Mod 5. Special Enhancement Mode.

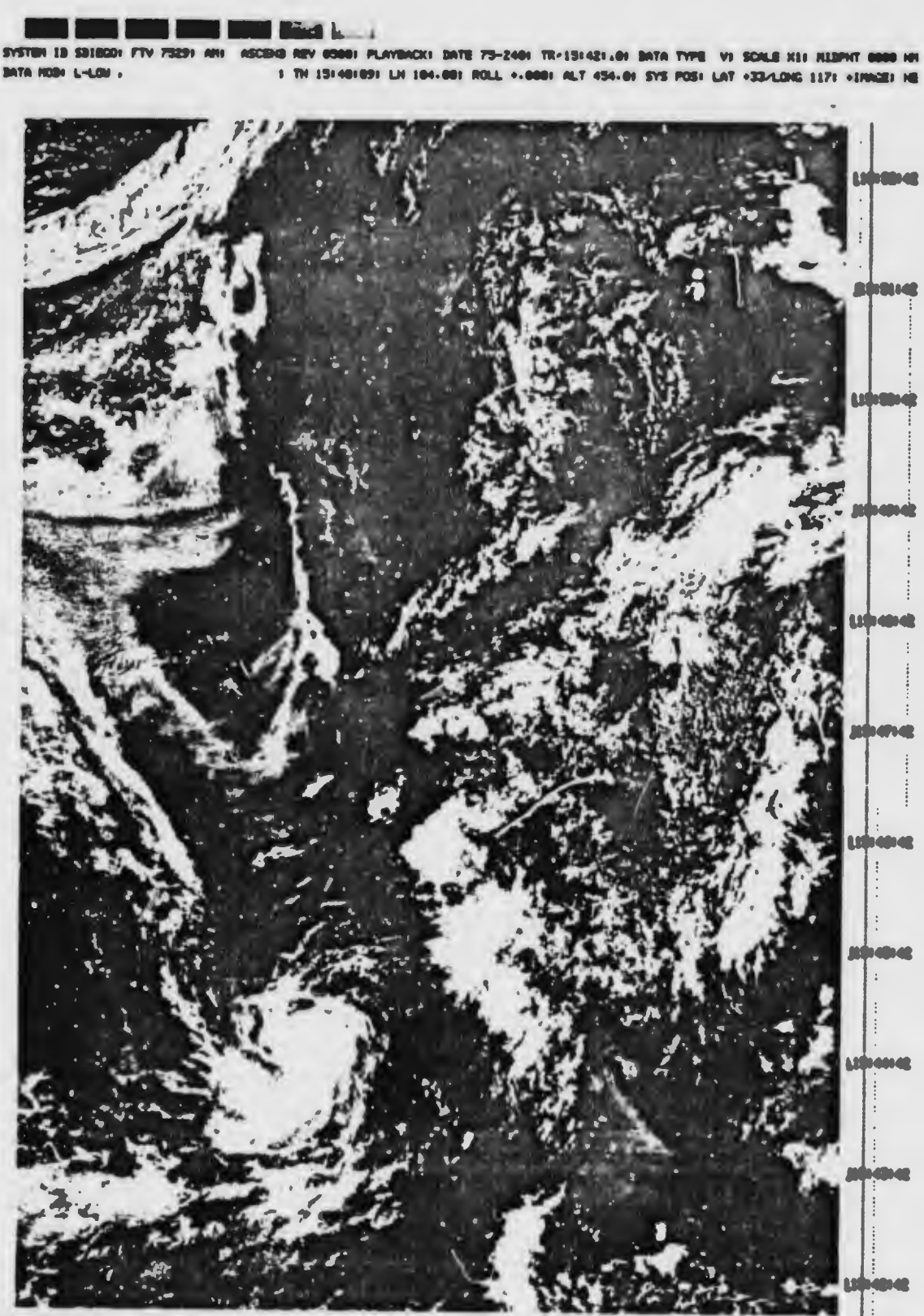

1B-5. Visible Data: VHR. Mod 1. Low Enhancement Mode.

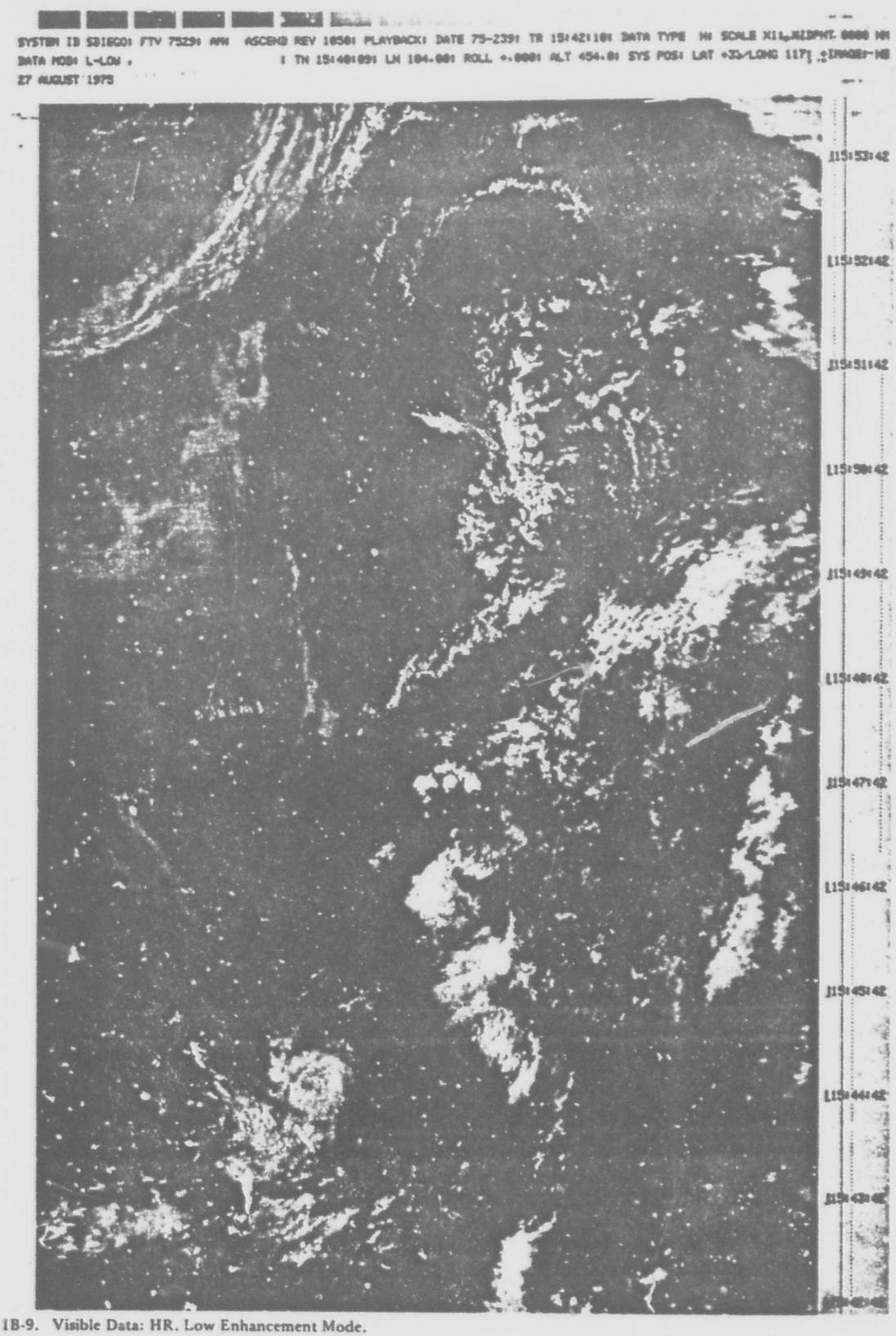

1B-9. Visible Data: HR. Low Enhancement Mode.

Visible Mode Data: VHR/HR Comparison
Mod 1. Low Enhancement Mode

HR (visible, high resolution, 2 nm) data are acquired simultaneously with the VHR direct readout transmissions. Fig. 1B-9 (right figure) shows HR data in the low enhancement mode for this particular series. The gray-shade presentation utilizes the same enhancement curve as that for low enhancement in the VHR data (Fig. 1B-5, left figure). A close examination of these two figures reveals the obvious lesser resolution of the HR (2 nm as opposed to 0.3 nm) data in comparison to the VHR, especially along the eastern and western edges of the HR data where resolution decreases from 2 nm at the center to 12 nm at the data edge. Nevertheless, the basic elements for meteorological interpretation are largely present and HR data must be considered as excellent backup data for the VHR.

HR data can be processed using all the modes that are available for VHR data. Normally, expanded scale is not used for HR data due to the wider spacing of its scan lines compared with VHR. There is one HR scan line produced for every six VHR scan lines. (See Section 1A-1.)

Visible Mode Data: HR (Nighttime)
Mod 1. Low Enhancement Mode

HR data from the descending (nighttime) portion of the spacecraft's orbit has several uses, depending on the amount of lunar illumination. When the lunar phase is one-half moon or greater, visible mode images have the same clarity as images obtained in sunlight. An example of low-light HR data over the Gulf of Mexico and the eastern United States is shown in Fig. 1B-10. Note that the imagery orientation annotation, SW (Southwest), appears in the lower left corner, with the legend upside down, in this nighttime presentation. The appearance of city lights and lighted highway systems is a striking characteristic of these data. The images of city lights have two uses. First, they serve to more accurately locate (or grid) the MI (infrared) data. Second, when the city lights appear diffuse, they give information about the optical thickness and particle sizes in the clouds between the light source and the satellite sensor. Close examination of HR data has also revealed that lights are occasionally visible from well-lighted fishing vessels, oil rigs, oil fires, forest fires, rice patty fires, and volcanoes. The aurora glow is visible in data acquired by this sensor as well as cloud areas illuminated by lightning flashes.

Meteorologically, the usefulness of the HR data is well illustrated in this example. Clear skies over the eastern United States suggests high pressure with east winds over the northern Gulf of Mexico and southwest winds over the Great Lakes area in advance of the squall line extending NE to SW through the central United States. The NMC surface analysis for 0000 GMT shows a center of high pressure just off the Carolinas and a surface ridge line extending from this area west-southwestward to southern Texas. From the HR data we infer an easterly wave over the Gulf of Mexico with a vorticity center just NW of the Yucatan Peninsula. The NMC analysis verifies the existence of a wave perturbation over the Gulf with a closed 1006-mb pressure center due west of Yucatan.

By superimposing a negative transparency of the MI data over the corresponding HR data, a unique 3-dimensional depiction of the atmosphere at night is obtained which is truly striking and very useful as an operational briefing aid.

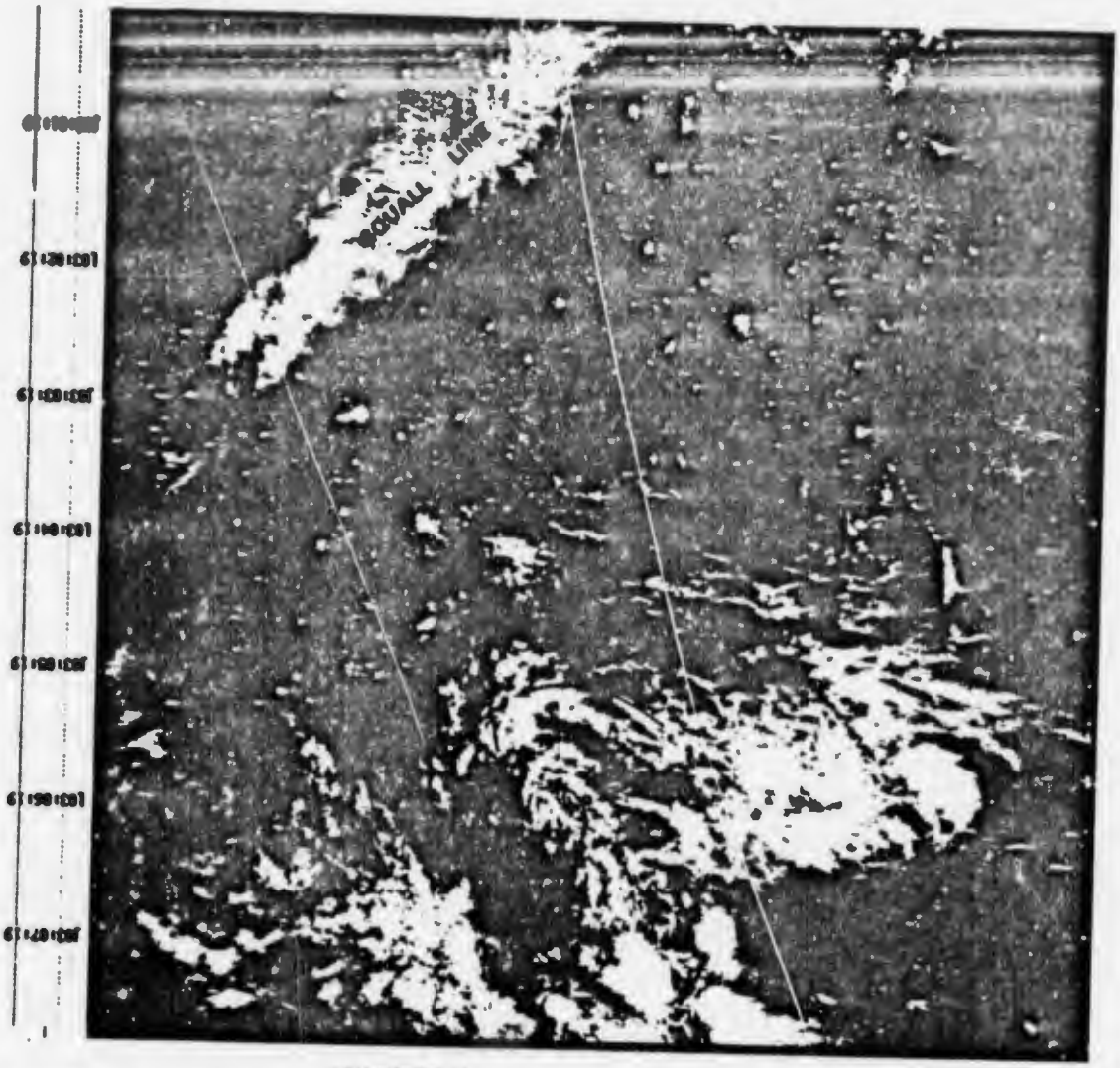

1B-10. Visible Data: HR (Nighttime). Low Enhancement Mode.

VHR-Expanded Mode Data
Mod 5. Special Enhancement Mode

The VHR can also be expanded to a scale of 1:7.5 million (X2) (800 nm horizontal swath) or 1:3.75 million (X4) (400 nm horizontal swath) with the complete range of enhancement modes available for normal scale (1:15 million) data. When VHR data are expanded no new information is created; it is simply an enlargement of the imagery which aids in visual identification of the small-scale features already present in the normal scale imagery. Expanded data can be processed directly from the spacecraft's transmission signal or replayed from a tape recording. Fig. 1B-11 is an example of a (X4) VHR Expand over Hurricane Jewel taken from the same data as earlier examples (Figs. 1B-4 through 1B-9). This presentation has been processed in the MOD 5 special enhancement mode. The usefulness of an expand capability is demonstrated in this example which shows a series of concentric bright arcs near the probable center of circulation. By noting the arc of smallest diameter, the center of circulation is defined. These arcs can also be seen in the normal scale data but are not obvious without a keen eye or magnifying glass.

Similar small-scale features of importance for operational applications are often revealed by choosing an expanded VHR depiction, in the appropriate enhancement mode, over the prime area of tactical interest.

1B-11. Visible Data: VHR(X4) Expanded. Mod 5. Special Enhancement Mode. 1549 GMT. 27 August 1975.

Infrared Mode Data
Block 5C and Block 5D

The two types of infrared data for the Block 5C spacecraft are MI and WHR (2.4 and 0.3 nm resolution, respectively). The corresponding infrared sensors for Block 5D are TS and TF (1.5 and 0.3 nm resolution, respectively).

The infrared mode sensors are co-located with the visible mode sensors. Common optics insure that the areas covered by the visible and infrared sensors are viewed simultaneously and in the same perspective. This arrangement allows direct comparison of the visible and infrared data, and permits the meteorologist to envision the three-dimensional aspects of the cloud scene generated by atmospheric motions.

The MI and TS, WHR and TF sensors were developed to serve several different purposes for the meteorological analyst. MI and TS data are used as the primary infrared data for comparison with VHR and LF visible data. They are also the more accurate infrared data for use in quantitative thermal determinations of cloud top or land/sea surface temperatures. MI and TS data are transmitted to tactical sites on both ascending (day) and descending (night) orbital passes. WHR and TF data are only available when VHR and LF data are not being sensed. Thus, WHR and TF data are the primary very high resolution imagery data available during nighttime orbital passes. They are used much as VHR and LF are: to identify the overall synoptic pattern and observe the details of cloud patterns and structure.

Infrared data may be processed in any of three separate modes: T-Normal, T-Threshold, and T-Expand. T-Normal is used to show the distribution of cloud top temperatures through the atmosphere and is displayed in up to 64 shades of gray in the range from 210 K - 310 K. T-Threshold is used for thermal contouring and has not more than four shades of gray. In this mode, the operator, through the teletype and computer interface units, selects three temperatures (T_1, T_2, and T_3) in the range between 210 K and 310 K. As an example, if the temperatures selected are: T_1 = 300 K, T_2 = 280 K and T_3 = 260 K, the hardcopy generator will produce a temperature contoured transparency showing four shades of gray. The darkest gray shade will represent temperatures of 300 K or higher. The next lighter gray shade will represent temperatures of 280 K to approximately 298.4 K. The lightest gray shade correspondingly will represent temperatures in the range 260 K to about 278.4 K. Finally, temperatures in the range 258.4 K or lower will appear white. If a negative version of this output is desired the operator simply flips the negative/positive switch on the display to the negative position. In this configuration gray shades are reversed such that colder temperatures appear black instead of white. This mode of display is very useful for overlay purposes since the IR can be superimposed over the visible mode positive data without blocking out details of low cloud structure. An impressive and very useful 3-dimensional depiction of the atmosphere is thus obtained.

In the T-Expand display mode two temperatures, T_1 and T_2, in the range between 210 K and 310 K are selected. The full dynamic range of gray shades from white at the low-end of the gray scale to black at the upper-end of the gray scale will then be devoted to depicting temperature variations within that temperature interval. For example, in the positive mode of data processing, if T_1 = 300 K and T_2 = 275 K, all temperatures 300 K and warmer will appear black. Similarly, all temperatures of 275 K and colder will appear white. 15 discrete gray-shade tones from light gray to dark gray depict intermediate temperatures in 1.5625 degree intervals.

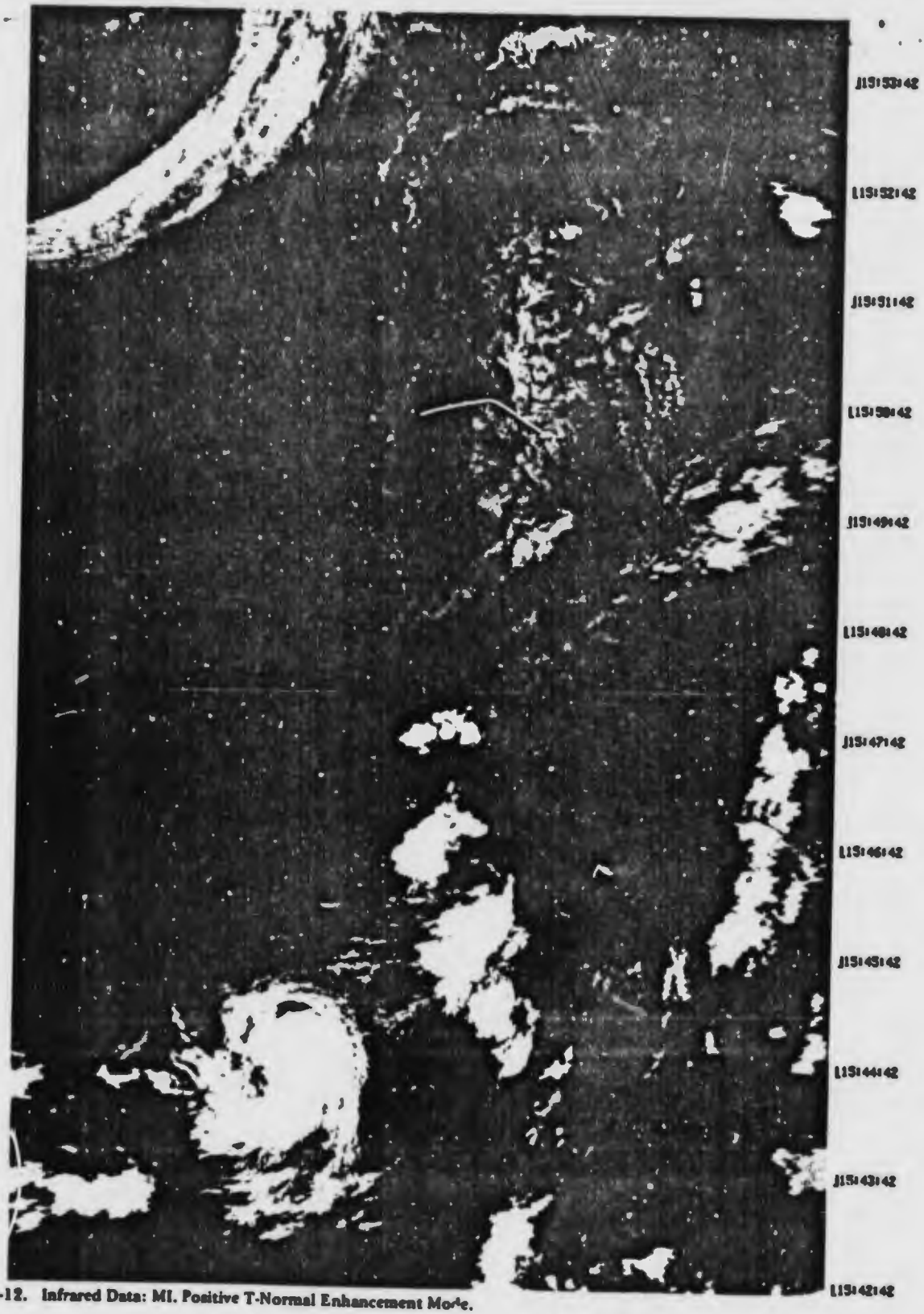

1B-12. Infrared Data: MI. Positive T-Normal Enhancement Mode.

1B-15. Infrared Data: MI. Negative T-Normal Enhancement Mode.

Infrared Mode Data: MI (Positive/Negative Mode Comparison)
T-Normal Enhancement Mode

Fig. 1B-12 is an example of MI infrared data processed in the positive T-Normal mode, where 64 gray shades depict the range of temperatures from 210 K - 310 K. The negative mode T-Normal presentation is shown in Fig. 1B-13. In comparing the two depictions, note the reversal of gray shade tones in the corresponding gray scales and the gradual merger from light to dark gray tones over the length of the gray scale.

Infrared Mode Data: MI
T-Expand Enhancement Mode. Range 275 K-300 K

For a detailed examination of the low-level thermal field, to obtain sea surface temperature differences, etc., a T-Expand mode may be selected as shown in Fig. 1B-14. This example shows features of the earth and atmospheric thermal field in the temperature interval 275 K - 300 K. Note the greater detail and contrast over land and water made possible through this mode selection as opposed to the T-Normal mode (Fig. 1B-12).

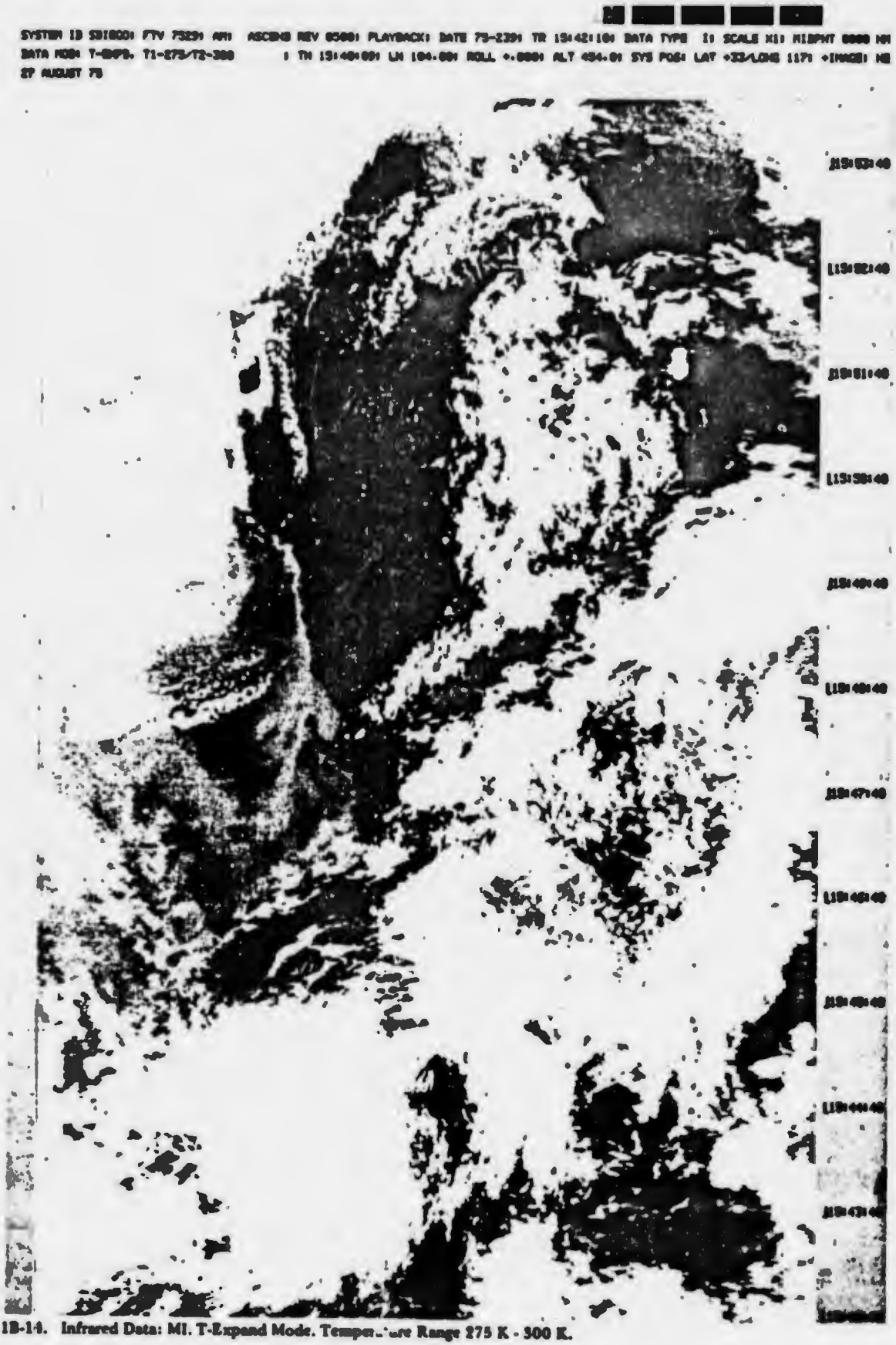

1B-14. Infrared Data: MI. T-Expand Mode. Temperature Range 275 K - 300 K.

Infrared Mode Data: MI
T-Expand Enhancement Mode. Range 210 K-235 K

A T-Expand designed to show features of high cloudiness in the temperature range 210 K - 235 K is shown in Fig. 1B-15. Here the lighter shades of gray depict cloud topography generally at the 300-mb level and higher. Such a depiction is useful for enroute flight forecasts of cloud distribution at various altitudes; for locating thunderstorms of greatest vertical extent; for analysis of tropical cyclone centers, etc. Note that much of the thin cirrus surrounding Hurricane Jewel and other areas is not rendered visible by this mode of presentation (see Fig. 1B-12). The emitting temperature of thin cirrus is contaminated by warmer temperatures radiating through the cirrus from the underlying surface so that the sensed radiation in thin cirrus areas is warmer than actual cloud temperature. Hence, thin cirrus will not appear in a T-Expand mode selected to display high cloud topography.

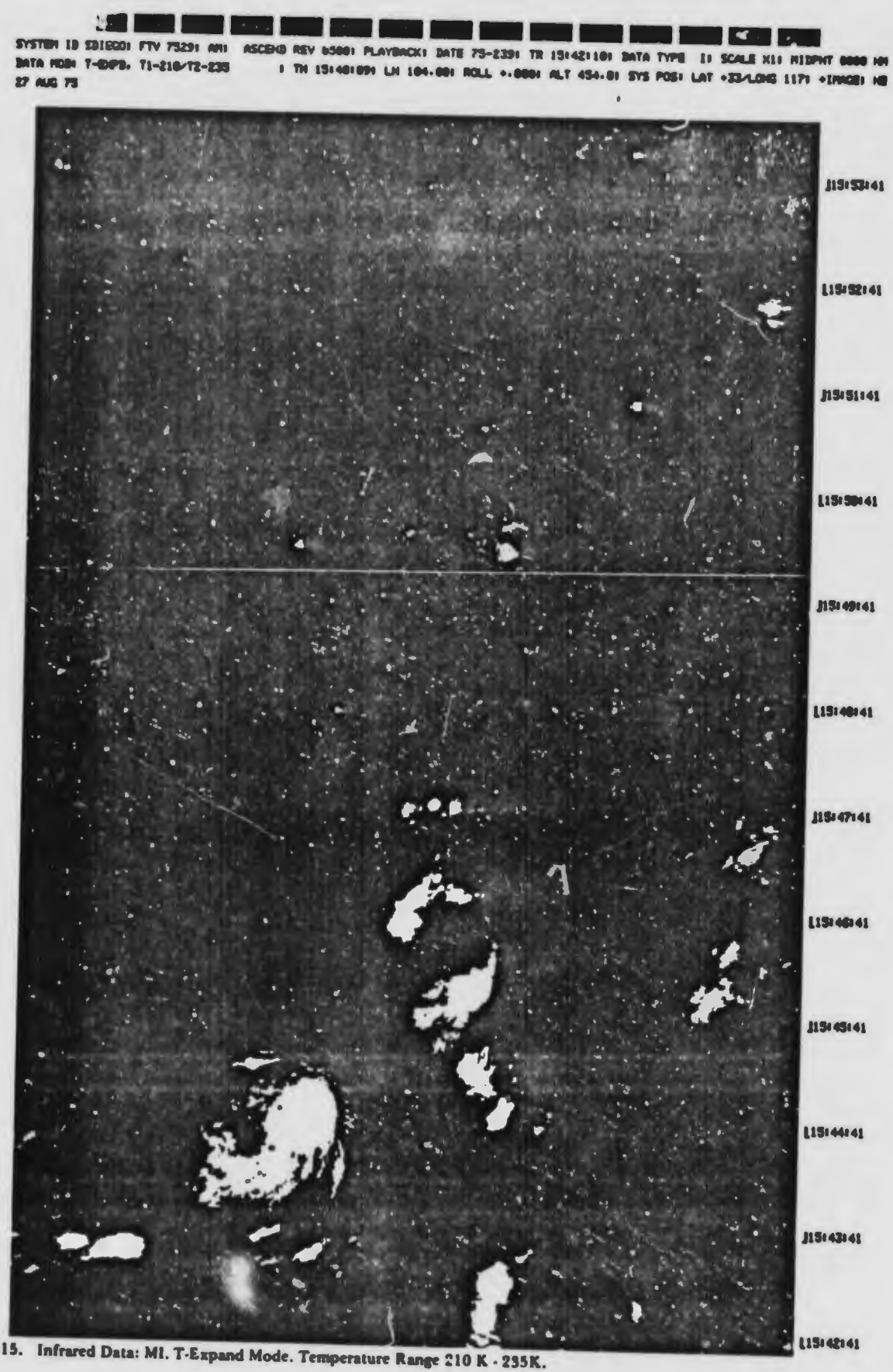

1B-15. Infrared Data: MI. T-Expand Mode. Temperature Range 210 K - 235K.

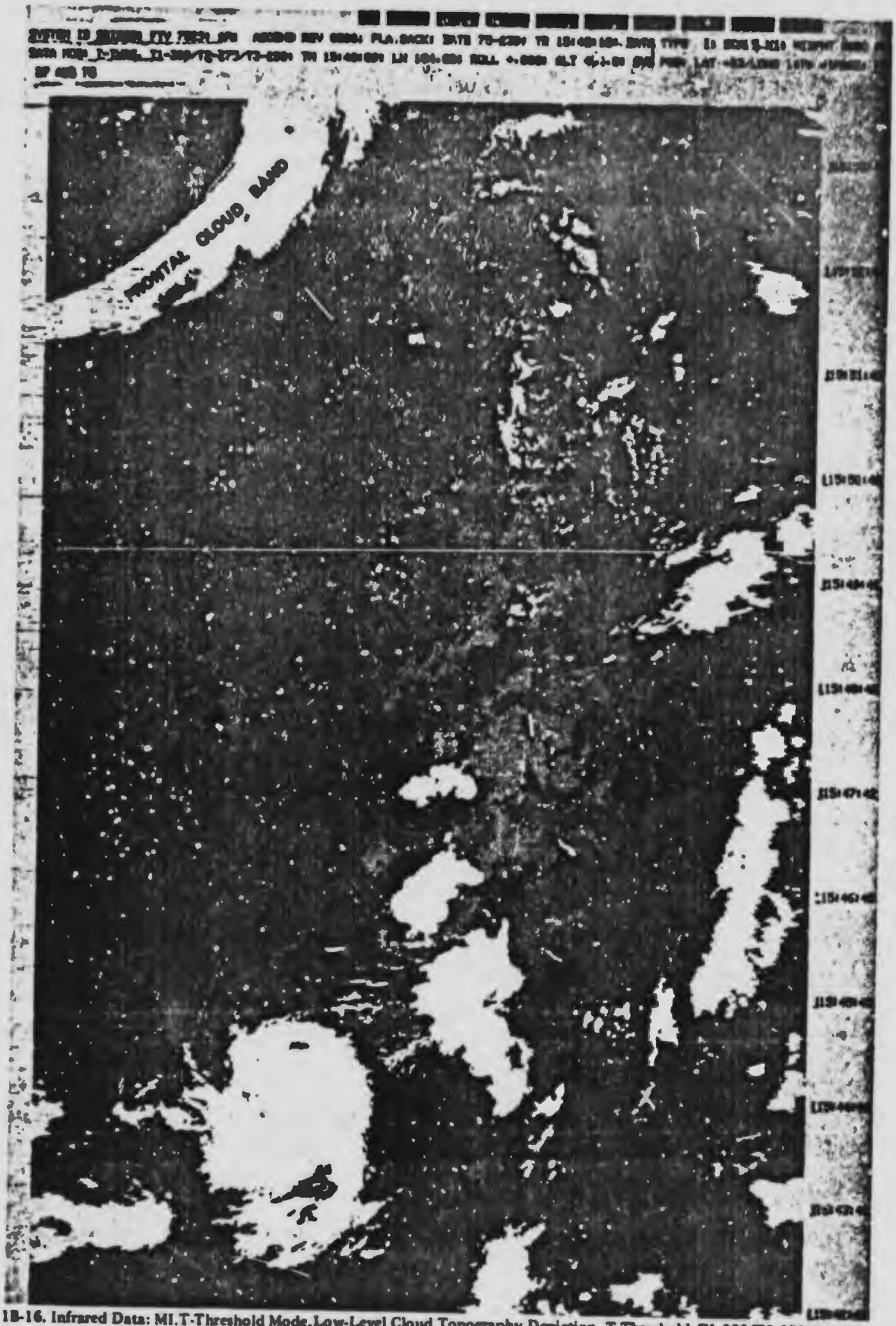

1B-16. Infrared Data: MI.T-Threshold Mode.Low-Level Cloud Topography Depiction. T-Threshold: T1-300/T2-275/T3-250.

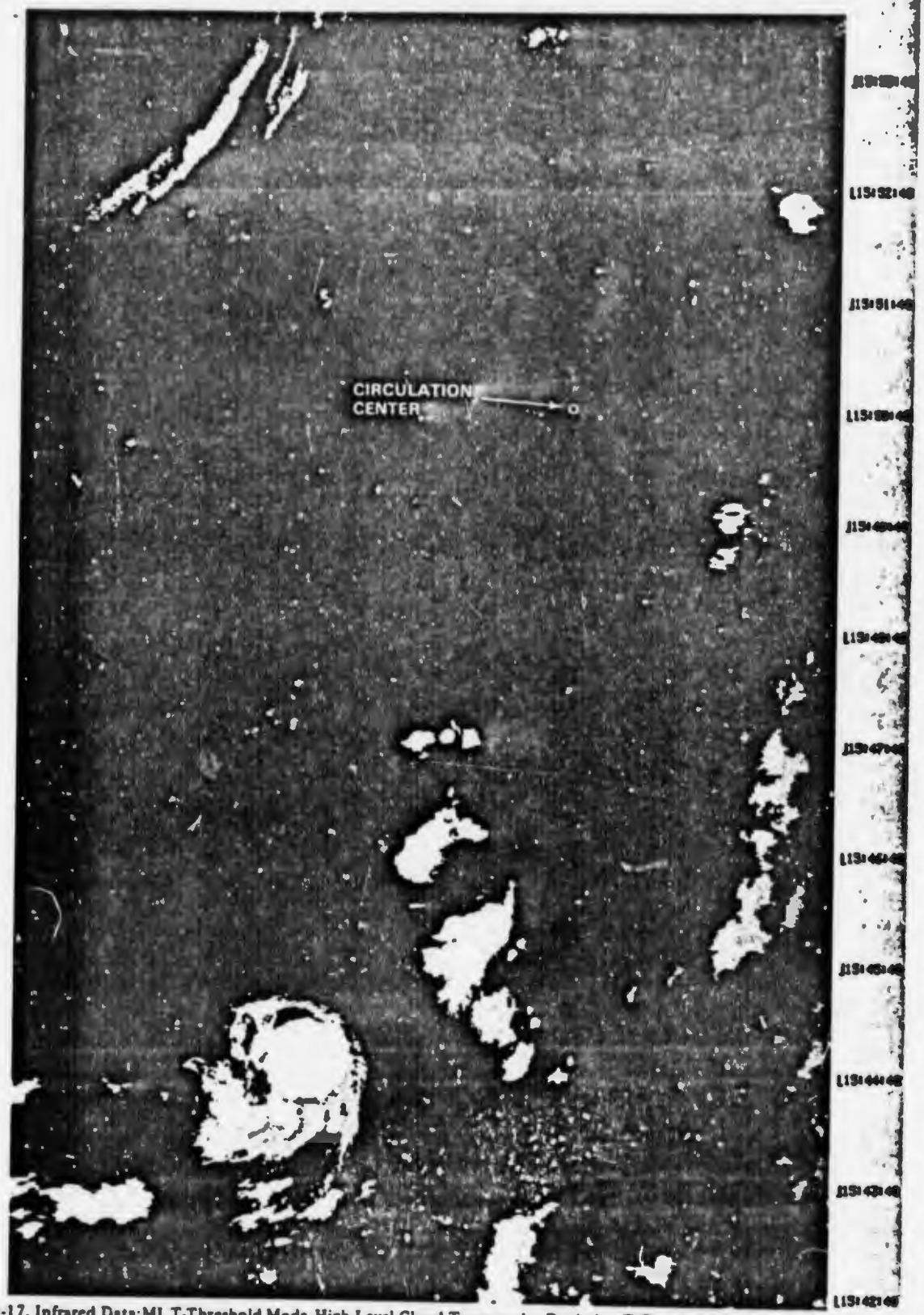

1B-17. Infrared Data: MI. T-Threshold Mode. High-Level Cloud Topography Depiction. T-Threshold: T1-230/T2-230/T3-210.

Infrared Mode: MI. T-Threshold Enhancement Mode
(Low/High Cloud Topography Depiction)
Low Cloud Depiction: T-Threshold: T1-300K/T2-275K/T3-250K
High Cloud Depiction: T-Threshold: T1-250K/T2-230K/T3-210K

Examples of the T-Threshold mode of depiction are shown in Figs. 1B-16 and 1B-17 for delineation of low and high-level cloud topography, respectively. This mode of display is especially useful for enhancing significant features of high and low-level wind circulations. For example the existence of a mid-tropospheric cyclonic circulation center is suggested by cyclonically curving gray shades southeast of the frontal system approaching the West Coast. The vorticity pattern is made more apparent in Fig. 1B-17 than in Fig. 1B-16 by the elimination or filtering out of underlying lower-level cloudiness, not connected with the circulation. The vorticity in this area, suggested by the satellite data, is substantiated by conventional reports and analyses which show a weak low-pressure center over the area.

1B-18. Infrared Data: WHR. Positive T-Expand Mode. Temperature Range 235 K - 310 K.

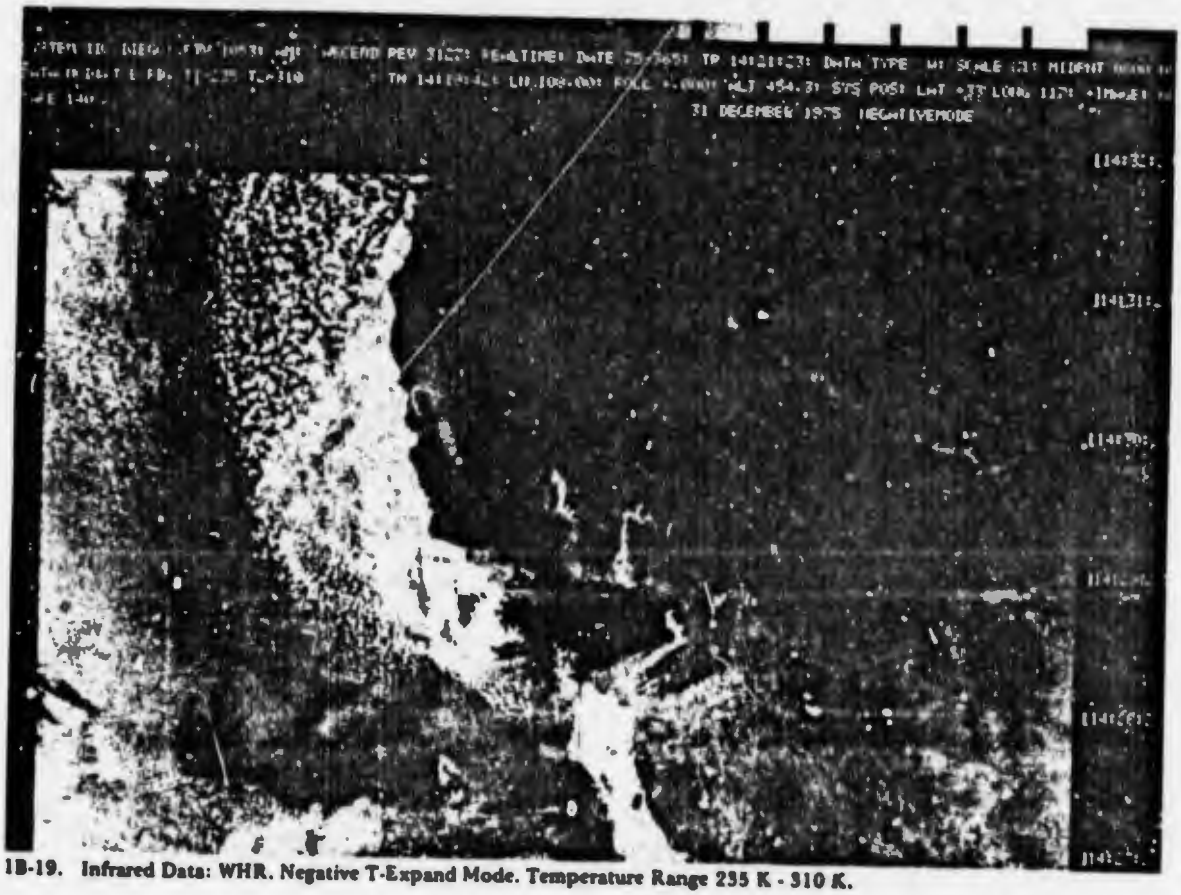

1B-19. Infrared Data: WHR. Negative T-Expand Mode. Temperature Range 235 K - 310 K.

Infrared Mode: WHR
T-Expand Enhancement Mode. Range 235 K-310 K

A final type of infrared data is the WHR (0.3 nm resolution, for Block 5C) and the TF (0.3 nm resolution for Block 5D). As with the lower-resolution infrared it is often desirable to produce these data in the T-Expand mode for enhancement of low level or upper level details. Figs. 1B-18 and 1B-19 show WHR T-Expand (T_1 = 235 K, T_2 = 310 K) data over the western United States area in the positive and negative mode of presentation, respectively. The high resolution capability of this sensor is immediately apparent. Note especially wave cloud details over the western mountain areas and delineation of dendritic snow patterns in the Sierra Nevada mountains, in Figs. 1B-20 and 1B-21, enlarged views of the positive and negative mode data.

This completes the general discussion of DMSP data output. It should be understood that the computer software associated with the Navy system provides for an evolution of data output which may vary significantly from those general examples presented in this section. Various enhancement modes are being developed for visible mode and infrared mode display which may ultimately become standard products of the future.

1B-20. Positive T-Expand Mode. (Enlarged View).

1B-21. Negative T-Expand Mode (Enlarged View).

1C Data Accuracy

Resolution

The DMSP sensors and Data Display System (DDS) were designed to provide high quality meteorological data and have it in the hands of the forecaster within five minutes after data transmission terminates. The system approach was taken to ensure that the resolution inherent in the basic sensor electronic signal would be faithfully preserved through amplification, recording, transmission, and display. Following deployment of both the ground equipment and the spacecraft, an evaluation was performed to see if, indeed, the imagery available to the forecaster met the engineering specifications. The results of these evaluations plus operational experience provide the basis for the material to follow.

The spatial resolution of each sensor was discussed in Section 1A. The sensors were engineered to provide subpoint spatial resolution of 0.3 nm for VHR and WHR data, 2 nm for HR data, and 2.4 nm for MI data. However, the resolution which is apparent in the film available to the forecaster is a function of:

a. Sensor lens/mirror aberrations.
b. Detector characteristics.
c. Frequency response of sensor electronics.
d. Smear due to image motion.
e. Tape recorder characteristics (if not direct readout).
f. Communications.
g. Ground station's characteristics/maintenance.
h. Height of satellite.
i. Relative contrast between object and the background.
j. Alignment of object to the scan line.
k. Others.

The spatial resolution and thermal accuracy of the DMSP system were evaluated under two Air Force projects. These evaluations showed that the sensor design resolution and achieved film imagery resolution were nearly equal. Geographical features apparent in VHR imagery were examined and compared with their known sizes indicated on aeronautical charts. Targets as small as one-half nm were visible. Smaller geographical targets were not present in the area for evaluation. HR data were examined, but not in as great a detail as VHR data. For HR it was found that 2 nm targets were visible in the data at subpoint. Due to foreshortening the 2 nm resolution degraded to approximately 12 - 14 nm at data edge. The variability was due to changing spacecraft altitudes, and the rectification of the imagery by the DDS to a constant scale, equal area projection, 450 nm nominal altitude. The spatial resolution does not degrade to less than 12 - 14 nm at data edge because the full scanning radiometer line sweep is truncated before the line reaches the "edge of the earth." Generally, for 1:15 million scale HR data, the spatial resolution averages 8 - 10 nm in the extreme right- and left-hand inch of data.

Nighttime HR data spatial resolution is much more dependent on light level and contrast than daytime HR data. It was not examined in great detail; however, experience has shown that nighttime HR imagery has the same spatial resolution as daytime data for high contrast targets during full-moon conditions. Slow degradation of resolution progresses to the half-moon illumination point, thereafter rapidly deteriorating to the quarter-moon point where objects lighted by moonlight are, for the most part, non-resolvable. The spatial resolution for light emitting objects (e.g., cities) remains the nominal resolution for any phase of moonlight.

One of the Air Force projects was a much more exhaustive effort to determine resolution. High altitude aircraft photographed clouds in the vicinity of the Hawaiian Islands. The dimensions of low clouds and land features from known altitudes were compared with VHR imagery from satellite passes within 15 minutes of the aircraft photographs. The results are shown in the following table:

Object Size (nm)	Percent of cases visible in VHR	Cases
0.2	39%	23
0.3	40	20
0.4	55	18
0.5	71	24
0.6	92	12
0.7	93	14

Percentage of objects visible in VHR data from different size groups.

It is interesting to note that a significant percentage of objects only 0.2 nm in size were detected by the VHR system; however, not all objects as large as 0.7 nm were detected. There are at least two important factors bearing on these results:

1. The land and cloud feature cases selected from the aircraft photographs were not restricted to the satellite subpoint region. The cases were distributed throughout the area viewed by the satellite; therefore, foreshortening effects would limit the number of small objects detectable by the VHR sensor.

2. The spectral range of the photographic film was different from the VHR sensor's. The photographic film was a conventional Kodak black and white emulsion which responds primarily to visible wavelengths. Very little blue and near-infrared response was present. Since the VHR sensor responds to considerable quantities of reflected near-infrared radiation, the VHR sensor pictures and aircraft photographs are not directly comparable. This is the probable reason why several bright clouds, clearly visible in the aircraft photographs, were unexpectedly missing in VHR imagery.

As a general rule of thumb, VHR imagery displayed in a 1:15 million scale has a spatial resolution of one-third to one-half nm within the first inch of data either side of subpoint. From one inch to two and one-half inches either side of the subpoint the spatial resolution degrades from one-half to one nm. From the two and one-half inch point to data edge the spatial resolution further degrades to two nm. These degradations are due to foreshortening.

Spatial resolution is more difficult to quantitatively determine for infrared sensors than it is for visible sensors. In the infrared the spatial resolving power of the sensor can be masked by the thermal accuracy of the sensing system. A target within view of an infrared sensor may have sufficient size to be detected by the sensor; however, if that target does not thermally contrast with the background by at least one shade of gray thermal difference; the target is not identifiable. Operational experience has shown that if an infrared target is at least 8°C different from its background, then the spatial resolution for MI data is 2.4 nm at subpoint degrading to 14 - 17 nm at data edge. WHR data has the same spatial resolution as VHR data; 0.3 nm at subpoint degrading to 2 nm at the data edge. For a nominal orbit the data edge is 803 nm away from the subpoint.

Thermal Accuracy

The thermal accuracy of the MI sensor is better than 1°C for the temperature range from 210 K - 310 K. Current WHR sensors have the same range, but the accuracy degrades from 1°C at 310 K to 3°C at 210 K. These are engineering values for the sensors derived from tests in a thermal vacuum chamber. The determination of absolute emission temperatures of the surface and clouds is further degraded due to contamination by atmospheric ozone, carbon dioxide, and water vapor. All of these major contaminants (there are some minor ones also) tend to decrease the emission received by the sensor when compared to the original target emission.

Fig. 1C-1 shows the absorption spectra for ozone, carbon dioxide, water vapor, and the solar spectrum. The interval from 8 - 13 μm, is outlined to indicate the spectral range for the MI and WHR sensors. Nowhere within this interval is the atmosphere totally transparent to infrared radiation. Carbon dioxide is considered to be a well mixed component of the atmosphere, and its absorption between 8 - 13 μm is small. Ozone, except for the peak near 9.6 μm, has relatively small absorption. Even though ozone is known to undergo variations in concentration within the troposphere, it is usually treated as a constant. The distribution of ozone and carbon dioxide concentrations within the atmosphere is difficult to measure, particularly on a synoptic basis. Their quasi-constant effect is treated as an add-on to water vapor absorption. The largest effect on the absolute thermal accuracy of infrared sensors comes from water vapor absorption. The quantity of water vapor varies horizontally, vertically, and with time. It has the least amount of absorption between 9.5 μm and 10.5 μm, and progressively increases in other intervals within the sensor range. The solar spectrum curve shows the total effect of all major and minor absorbers within the sensor range. It is clear that the atmospheric window is not clean. Even without the ozone absorption spike the atmospheric window is considerably smudged at the edges by other absorbers, primarily water vapor. The net attenuation effect must be considered when seeking absolute temperature values from infrared sensors.

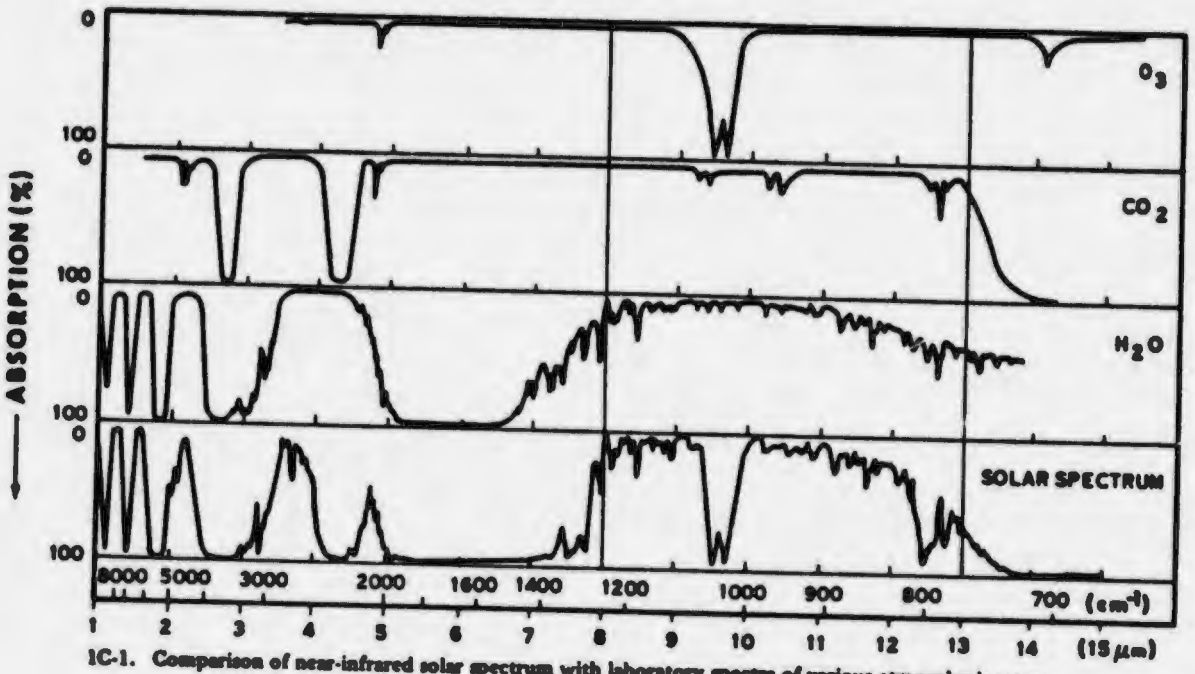

1C-1. Comparison of near-infrared solar spectrum with laboratory spectra of various atmospheric gases.

An examination of data collected during Air Force experiments has shown that the MI sensor detected the sea surface temperature in cloudiness and relatively dry areas of subtropical highs 1 - 2°C too cold. For colder waters, near 70N, the sea surface temperature was sensed 3°C too cold. Other experiments have examined the attenuation problem in greater detail. It has been shown that a moist tropical oceanic atmosphere has a considerably larger effect on the absolute thermal accuracy of the MI sensor. It has been determined that sea surface temperature has been sensed as much as 12°C too cold with sensor scan angles (β) greater than 31.1° as illustrated in Fig. 1C-2. This results from the sensor scanning through deeper layers of atmosphere. It has been found that as the sensor ages, further degradation occurs.

Similar temperature discrepancies have been determined for cloud tops sensed by the MI sensor, thus causing an analysis of cloud top altitude of 3,000 - 5,000 feet too high for both cumulus and thick cirrus type clouds.

The first WHR sensor was not flown until November 1972. An evaluation was performed on its response characteristics by U.S. Air Force personnel. The result is shown in Fig. 1C-3. In general, the evaluation showed that cold objects were being detected 20°C too cold, and that warm objects were being detected 15°C too cold. Coincident MI data were much more accurate, showing the emitted temperature to be 5°C colder than the observed temperature over a range from 230 K - 300 K. As the WHR sensor ages in space and contamination collects on the radiative cooler, its thermal response degrades further. For these reasons WHR data are used for imagery rather than quantitative temperature determination. The MI sensor is much better suited to determine accurate emissive temperatures.

Theoretical Attenuation Corrections

It is apparent from experiments that atmospheric attenuation factors are different for each site depending on its location and season. Many sites have a continuing evaluation program so that accurate temperatures (cloud heights) can be obtained for mission support. To assist those who do not have access to site peculiar calibration data, theoretical atmospheric attenuation curves for a standard atmosphere were developed for the MI sensor. Fig. 1C-2 shows the geometry of the attenuation problem and contains the symbols used in the theoretical

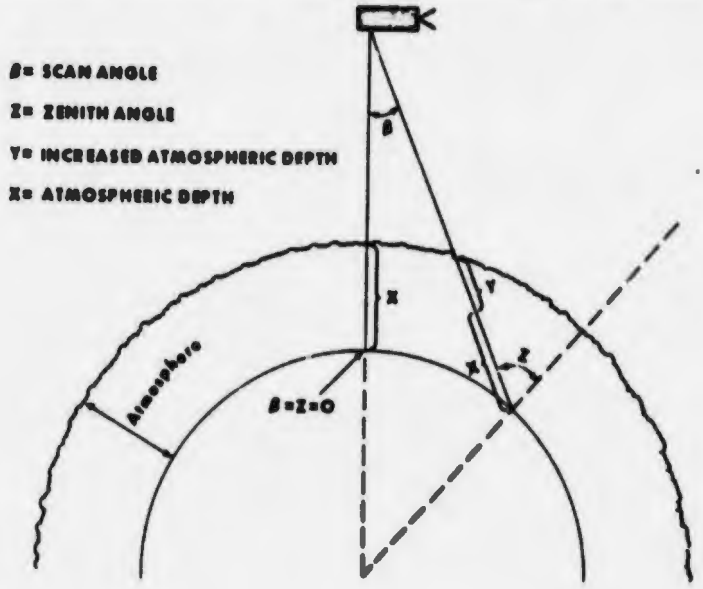

1C-2. Attenuation geometry.

1C-3. WHR temperature response to known radiating bodies.

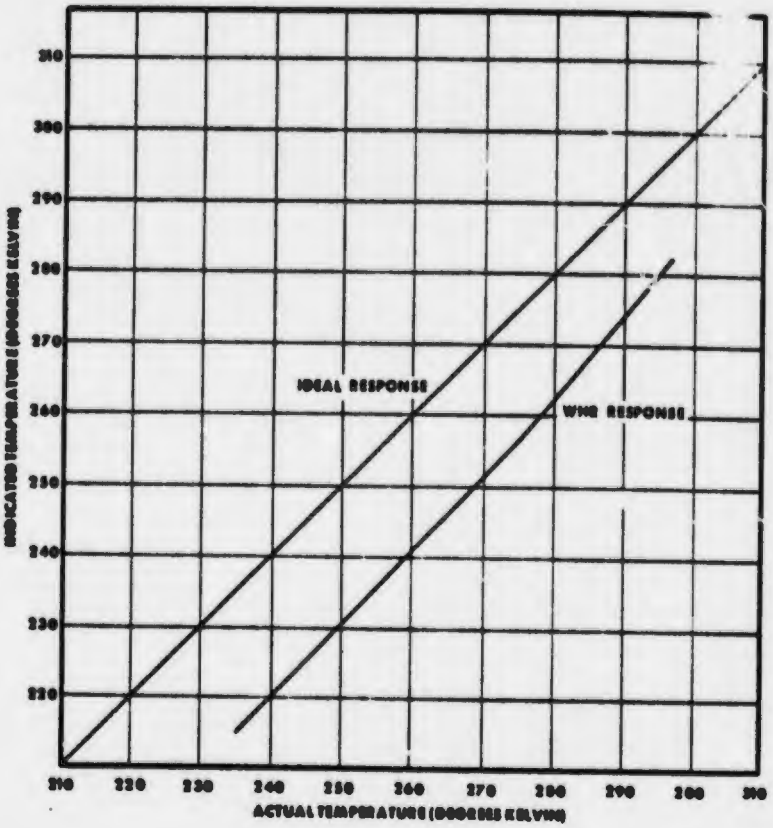

1C-4. Zenith (Z) and scan (β) angle overlay.

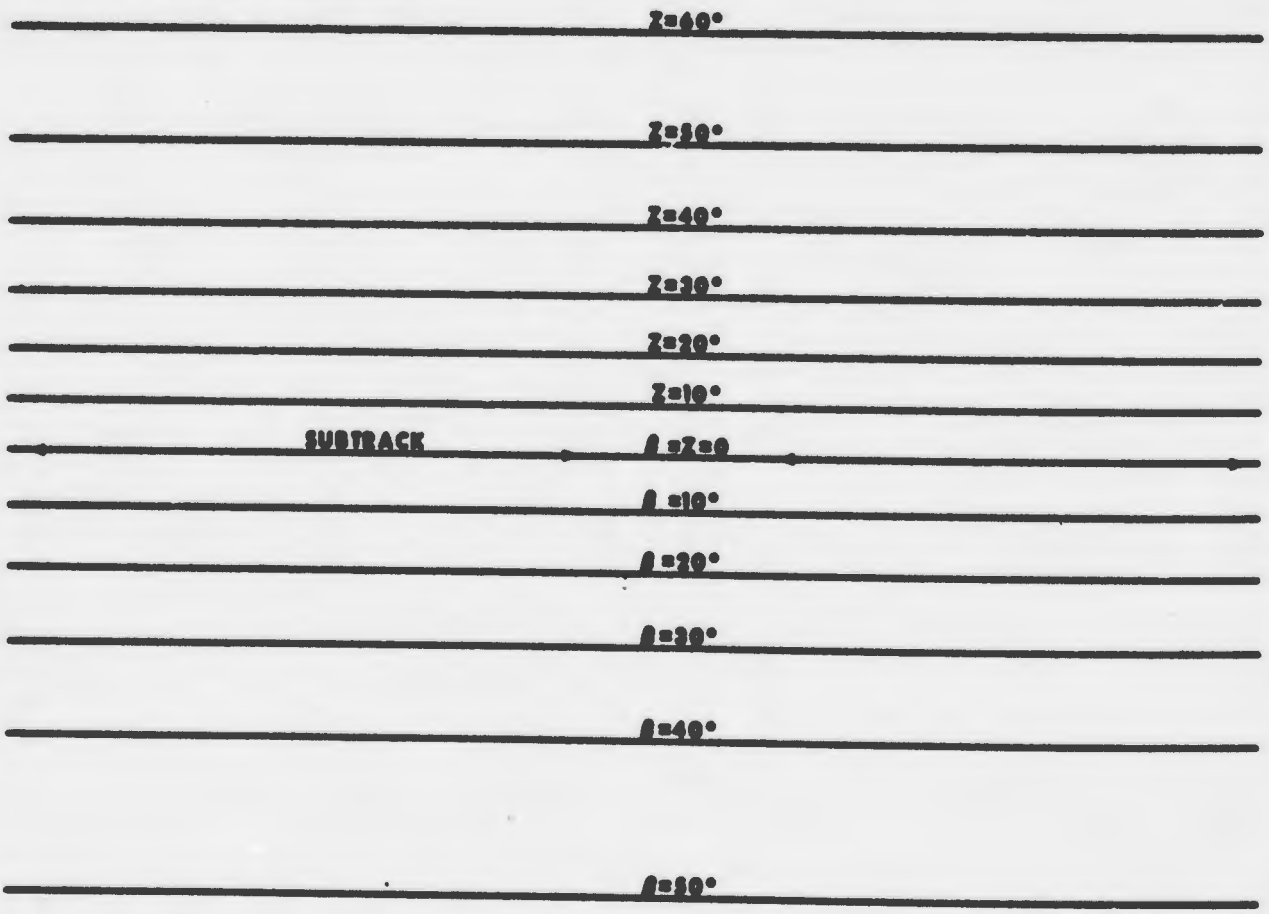

correction factors. The first step is to determine the effective radiating temperature (ERT) of the target from the MI data. This can be done by visually matching gray shades or using a densitometer. Next, determine the zenith angle (Z) for the target. This can be done by producing a transparency copy of Fig. 1C-4 with 6.3 inches between $\beta = 50°$ and $Z = 60°$. Fig. 1C-4 is for 1:15 million scale data. The Y-value (increased atmospheric depth) correction is determined by using Fig. 1C-5. Enter Fig. 1C-5 with the ERT and zenith angle. The resulting correction can be read as either temperature or the approximate height error if the radiating target is a cloud. The X-value (atmospheric depth) correction is determined by using Fig. 1C-6. This figure provides an ERT correction due to the moisture present in a standard atmosphere. As in Fig. 1C-5, the correction can be read as either temperature or approximate cloud height error.

For both Fig. 1C-5 and Fig. 1C-6, the temperature corrections are added to the ERT, and the cloud height corrections are subtracted from the cloud height determined by using the ERT and radiosonde temperature vs altitude information.

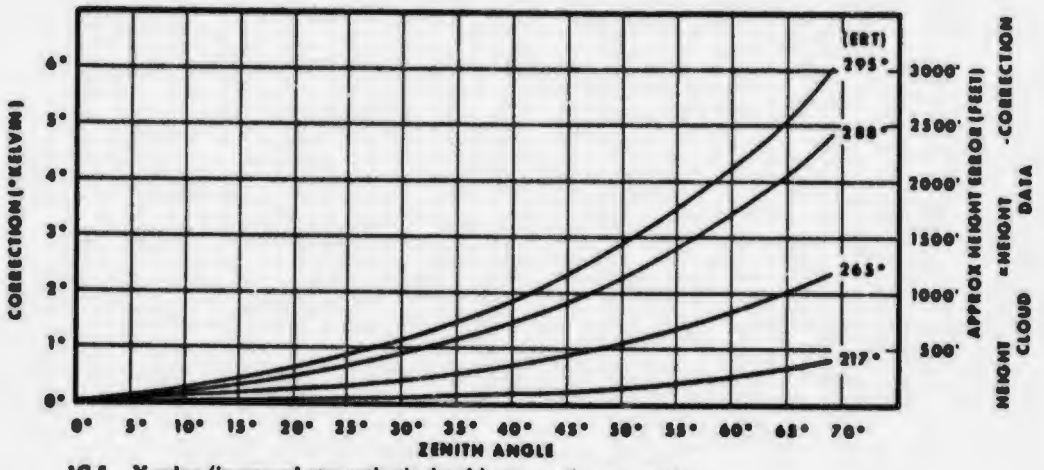

1C-5. Y-value (increased atmospheric depth) attenuation correction.

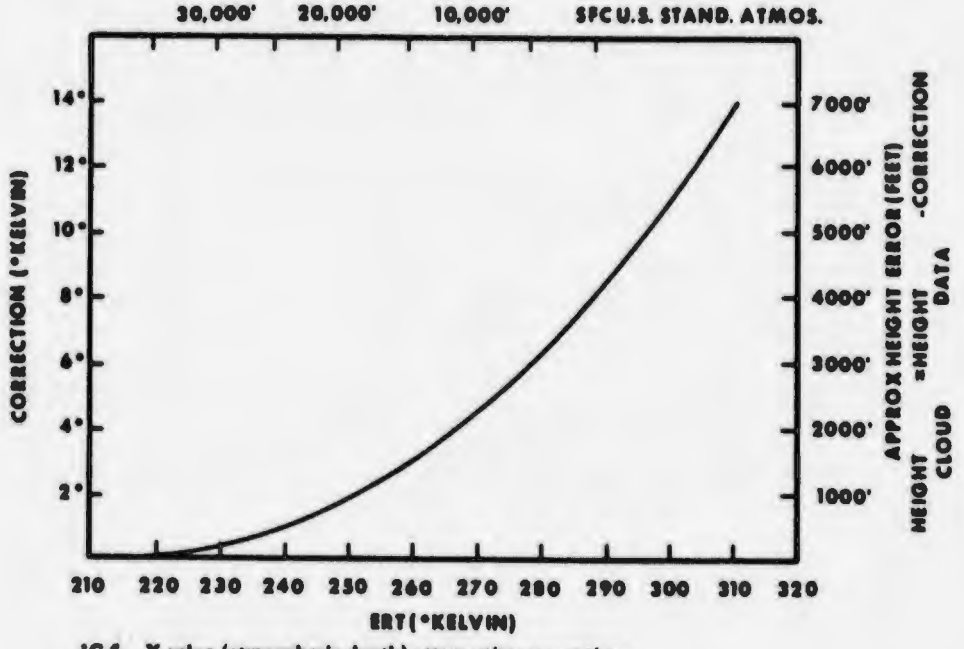

1C-6. X-value (atmospheric depth) attenuation correction.

VHR Negative Mode Processing

The bit-frame structure is similar for both VHR and WHR data. Because of this it is possible to process VHR data as if it were WHR. In this manner all of the enhancement choices available to WHR (temperature expand and thresholding) are also available for VHR data. In the normal VHR display solar energy incident on the earth scene is reflected to the sensor and displayed as a positive image (dark objects appear dark, light objects appear light). When using the VHR Negative mode the image is inverted (dark objects appear light, light objects appear dark). Since visible data are processed as if they were infrared, and the infrared processing is accomplished in terms of temperature, then it is necessary to determine the correspondence between albedo and temperature.

In order to convert from temperature to albedo the calibration of the VHR sensor must be known. This sensor is calibrated to give a fixed voltage when viewing a 100% albedo target at subpoint. The full range response of the VHR sensor is 0 - 4.0 volts. On spacecraft FTV 1524 and FTV 2525 the calibration voltage was 2.9 volts. For FTV 3526 it was 2.39 volts. Holding the calibration voltage at these low levels permitted the sensor to respond to higher illumination values from targets well removed from the subpoint. However, experience showed that this condition seldom occurred near noon. Therefore, on later spacecraft the calibration has been different for morning and noon satellites. Morning satellites (e.g., FTV 7529) have the calibration voltage set at 2.5 volts. Noon satellites (e.g., FTV 5528) have the calibration voltage set at 4.375 volts. This means that a 100% albedo subpoint target will oversaturate the sensor; however, this rarely occurs and it proved advantageous to expand the dynamic range of the sensor over a slightly smaller range of albedos.

It is possible to represent albedo values as equivalent temperature settings (ETS) if two assumptions are reasonably valid. (1) Assume the illumination field is uniform throughout the scan of the earth scene. This is a good approximation for a spacecraft near a noon orbit. It is not as good for a morning orbit, so VHR negative mode is seldom used for a morning orbit satellite. (2) Assume the sensor control of along-track gain settings maintains a constant voltage output as a function of albedo input (e.g., at both 20N and 60N a 100% albedo target would show the same voltage). Barring a sensor malfunction, this is a good assumption. The following table lists the conversions between albedo and ETS for FTV 5528.

Earth-Scene Albedo	Output Voltage	Percent of 4.0 Calibration Voltage	Equivalent Temp. Setting (ETS)
100%	4.375	109.4%	319.4
90	3.9375	98.4	308.4
80	3.5	87.5	297.5
70	3.0625	76.6	286.6
60	2.625	65.6	275.6
50	2.1875	54.7	264.7
40	1.75	43.8	253.8
30	1.3125	32.8	242.8
20	0.875	21.9	231.9
10	0.4375	10.9	220.9
0	0	0	210

Conversion of earth-scene albedo to voltage, calibration, and ETS for a noon satellite.

The earth-scene albedo for any given ETS may be determined by Equation 5-4.

$$\text{Albedo} = \frac{\text{ETS} - 210}{1.094}$$

For example, an ETS of 250 K corresponds to an albedo of 36.6%.

With infrared data a base temperature is selected and the shades of gray are distributed over a temperature range colder than the base temperature. For example, with a normal mode temperature of 310 K selected the temperatures in the field-of-view between 310 K and 210 K will be distributed over 64 shades of gray. However, the VHR negative mode selected base ETS represents the lowest albedo to be displayed and the shades of gray are distributed over an albedo range toward higher albedo values. For example, the selection of 310 K ETS will produce VHR negative mode output with the 64 shades of gray distributed from 91.4% - 0. The range in this case is not 100% because of the 4.0 volt limit on the output of the VHR sensor. Due to this voltage limit albedos higher than 91.4% cannot be displayed. It is important to remember that high albedo objects will appear dark.

Many uses can be made of VHR negative mode products. Some of them are: cloud albedo studies; terrain enhancements; precipitation intensity/quantity vs cloud albedo determination; albedo of river flood plains for river/flood forecasting; large scale land use study and changes in land use.

Section 2

Image Analysis/ Basic Concepts of DMSP Data Intepretation

2A Sunglint

Case Studies

2B Anomalous Gray Shades

Case Studies

2C *Barrier Effects*

Case Studies

2A Sunglint

Sunglint Patterns

Sunglint or "sun-glitter" is observed whenever the sun's rays are reflected off of a water surface (ocean, lake, river, delta, swamp, etc.). Sunglint patterns are regularly observed in the visible imagery obtained from geostationary and polar-orbiting satellites. The patterns vary in size, shape, and intensity of reflection depending on (1) the geometry of the scene (relative positions of the satellite subpoint, the area viewed, and the solar subpoint), (2) the characteristics of the image forming system), (3) sea state (smoothness or roughness of the water surface, and (4) the low-level distribution of atmospheric aerosols and moisture.

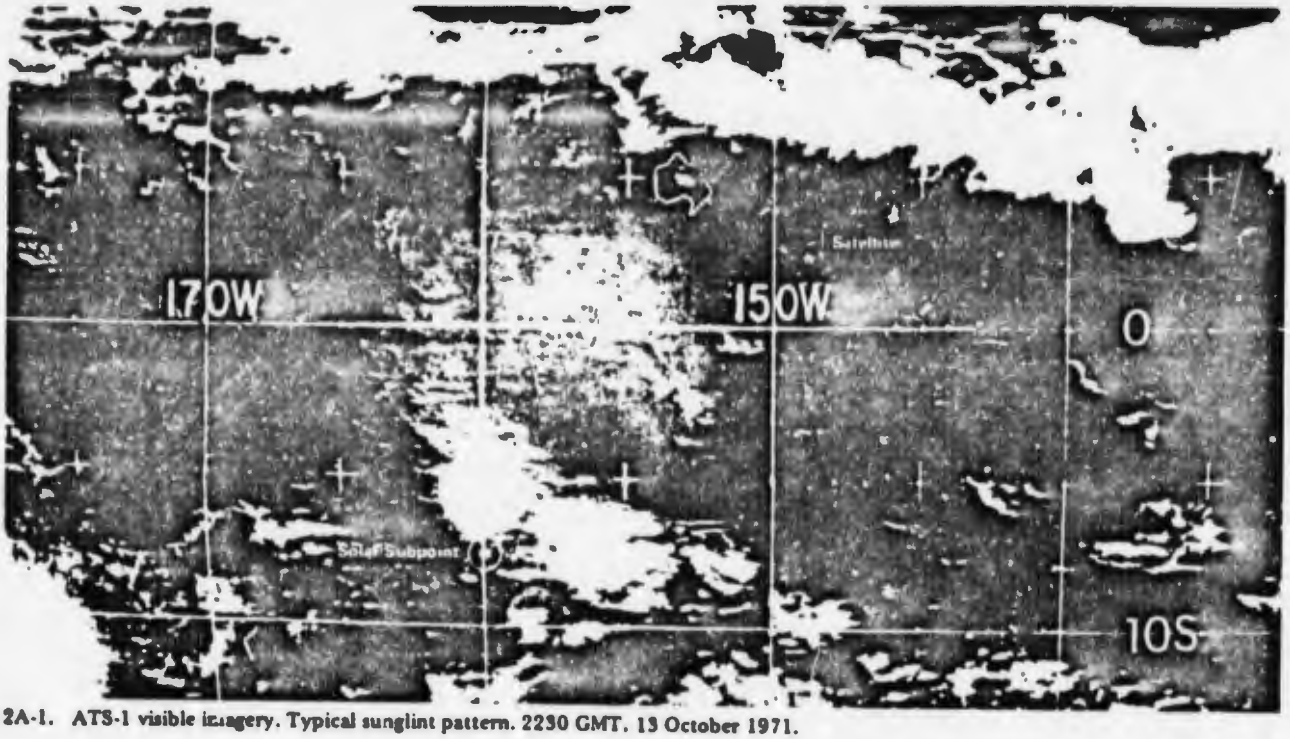

2A-1. ATS-1 visible imagery. Typical sunglint pattern. 2230 GMT. 13 October 1971.

Sunglint Patterns in Geostationary Satellite Data

An example of ATS-1 (geostationary orbit) imagery showing sunglint is reproduced in Fig. 2A-1. On this day, the sun's image appears as a large, diffuse, near circular reflection. The numerous short, bright streaks are a combination of cirrus streamers from convective activity to the south and low-level cloud lines. For reference purposes, the satellite subpoint is located at 2N and 149W and the solar subpoint at 8S and 160W. Note that the sunglint area falls between these points.

The sunglint area always falls in the region between the satellite subpoint and the solar subpoint, except when these two points coincide. Then the sunglint is centered over the points. When a water surface is smooth (glassy or only small wavelets are present) the sunglint area will be small and intensely brilliant; the most brilliant reflection will occur at the location of the specular point. The specular point is the point on the great circle arc passing through the satellite subpoint and the solar subpoint where the angle of incidence of the sun's rays on a horizontal plane (measured from the local zenith) is equal to the angle of reflection of the sun's rays to the satellite in space (See Fig. 2A-4).

From geostationary orbit satellites, sunglint can only be observed over the tropics. These satellites are launched in an equatorial orbit around the earth and, in general, the satellite subpoint remains above a given equatorial geographical area for long time periods. The solar subpoint, on the other hand, moves slowly north and south according to the season within the limits of 23.5N and 23.5S latitude. Since sunglint always falls in the region between the satellite subpoint and the solar subpoint, sunglint is observed only over the tropics from geostationary orbit satellites. During the time interval of a picture taking sequence (about 25 minutes) the satellite subpoint and solar subpoint positions can, for all practical purposes, be considered as fixed in location. Thus the shape of the sunglint area over the open ocean will vary from circular when the satellite/solar subpoints coincide to oval shaped when they are relatively far apart.

2A-2. DMSP visible mode data. Typical sunglint pattern. 1853 GMT. 8 April 1974.

Sunglint Patterns in Line-Scan, Polar-Orbiting Satellite Data

Sunglint patterns appear uniquely different in the DMSP polar-orbiting satellite data and other polar-orbiting satellites having line-scan radiometer sensor systems. The reason for this is that the spacecraft is moving rapidly relative to the earth during the image recording sequence and the sun versus satellite geometry, as a result, is not fixed as in a picture taking sequence from a geostationary orbit satellite.

Fig. 2A-2 shows a typical DMSP sunglint pattern obtained in a direct readout mode at San Diego, California. The sunglint pattern stretches from the bottom to the top in the central portion of the picture. The satellite subpoint track (dashed line) passes just to the left of an axis which would separate the sunglint pattern into two nearly symmetrical halves. In this example, the primary specular point (6.3N, 109W) and the solar subpoint (7.4N, 103W) are located off of the imagery to the southeast of the satellite subpoint track (See Fig. 2A-3).

Fundamental Sunglint Geometrical Relationships in DMSP Data

Sunglint geometrical relationships in DMSP data are illustrated in the schematic of Fig. 2A-3. As the spacecraft travels northward, orbiting at about 833 km (450 nm), it arrives at point A. At this point, if the satellite sensor could scan the ocean surface along a line connecting the satellite subpoint and the solar subpoint, it would detect specular reflection at point X, where the horizontal or zero-slope reflection occurs. The circle around point X represents the sun's image reflected off of the water (not shown in true shape or size).

However, the DMSP satellite has a scanning radiometer imaging system that sweeps from horizon to horizon, perpendicular to the satellite subpoint track. At point A, therefore, the imaging sensor does not view the specular point X but other points along the scan line well to the south of the specular point. Since the ocean is rarely glassy, except over very limited areas, the sloping surfaces of small waves act like thousands of small mirrors. As the waves change size and shape some of the sun's rays will be reflected toward the satellite imaging sensors. This nonspecular light can produce a relatively large diffuse sunglint area surrounding the specular point X that can be recorded by the satellite sensors.

The image of the sun's disk is not a point but covers a finite area on the earth's (ocean) surface. Thus, under relatively uniform, low sea states, brilliant reflections can be recorded along scan lines prior to the time a spacecraft sensor scan line intersects the specular point.

Upon arrival at point B, the satellite scanner views directly across the specular point X. This is the primary specular point (PSP). The PSP and the solar subpoint lie on the great circle arc perpendicular to the satellite subpoint track at point B.

When the sea is calm, a brilliant reflection is observed at the PSP. In the case studies which follow, the location of the PSP is of fundamental importance in the interpretation of DMSP sunglint patterns.

As the satellite continues northward, sunglint with decreased intensity will be scanned until the distance between the satellite subpoint and solar subpoint becomes so large that even nonspecular reflection by surface waves is not directed toward the spacecraft and the sunglint can no longer be detected.

The above comments on the appearance of sunglint in DMSP imagery refer specifically to what is observed along the scan lines at the points A, B, C, and D on the satellite subpoint track in Fig. 2A-3. Since DMSP imagery consists of a series of contiguous scan lines, the sun's image in Fig. 2A-3, will appear along all scan lines between A to slightly beyond C. At point D, sunglint cannot be detected. The net effect is to produce a banded sunglint pattern as shown in Fig. 2A-2. This example clearly illustrates the effect of increasing distance between the satellite subpoint and the solar subpoint; resulting in the reduced sunglint intensity to the north of the primary specular point (or to the south, in DMSP imagery extending to the south of the primary specular point).

Sunglint patterns are observed in most daytime DMSP passes. The effect will be minimized for a direct readout site in the Northern Hemisphere at winter solstice and maximized as the sun progresses to a summer solstice position, depending on the northern latitude of the direct readout location.

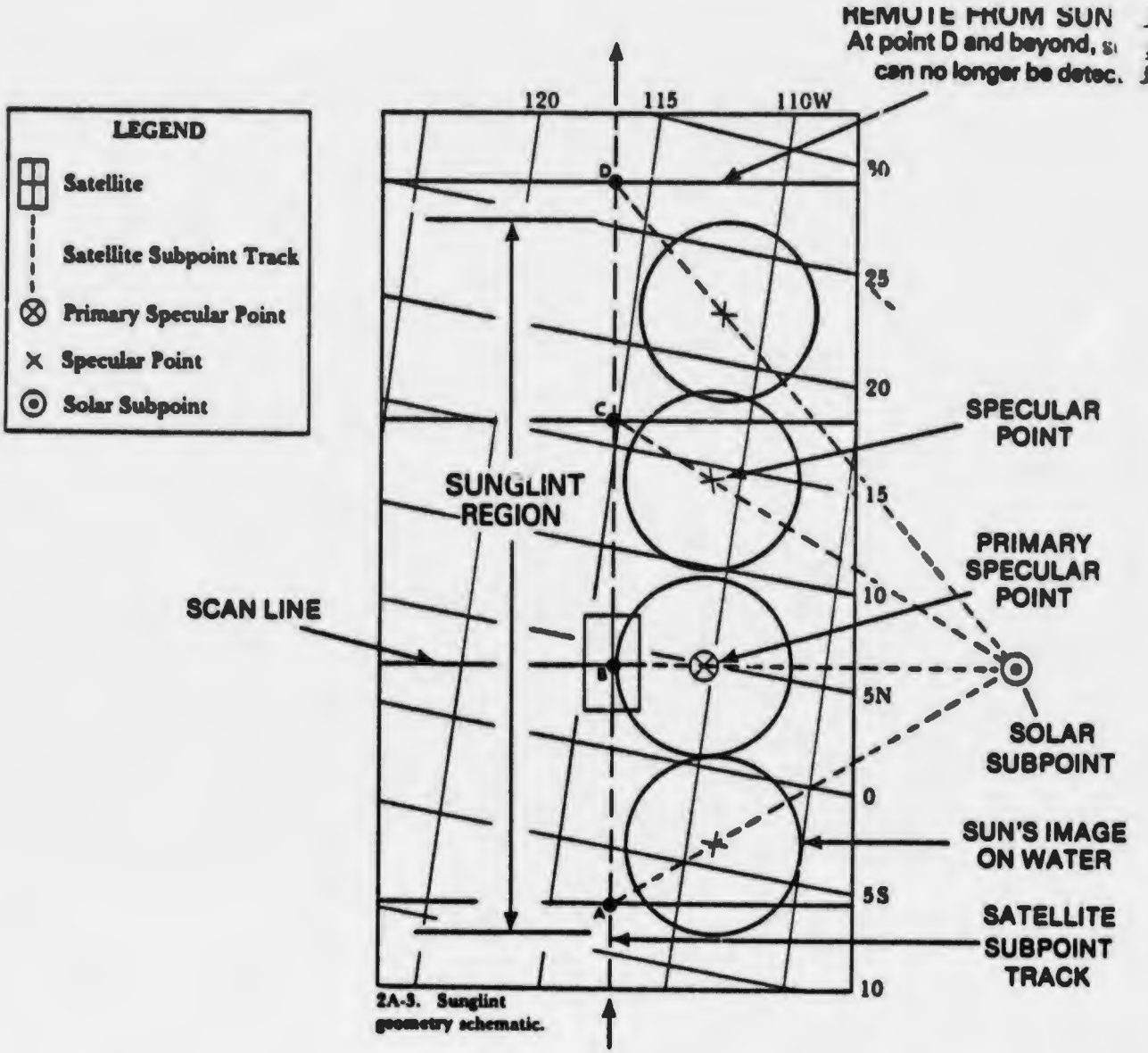

2A-3. Sunglint geometry schematic.

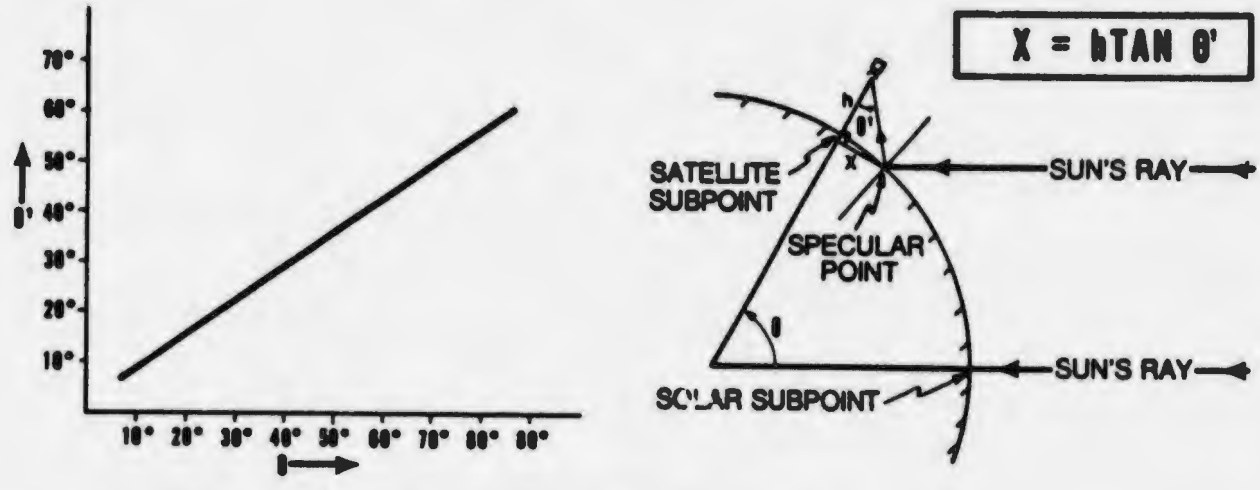

2A-4. Nomogram used to calculate central position of DMSP sunglint pattern.

TE FROM SUNGLI
: D and beyond, sungli
o longer be detected

One can calculate the location of the PSP in an anticipated DMSP sunglint pattern by use of the nomogram in Fig. 2A-4. A gnomonic projection must be used for calculating great circle distances and the latitude/longitude intersection angles. For general interpretation, however, it may suffice to note that sunglint patterns should appear on the eastern side of data acquired with morning ascending nodes; in the center portion of data acquired with near-noon ascending nodes; and on the western side of data acquired with late afternoon ascending nodes.

Sea state and atmospheric aerosols and moisture can modify the normal pattern so that sunglint may not be detected or, if detected, it appears asymmetrical or offset from the normally anticipated pattern.

Some rather complicated studies, requiring computer services, have indicated that wind speed and direction can be determined grossly from the sunglint pattern (Kornfield, 1974). These studies have been conducted applying statistical relationships to data from geostationary satellites. Similar relationships, further complicated by the geometry of polar-orbiting satellites, should eventually be developed. With wind direction assumed constant, to a certain limit, sunglint patterns over regions of increased wave height are enlarged in comparison to sunglint patterns over calmer seas. Similarly, total reflected brightness per unit area is reduced over areas of increased wave height. Reduction is such that little sunglint can be detected in extremely rough sea areas. Calmer seas reflect intensely over a small area.

Other important principles are suggested but require verification. For example, changes in sea state affecting height, period, and direction, separately or in a combined manner, definitely influence total reflectivity measured from a given area. A symmetrical sunglint pattern, as shown in Fig. 2A-2, implies relatively uniform moisture and sea state conditions. By the same reasoning, asymmetrical patterns suggest variable conditions. In some instances a few ship reports concerning sea state may provide the clue for interpreting the pattern observed.

Procedure for use of nomogram (Fig. 2A-4) for calculating the location of the primary specular point (PSP).

1. Plot the satellite subpoint track on gnomonic projection base chart.
2. Locate position of solar subpoint on base chart.
3. From the solar subpoint draw a line perpendicular to the satellite subpoint track.
4. Measure the distance from the solar subpoint to the intersection of the perpendicular line to the satellite subpoint track in n mi. Convert to degrees of latitude (1 degree latitude = 60 n mi) to obtain Θ.
5. Enter Θ in the nomogram (Fig. 2A-4) and find Θ'.
6. Use formula $x = h \tan \Theta'$ to calculate the distance of the PSP from the satellite subpoint along the perpendicular line to the solar subpoint.

SPECULAR POINT

PRIMARY SPECULAR POINT

SOLAR SUBPOINT

SUN'S IMAGE ON WATER

SATELLITE SUBPOINT TRACK

= hTAN θ'

SUN'S RAY

SUN'S RAY

Reference

Kornfield, J.I., 1974: On the determination of sea surface wind or stress from sunglint observed by an earth synchronous satellite. Measurements from Satellite Systems, 1-60, Space Science and Engineering Center, Univ. of Wisconsin.

Calm wind zone intersecting the primary specular point

The reflected brightness in sunglint on the sea surface is related to the sea state and variations in sea state in the sunglint area. A theoretical sea-surface sunglint reflected brightness pattern that would be obtained in an instantaneous satellite photograph where a perfectly calm wind zone overlies the specular point is illustrated in Fig. 2A-5. The pattern assumes a 5 m sec^{-1} (10 kt) wind background and a calm wind swath through the shaded area. Note that the intensity of reflection is strongest, attaining a value of over 5,000 units, at the specular point. The reflected intensity decreases rapidly in the calm wind areas immediately adjacent to the east and to the west. The pattern for scanning radiometer data, as in DMSP, is elongated to the north and south and highly elliptical in comparison to Fig. 2A-5, since the DMSP satellite is continuously moving northward and the pattern is continually shifting as the data are acquired. Because of this the sunglint data extend across a far greater range of latitude. In turn the area where rather brilliant reflection can be measured is not confined to one point but extends several degrees north and south of the primary specular point (see Fig. 2A-3). The reflectance east and west of this point under calm wind conditions decreases rapidly however, approximately as shown in Fig. 2A-5.

In Fig. 2A-6 a DMSP example of sunglint at the PSP is shown. Theoretically, for calm seas, the reflection of the sun's image off of the water would be much smaller than shown in this example (approximately 32 nm in diameter). Hence, seas cannot be calm and

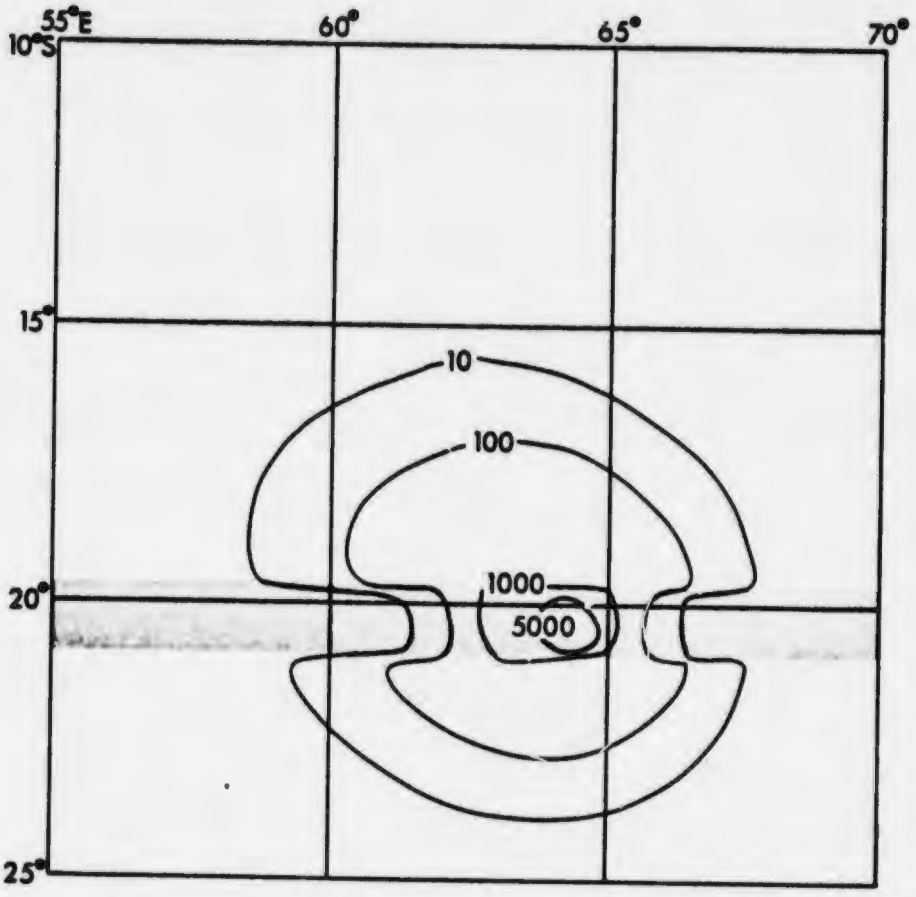

2A-6. Theoretical sea-surface sunglint for a composite pattern; 5 m sec^{-1} wind background and a calm wind in an east-west swath (shaded) through the specular point. Isopleths are relative reflected intensity per 10^4 steradian incident flux; satellite subpoint, 21.5S, 65.5E; solar subpoint, 5.8S, 95.6E; satellite height, 722 km. (Courtesy McClain and Strong, 1969).

some diffuse reflection is received from wavelets and surface ripples which nevertheless saturates the spacecraft sensor. Calm conditions apparently extend into the black areas east and west of the PSP as reflected intensity drops to near zero in a manner analogous to the theoretical presentation of Fig. 2A-5.

Sunglint patterns such as this have been found, in many instances, to delineate the position of the surface ridge line (Anderson, 1974).

Important Conclusions

1. Brilliant reflection off of the water or ocean surfaces indicates an area of calm winds and calm seas (long-period swell neglected).

2. Dark areas adjacent to the brilliant reflection also indicate calm wind zones adjacent to the PSP.

3. The diffuse sunglint areas indicate non-calm conditions.

References

Anderson, R.K., et al., 1974: Applications of meteorological satellite date in analysis and forecasting. *ESSA Techn. Report NESC 51 (including Supplement, Nov., 1971, and Supplement No. 2, March 1973)*, National Environmental Satellite Service, NOAA, Washington, D.C., 350 pp.

McClain, P.E., and A.E. Strong, 1969: On anomalous dark patches in satellite-viewed sunglint areas. *Mon. Wea. Rev.*, 97, 875-884.

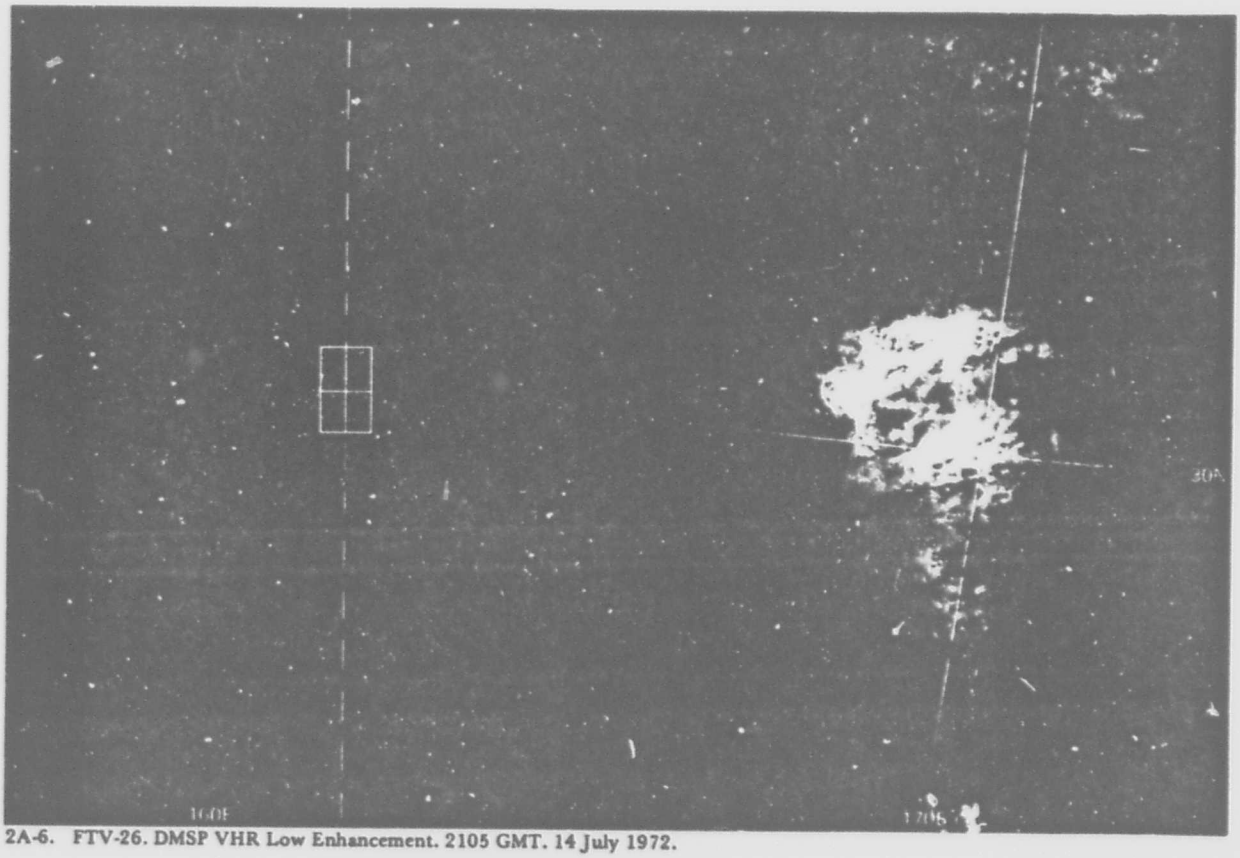

2A-6. FTV-26. DMSP VHR Low Enhancement. 2105 GMT. 14 July 1972.

Case 2 Sunglint

Identification of surface ridge lines

In this example (Fig. 2A-7) brilliant sunglint is observed at the primary specular point (PSP) near 23N, 147E. The notched or indented border in the sunglint pattern just to the west of this point is an indication of calm seas in that area. The low-level ridge line ideally would be expected to cross the two areas. A streamline analysis (Fig. 2A-8) of surface winds verifies the presence of a sharp ridge through the two areas and extending westward.

Note that the ridge line in its western extremity overlies a clear area that is a darker shade of gray than most of the surrounding area. Since strong subsidence is found along a ridge line, air should be dryer in this zone. Hence there should be less scattering of light due to the presence of condensation particles. Since seas are also slight in this area less light is reflected to the spacecraft sensor and the area appears darker as shown. Similar dark regions have been frequently noted in areas of suspected strong subsidence in advance of frontal bands, squall lines (See Fig. 1B-7), etc.

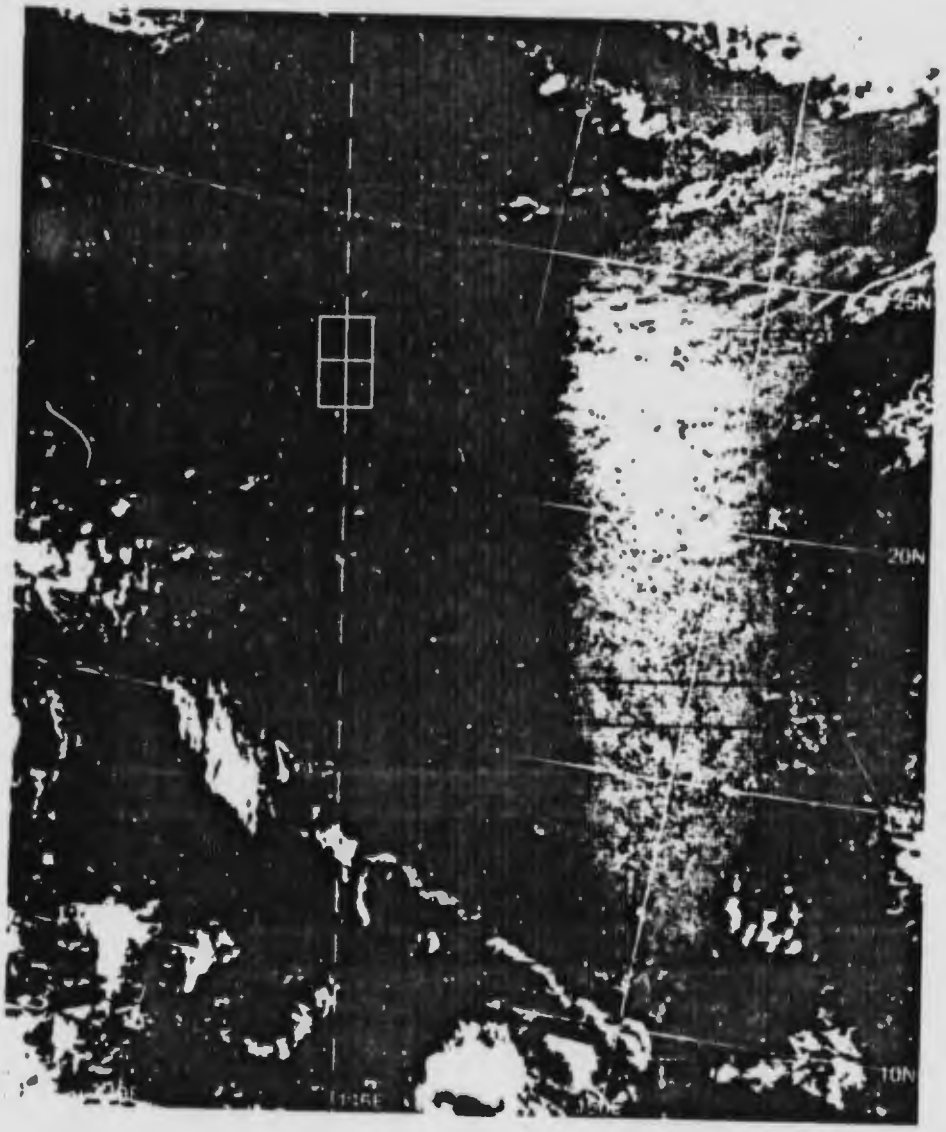

2A-7. FTV-29. DMSP VHR Low Enhancement. 2252 GMT. 17 July 1974.

Fig. 2A-9 is the Fleet Numerical Weather Central (FNWC), Optimum Ship Routing (OTSR) wave-height analysis, superimposed over the DMSP data, which verifies the slight seas in the ridge line area. The sunglint pattern broadens east and west, to the north of the PSP. This broadening correlates with rougher sea conditions indicated by seas greater than 6 ft. to the north.

Important Conclusions

1. Low-level ridge lines can be located from DMSP sunglint data. The ridge line connects the area of brilliant specular reflection with indented dark areas west and/or east of the specular zone and may continue to be defined in the dark shade of gray further west or east of the point of indentation.

2. Sunglint patterns broadening to north or south of the PSP normally relate to rougher seas.

2A-8. FTV-29. DMSP VHR Low Enhancement. 2252 GMT. 17 July 1974. Surface Streamline Analysis. 0000 GMT. 18 July 1974.

d (FNWC), Optimum
erimposed over the
ridge line area. The
rth of the PSP. This
is indicated by seas

P sunglint data. The
ular reflection with
cular zone and may
further west or east

of the PSP normally

2A-9. FTV-29. DMSP VHR Low Enhancement. 2252 GMT. 17 July 1974.
Fleet Numerical Weather Central (OTSR) Wave-height Analysis (feet). 0000 GMT. 18 July 1974.

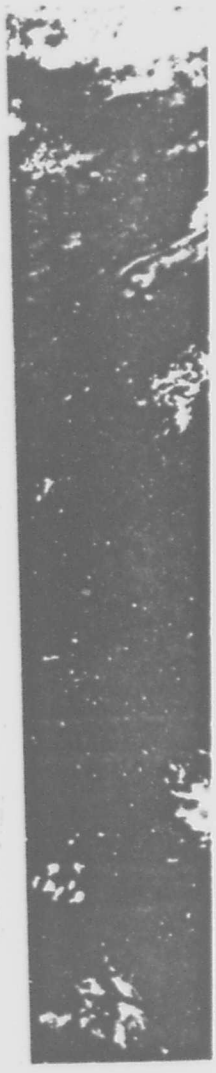

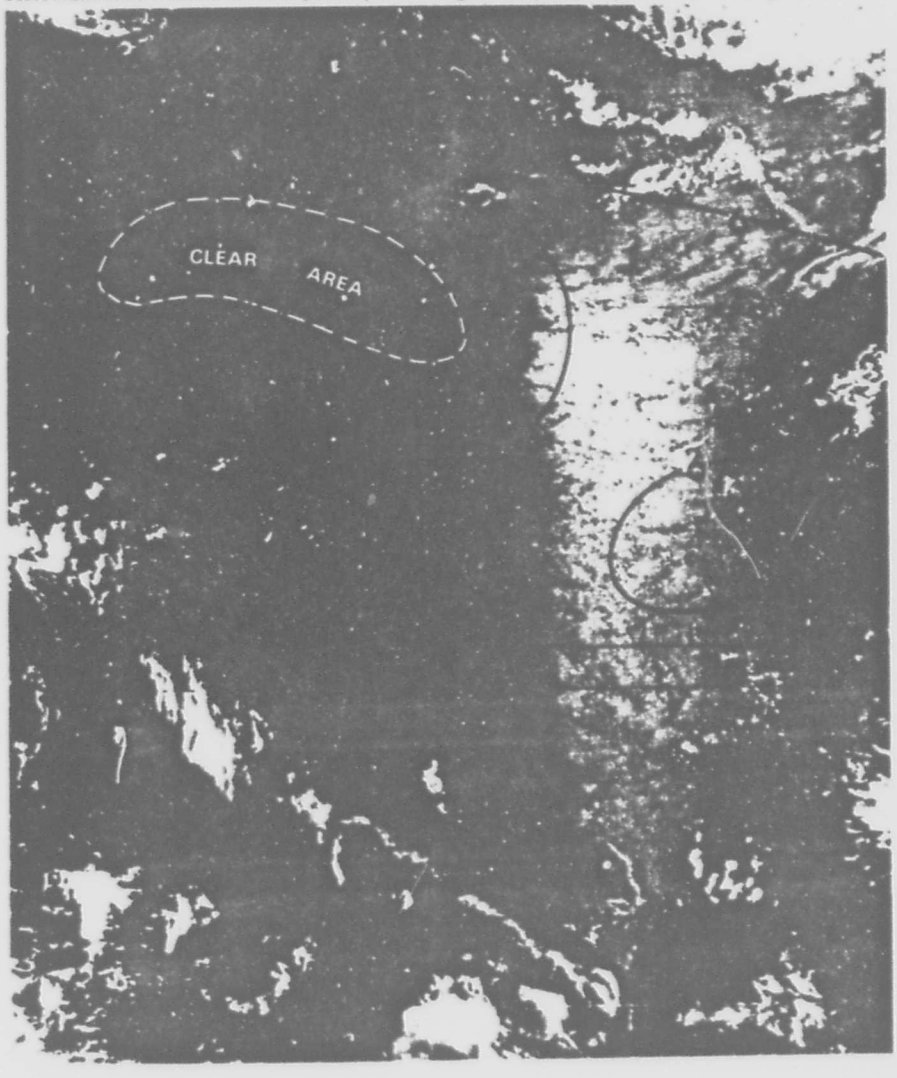

Case 3 Sunglint

Surface chart high pressure area reanalysis
Identification of calm wind areas removed from the primary specular point

Brilliant specular reflection appears in this DMSP imagery (Fig. 2A-10) near 25N, 171E. The pattern suggests a ridge line intersecting the dark (calm) areas frequently found in advance of frontal systems.

An operational surface pressure analysis superimposed on the picture, however, gives no indication of a ridge in the area and, in fact, shows a high pressure center over 1,000 nm to the northwest. Sparsity

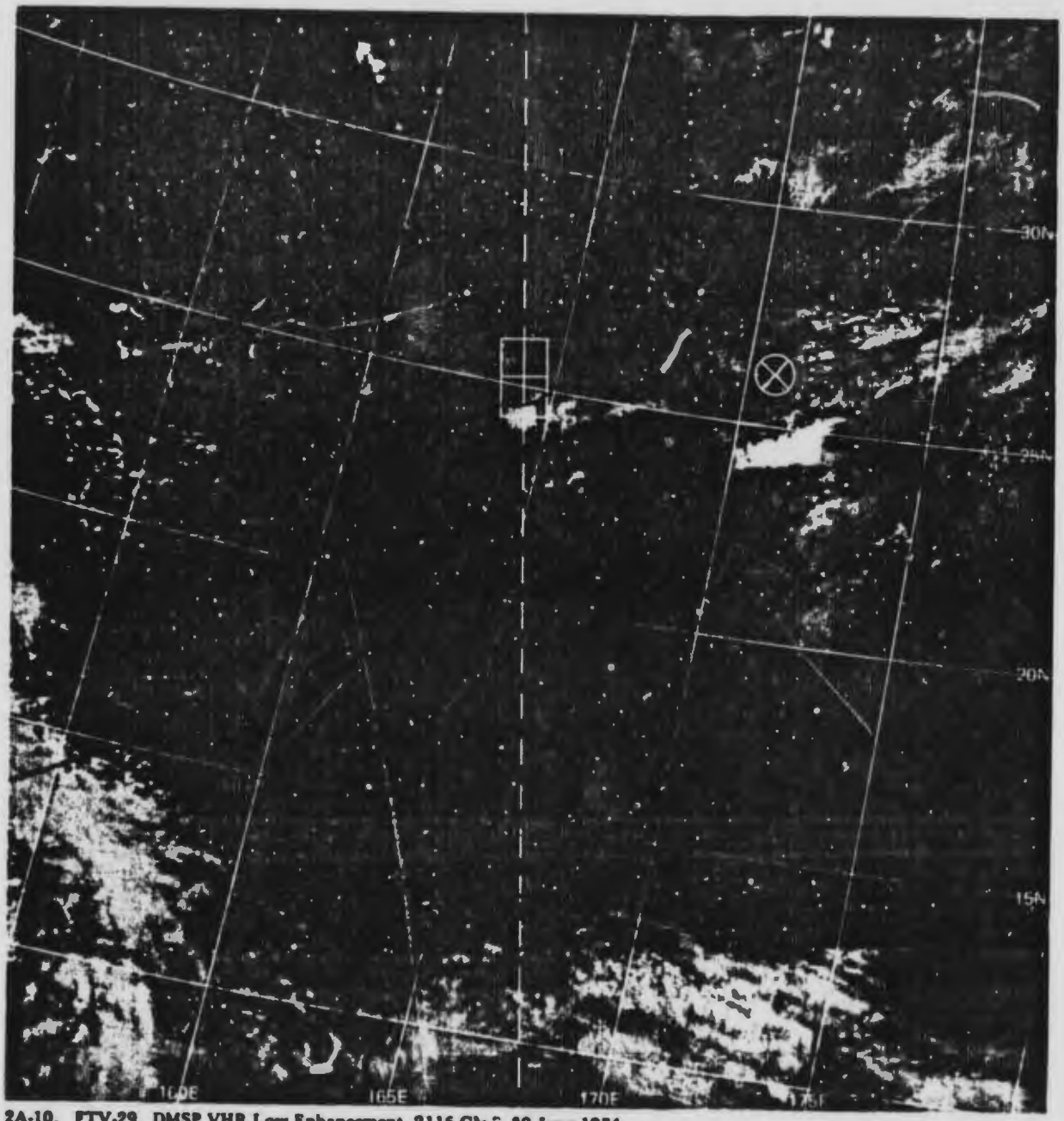

2A-10. FTV-29. DMSP VHR Low Enhancement. 2116 GMT. 30 June 1974.
Surface Pressure Analysis. 1800 GMT. 30 June 1974.

of conventional reports undoubtedly led to this error in analysis. In Fig. 2A-11, the streamline analysis shows that a ridge line through the brilliant sunglint area can be accommodated without violating any of the existing surface wind reports. The pressure analysis could have been similarly adjusted. This case demonstrates the value of using satellite data to assist in drawing surface pressure contours or streamlines for a more realistic analysis.

Note the additional multiple dark areas along 175E longitude to the southeast of the brilliant sunglint area. Such areas frequently suggest slight sea areas away from the primary specular point (PSP). This may not always be the case since thin cirrus cloudiness and aerosols can also reduce reflection in a sunglint area and cause the appearance of dark areas. Infrared data can often assist in resolving such ambiguities.

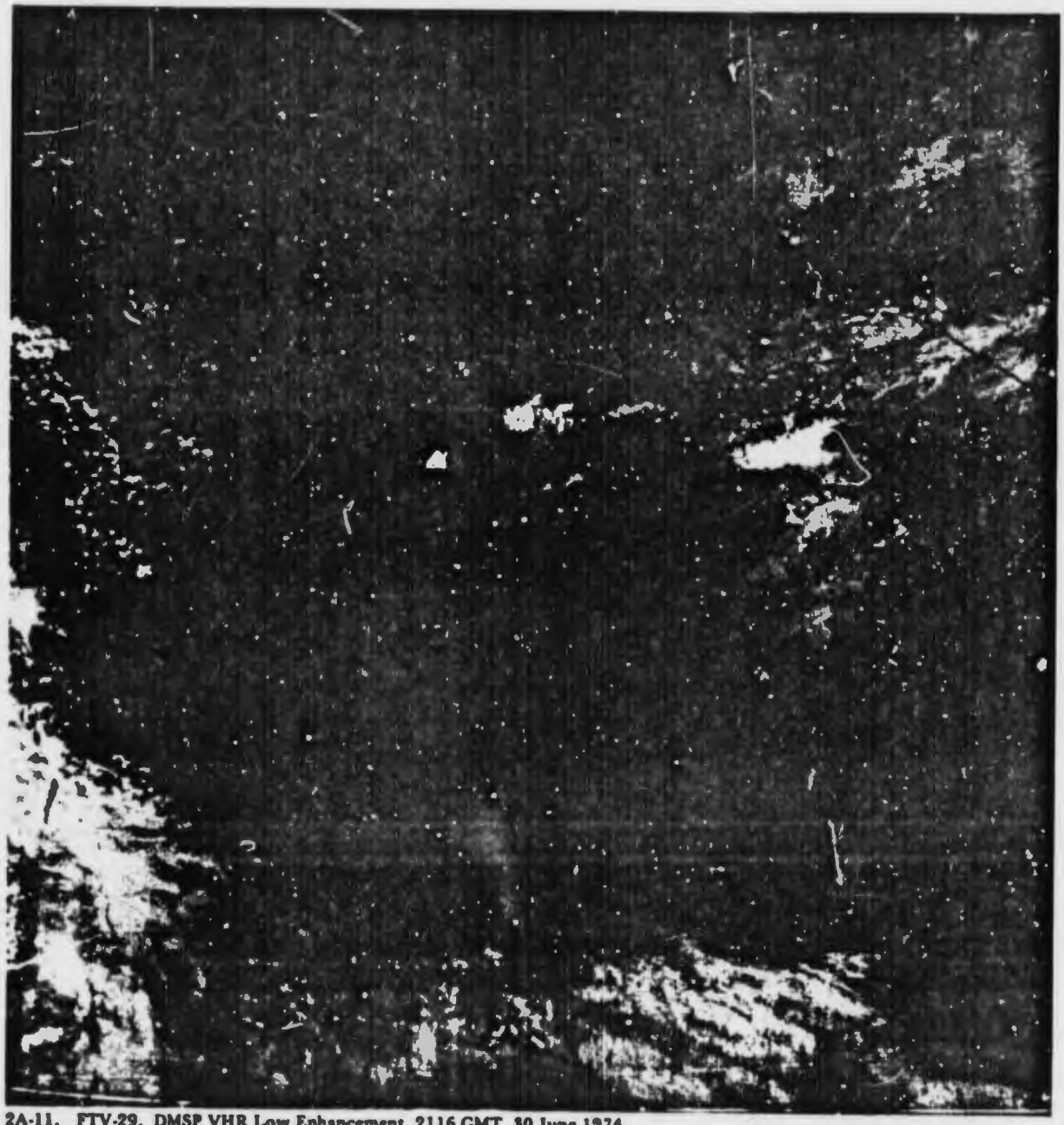

2A-11. FTV-29. DMSP VHR Low Enhancement. 2116 GMT. 30 June 1974.
Surface Streamline Analysis. 1800 GMT. 30 June 1974.

If multiple dark areas defining slight seas in sunglint patterns can be found, one might anticipate that multiple brilliant areas extending north and south of the PSP indicating slight sea areas might also be found. An example of this is shown in Fig. 2A-12, where brilliant sunglint over calm seas is located west of the Philippines, southwest of Taiwan and just off the southeast China coast. The PSP is located to the west of the Philippines. This depiction emphasizes the relative insensitivity of the DMSP sensor in detecting radiation intensity changes from areas near the PSP in a north or south direction. Intensity of radiation received under calm sea conditions decreases rapidly east and west of the PSP as shown earlier in Fig. 2A-5 and Fig. 2A-6. However, it is not unusual to have brilliant reflection, as in this example, several degrees north or south of the PSP. One reason for this may be that the spacecraft sensor saturates rapidly and does not distinguish between variations of intense reflections. One must always realize that whenever strong sunglint appears at a point other than the PSP that the seas cannot be perfectly calm and that some wave motion is necessary to reflect the sun's rays toward the spacecraft sensor.

Important Conclusions

1. Calm seas are indicated by brilliant reflection at the PSP and in adjacent dark areas extending to the east and west.

2. Calm seas in a sunglint pattern can be used to define the position of surface ridge lines.

3. Additional brilliant patterns near the center of sunglint and dark areas at the edge of sunglint may define other slight sea or calm areas and ridge lines.

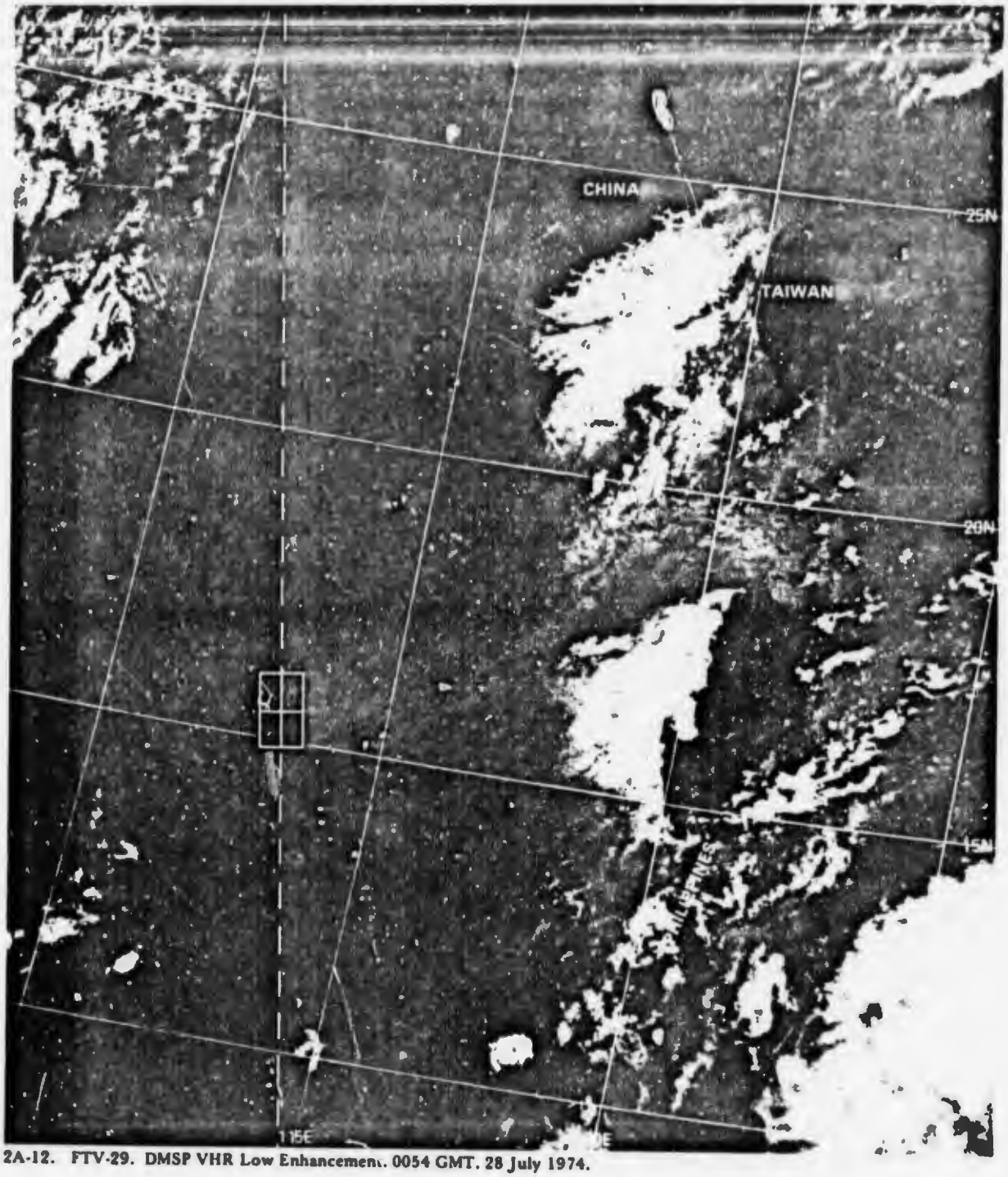

2A-12. FTV-29. DMSP VHR Low Enhancement. 0054 GMT. 28 July 1974.

Calm wind zone not intersecting the primary specular point
Identification of strong wind areas near the primary specular point

When a calm wind zone is well to the north or to the south of the primary specular point (PSP) reflectivity in the calm zone is minimized. The calm zone will appear as a black area or strip interrupting the more homogeneous sunglint pattern. Fig. 2A-13 shows the theoretical sunglint pattern that would result for an instantaneous satellite photograph of sunglint assuming a 5 m sec^{-1} (10 kt) wind background and a calm wind (shaded area) in an east-west swath north of the PSP. In DMSP data, as in the preceding example, brilliant areas are observed at some distance to the north or south of the PSP. At distances of about 10 degrees of latitude, or more, to the north or south of the PSP, dark swaths extending across the sunglint pattern are observed.

In Fig. 2A-14 a black swath is apparent extending across the sunglint pattern centered near longitude 137E. The PSP is well to the north. The presence of such a black strip frequently correlates with the position of a surface ridge line. Fig. 2A-15 shows surface wind reports and streamlines superimposed on the DMSP data which substantiate light winds and the presence of a ridge as indicated. Note that in the area of the PSP, where winds have quite a long fetch from the southwest, reflectivity per unit area is reduced indicating rougher seas in comparison to the calmer seas further to the south.

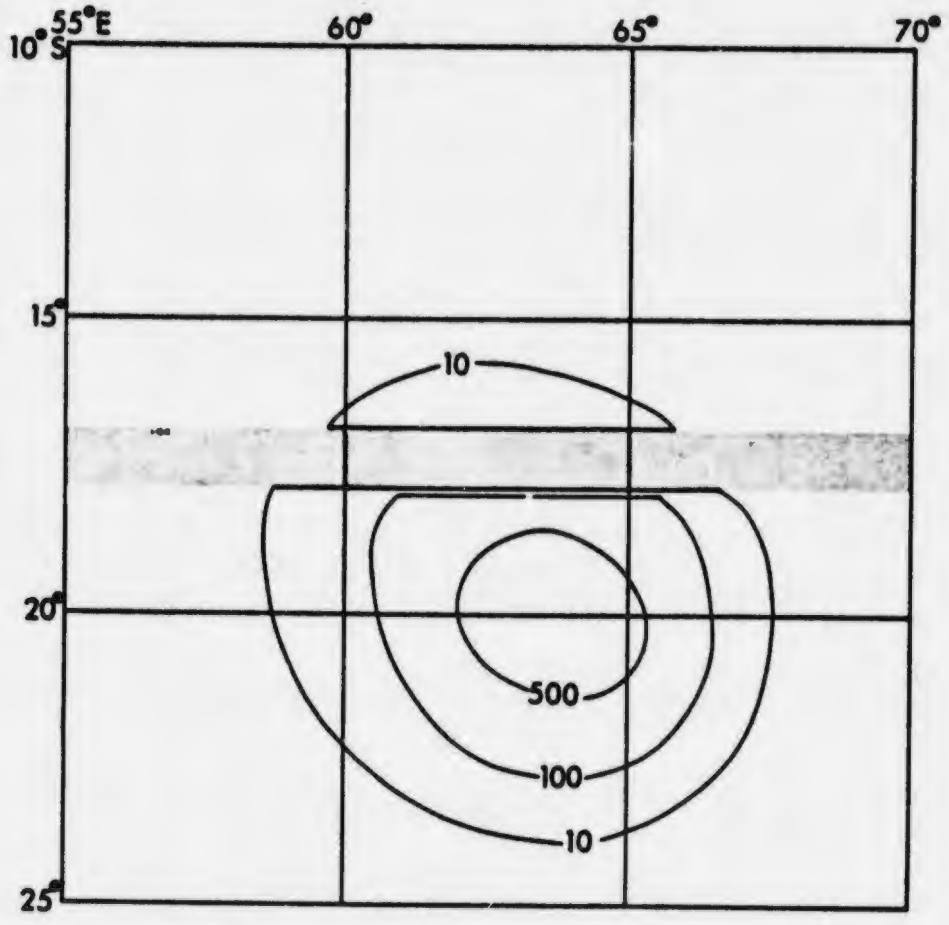

Fig. 2A-13. Theoretical sea-surface sunglint for a composite pattern; 5 m sec^{-1} (10 kt) wind background and a calm wind in an east-west swath near specular point (shaded). Isopleths are reflected intensity per 10^6 steradian incident flux; satellite subpoint, 21.5S, 65.5E; solar subpoint, 5.8S, 35.6E; satellite height, 722 km. (Courtesy of McClain and Strong, 1969).

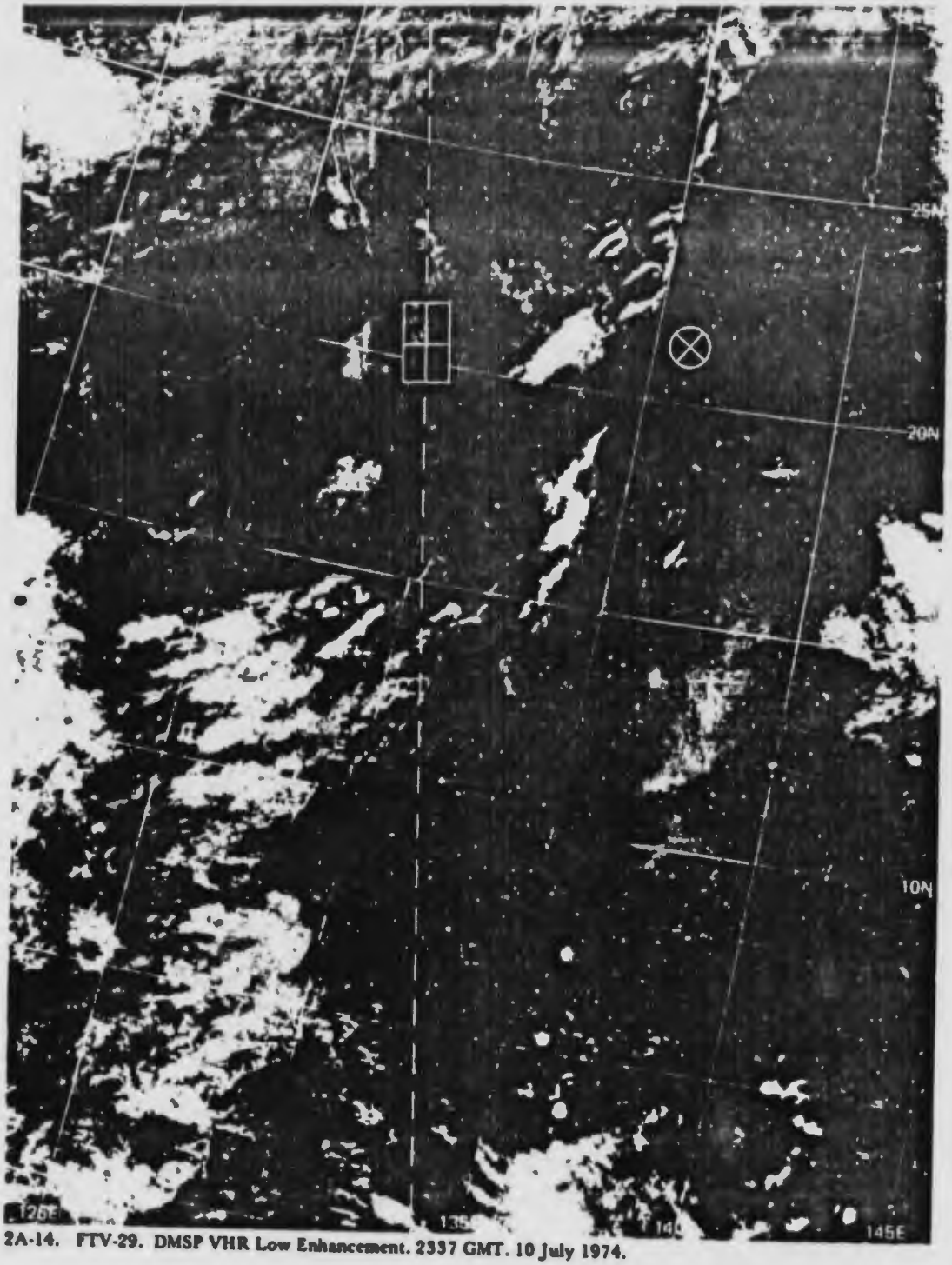

2A-14. FTV-29. DMSP VHR Low Enhancement. 2337 GMT. 10 July 1974.

Important Conclusions

1. Black swaths across sunglint areas, to the north or south of the PSP, usually correlate with surface ridge lines over areas of low winds and low-sea state.

References

McClain, P.E., and A.E. Strong, 1969: On anomalous dark patches in satellite-viewed sunglint areas. *Mon. Wea. Rev.*, 97, 875-884.

2A-15. FTV-29. DMSP VHR Low Enhancement. 2337 GMT. 10 July 1974.
Surface Wind Reports and Streamline Analysis. 0000 GMT. 11 July 1974.

or south of the PSP,
eas of low winds and

lous dark patches in
84.

Identification of surface ridge lines and calm sea areas removed from the primary specular point

A sequel to the preceding case (Case 4) is shown in this DMSP image over the Eastern Pacific (Fig. 2A-16). Sunglint is apparent in this noontime pass extending northward near longitude 135W. The pattern again is interrupted by a dark strip extending through an area of maximum sunglint return near 30N, 135W. Since the primary specular point (PSP) is well to the south, near 19N (Solar subpoint, 21N), the pattern again suggests a calm wind and calm sea condition which should define high pressure and a ridge line axis oriented along the dark strip. Fig. 2A-17 shows surface reports and streamline analysis which verify these assumptions.

Note that as in the previous case, highest reflectivity is associated with the implied area of lowest sea state. In fact the gray shade

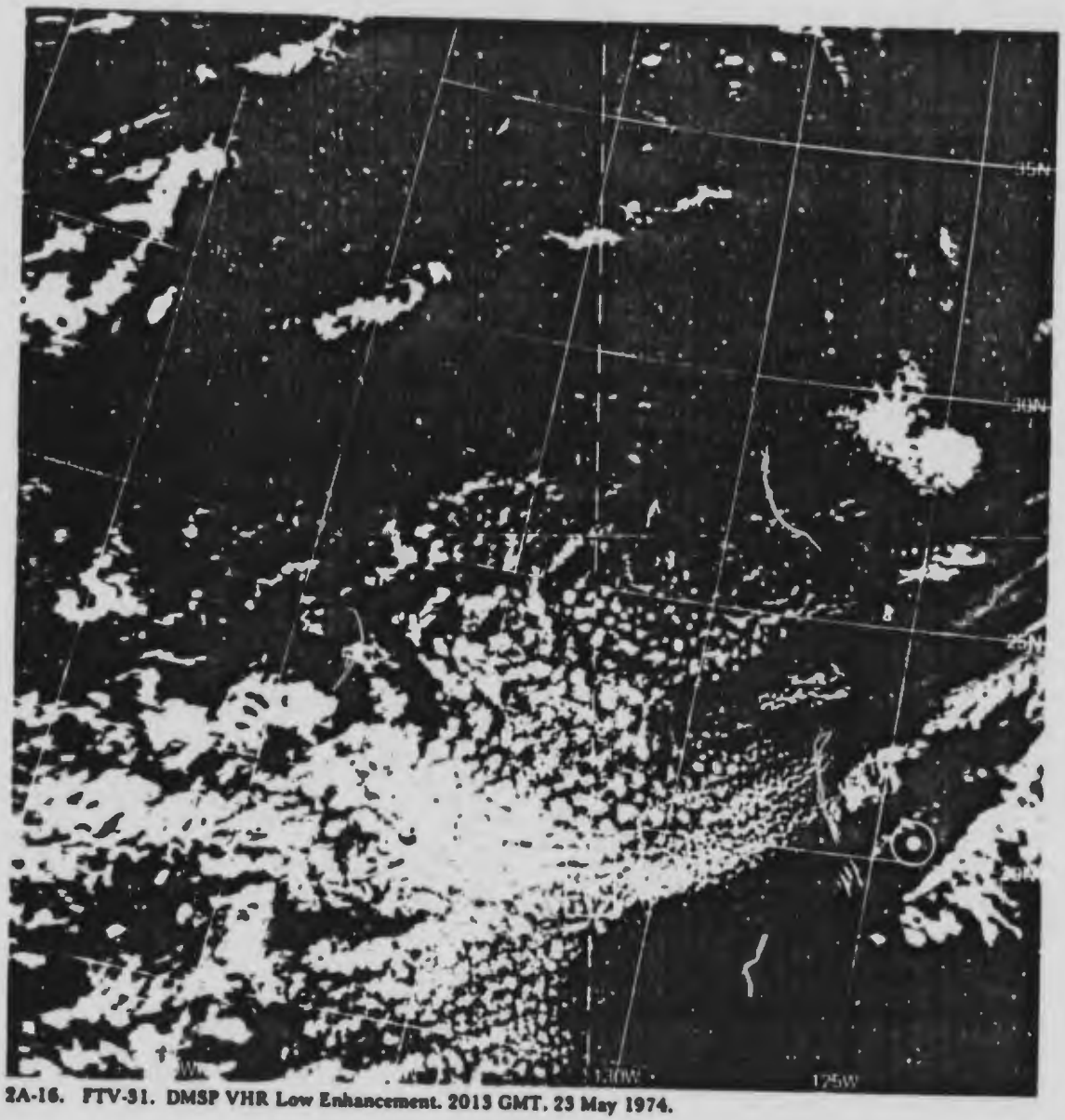

2A-16. FTV-31. DMSP VHR Low Enhancement. 2013 GMT. 23 May 1974.

contours of highest reflectivity suggest a "Bull's-eye" pattern over the dark strip area. This sunglint pattern has special significance. Under conditions of uniform sea state, one would anticipate a decreasing intensity sunglint return the greater the distance north or south of the PSP. A brightness maximum removed from the PSP implies low sea state conditions over that area. If a dark strip, in addition, runs through the area, positive identification of calm seas and ridge line axis is normally obtained.

Important Conclusions

1. A dark strip interrupting a sunglint pattern, with the PSP well to the north or south, usually implies calm seas with a surface ridge line axis extending through the area.

2. Bright areas at any location, north or south of the PSP, in a sunglint pattern imply slight sea conditions in the area. Conversely, broad, intervening areas of reduced brightness are associated with areas of increased sea heights.

2A-17. FTV-31. DMSP VHR Low Enhancement. 2013 GMT. 23 May 1974.
Surface Wind Reports and Streamline Analysis. 1200 GMT. 23 May 1974.

Identification of shallow ocean areas in sunglint areas

This DMSP image (Fig. 2A-18) shows a sunglint pattern stretching from Borneo across the South China Sea to the southern coast of Indo-China. The interruption of the sunglint pattern by the black strip crossing it just north of Borneo is indicative of a probable low-sea state strip due to calm winds over the area. In this instance the primary specular point (PSP) is located over China near 25N. Under such a condition solar reflection to the spacecraft sensor is minimized in the calm area to the south.

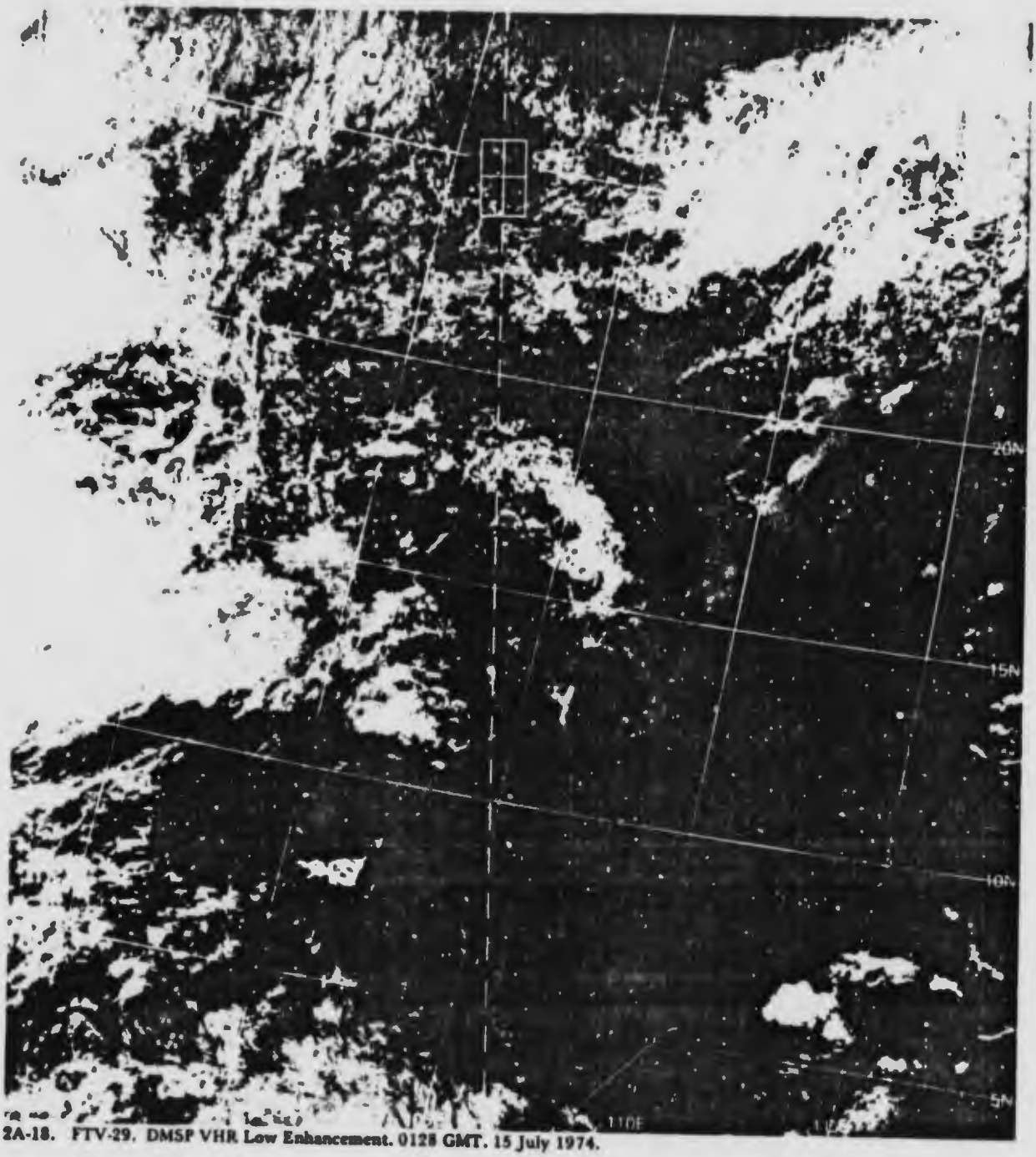

2A-18. FTV-29. DMSP VHR Low Enhancement. 0128 GMT. 15 July 1974.

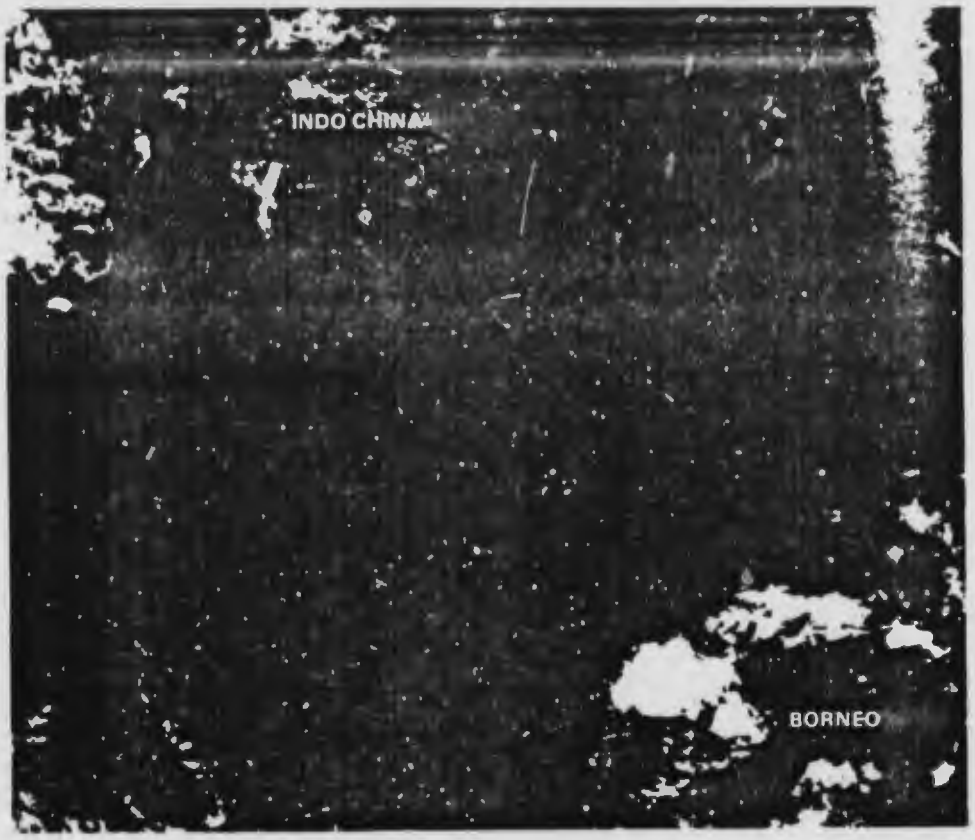

2A-19. Enlarged View. FTV-29. DMSP VHR Low Enhancement. 0128 GMT. 15 July 1974.

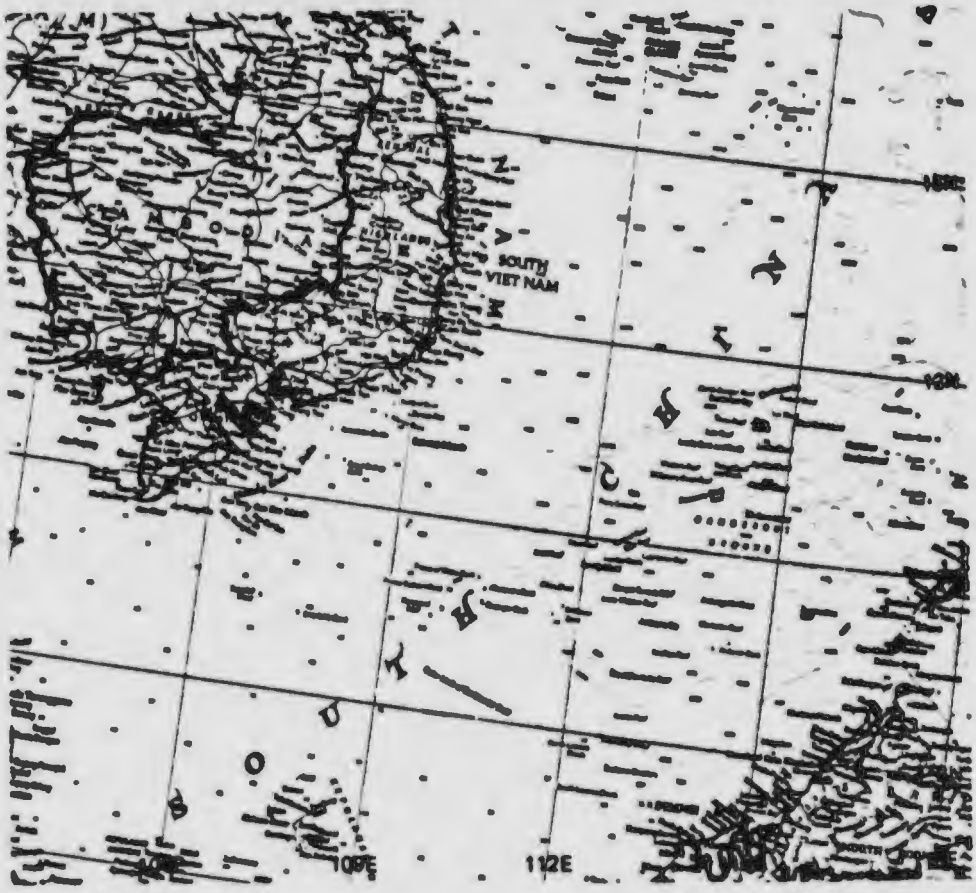

2A-20. Geographical Map. South China Sea Area.

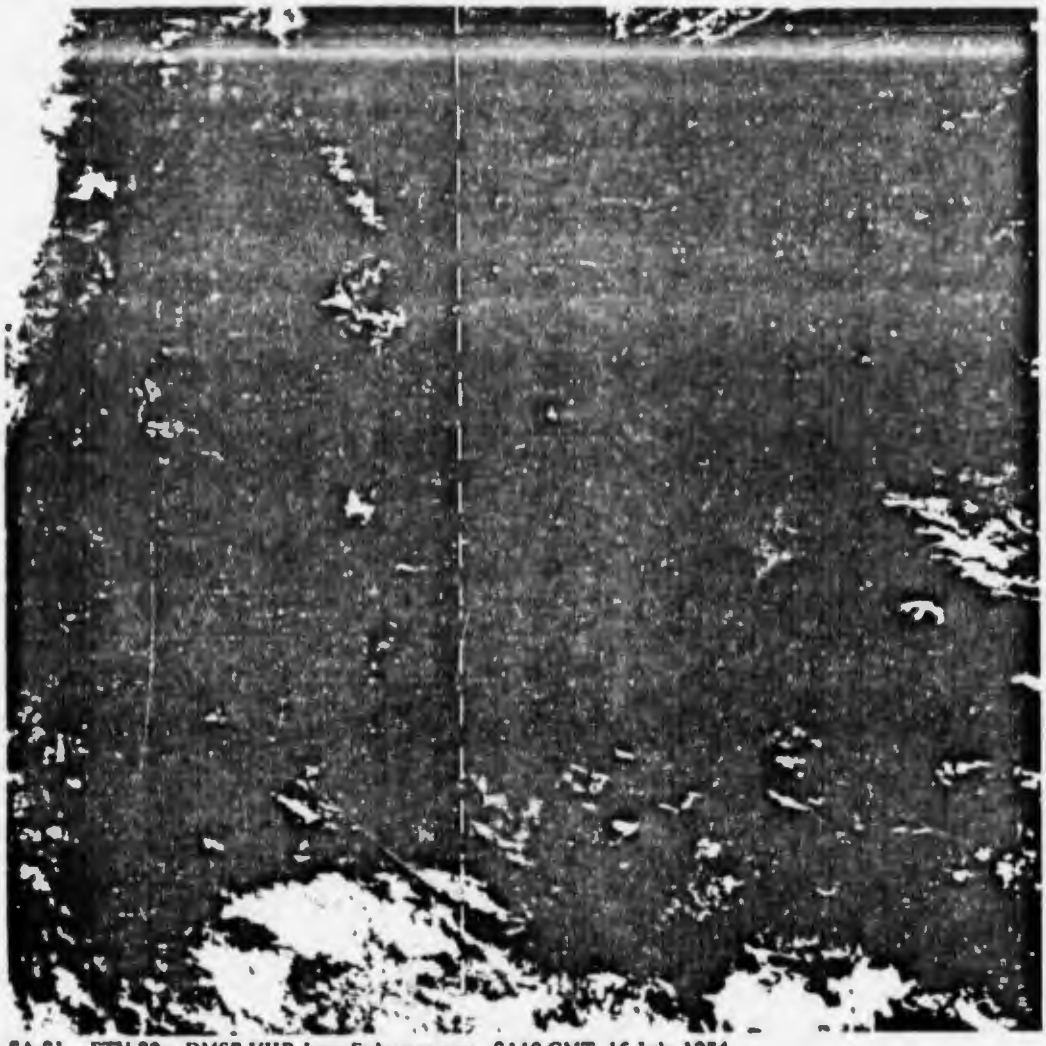

2A-21. FTV-29. DMSP VHR Low Enhancement. 0110 GMT. 16 July 1974
Surface Wind Reports and Streamline Analysis. 0000 GMT. 16 July 1974

This case is especially interesting since the black area (Fig. 2A-19) overlies a portion of a notorious shallow bank in the South China Sea marked "Dangerous Ground" (Fig. 2A-20). Ocean swell could be rather drastically reduced by such a barrier. Under conditions of light winds it would seem probable that this area and other similar shoal areas would be favored for calm or slight sea conditions.

This proved to be the case on the following day (Fig. 2A-21) where again the sunglint pattern is interrupted by a dark strip very near the same area. On this date surface wind reports and a streamline analysis verify calm to very light winds over the area with a ridge line axis suggested by the streamlines in the "black strip" area.

Important Conclusions

1. Sunglint patterns interrupted by a dark strip running through the sunglint area frequently define an area of calm winds and calm seas correlated with a surface ridge line axis.

2. Shallow banks or shoals under conditions of light winds may be favored areas for relatively calm seas and therefore may appear frequently as dark or very bright areas in satellite data depending upon satelli e/sun angle relationships.

Case 7 Sunglint

Identification of mountain-gap winds in sunglint areas

When colder air builds up on one side of a mountain range under stable conditions it will have a tendency to spill through and, in fact, accelerate, in jet-like fashion, through mountain gaps toward lower pressure. Scorer (1952) documented such effects in the Strait of Gibraltar and outlined some of the basic principles involved.

He found, for example, that the effect is most pronounced in those situations having a marked low-level inversion or isothermal layer just below mountain top level. In those instances the height of the inversion was greatest on the cold air or upwind side of the mountain gap and lower to the lee. A pressure gradient through the pass toward lower pressure is thus maintained for some time (a matter of many hours) permitting an extreme acceleration of the wind to speeds up to 100 kts in the lower or cold air portion of the atmosphere. Vertical shear is also extreme so that above the inversion, under the same circumstance, light winds of variable direction may be found. Large standing eddies are frequently found on the side of the emerging jet. Scorer detected the eddies in the surface isobaric pattern. These high-speed wind patterns can now also be seen in satellite data.

Fig. 2A-22 is a DMSP image of the Iberian Peninsula-North African area. A sunglint pattern appears over this area. The pattern is interrupted by a dark, elongated elliptical swath extending to the west of the Strait of Gibraltar. Normal interpretation of sunglint interruption by a dark gray shade is to attribute the effect to calm winds and calm seas at some

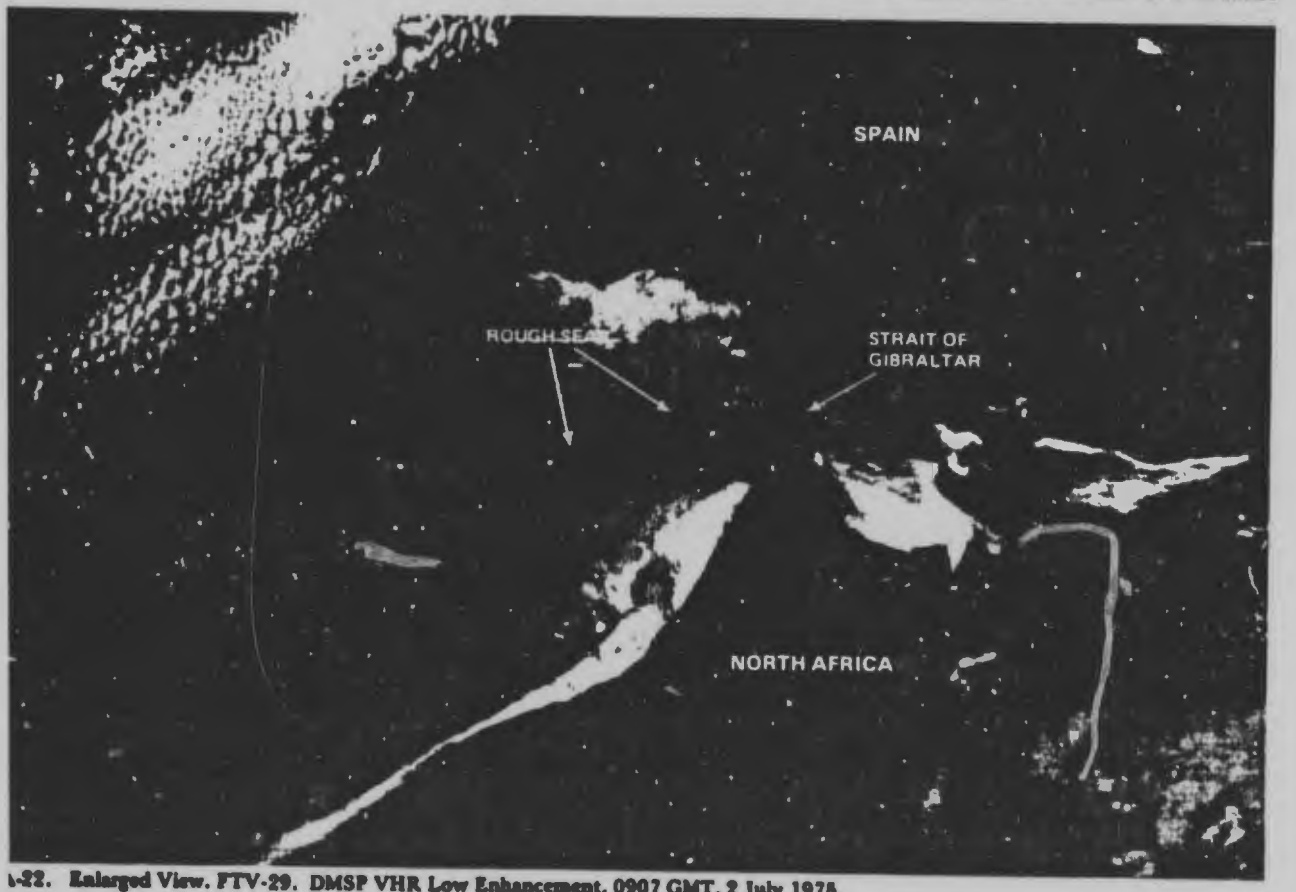

2-22. Enlarged View. FTV-29. DMSP VHR Low Enhancement. 0907 GMT. 2 July 1975.

distance from the primary specular point (PSP). (See Fig. 2A-14). Since the PSP for this example was calculated to be near 25.5N and 5.5W, well to the south, over Africa (Fig. 2A-23) such a conclusion seems pertinent to this example. Calm sea state in this case, however, does not seem logical since the Strait of Gibraltar and other straits are known producers of strong winds, not calm winds. An alternate argument may be proposed which attributes such an effect to rough seas rather than calm seas. Assume a sunglint pattern of diffuse reflection at some rather large distance from the PSP. Theory holds that the larger the area of diffuse reflection the stronger the winds and the weaker the reflection per unit area. If a local wind, such as the Gibraltar jet, were blowing through such an area the reflection per unit area under the jet would be even more reduced than the reflection from the surrounding areas. Hence this area would appear black or darker than the surrounding areas. This appears to be the most logical explanation for the pattern shown in this example.

Surface reports for 0900 GMT, within a few minutes of the time of this pass, indicate a general easterly flow over France, Spain and North Africa which changes to northerly over the eastern Atlantic. Note that despite relatively light winds, in general, a 40 kt easterly wind is reported within the Strait of Gibraltar! An obvious conclusion is that the mountain-gap Strait of Gibraltar low-level jet is occurring and that its presence and extent is uniquely revealed by the DMSP interrupted sunglint pattern. The dark notch in the sunglint pattern west of the elliptical shaped area, normally taken as an effect of calm seas, in this case is an indication that seas in that area are also rougher than seas to the north and south. The rough sea area caused by the jet thus appears to extend to at least 35N, 9W, or more than 150 nm west of the entrance to the Strait. Parallel cloud lines between 30-35N, 10-15W may be gravity waves formed on the inversion interface as a result of impulses received from the low-level Gibraltar jet. If this hypothesis is correct, the existence of such lines may be another indication of strong winds blowing through the Strait of Gibraltar.

Important Conclusions

1. A Strait of Gibraltar low-level jet, can often be detected in DMSP sunglint data.

2. The appearance of a dark elliptical-shaped area within a sunglint pattern to the east or west of the Strait is often an indication of strong, low-level winds and rough seas in that area. Note that the reverse of this, namely calm seas, may sometimes give a similar indication. However, in this case the dark areas would extend to both the east and west of the Straits. Ambiguities must be resolved by considering the satellite data in context with other available observations.

3. Parallel, low-level cloud lines west of the Strait of Gibraltar may be an indication of gravity waves formed as the result of impulses received from the low-level Gibraltar jet. They may also be useful as indicators of the existence of such a wind.

4. Principles of analysis pertinent to this case are equally valid when applied to other mountain-gap winds such as the mistral, bora and Santa Ana.

References

Scorer, R.S., 1952: Mountain-Gap Winds; A Study of Surface Wind at Gibraltar, Quart. J.R. Meteor. Soc., 61: 53-61.

2A-29. FTV-29. DMSP VHR Low Enhancement. 0907 GMT. 2 July 1975.
Surface Wind Reports and Streamline Analysis. 0900 GMT. 2 July 1975.

Case 8 Sunglint

Identification of rivers, lakes, and flooded regions in sunglint areas

2A-24. FTV-31. DMSP VHR Low Enhancement. 0329 GMT. 27 July 1974.

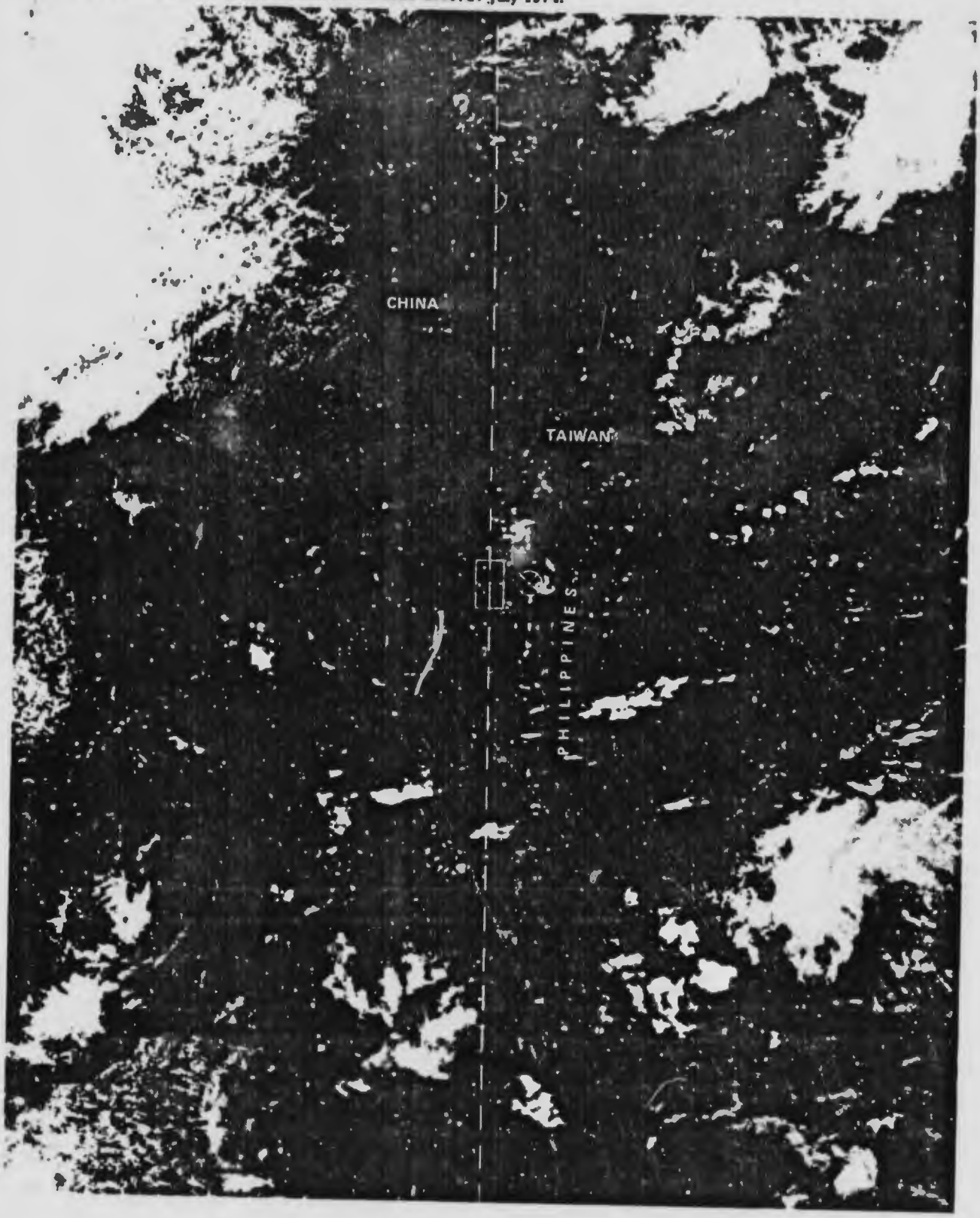

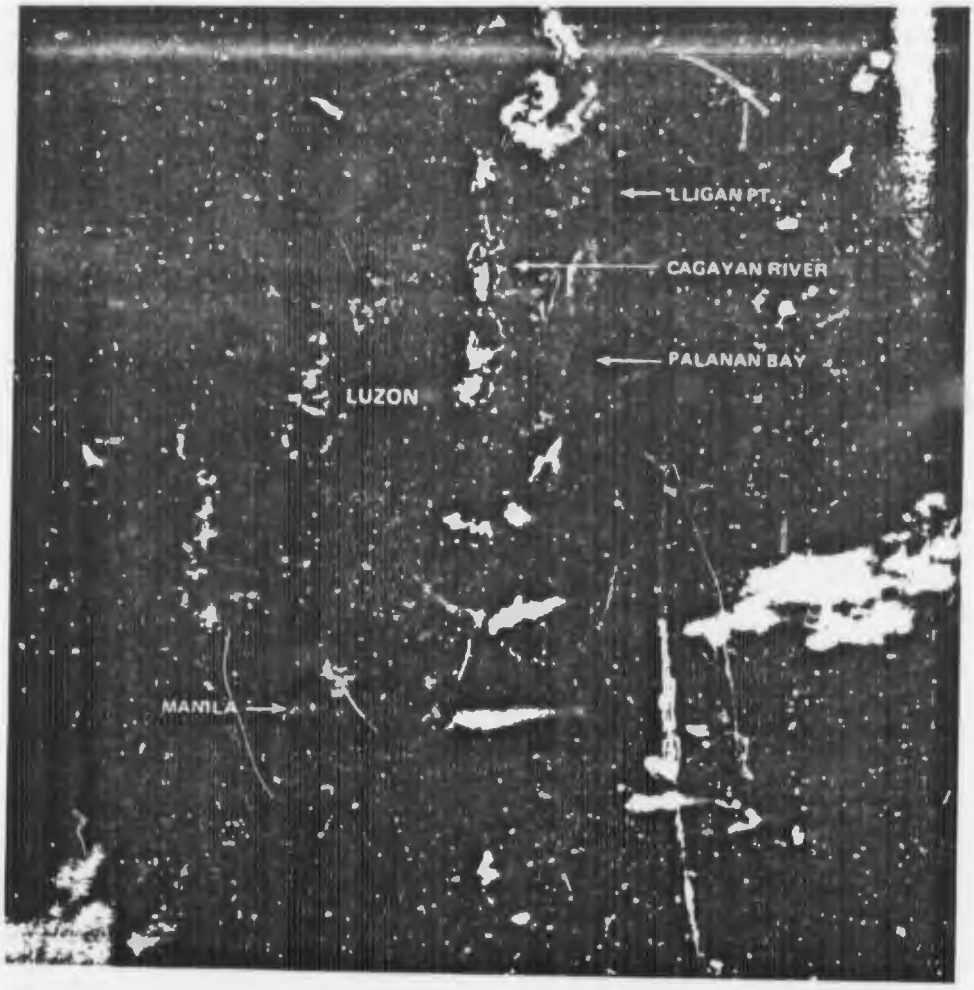

2A-25. Enlarged View. FTV-31. DMSP VHR Low Enhancement. 0329 GMT. 27 July 1974.

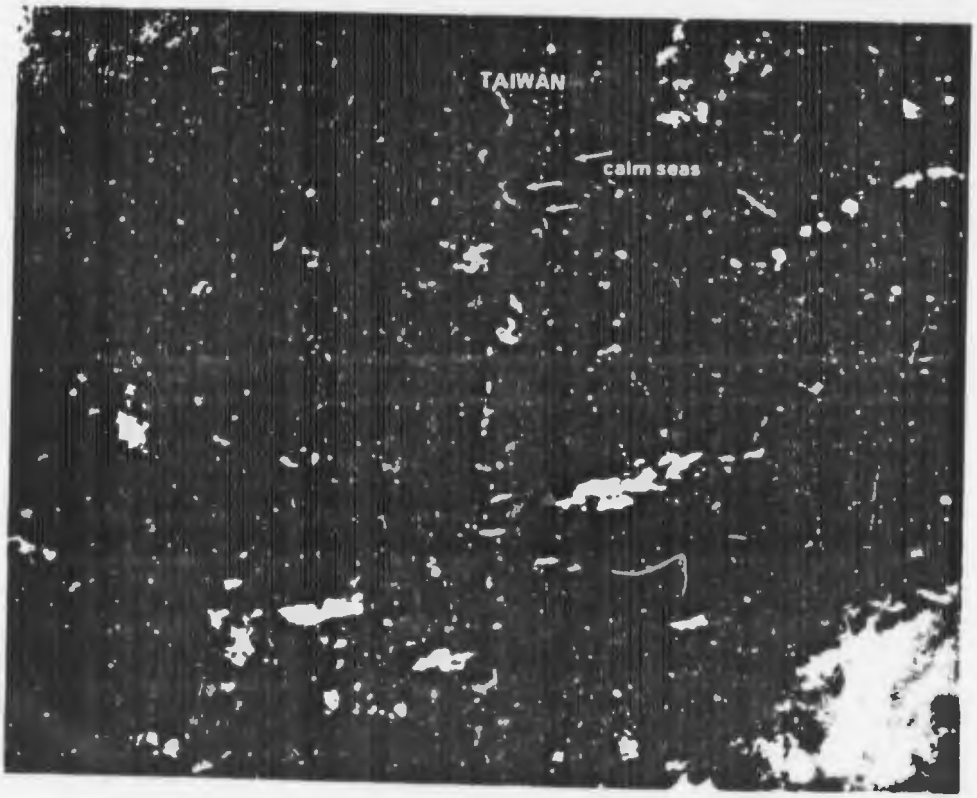

2A-26. FTV-31. DMSP VHR Low Enhancement. 0329 GMT. 27 July 1974. Ship Surface Wind Reports. 0000 GMT. 27 July 1974.

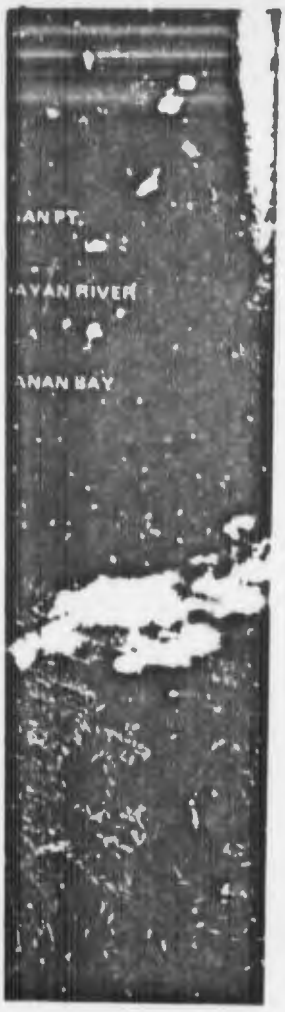

Sunglint over rivers, lakes, and flooded areas is frequently detected in DMSP VHR depictions. Fig. 2A-24 is a DMSP image showing sunglint parallel to the satellite subpoint track over Taiwan and the Philippine Islands. Brilliantly outlined near the primary specular point (PSP) is the Cagayan River with major tributaries and flooded areas apparent stretching toward Manila (Fig. 2A-25).

If a plot were made of all specular points as the satellite moved from south to north, a smooth, large radius curve would be generated just east of the satellite subpoint (see Fig. 2A-3). Black or non-reflective areas to the east and west of this curve normally denote calm seas. The area just east of the southern tip of Taiwan is such an area (Fig. 2A-26).

Ship reports (Fig. 2A-26) confirm the calm to very light winds existing over the area. It is notable in this instance that the sunglint pattern is quite narrow, indicative of low-sea state conditions. Had stronger winds and rougher seas prevailed, diffuse reflection would have caused the sunglint pattern to broaden.

Sunglint reveals the probable position of the land breeze front stretching southward just off the east coast of Luzon from Lligan Point (extreme northeast Luzon) to Palanan Bay and then again in a small section further south. This image was obtained at approximately 1130 LST, when a reversal from the land breeze circulation to a sea breeze circulation would be expected to commence. Under such circumstances wind speeds in-shore from the dissipating land breeze front would be essentially calm and sea state reduced. Such a condition is implied by the greater reflectance measured in this area by the DMSP sensor.

Important Conclusions

1. Sunglint is useful in detecting rivers and flooded areas over land.
2. The position of the land breeze front may sometimes be detected in the sunglint patterns occurring along coastal areas.
3. A narrow sunglint band is an indication of light winds and slight seas within the sunglint area.

Case 9 Sunglint

False identification of thunderstorm lines in sunglint areas

2A-27. FTV-28. DMSP VHR Low Enhancement. 0514 GMT. 7 August 1973.

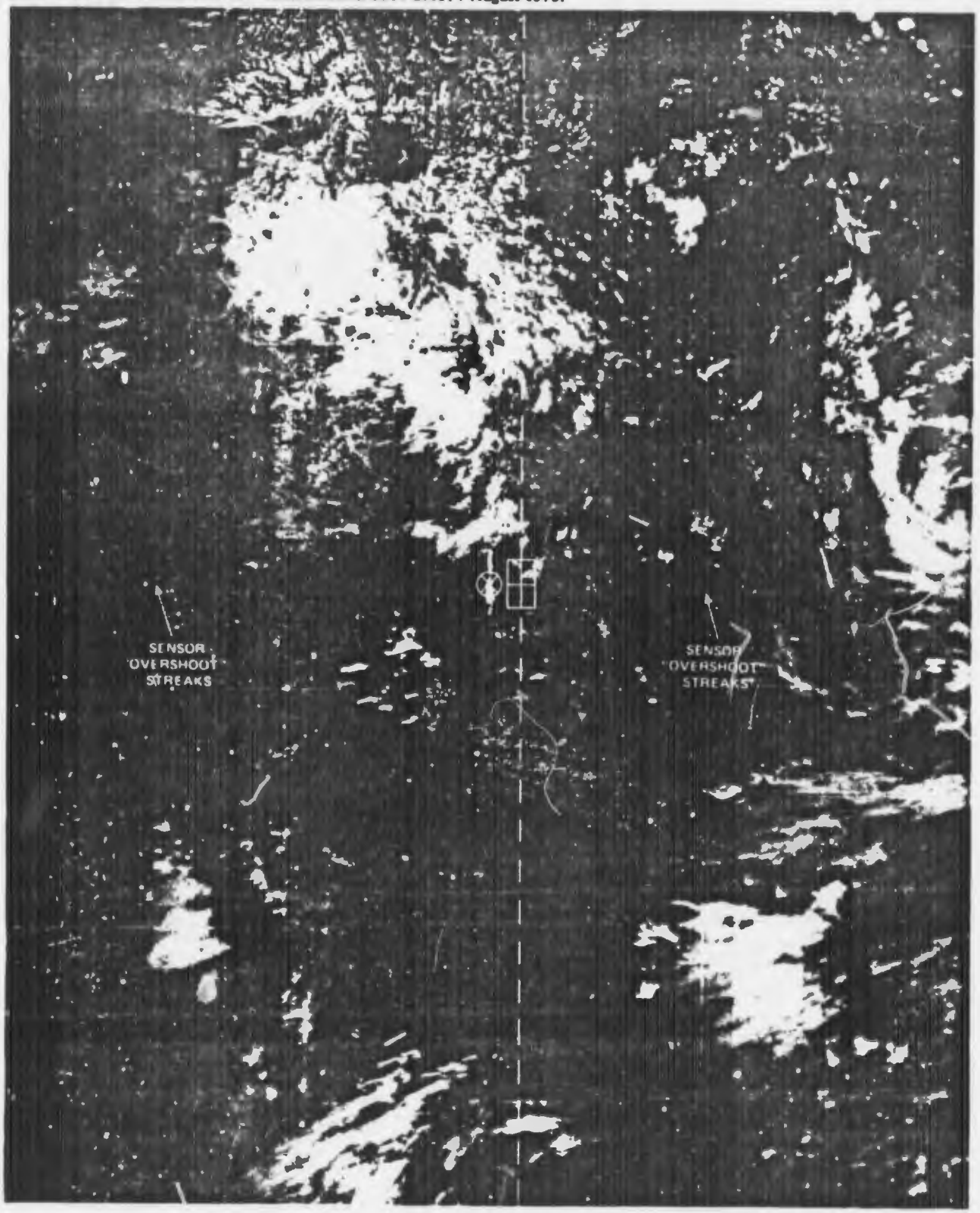

Sunglint appearing over a land area in central Thailand (Fig. 2A-27) might inadvertently be mistaken for a line of thunderstorms unless closely examined. Inspection (Fig. 2A-28) will reveal that portions of the pattern are dendritic, revealing the branching nature of river inlets and tributaries highlighted by sunglint. The PSP is located directly over this pattern.

"Over-shoot" of the sensor system, in attempting to adjust from the brilliant sunglint pattern to the far less reflective surroundings, results in horizontal, black streaks east and west of the sunglint area (Fig. 2A-27).

2A-28. Enlarged View. FTV-28. DMSP VHR Low Enhancement. 0514 GMT. 7 August 1973.

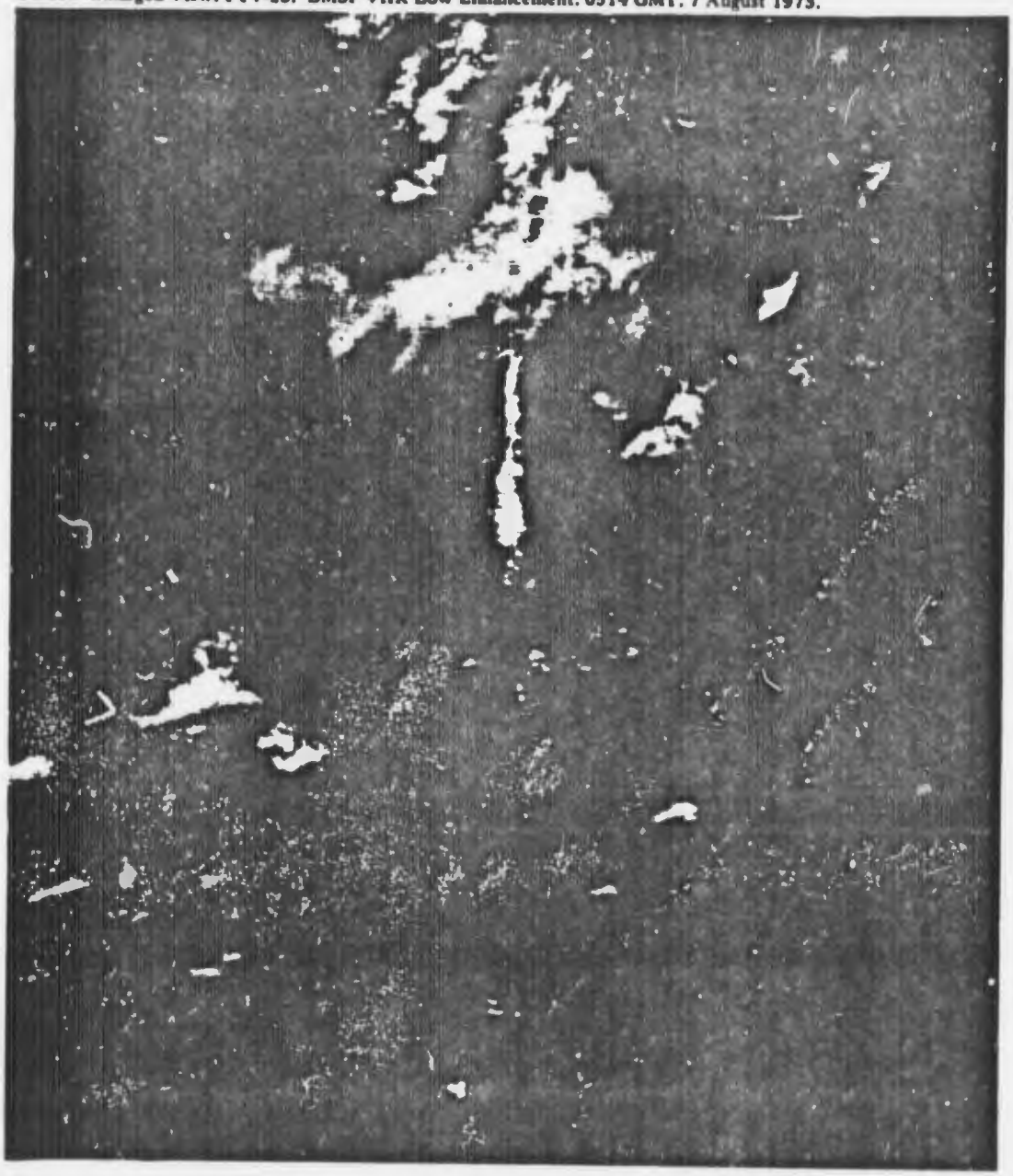

2B *Anomalous Gray Shades*

Anomalous Gray Shade Patterns.

Anomalous gray shades is a term applied to the light-tone and occasional dark-tone gray shade patterns observed over water (oceans) and land areas in cloud-free or nearly cloud-free regions in DMSP VHR (Visible) imagery. For the Navy tactical weather forecaster, the analysis and interpretation of anomalous gray shade patterns for operational purposes is important because the patterns provide insights into atmospheric and oceanographic processes occurring in the area.

The observation of anomalous gray shades can often be related to the presence or absence of atmospheric moisture in cloud-free areas, or to the presence of broken fields of cumulus, stratocumulus, or alto/cirrocumulus cloud elements, each of which are too small to be resolved within the 1/3n mi resolution limit of the DMSP VHR sensor. In addition, anomalous gray shades are also found (1) in areas of incipient cloud development, (2) along edges of increasing (or dissipating) layers of stratus or stratocumulus cloudiness, (3) in areas of developing or dissipating fog, (4) in haze areas over land, open ocean, or along coastal regions and, (5) in cirrus cloudiness areas.

Areas of blowing sand and dust, smoke from forest fires, oil rigs, etc., and air pollution may also show light-tone or dark-tone gray shade patterns. Gray shade patterns in shallow water are related to bottom topography. The outflow of muddy water or sediment from rivers into the oceans and turbid water areas in bays or along coastal regions also appear as light-tone areas in DMSP VHR imagery.

Case I Anomalous Gray Shades

High humidity/low humidity areas remote from sunglint region[1]

The appearance of anomalous gray shades in DMSP imagery is due to the expanded spectral interval of the VIIR sensor which extends roughly from 0.4 to 1.1 μm. Anomalous gray shades are often produced by the reflection and scattering of light off of condensation (haze) droplets in this spectral interval.

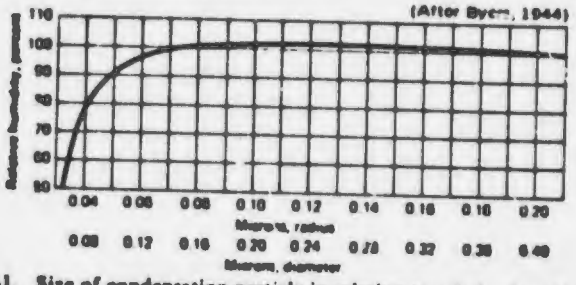

2B-1. Size of condensation particle in relation to relative humidity.

The graph in Fig. 2B-1 shows relative humidity as a function of condensation particle size. It can be seen that the relative humidity increases rapidly as the condensation particle diameter size increases from 0.06 to 0.14 μm. At 0.08 μm particle diameter, scattering is effective for the DMSP sensor. This particle size according to the graph, indicates relative humidities of about 80%. In general, relative humidities of these values would be found along the edges of fields of developing or dissipating status or stratocumulus clouds.

According to Byers (1944), condensation is a continuous process beginning at low humidities. As the relative humidity rises, condensation particle size increases and hazy conditions appear. As the haze becomes thicker and visibilities decrease, the size of the condensation particles continue to increase in diameter, until visible cloud or fog is produced. Thus, according to Byers, hazy conditions should be the forerunner, and also, the end product of clouds and fog.

The ability of the DMSP sensor to detect haze droplets as suggested above, is related to the size of the droplets (diameter) relative to the wavelength of the incident radiation. It is also related to the background brightness underlying the haze layer (Johnson, 1954).

In Fig. 2B-2 a narrow, bright marine stratus/fog band extends from the coastal area over the Pacific and southward where it broadens into a wide broken pattern. At this time, the primary specular point and the solar subpoint are well to the south so that this area is remote from sunglint. Fig. 2B-3 reveals lighter-tone stripe on either side of the bright stratus/fog off of Pt. Arguello and to the south. The stripe show the distinctive appearance of anomalous gray shades in DMSP VHR imagery. In addition, note the uniformity and areal extent of the gray shade pattern further to the south, in contrast to the striated cloud formation to the west. This is also a distinguishing characteristic between clouds and anomalous gray shades. In the anomalous gray shade areas, the darker tones indicate smaller condensation particle sizes and less dense haze conditions, and the lightest tones indicate the areas of higher humidity and more dense haze conditions. Reduced low-level visibilities therefore can be expected in the areas of the lightest tones.

1. An area remote from a sunglint region is defined as an area where sunglint from the ocean surface can no longer be detected, regardless of the sea state in the area. (See Fig. 2A-3).

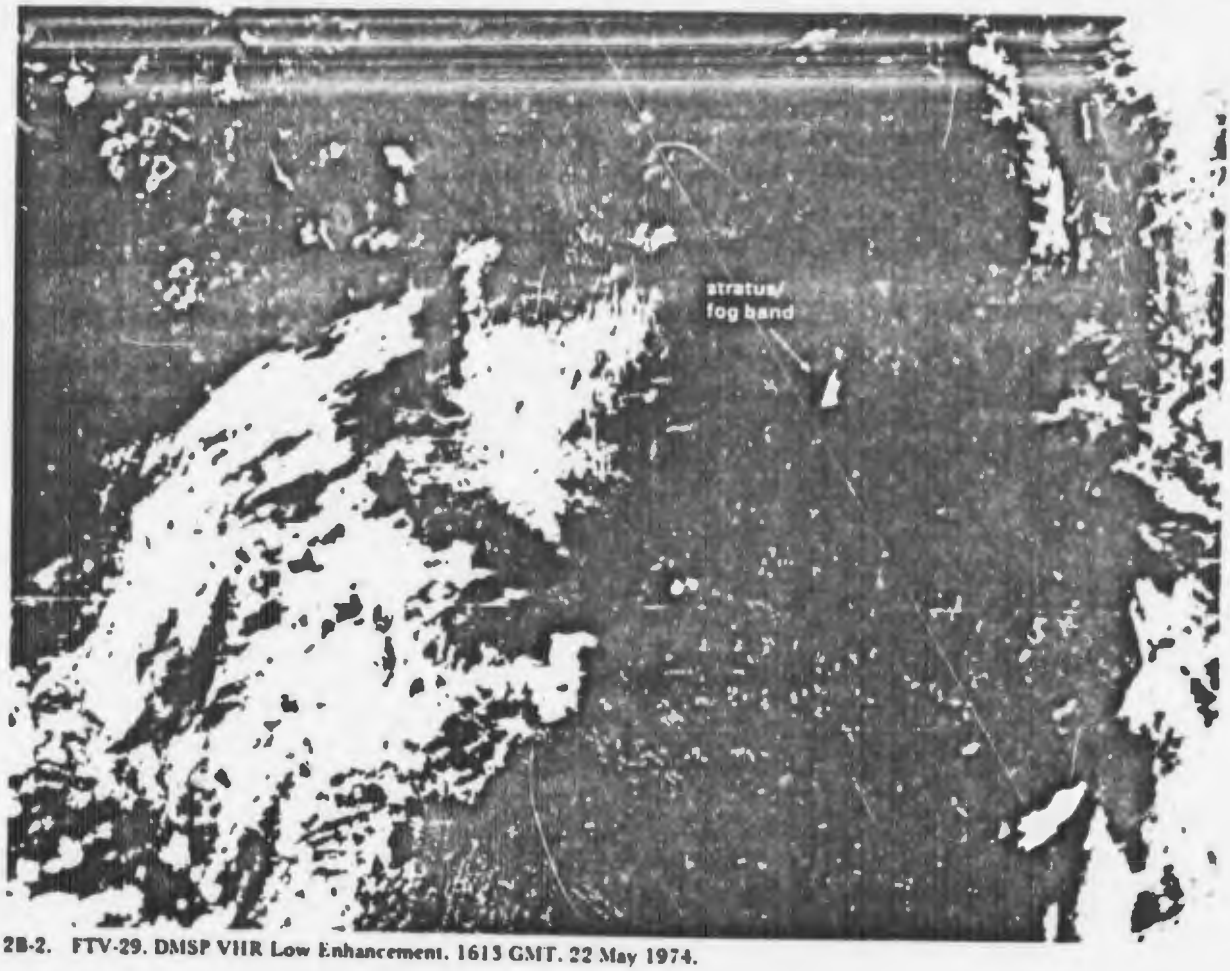

2B-2. FTV-29. DMSP VHR Low Enhancement. 1613 GMT. 22 May 1974.

On a DMSP pass (Fig. 2B-4) about two hours later, the stratus/fog off of Pt. Arguello has dissipated; however, a small anomalous gray shade band remains in the area. *This change is a positive verification that the anomalous gray shade band is the high humidity end product of the stratus/fog band dissipation, consistent with Byers (1944) observation.* To the south, a layer of bright stratocumulus has developed in the area of the broad anomalous gray shade pattern observed in Fig. 2B-3. Dark-tone gray shades are apparent between this cloudiness and the West Coast. The appearance of a dark-tone area along the coast to Pt. Arguello in place of the light-tone areas in Fig. 2B-3 indicates a rapid drying out of the air with a corresponding reduction in the size and number of condensation particles. In this area, remote from sunglint, the reduction in haze particle size results in a corresponding decrease in non-specular reflection of light to the satellite and the area appears dark in the imagery. Low-level visibilities should be greatly improved in these areas.

Important Conclusions

1. Anomalous gray shade bands are often the high humidity end products of stratus/fog band dissipation.

2. Light-tone gray shade areas, remote from sunglint patterns, at the edges of stratus/fog or stratocumulus are regions of high humidity associated with a concentration of large-size condensation particles and haze. Low-level visibilities are generally reduced in these areas.

3. Dark-tone gray shade areas adjacent to lighter-tone gray shade areas, remote from sunglint, are regions of lower humidity and less hazy conditions. Low-level visibilities are generally higher in these areas.

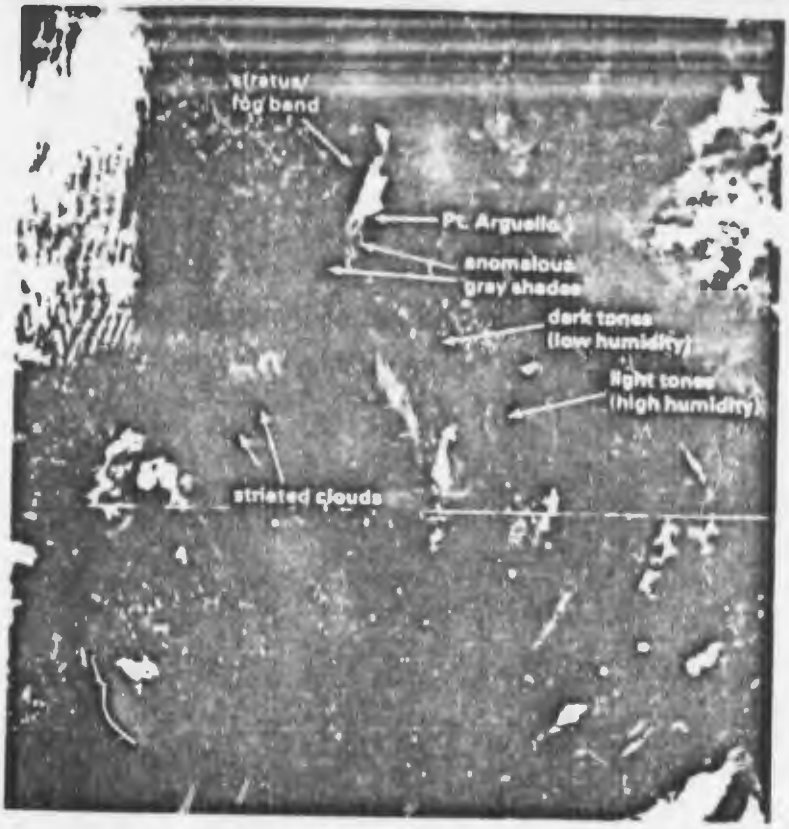

2B-3. FTV-29. Enlarged View. DMSP VHR Low Enhancement. 1615 GMT. 22 May 1974.

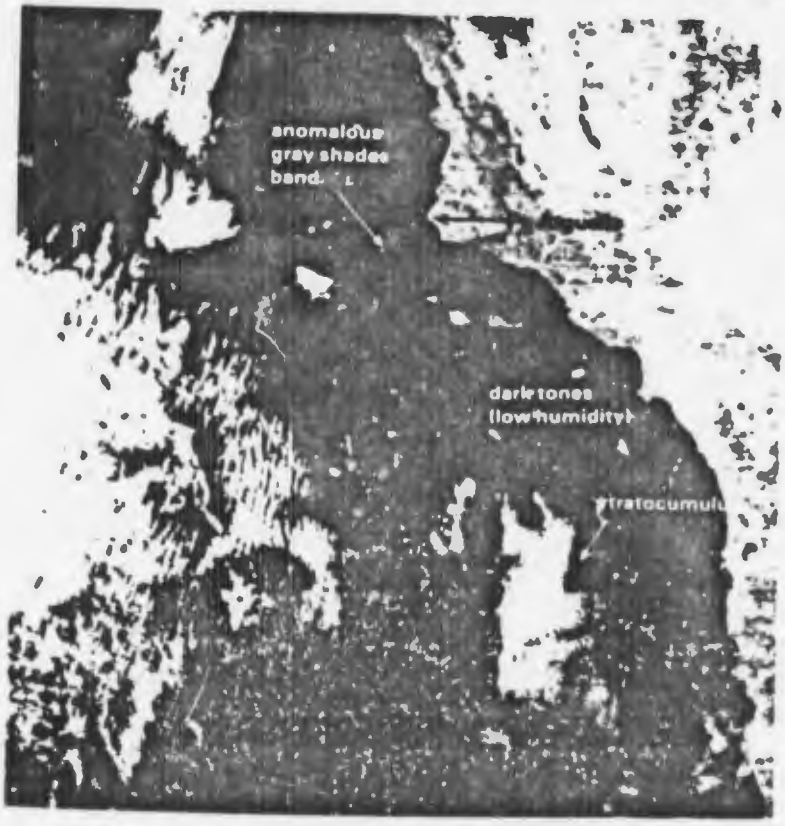

2B-4. FTV-31. Enlarged View. DMSP VHR Low Enhancement. 1850 GMT. 22 May 1974.

References

Byers, H.R., 1944: *General Meteorology*. New York, McGraw-Hill Book Co., 494 pp.

Johnson, J.C., 1954: *Physical Meteorology*. Technology Press of the Mass. of Tech., John Wiley & Sons, New York and Chapman & Hall Ltd., London, 393 pp.

Case 2 Anomalous Gray Shades

Gray shade patterns produced by mist and spray in high sea areas over an open ocean

In Fig. 2B-5, the light-tone, cone-shaped gray shade pattern off of the northwest coast of the United States might easily be misinterpreted as a sunglint pattern similar to that shown in Fig. 2A-2 on page 2A-3. However, this is an anomalous gray shade pattern produced by the sun's reflection off of mist and spray dispersed by strong winds in an area of heavy seas. The light-tone areas are sharply defined (Fig. 2B-6) and the overall pattern merges with the stratocumulus cloudiness to the south and the frontal band cloudiness to the northwest.

In Fig. 2B-7, DMSP MI imagery [hereafter referred to as IR (infrared)] shows the high-level cloudiness in the frontal band; however, the stratocumulus cloudiness is barely revealed in the dark-tone areas. In addition, note that the anomalous gray shade pattern is not observed in this imagery, indicating that the temperature differences produced by this pattern are too small to be detected by the IR sensor.

The surface analysis (Fig. 2B-8) reveals that the light-tone gray shades are in a tight pressure gradient area, with winds up to 26 meters per second (50 kts) off of the Oregon coast. Air temperatures are generally warmer over the light-tone gray shade area in comparison to the sea surface temperatures, so that the low-level flow is thermally stable and convective cloudiness is inhibited.

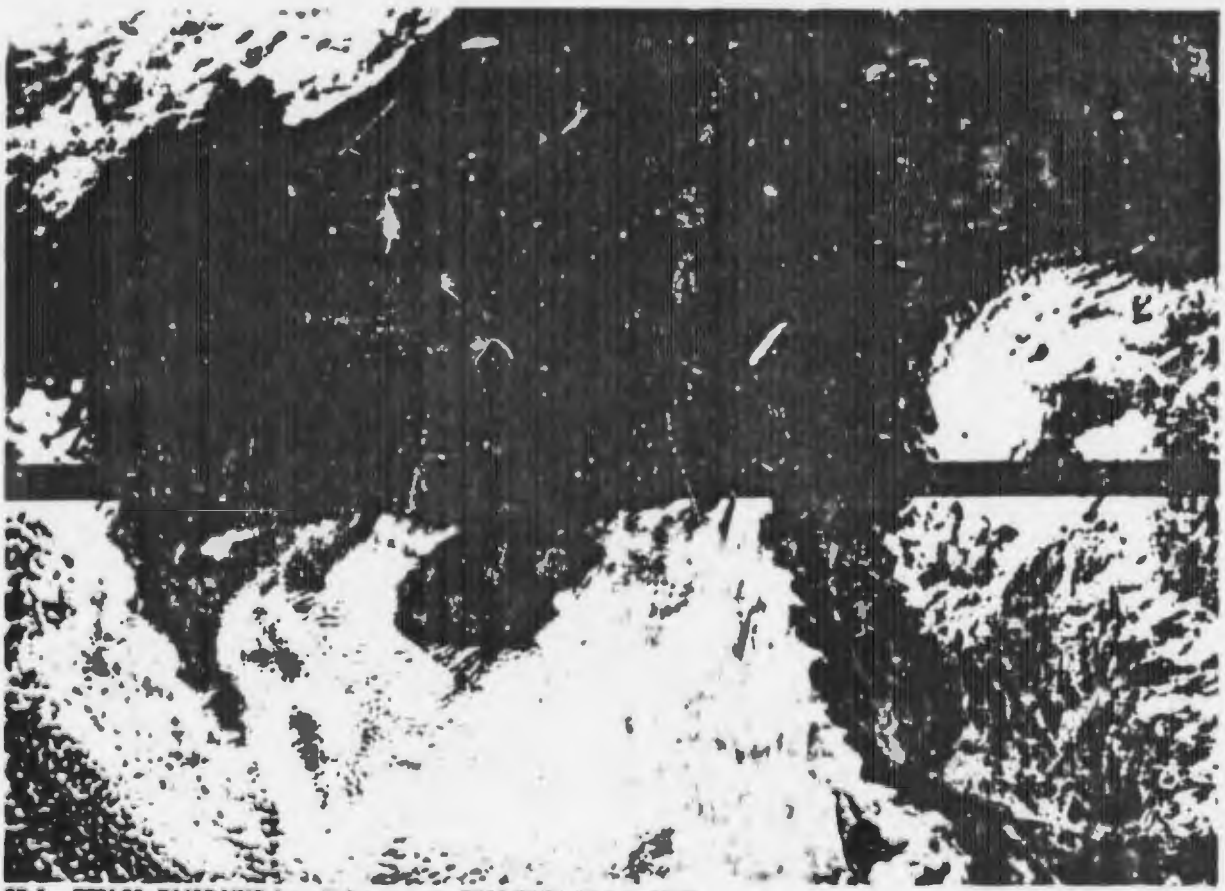

2B-5. FTV-28. DMSP VHR Low Enhancement. 2017 GMT. 13 July 1979.

2B-6. FTV-28. Enlarged View. DMSP VHR Low Enhancement. 2017 GMT. 13 July 1973.

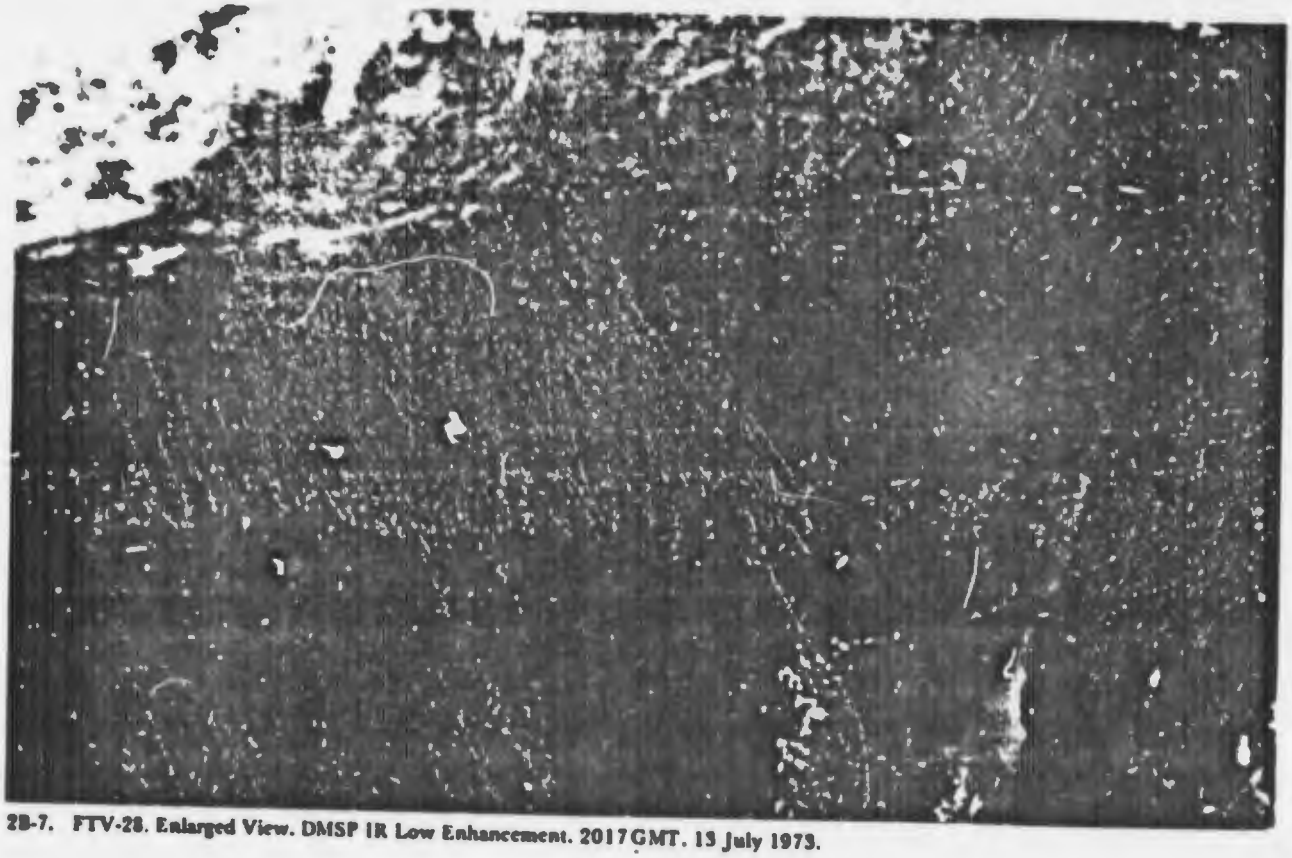

2B-7. FTV-28. Enlarged View. DMSP IR Low Enhancement. 2017 GMT. 13 July 1973.

2B-8. FTV-2B. DMSP VHR Low Enhancement. 2017 GMT. 13 July 1973.
Surface Pressure Analysis. 0000 GMT. 14 July 1973 (red).
Sea Height Analysis. 1800 GMT. 13 July 1973 (blue).

The Fleet Numerical Weather Central (FNWC) sea-height analysis superimposed on the DMSP imagery, in Fig. 2B-8, shows sea heights ranging from 6 to 15 ft. in the lighter areas of the anomalous gray shade pattern. Sunglint from the ocean surface can be ruled out as a cause for this anomalous gray shade pattern since rough seas in the area would effectively disrupt any sunglint pattern. In addition, it is very unlikely that a symmetrical pattern such as this could be generated in seas showing the large wave height variation observed in the anomalous gray shade area. However, spray from the heavy seas, dispersed by strong winds, can create mist and high humidity conditions at low levels which would reflect non-specular light to the satellite to produce the anomalous gray shade pattern.

Ship reports (Fig. 2B-8) indicate high humidities in the area with numerous temperature-dewpoint differences ranging from zero to 2°F and visibilities show occasional reductions to 2 nm or less. In the dark-tone gray shade area, where sea heights are less than 3 ft, temperature-dewpoint differences increase to 4°F and visibilities of up to 25 nm are reported.

Important Conclusions

1. Anomalous gray shade patterns can be produced by mist and haze generated by high winds over the open ocean under conditions of thermally stable low-level flow.

2. Such gray shades may be misinterpreted as sunglint associated with uniform sea state conditions over the open ocean.

3. The light-tone gray shades in such circumstances denote areas of high winds, increased sea state, moist air and poor low-level visibilities. Dark gray shade areas adjacent to such lighter areas are indicative of lower wind speeds, decreased sea state, drier air and increased visibilities.

Case 3 Anomalous Gray Shades

High sea state area produced by strong offshore mountain-gap winds; remote from sunglint region

Marine mist/haze related anomalous gray shade patterns can be produced by strong wind driven spray from mountain-gap winds streaming across coastal waters.

Fig. 2B-9 is a DMSP VHR image of the Mediterranean-Southern Europe area when a strong mistral wind system was observed over the Gulf of Lion. The mistral is a north wind which blows down the Rhone Valley into the Gulf of Lion (Reiter, 1975). Offshore winds often exceed 60 kts. At times gale force winds may extend across the Mediterranean to the Algerian coast.

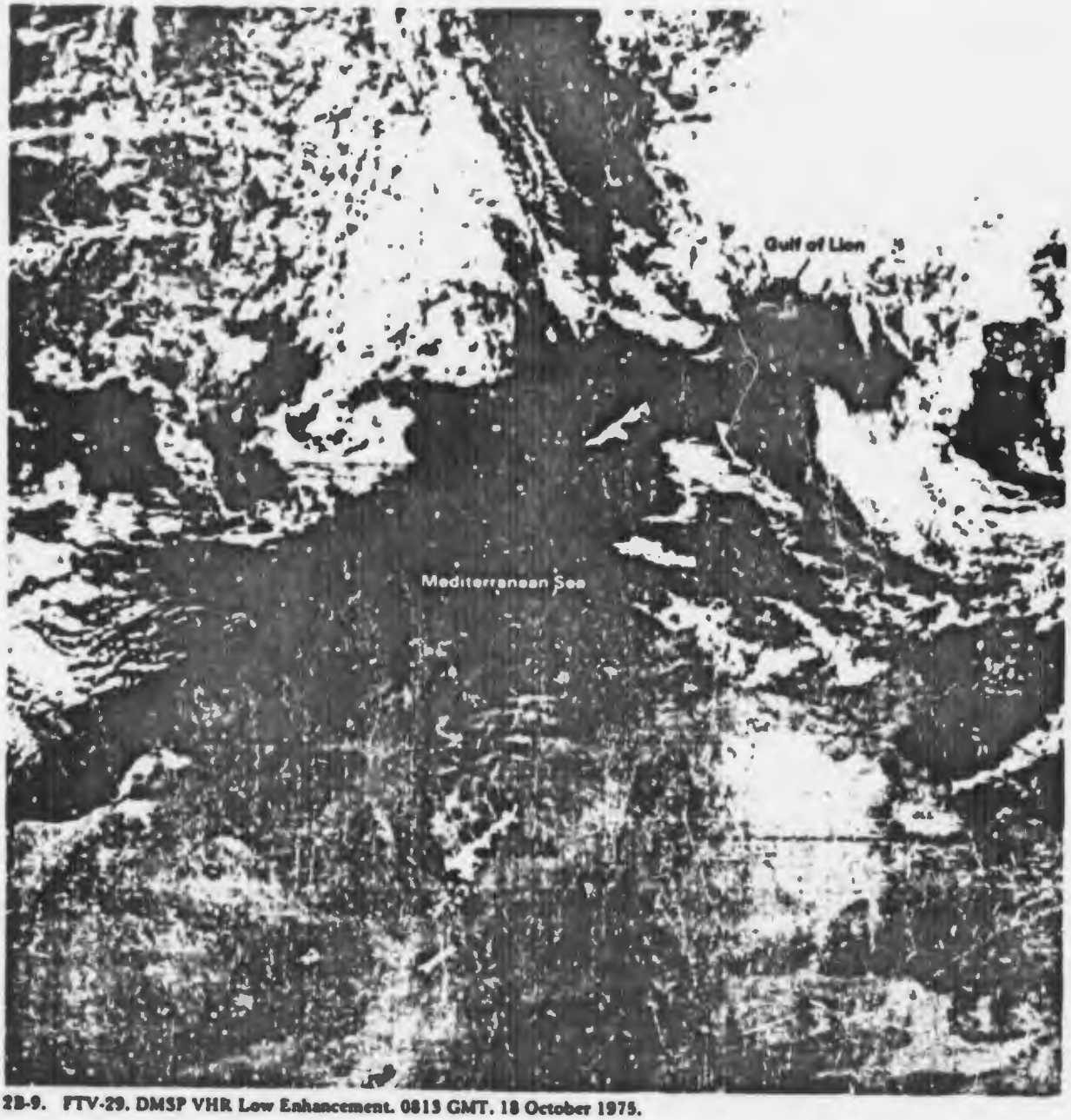

2B-9. FTV-29. DMSP VHR Low Enhancement. 0813 GMT. 18 October 1975.

For this case, the primary specular point is located well to the south in the Southern Hemisphere, so that sunglint effects from the ocean surface can not be detected over the Mediterranean.

The anomalous gray shade pattern (Fig. 2B-10) in the Gulf of Lion is produced by the marine mist/haze conditions created by strong mistral winds blowing spray off of the tops of waves in the seas offshore. In the anomalous gray shade area, the concentration of mist/haze droplets reflect more non-specular light to the satellite than the surrounding cloud-free sea regions (see Case 2).

Reference

Reiter, E.R., 1975: Handbook for Forecasters in the Mediterranean, ENVPREDRSCHFAC Technical Paper 5-75, Naval Environmental Prediction Research Facility, Monterey, Calif., pp 374.

2B-10. FTV-29. Enlarged View. DMSP VHR Low Enhancement. 0813 GMT. 18 October 1975.

Case 4 Anomalous Gray Shades

High humidity areas over land

Light-tone gray shades observed adjacent to stratus or stratocumulus clouds over the ocean are related to moist atmospheric conditions at low levels. Similar anomalous gray shade patterns are observed adjacent to fog or stratus areas over land.

Fig. 2B-11 is a DMSP VHR image over the southern United States showing a tropical depression which has just moved inland from the Gulf of Mexico. Sunglint can be observed to the south of the storm. The elongated bright band to the north is an area of fog and anomalous gray shades which lies in the peripheral subsidence area ahead of the storm (Fett, 1964).

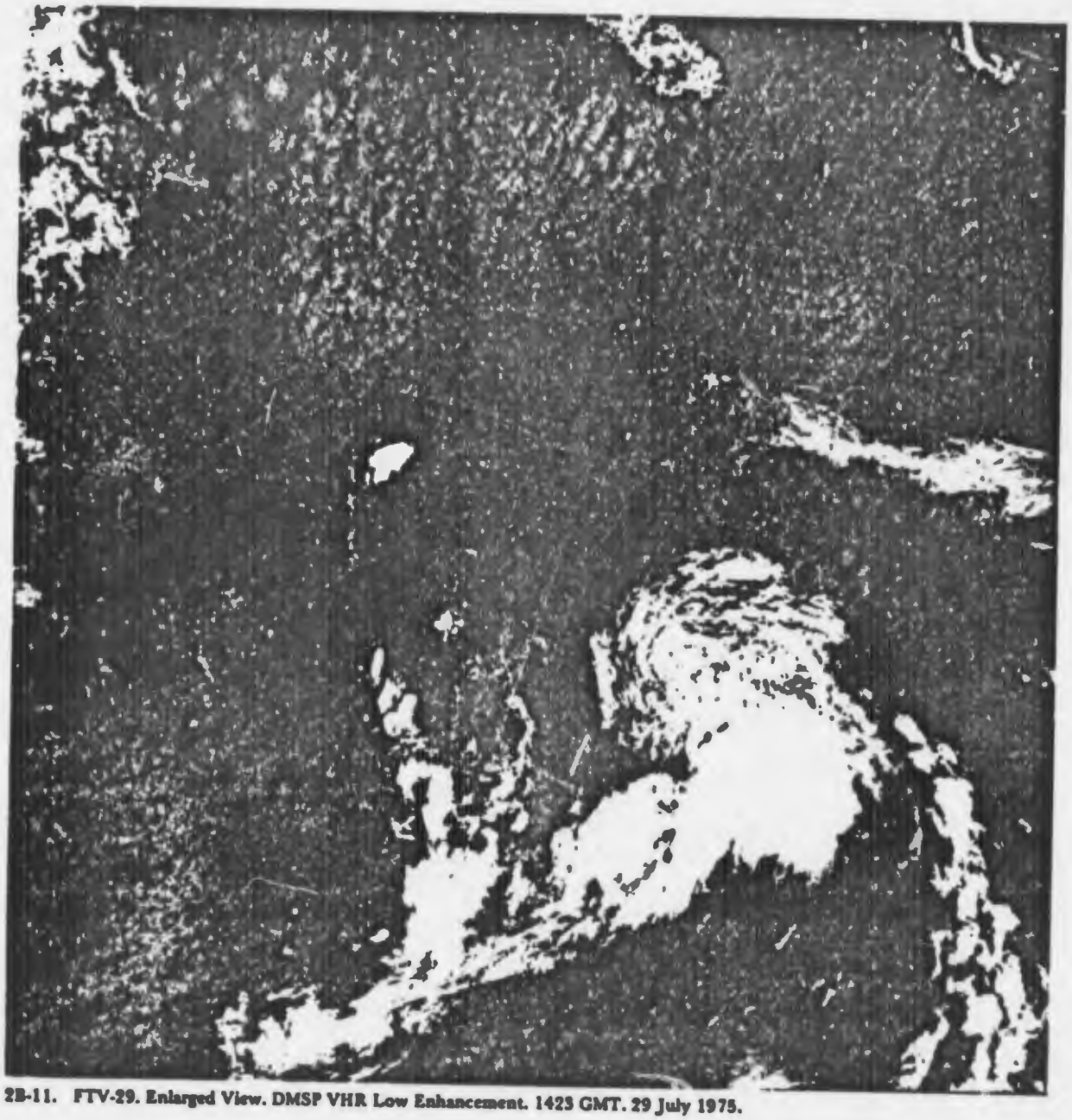

2B-11. FTV-29. Enlarged View. DMSP VHR Low Enhancement. 1423 GMT. 29 July 1975.

In an enlarged view (Fig. 2B-12), the brightest areas are thick patches of fog. Note how clearly the banded light-tone gray shade steps are displayed in the anomalous gray shade pattern surrounding the fog areas. These are high humidity areas or areas of smoke and other large particle size air pollutants reflecting non-specular light to the satellite. The narrow dark-toned band around the edge of the storm is an area of pronounced subsidence where reflection from large particle haze droplets is minimized. However, humidity is high and water vapor absorption effects in the near infrared reduce transmittance (see Case 9). Surface observations indicate low visibilities in the fog and in the light-toned anomalous gray shade areas.

Important Conclusions

1. Anomalous gray shade patterns are observed over land as well as ocean areas.

2. Low-level visibilities are reduced in the anomalous gray shade patterns associated with fog over land.

Reference

Fett, R.W., 1964: Aspects of hurricane structure: New model considerations suggested by TIROS and Project Mercury observations. *Mon. Wea. Rev.*, 92, 43-60.

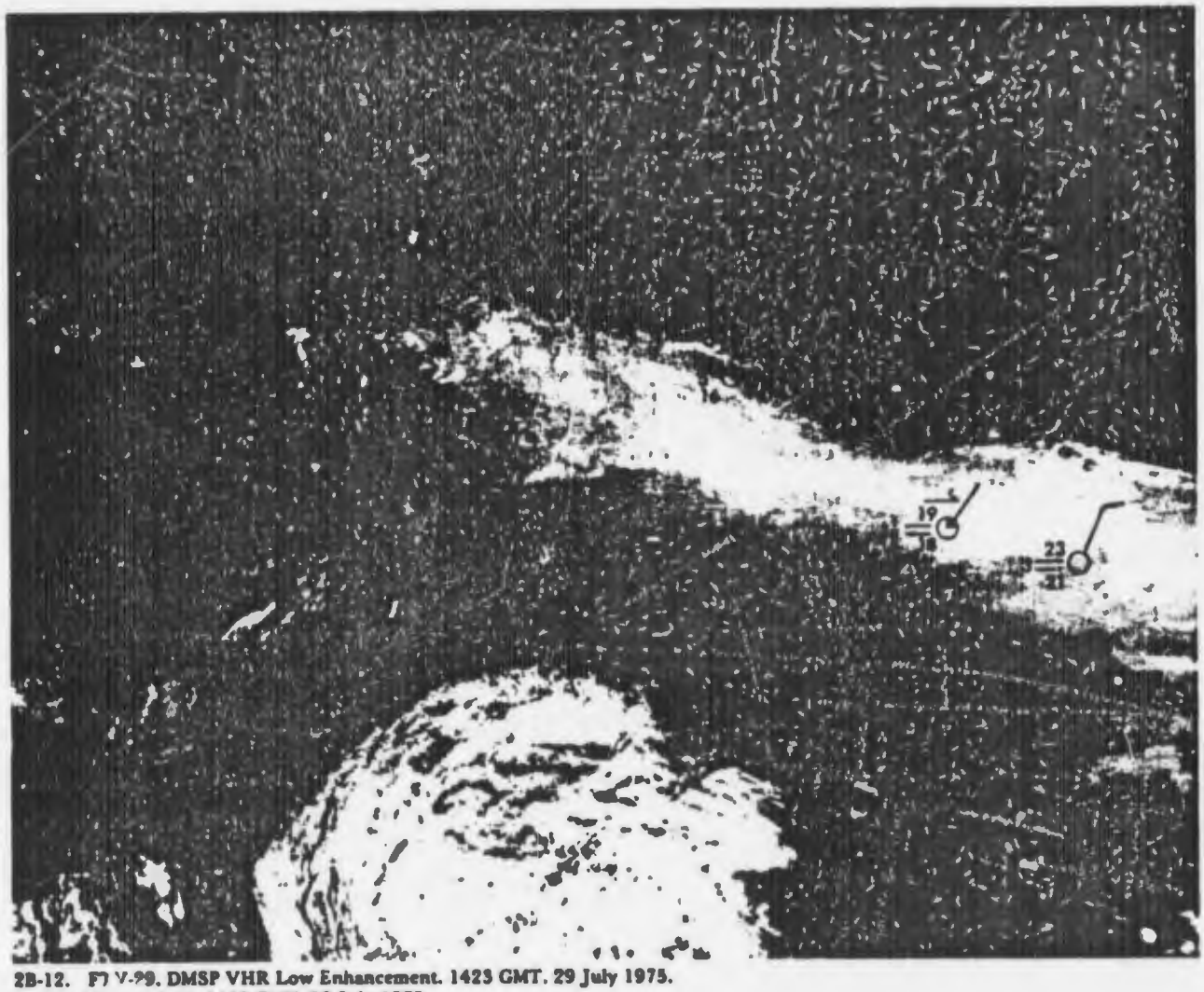

2B-12. F7 V-99. DMSP VHR Low Enhancement. 1423 GMT. 29 July 1975. Surface Observations. 1200 GMT. 29 July 1975.

Case 5 Anomalous Gray Shades

High humidity areas over land; remote from sunglint region

Fig. 2B-13 is a DMSP VHR image over the Mediterranean showing areas of fog and anomalous gray shade patterns over the Po River Valley and the Adriatic Sea.

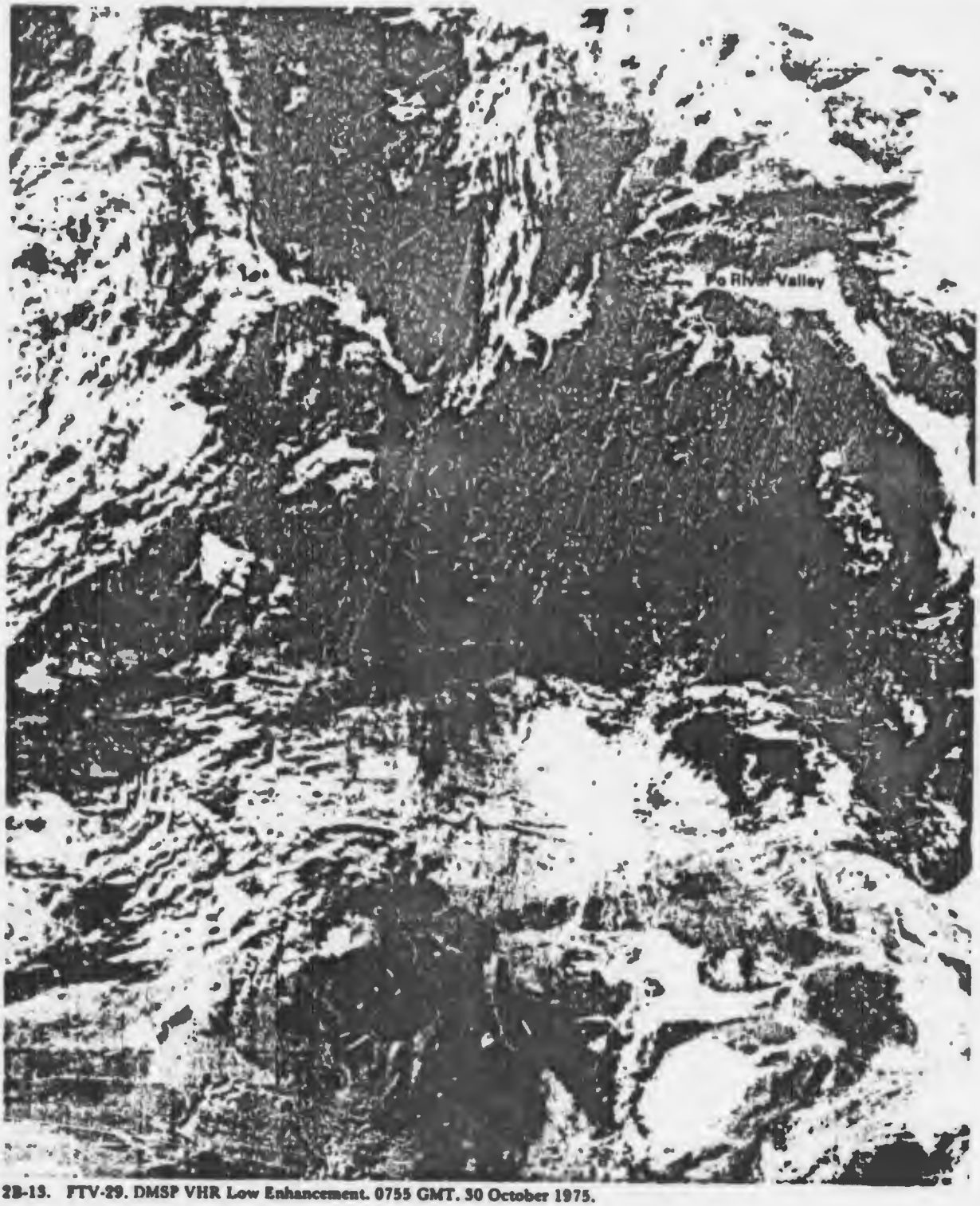

2B-13. FTV-29. DMSP VHR Low Enhancement. 0755 GMT. 30 October 1975.

In the enlarged view (Fig. 2B-14), the fog areas appear as bright, white patches. A nearly uniform middle-tone anomalous gray shade pattern is associated with thinner fog areas in the Po River Valley. Surface reports substantiate the foggy conditions and poor visibilities suggested by the DMSP data over that area and extending into the Adriatic Sea.

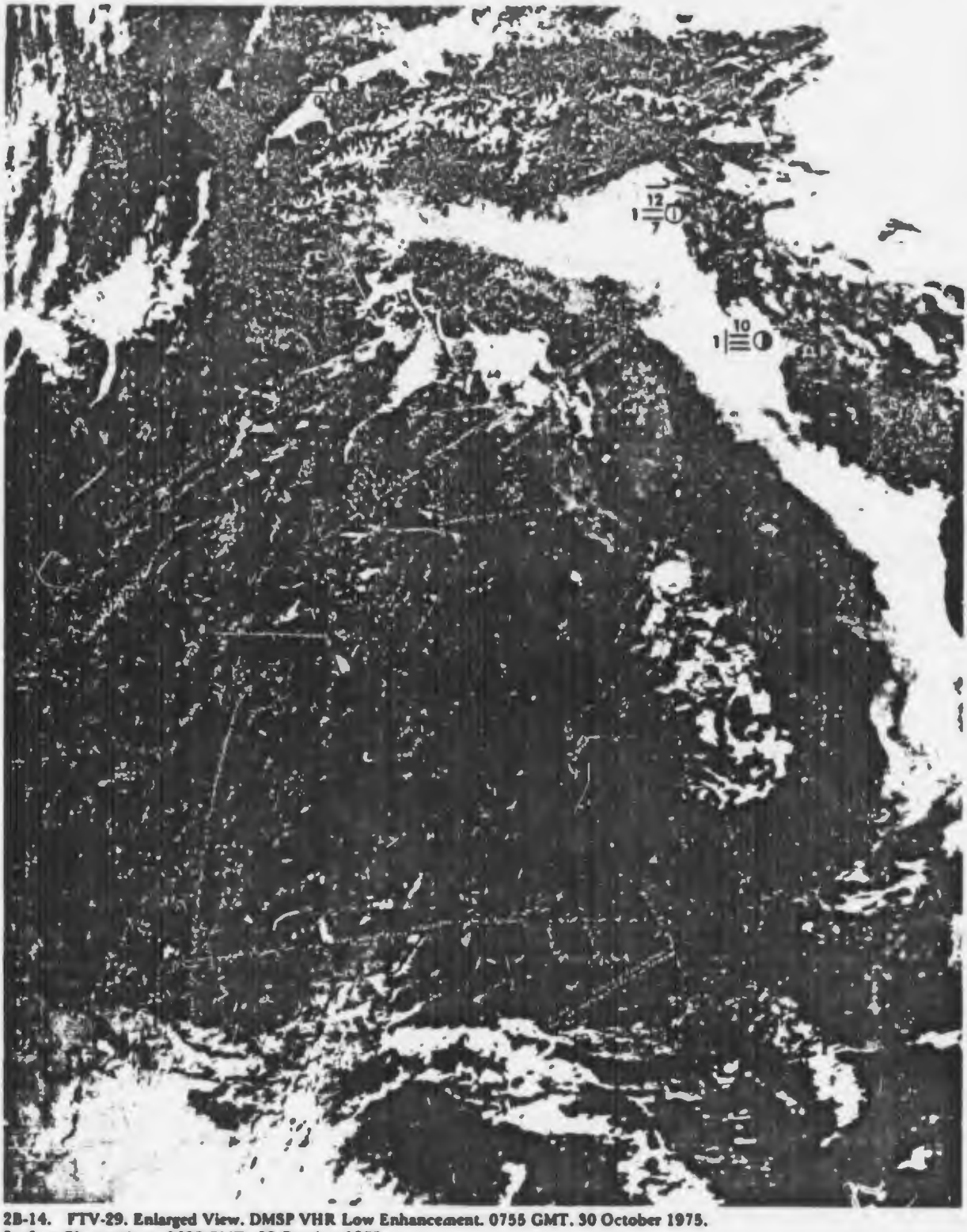

2B-14. FTV-29. Enlarged View. DMSP VHR Low Enhancement. 0755 GMT. 30 October 1975. Surface Observations. 0600 GMT. 30 October 1975.

Case 6 Anomalous Gray Shades

Coastal offshore flow (land breeze) effects

Anomalous gray shade patterns paralleling coastlines are frequently observed in DMSP VHR data. The gray shades sometimes conform to the outlines of shallow water areas where there is sufficient bottom reflectivity. In these areas the same bottom features are generally visible from day to day depending on satellite perspective, and oceanographic and atmospheric conditions. Sometimes anomalous gray shades paralleling coastlines are visible on one orbit and are not apparent on a succeeding orbit on the same day over the same area.

Expanded mode imagery (Fig. 2B-15) shows a light-tone anomalous gray shade strip paralleling most of the west coastline of the Baja Peninsula. The pattern does not conform to shallow water contours and is not observed every day. With the solar subpoint near 22°S, in the Southern Hemisphere, sunglint is not a factor in this case.

It is a matter of common observation that inversion dominated west coastal areas are often unusually misty because of the action of breaking surf and the consequent ejection of large numbers of condensation particles (primarily salt nuclei) into the atmosphere. Such particles have a chemical affinity for water vapor even when the air is not saturated.

On cloudless winter nights, such as prevailed in this example, the land cools quite rapidly and a strong thermal gradient is produced between the cold land and much warmer water. The land breeze is produced because of this gradient and emphasized because of the mountainous terrain off the Baja Peninsula. As soon as the cold air moves off the coast and over the warmer water it is rapidly modified due to water evaporation. The salt nuclei grow in size and the air under the inversion becomes very hazy. Such a condition is extended by the land breeze to the seaward limit of the land breeze circulation and may persist until late morning hours and a counter-current sea breeze is established.

The imagery, acquired at about 1100 Local Standard Time, shows land-breeze effects near its maximum extent over the ocean.

The anomalous gray shade strip is made visible by non-specular reflection of light off of heavy concentrations of marine haze. Low-level visibilities will generally be reduced in these areas. If, later in the day, a counter-current sea breeze does not blow directly on shore, but parallel to the shore, as is frequently the case (Sutton, 1953), the anomalous gray shade strip will persist into mid-afternoon.

Important Conclusions

1. Anomalous gray shade patterns paralleling coastlines appear when a land breeze carries heavy concentrations of haze droplets seaward.

2. Low-level visibilities tend to be reduced in the anomalous gray shade area.

References

Sutton, O.G., 1953: *Micrometeorology*. New York, McGraw-Hill Book Co., 333 pp.

2B-15. FTV-28. DMSP VHR Low Enhancement Expanded. 1855 GMT. 8 December 1973. Surface Observations. 1800 GMT. 8 December 1973.

Case 7 Anomalous Gray Shades

Surf related effects along coastlines

Two successive DMSP VHR passes, about 3-hours apart (previously used in Case 1), illustrate the persistence of anomalous gray shades due to the concentration of haze along coastlines.

The first pass (Fig. 2B-16) is an enlarged section of Fig. 2B-2 showing an anomalous gray shade pattern associated with a stratus/fog band off of Pt. Arguello. Note that a uniform middle-tone gray shade is observed over the cloud-free ocean between the coastline and the stratocumulus layer to the west, except for the dark-tone area to the northwest. The uniform middle-tone gray shade area is marine haze over the ocean.

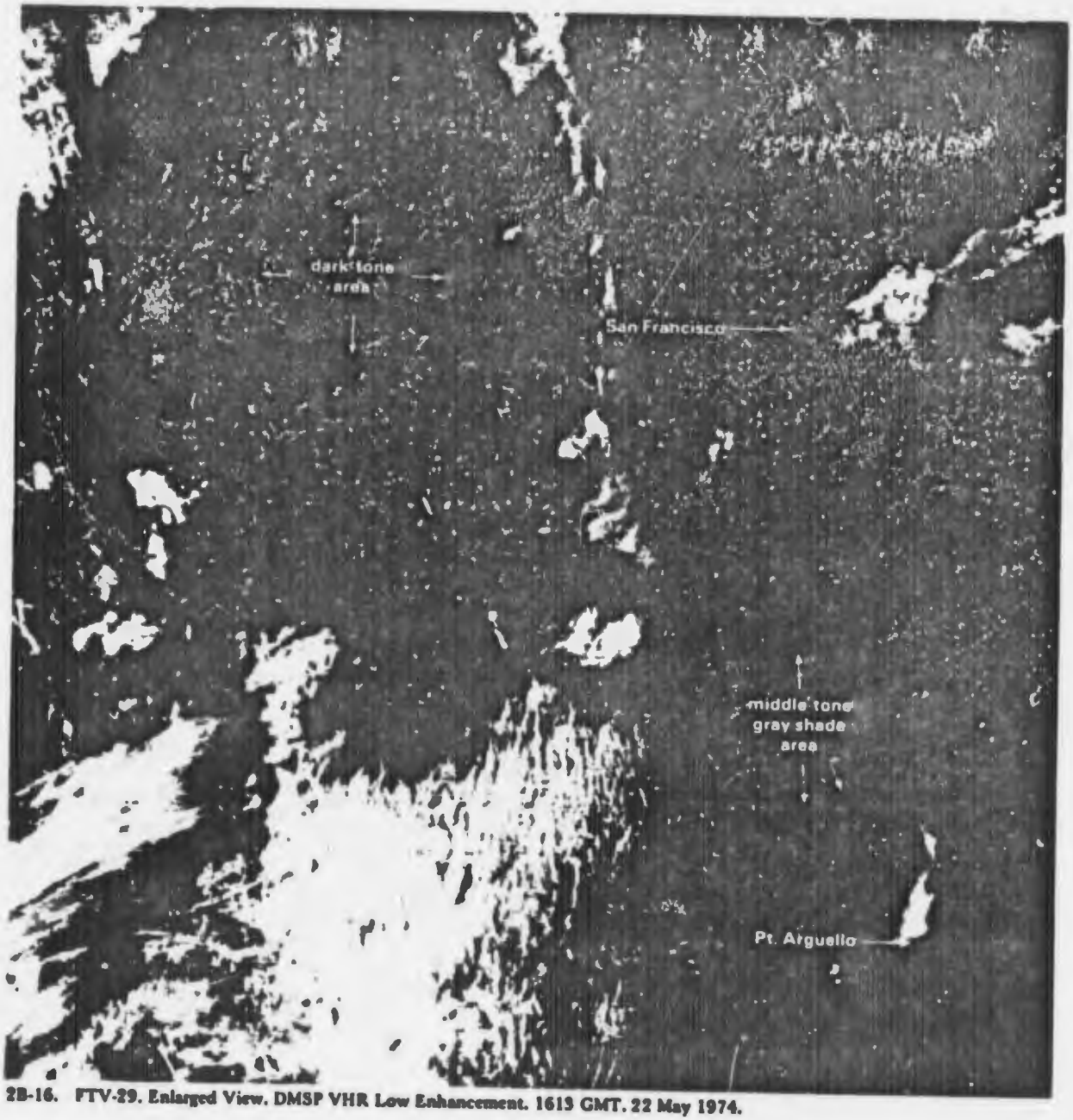

2B-16. FTV-29. Enlarged View. DMSP VHR Low Enhancement. 1615 GMT. 22 May 1974.

Three hours later (Fig. 2B-17) a pronounced change has occurred in the uniform middle-tone gray shade pattern. Notice that the area midway between the coastline and the stratocumulus cloudiness has acquired a dark tone. However, a narrow anomalous gray shade strip remains along the coastline.

The change in the pattern over the ocean may be related to increased vertical mixing due to late-morning convective heating at low levels in the cloud-free areas. The persistence of the anomalous gray shade strip along the coastline may be attributed to the action of breaking surf which concentrates large numbers of condensation particles (primarily salt nuclei) into the atmosphere over this area. Such particles have a chemical affinity for water vapor even when the air is not saturated. As the particles grow in size a haze layer is developed and revealed in DMSP imagery as an anomalous gray shade strip.

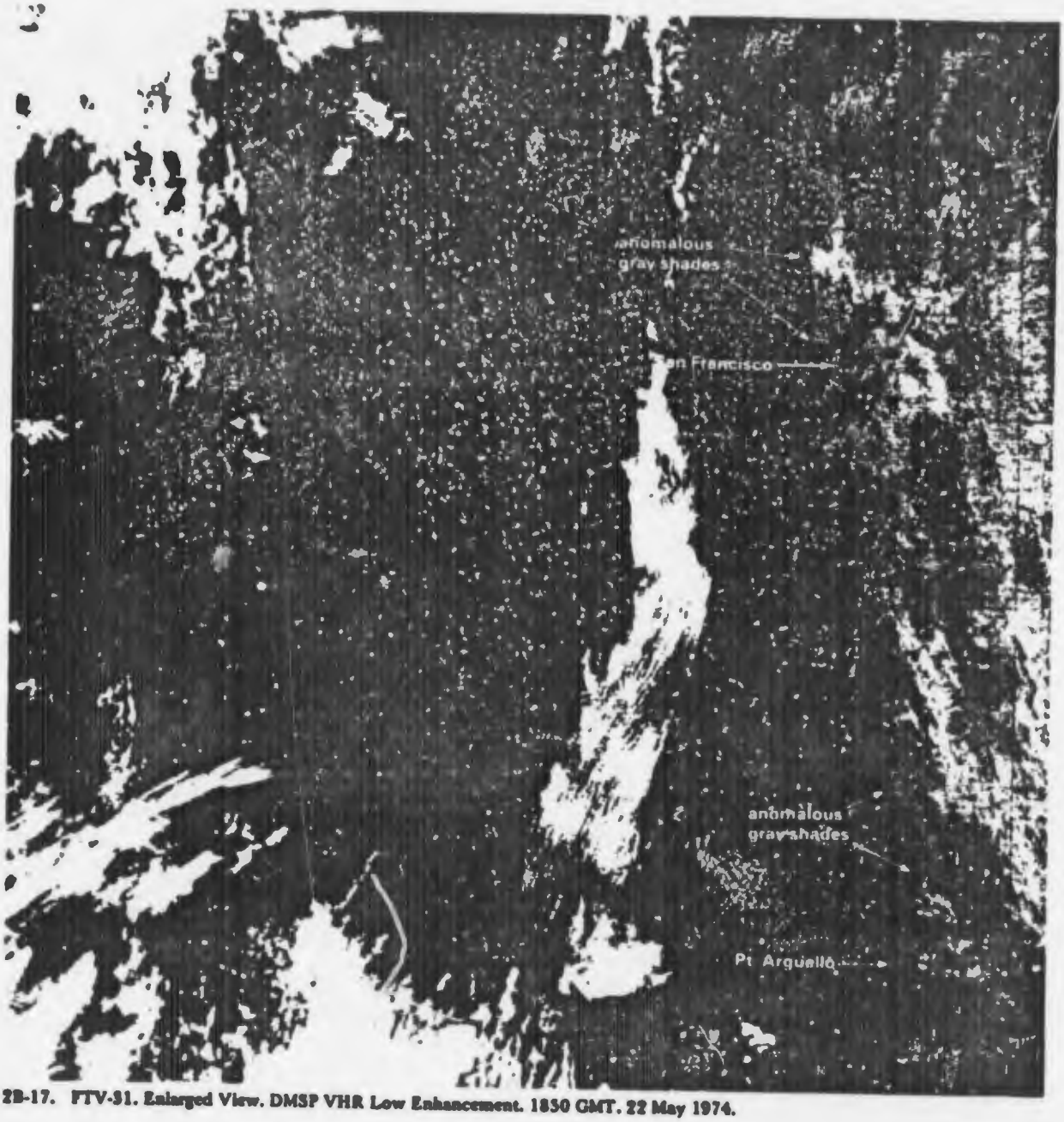

2B-17. FTV-31. Enlarged View. DMSP VHR Low Enhancement. 1830 GMT. 22 May 1974.

Case 8 Anomalous Gray Shades

Bottom topography in shallow water areas

Fig. 2B-18 is a special enhancement mode DMSP VHR image. It was reprocessed as though it were high resolution infrared (WHR) data to enhance and emphasize the anomalous gray shade patterns over shallow water in the Bahama Islands area. These data were prepared by Keesler Air Force Base DMSP training personnel on Air Force ground station equipment. These effects can also be produced on Navy DMSP ground equipment by gray shade manipulation of the enhancement curves used in processing VHR data.

Exceptional detail of ocean water depth variations over the Bahama Islands and other similar island chains can sometimes be obtained. The ability of the DMSP imagery to reveal shallow water areas is dependent upon the reflectivity of the ocean bottom and the clarity of the overlying water. Sea state and atmospheric conditions also affect shallow water views. In this example the gray shade contours defining the Bahama Banks virtually coincide with the 5 fathom bottom isopleth (not shown). Other light-tone gray shades occurring adjacent to cloudy areas consist of haze droplets or are the high-humidity debris of earlier cloud dissipation.

A *Gemini XII* photograph of the same area is shown for comparison.

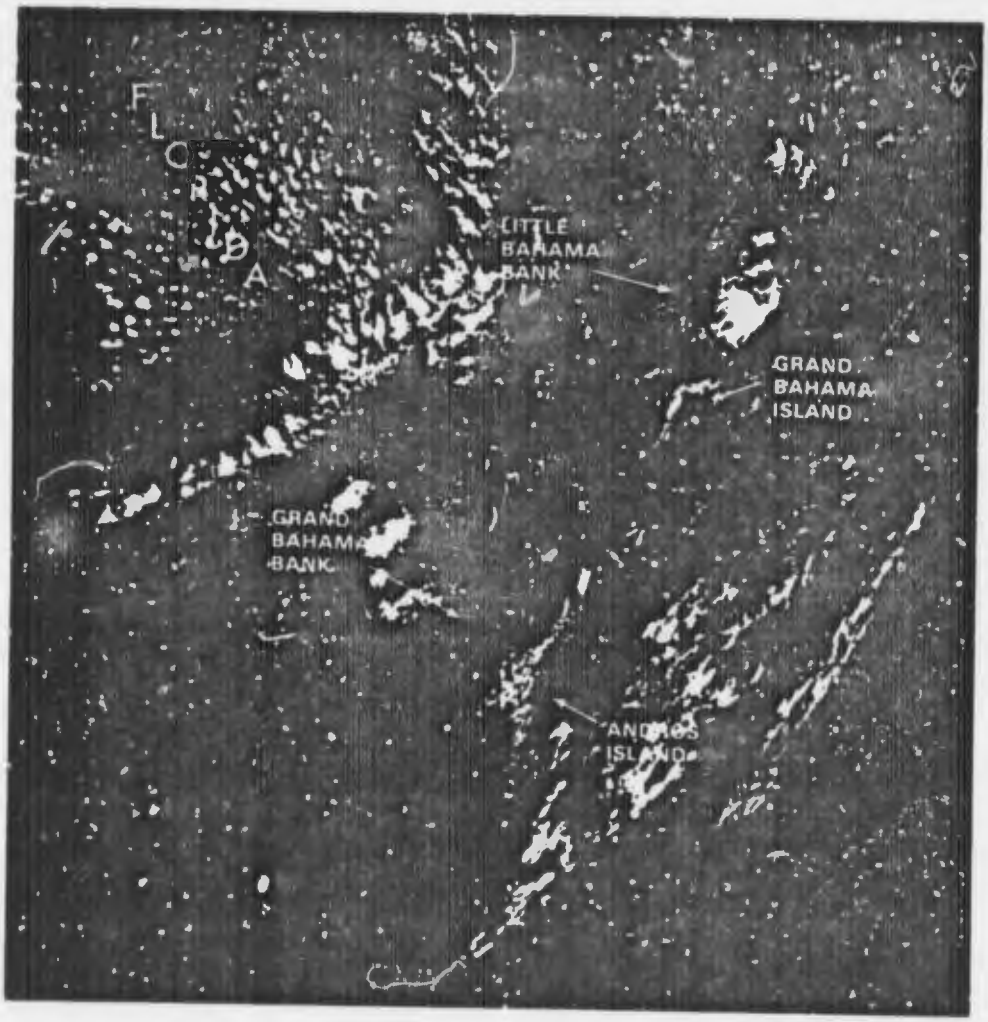

Gemini XII photograph of the Bahama Island area.

2B-18. DMSP VHR, processed as WHR (300x4) 300-275 Temperature range, showing 16 gray shades. 26 August 1974.

Case 9 Anomalous Gray Shades

High humidity/low humidity areas in sunglint region

In sunglint areas over the open ocean many anomalous gray shade patterns appearing in DMSP VHR imagery can be related to low-level atmospheric moisture. The difficulty of definitive interpretations regarding these anomalous gray shades must be appreciated. The factors which influence reflectance include (1) sea state, (2) background brightness of the underlying surface (water or land), and (3) atmospheric moisture. Sea state can be smooth or rough, background brightness can be dark or light; atmospheric moisture effects are even more complicated and are influenced by particle size (large or small) and effects of water vapor absorption within the atmosphere. Large moisture particles scatter or reflect sunlight directionally which increases reflection to the spacecraft sensor. Small particles scatter light in all directions and so less light is reflected to the satellite.

The DMSP spectral interval (0.4 - 1.1 μm) extends into the near IR where water vapor absorption becomes a significant factor. Fig. 2B-19 shows absorptivity curves for the atmosphere and for water vapor alone. Notice that there are several significant wavelengths where water vapor absorption in the near IR (0.7 - 1.0 μm) is pronounced. As an example, atmospheric transmittance is reduced about 23% for one air mass thickness and about 46% for two air mass thicknesses in the 0.94 μm absorption band. As a result of the double path length of solar radiation reaching the satellite, water vapor can reduce the amount of sunglint reflected to the satellite (AWS, 1974).

Fig. 2B-20 is an enlarged section of a DMSP VHR image showing gray shade variations within a sunglint pattern off of the west coast of the United States. Hazy areas showing the dark gray shades may be interpreted as the result of the combined effect of atmospheric scattering and water vapor absorption. Lighter gray shades similarly may result from the diffuse reflection of sunlight by larger diameter haze particles and cloud debris (neglecting possible sea state effects).

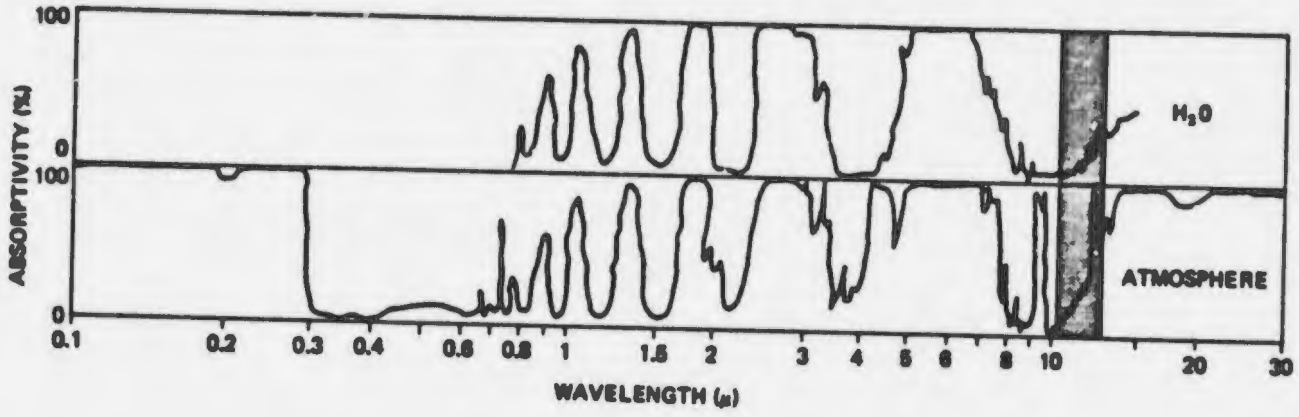

2B-19. Absorptivity curves for atmosphere and water vapor.

2B-20. FTV-29. DMSP VHR Low Enhancement Expanded. 1632 GMT. 21 May 1974.

Case 10 Anomalous Gray Shades

High humidity areas in sunglint regions.

Fig. 2B-21 is a DMSP VHR image of anomalous gray shade patterns under conditions of intense sunglint. The bright area of sunglint in the Gulf of California is coincident with near calm winds and seas. In a close-up view (Fig. 2B-22), notice that some of the visible clouds appear as dark-tone gray shades in the sunglint area. This is an excellent example of the reversal of gray shade tonality where clouds appear as dark tones against the lighter sunglint background of the sea.

Some of the difficulties in defining anomalous gray shades as moisture effects in sunglint areas is brought out by this example. Note the dark-tone gray shade pattern in the rough sea region just off of the southern tip of the Baja Peninsula. This dark-tone gray shade area is similar in tone to the adjacent moist, cloudy area to the east. However, the moist, cloudy area has a distinct mottled, textured appearance which identifies it as a cloud pattern rather than a sea state condition.

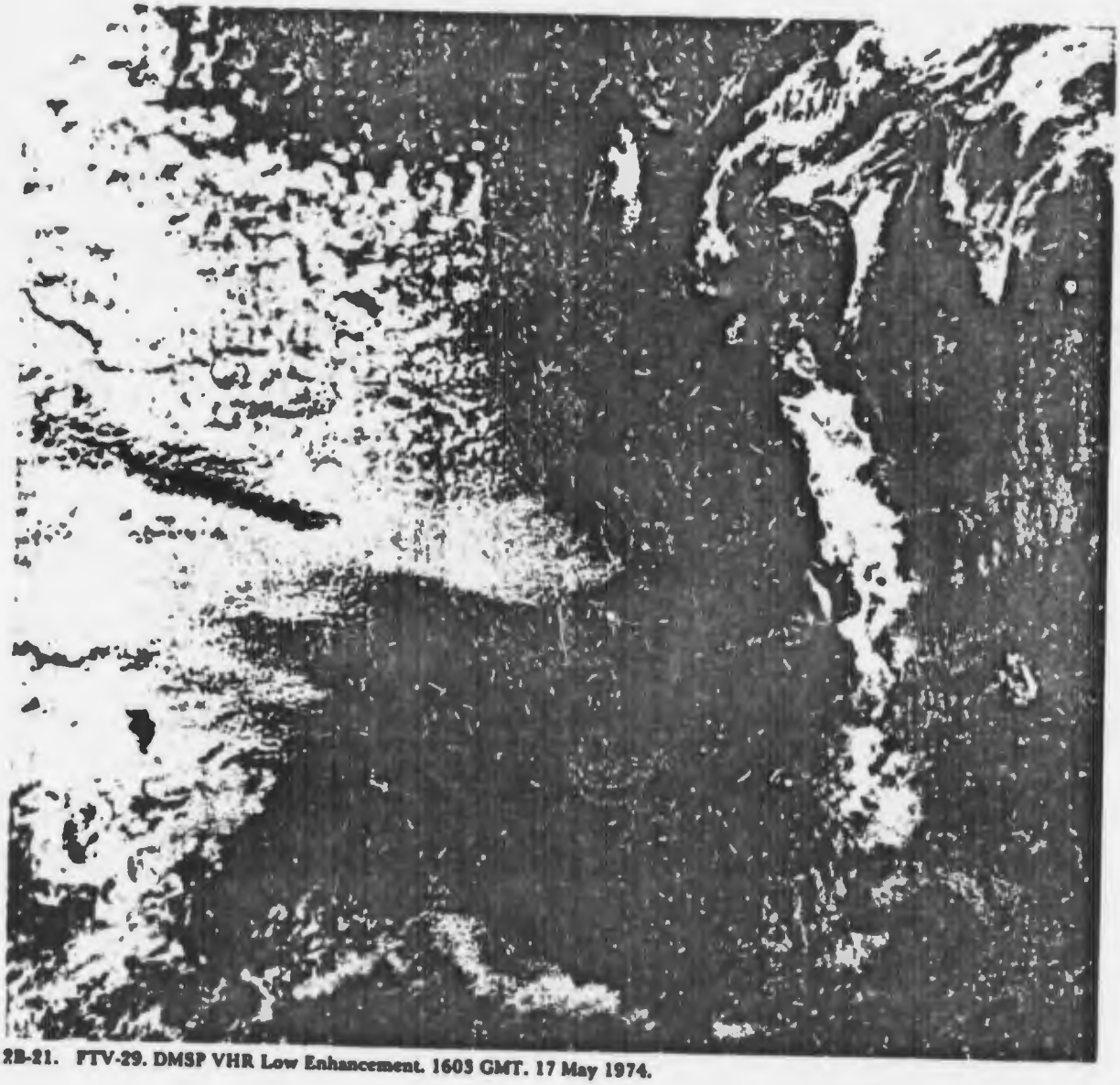

2B-21. FTV-29. DMSP VHR Low Enhancement. 1603 GMT. 17 May 1974.

The reversal of cloud gray shade tonality is emphasized when the stratocumulus pattern in sunglint (dark clouds against light sunglint sea background) is compared with the area of stratocumulus cloudiness to the northwest, outside of the sunglint area, where clouds appear white against a dark sea background.

2B-22. FTV-29. Enlarged View. DMSP VHR Low Enhancement. 1603 GMT. 17 May 1974.

Case 11 Anomalous Gray Shades

Cirrus cloudiness effects

It has long been noted that much of the cirrus-type cloudiness is not always apparent in visible imagery from meteorological satellites. This is related to the fact that maximum reflection and scattering of incident solar radiation from cloud layers is in the forward direction, with only a small secondary backscattering maximum (Rao, 1975). In other words, the satellite is in an optimum position to sense thin cirrus cloudiness (and other thin layers of moisture particles or aerosols) when it scans in the direction of the sun, and may not be able to sense thin cirrus, etc., when scanning in the direction away from the sun.

To illustrate this phenomena, Fig. 2B-23 shows a DMSP VHR depiction of Tropical Storm Wendy (September, 1974) just south of the China coast. Note that in the area southeast of the storm there is little or no indication of upper-level cloudiness. However, in the

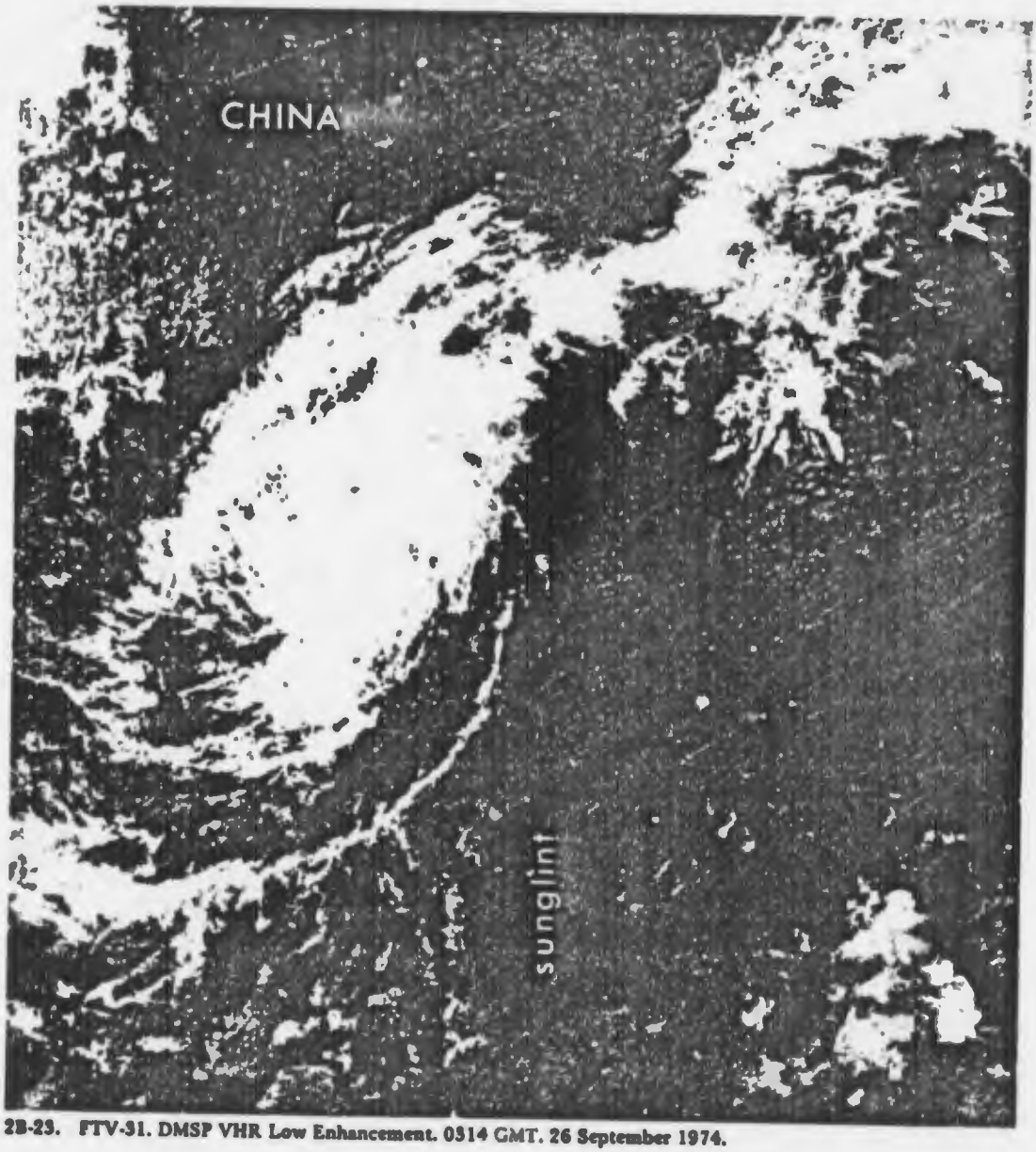

2B-23. FTV-31. DMSP VHR Low Enhancement. 0314 GMT. 26 September 1974.

corresponding IR imagery (Fig. 2B-24), banded streaks of colder temperatures in the area, implying upper-level cloudiness, are clearly evident.

The typical DMSP sunglint pattern can be observed (Fig. 2B-23) extending northward through the middle of the imagery, indicating a noon-time pass. As a result, the satellite, at this location, can sense only backscattered radiation in the directions from below and to the east and west. An obvious conclusion is that spacecraft with noon ascending nodes are poorly suited for detecting thin cirrus in all directions. Spacecraft with an early morning ascending node are better suited for detecting cirrus to the east. Spacecraft with afternoon ascending nodes are better suited for detecting cirrus to the west.

This example emphasizes the importance of using corresponding IR imagery in conjunction with visible imagery in arriving at an estimate of cirrus cloudiness over a given area.

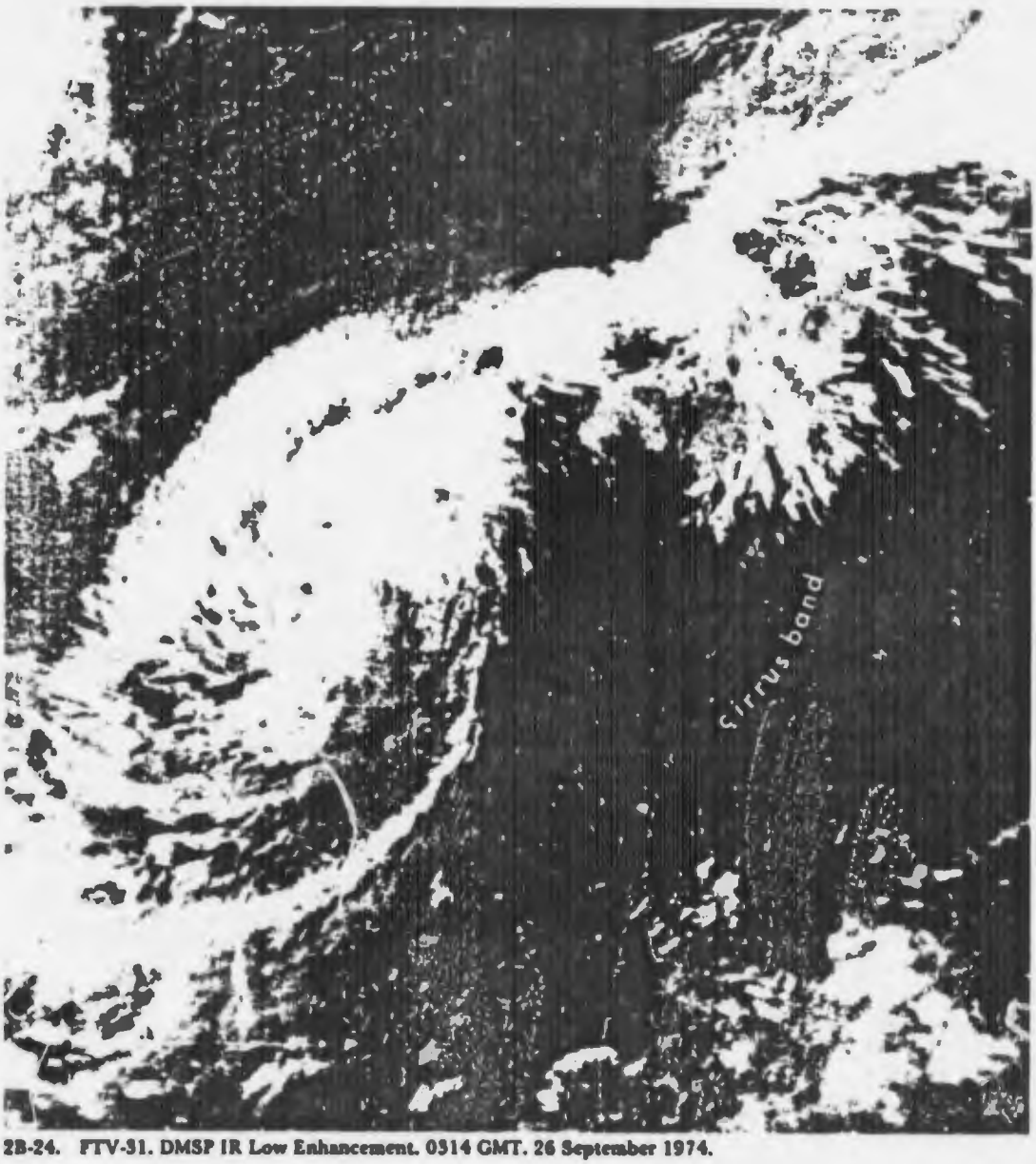

2B-24. FTV-31. DMSP IR Low Enhancement. 0314 GMT. 26 September 1974.

Case 12 Anomalous Gray Shades

Cirrus cloudiness effects

Anomalous gray shade patterns are observed with upper-level cloudiness as well as with low-level cloudiness. At upper levels, anomalous gray shades are found in cirrus areas. Fig. 2B-25 is an enlarged DMSP VHR view of cirrus cloudiness emanating from a large thunderstorm cluster over the Pacific and extending across the Baja Peninsula and the Gulf of California.

Between this thunderstorm cluster and Baja, identifiable bright, white patches and bands of cirrus cloudiness can be seen. Similarly, cirrus cloud streaks cover the northern portion of the Gulf of

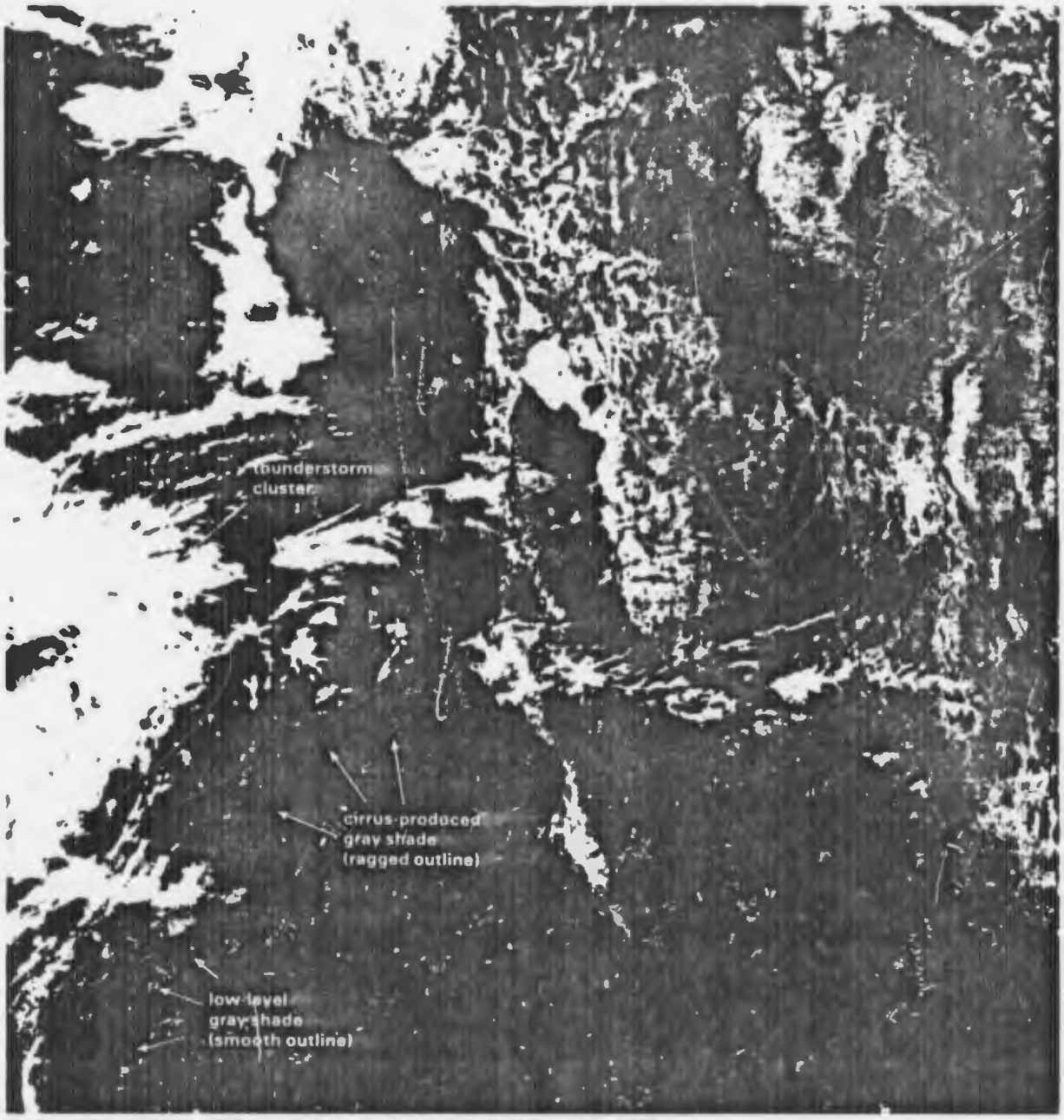

2B-25. FTV-28. DMSP VHR Low Enhancement. 1914 GMT. 6 November 1975.

California. A bright, white cirrus cloud band also extends from central Baja over the Gulf of California and Mexico.

A close examination of the VHR imagery reveals that anomalous gray shade patterns surround the cirrus patches and bands between the thunderstorm cluster and Baja. The gray shade cirrus patterns have a distinctive ragged outline in contrast to the smooth outline gray shade pattern associated with the low-level clouds to the south of the thunderstorm cluster.

Fig. 2B-26 is a corresponding IR view of the area. The anomalous gray shades in the VHR data appear in the IR data as bright white areas indicative of cirrus cloudiness, while gray shades associated with the low-level cloudiness cannot be detected.

2B-26. FTV-28. DMSP IR Low Enhancement. 1914 GMT. 6 November 1978.

Case 13 Anomalous Gray Shades

Cirrus cloudiness effects.

In this DMSP VHR depiction (Fig. 2B-27), a dark gray shade pattern interrupted by light gray streaks is apparent off the coast of North Vietnam. In the Gulf of Tonkin, during the southwest monsoon, downslope motion from the Annam Mountains, exerts a profound drying influence on air flowing over the Gulf. A scattering of light from haze droplets, the number of which are reduced significantly in the downslope process, is also reduced. This reduced reflectivity in areas on the edge of a sunglint pattern will create an area which appears darker than normal. The light gray streaks extending out over the water along the coastline under these sunglint conditions are often found to correspond to rough water areas, which produces a brighter sunglint return and are caused by mountain-gap winds blowing out over the water (See Section 3, Barrier Effects).

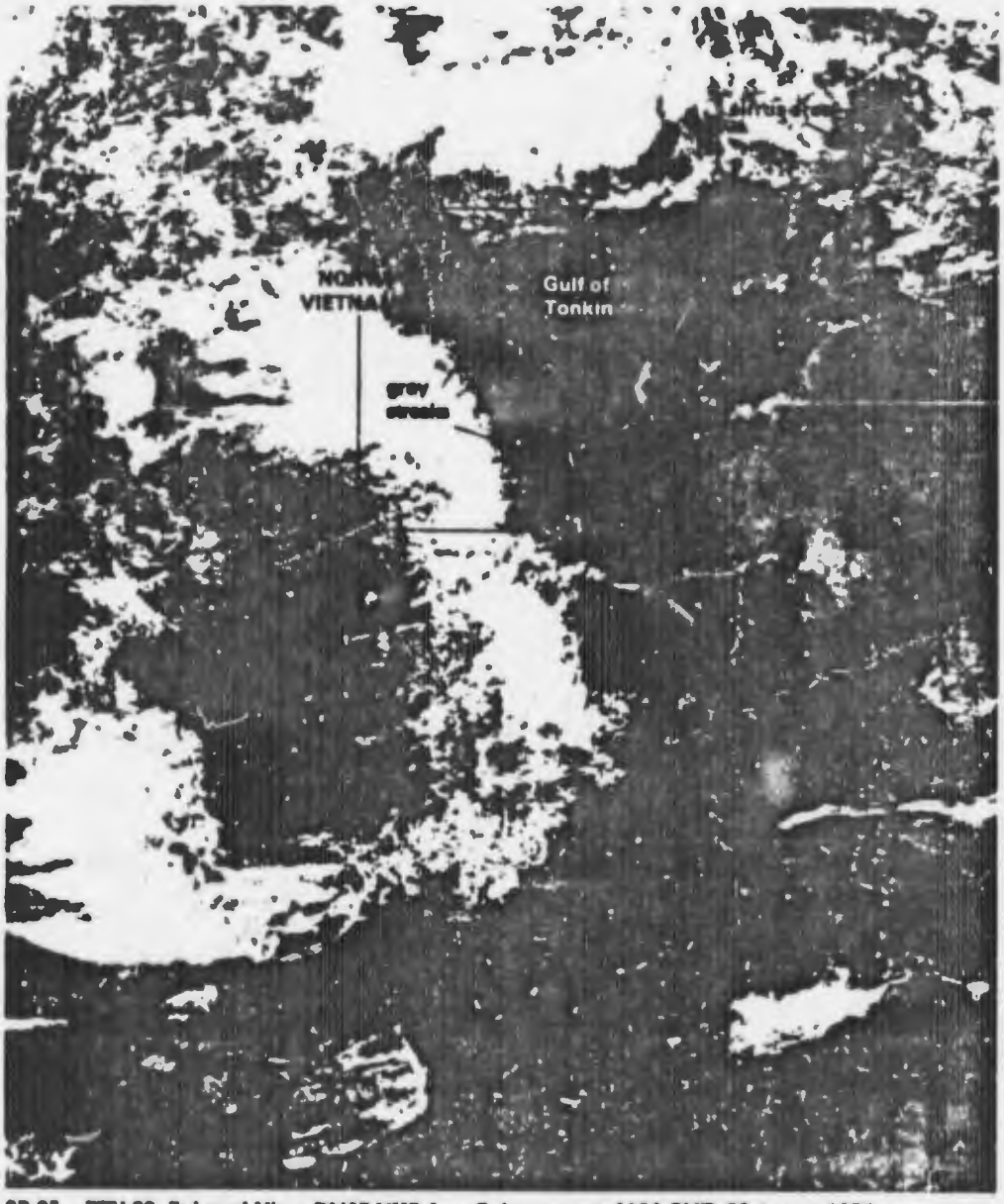

2B-27. FTV-29. Enlarged View. DMSP VHR Low Enhancement. 0126 GMT. 23 August 1974.

However, the gray streaks are not aligned with mountain passes, so mountain-gap winds cannot be the cause. Again the corresponding IR data (Fig. 2B-28), reveals that cirrus bands are the cause for the light gray shades. If the IR data were superimposed on the VHR data, it would be found that each band or patch of cirrus in the IR match the location of the light gray streaks over the dark area in the VHR data.

In addition, notice the appreciable cirrus over the brighter sunglint area east of Hainan Island as indicated in the IR data. These clouds are not apparent in the VHR data due to lack of contrast between the bright clouds and the corresponding bright sunglint background.

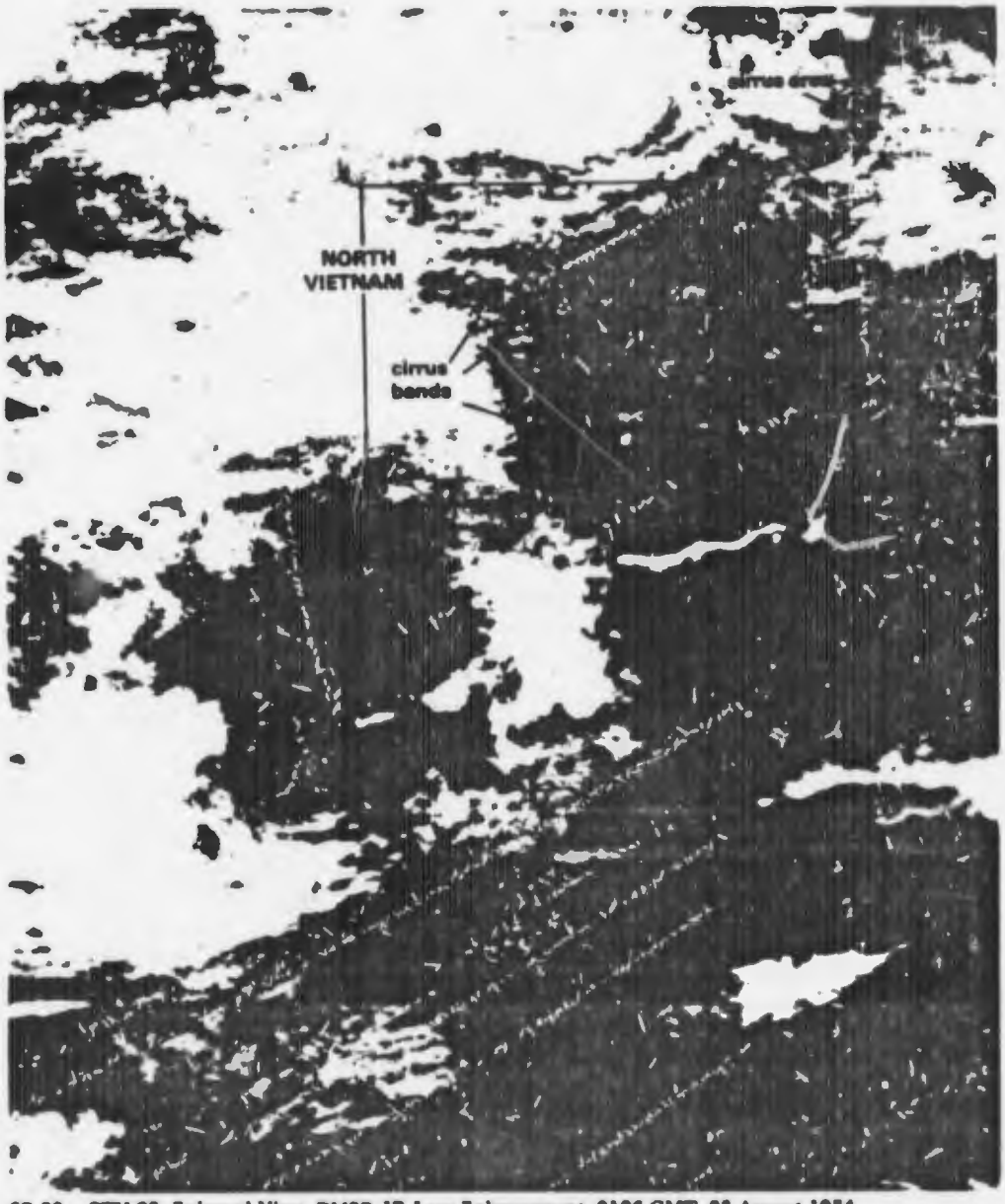

2B-28. FTV-29. Enlarged View. DMSP IR Low Enhancement. 0126 GMT. 23 August 1974.

Case 14 Anomalous Gray Shades

Cirrus cloudiness effects

DMSP nighttime visible or "H" data, are often surprisingly insensitive to radiation from cirrus cloudiness while the corresponding IR data over the same area gives a strong response. Fig. 2B-29 is a DMSP nighttime visible mode view over the South China Sea, showing some anomalous gray shades to the west of Luzon. These gray shades would suggest very little significant cloudiness over this area. The

2B-29. FTV-31. DMSP HR Low Enhancement. 1622 GMT. 30 September 1974.

corresponding IR depiction (Fig. 2B-30), however, indicates that dense cirrus cloudiness is present over this area which could be a matter of importance for certain tactical operations. This case again re-emphasizes the importance of relating visible to IR data to gain an accurate assessment of total cloudiness.

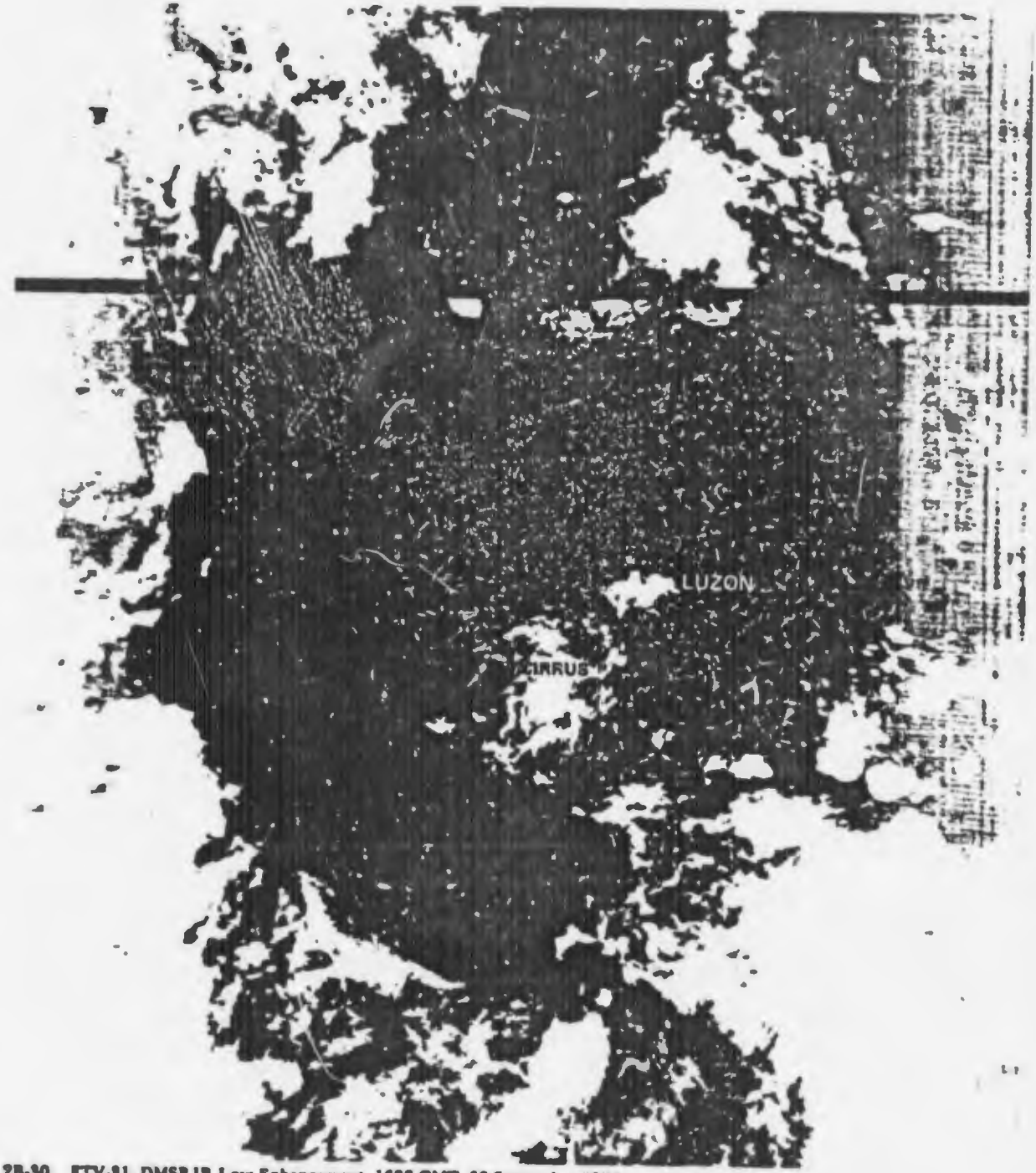

2B-30. FTV-31. DMSP IR Low Enhancement. 1622 GMT. 30 September 1974.

Case 15 Anomalous Gray Shades

Muddy (sediment) and turbid water effects

Anomalous gray shade patterns may appear as a result of the outflow of muddy or turbid water from major river systems into the seas and oceans. In Fig. 2B-31, a DMSP VHR depiction reveals faint, light-tone gray shades in the area of the Yellow Sea between China and Korea. In an enlarged view of this area (Fig. 2B-32) the gray shades can be seen extending offshore from the mouths of the Yangtze and Yangki

2B-31. FTV-28. DMSP VHR Low Enhancement. 0405 GMT. 30 January 1975.

Rivers caused by muddy water sediment, or silt carried seaw... An edge of the lighter-tone gray shade area separating turbid wat... rom clearer water (dark-tone) to the north can be detected extending ross the Yellow Sea from China to just south of Cheju Do Island.

Landsat data (Fig. 2B-33) were available over the same area at about the time of the DMSP pass. The same V-shaped cloud area can be detected in both the DMSP and the Landsat imagery. The anomalous gray shade apparent in the DMSP view appears as a series of swirls and eddies in the much higher resolution Landsat data. The separation of turbid water to the south from clearer water to the north also appears in both views. The position of this boundary correlates very well with the position of the South Korean coastal oceanographic front frequently found in that area (Huh, 1974).

Water coloration is affected not only by silt but also by chlorophyll. Blue water is associated with the absence of chlorophyll, while green water contains a vast amount of chlorophyll. Such differences in coloration translate into reflectivity and possible temperature differences. Therefore, it is possible, though not yet documented, that current systems of the open ocean may contribute to anomalous gray shades that can be detected by the DMSP spacecraft, and yield clues concerning the location of oceanographic fronts.

References

Huh, O.K., 1974: Coastal oceanographic use of the U.S. Air Force Defense Meteorological Satellite Program (DMSP). Naval Oceanographic Office, Washington, D.C., 56 pp.

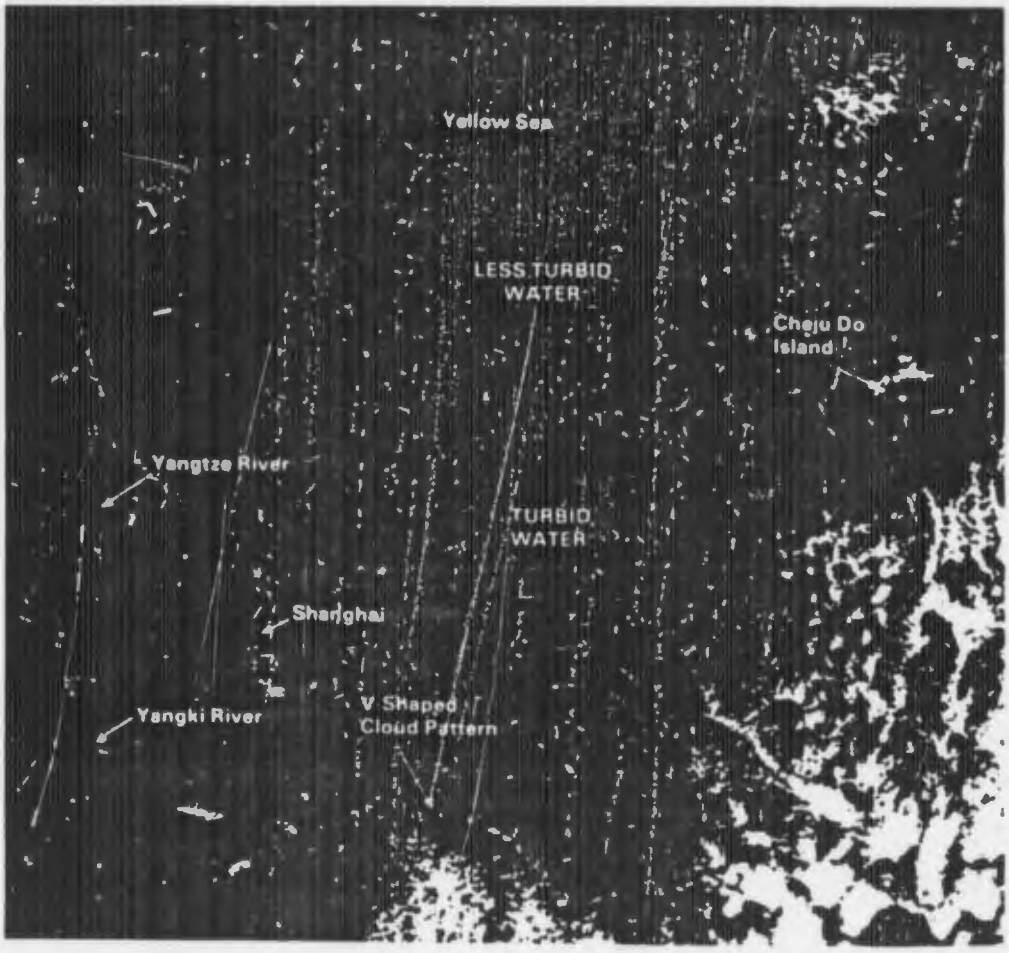

2B-32. FTV-28. Enlarged View. DMSP VHR Low Enhancement. 0405 GMT. 30 January 1973.

silt carried seaward.
ating turbid water fi
etected extending acr
ju Do Island.

r the same area at abou
aped cloud area can b
magery. The anomalou
as a series of swirls and
data. The separation of
o the north also appears
orrelates very well with
l oceanographic front

but also by chlorophyll.
chlorophyll, while green
ll. Such differences in
possible temperature
t yet documented, that
bute to anomalous gray
ecraft, and yield clues
.

U.S. Air Force Defense
l Oceanographic Office,

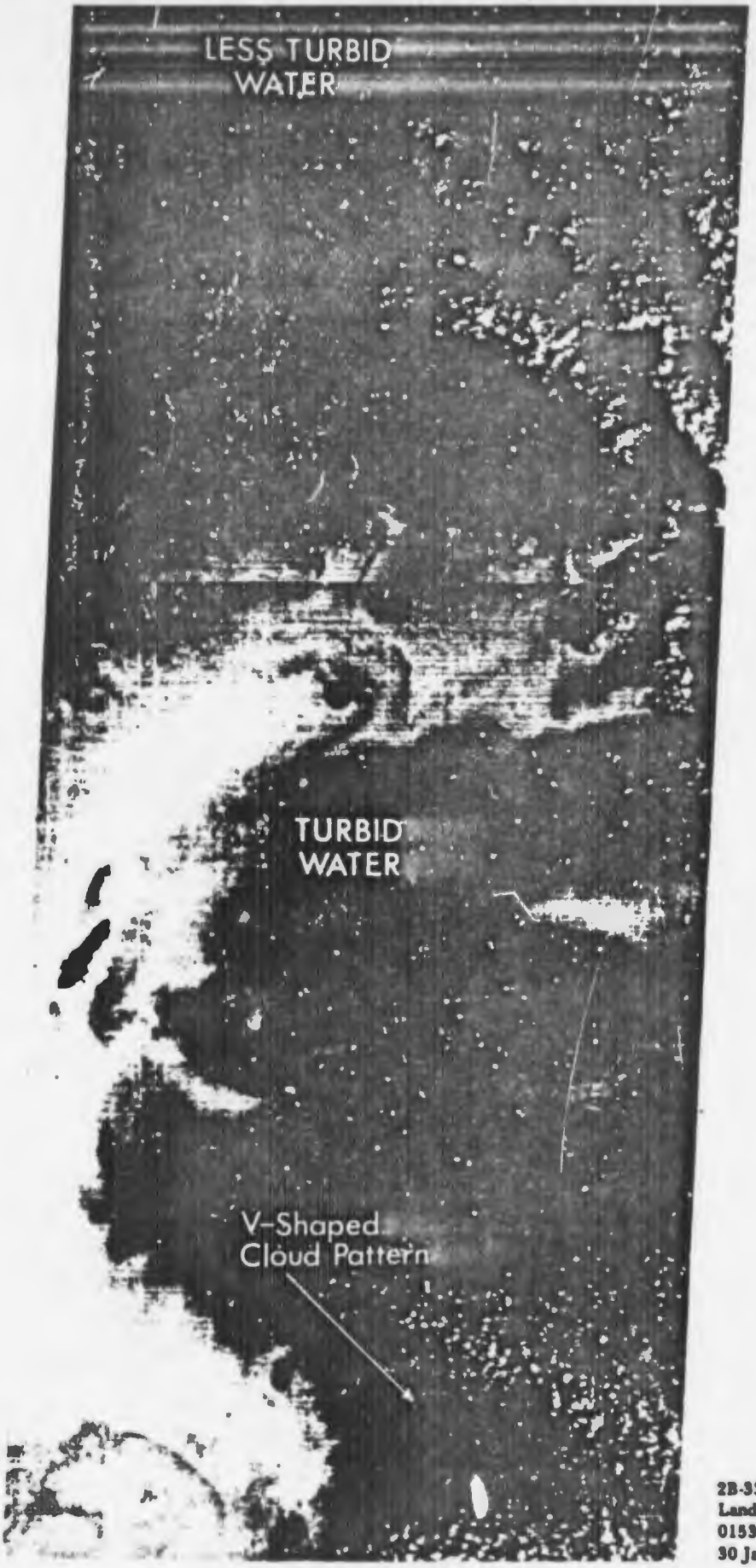

2B-33. Enlarged View.
Landsat Data.
0153 GMT.
30 January 1973.

Case 16 Anomalous Gray Shades

Anomalous gray shades due to dust

If haze droplets can scatter incident solar radiation, thereby changing the reflectivity of the area and rendering the haze visible, the same should hold true for atmospheric aerosols including dust, smoke, and other atmospheric pollutants. The DMSP VHR depiction (Fig. 2B-34) shows an example of the outbreak of a sirocco moving off the coast of Libya, North Africa. The enlarged view of this area (Fig. 2B-35) shows that the anomalous gray shade caused by dust and blowing sand is clearly visible against the darker waters of the Mediterranean. Positive verification of the sirocco is shown by the superimposed wind report 1200 GMT, 22 Oct 1975 from station HLGN (063) of forty knot southerly (190°) winds and blowing sand. The winds at this time had increased in velocity from an earlier 0600 GMT report of south-southeasterly (160°) at twenty knots.

2B-34. FTV-31. DMSP VHR Low Enhancement. 1032 GMT. 22 October 1975.

2B-35. FTV-31. Enlarged View. DMSP VHR Low Enhancement. 1032 GMT. 22 October 1975.

Case 17 Anomalous Gray Shades

Blowing sand and dust effects

Santa Ana conditions bring very warm, dry air from the desert out over the Los Angeles bight. When winds are strong, sand and dust fill the air causing serious restrictions to visibility.

An example of a Santa Ana in DMSP VHR imagery is shown in Fig. 2B-36. Sunglint is scattered and reflected by dust and sand particles creating an anomalous shade of gray. Superimposed wind reports confirm strong lower-level flow. Although surface wind reports in the area were not as strong as shown by the wind reports at 1,000 mb and 850 mb, a downward transport of momentum in the area is sufficient to cause gusty wind conditions, giving rise to the sand and dust blown out to sea as indicated in the imagery.

2B-36. FTV-28. Enlarged View. DMSP VHR Low Enhancement. 1906 GMT. 4 April 1973.

Case 18 Anomalous Gray Shades

Smoke effects from large fires

One of the largest fires in the United States occurred in the Los Angeles, California area in late November 1975. Strong Santa Ana winds fanned a brush fire into major proportions, destroying more than 45,000 acres. The DMSP VHR image of the fire area is shown in Fig. 2B-37. An anomalous gray shade plume extends westward from the Los Angeles area and obscures Santa Catalina and other of the Channel Islands. A pronounced low-level temperature inversion was located over the area. The low-level inversion undoubtedly contributed to the opacity of the smoke which eventually becomes less reflective and more transparent to the west. The further development of the smoke on the following day is shown in Fig. 2B-38. Note that the smoke appears less dense and more transparent in this view than on the preceding day—an indication that the fire was decreasing in intensity. Note that the anomalous gray shades completely obscure coastal land features in the area of the fire.

2B-37. FTV-29.
Enlarged View. DMSP
VHR Low Enhancement.
1530 GMT.
24 November 1975.

2B-38. FTV-29.
Enlarged View.
DMSP VHR Low Enhancement.
1511 GMT. 25 November 1975.

Case 19 Anomalous Gray Shades

Aircraft condensation trails (contrails)

Contrails are frequently noted in DMSP data, both in the VHR and in the IR depictions. Contrails, as noted from ground observations, are easily distinguishable from other cloud formations. They also appear distinctive in satellite data.

Fig. 2B-39 is a DMSP image of a contrail formation extending from the Missoula Omni Range, south of Flathead Lake, Montana, on a direct course to Lakeview Omni Range west-southwest of Lake Albert. Loss of the contrail northeast of Lake Albert suggests that the aircraft had initiated descent procedures for letdown into the Klamath Falls, Oregon area. The corresponding IR view is shown in Fig. 2B-40.

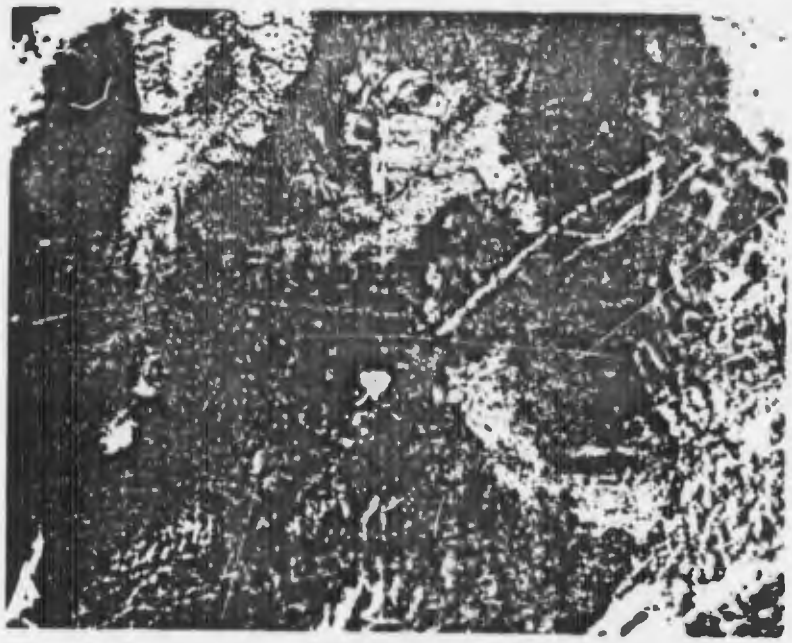

2B-39. FTV-28. Enlarged View. DMSP VHR Low Enhancement. 2015 GMT. 17 August 1973.

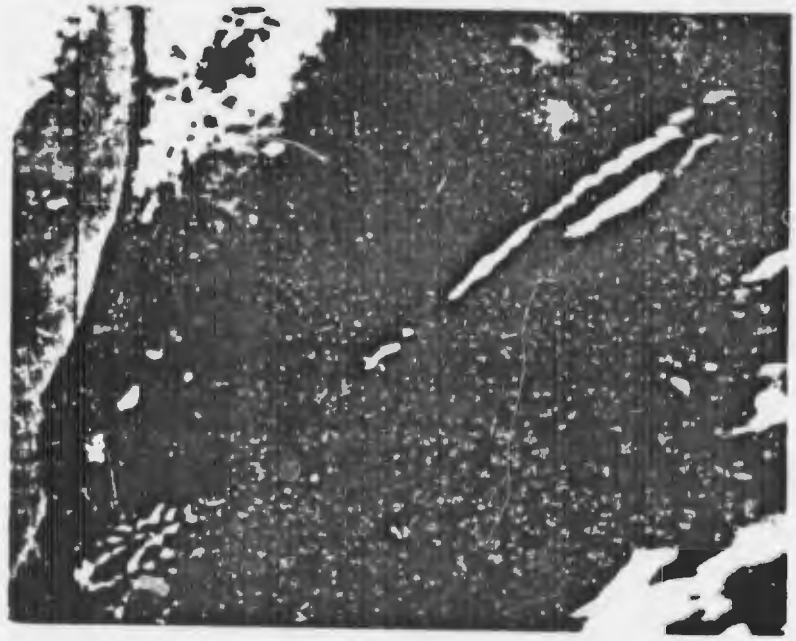

2B-40. FTV-28. Enlarged View. DMSP IR Low Enhancement. 2015 GMT. 17 August 1973.

, both in the VHR and
round observations, are
ions. They also appear

mation extending from
Lake, Montana, on a
thwest of Lake Albert.
ggests that the aircraft
to the Klamath Falls,
in Fig. 2B-40.

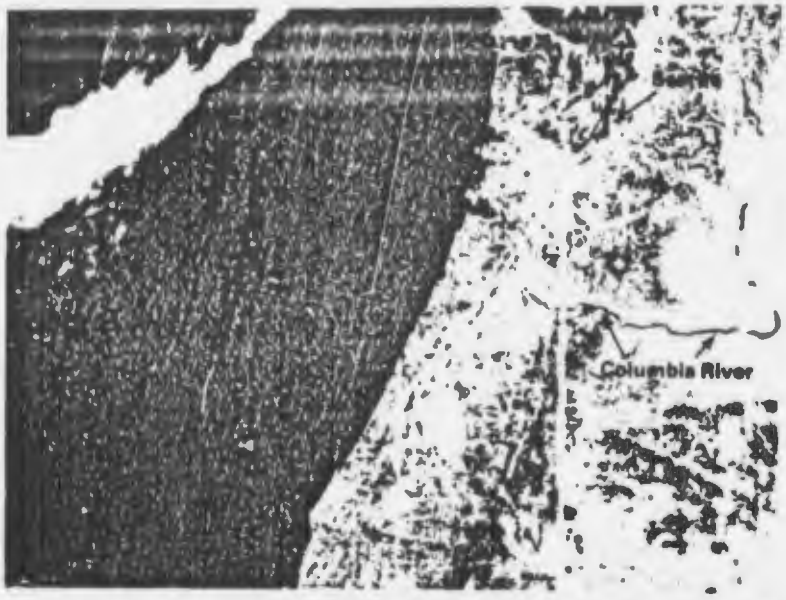

2B-41. FTV-
Enlarged Vie
DMSP VHR
Low Enhance
1917 GMT.
4 September

2B-42. FTV-
Enlarged Vie
DMSP IR
Low Enhance
1917 GMT.
4 September

Another example of contrail formation observed as anomalous gray shades is shown in Fig. 2B-41 extending to the south of the Seattle VORTAC. Fig. 2B-42 is the corresponding IR depiction. As previously noted with cirrus cloudiness, the IR is much more responsive in the delineation of contrails than is the VHR. In fact, as with cirrus cloudiness, contrails in the VHR may degenerate from visible cloud-like features to anomalous gray shade patterns, or be apparently invisible in the VHR, but still readily detectable in the IR. The two contrails over the mouth of the Columbia River appear to have been generated along airways route Victor 27-East. This route structure implies a flight at 18,000 feet MSL or lower. The longer contrail extending south southwest is along the high altitude route structure J1, implying a flight at altitudes above 18,000 feet MSL. The Navy forecaster aware of incoming air traffic may be able to link a specific aircraft and flight level to tell-tale contrail appearing in the DMSP data. Since contrail formation is dependent on small temperature – dewpoint spreads at the aircraft's flight level, this type of information yields additional, important clues to the structure of the atmosphere, at the time of the observation.

2C Barrier Effects

Barrier Effect Patterns

Topographic features can act as barriers to atmospheric flow. For example, a mountain range can act in varying degrees as a barrier, and air may be forced over the range, around the range, or channeled through gaps or valleys in the range. Similarly—islands, island chains, peninsulas, and projecting corners of coastlines provide barriers to atmospheric flow; and in addition provide barriers to swell and sea waves, producing wave refraction effects and reduced sea heights in their lees.

When clouds are present in the flow approaching an island barrier, lee clearing effects, cloud plumes, and cloud eddies (Kármán vortices) can be produced. Under cloud-free conditions, topographic barriers can induce changes in the aerosol and moisture content of the air passing over or around the barriers. With the expanded visible spectral range into the near infrared (0.4 to 1.1μm), the DMSP VHR sensors can detect aerosol/moisture variations in the atmosphere, particularly at low levels and over the open ocean. These aerosol/moisture variations are revealed as the anomalous gray shades described in Section 2B. The tonality of the barrier induced aerosol/moisture effects can vary from dark tones to light tones, depending upon the presence or absence of sunglint over the area.

Case 1 Barrier Effects

Mesoscale cloud eddies and cloud plumes

Fig. 2C-1 is DMSP VHR Expanded mode imagery illustrating the importance of topography in influencing downstream cloud patterns. The area of interest is shown within the area outlined. An enlargement of this area (Fig. 2C-2) shows the islands of Socorro and San Benedicto. Socorro has a 1200 m mountain which disrupts the northerly flow sufficiently to produce the intricate pattern of mesoscale cloud eddies downstream. Previous studies have established that the "... conditions necessary for development of these cloud eddies are a strong low-level inversion which caps the stratocumulus field, an island barrier that pierces the inversion, and a persistent low-level wind flow in the 5 to 13 m sec $^{-1}$ range " (Anderson, 1974).

This same study indicates that the eddies tend to break down if the wind speed exceeds 13 m sec $^{-1}$ and that they will not form if the wind speeds are less than 5 m sec $^{-1}$. San Benedicto Island does not have sufficient size or elevation to produce the eddy cloud pattern but instead, through turbulent vertical motion, a long, narrow cloud plume is formed which extends well to the south of the island.

Fig. 2C-3 is another example of a long cloud plume, extending to the south of Guadalupe Island. The 0000 GMT 11 April 1974 RAOB for Guadalupe reveals a low-level inversion beginning near 700 m altitude. Wind speeds were strong on this day, preventing the formation of Von Karman vortices. The 200 m level winds were reported to be 18 m sec^{-1} from a direction of 330°, in good agreement with the alignment of the cloud plume. Wave-like cloud formations superimposed on downstream cloudiness suggests a gravity wave perturbation on the inversion induced by the island barrier which extends to a height of 1402 m. The gravity wave formation implies unstable low-level lapse rates, with stability concentrated at the inversion interface. Such a condition was actually verified by the Guadalupe RAOB, giving rise to a typical Kelvin ship wave (see Case 3). The alternate dissipation and generation of low-level cloud forms emphasizes the sensitivity of the marine layer air to the effects of vertical motion in producing cloudiness.

Reference

Anderson, R.K., et al., 1974: Applications of meteorological satellite data in analysis and forecasting. *ESSA Techn. Report NESC 51 (including Supplement, Nos., 1971, and Supplement No. 2, March 1973)*, National Environmental Satellite Service, NOAA, Washington, D.C., 350 pp.

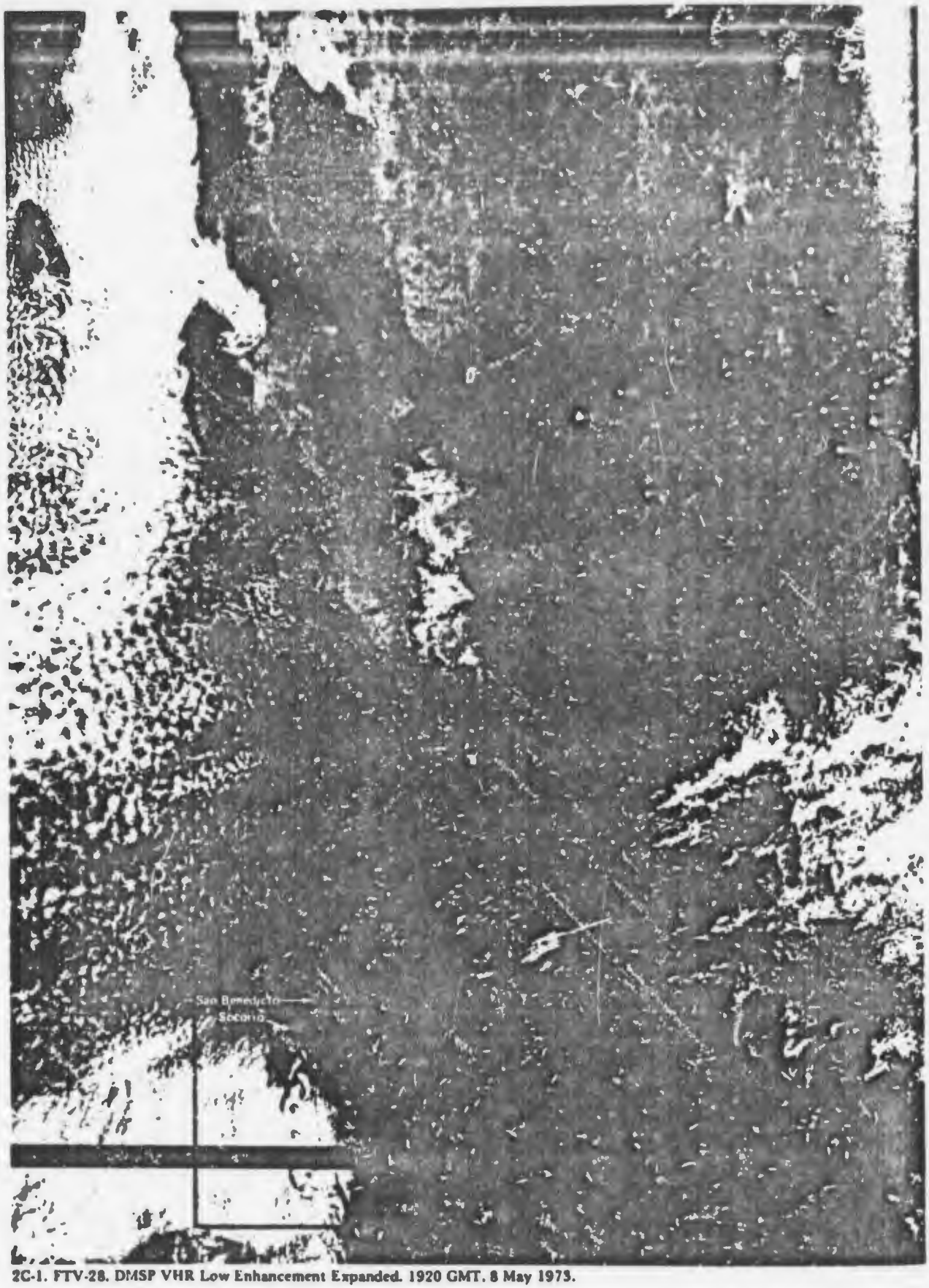

2C-1. FTV-28. DMSP VHR Low Enhancement Expanded. 1920 GMT. 8 May 1973.

2C-2. FTV-28. Enlarged View. DMSP VHR Low Enhancement Expanded. 1920 GMT. 8 May 1973.

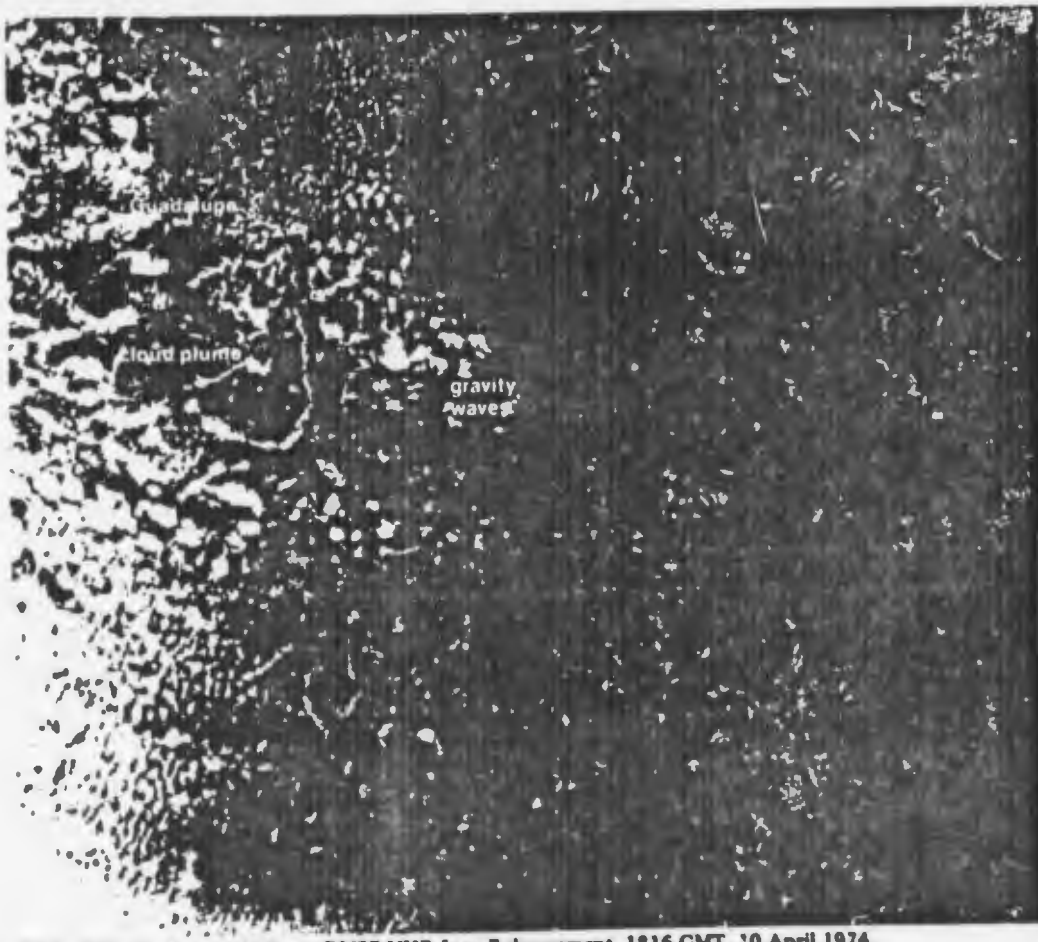

2C-3. FTV-28. Enlarged View. DMSP VHR Low Enhancement. 1816 GMT. 10 April 1974.

Case 2 Barrier Effects

Low-level flow, under stable atmospheric conditions, diverting around an island barrier

The importance of specific atmospheric conditions in determining environmental effects of an island barrier has been the subject of many studies, but very few of them incorporate evidence from meteorological satellites.

Edinger and Wurtele (1972) were among the first to point out some important aspects which they related to satellite observations. Wurtele (1957) computed the theoretical distribution of vertical motion, assuming airflow past a barrier in which the stability of the air is continually distributed in a stable stratification, i.e., a lapse rate less than adiabatic. Fig. 2C-4 shows the results which indicate a crescent-shaped area of descending motion downstream to the left and right of the barrier. The descending motion in this example is the first such area in a series of alternate rising and descending motions associated with a standing 3-dimensional internal gravity wave, formed as a result of the barrier effect. Satellite examples in the referenced article show clear areas adjacent to the islands in only the first descending branches of vertical motion. The authors concluded that the gravity wave was not strong enough to produce the secondary areas of descending motion implied by the schematic of Fig. 2C-4.

References

Edinger, J.G., and M.G. Wurtele, 1972: Interpretation of some phenomena observed in Southern California stratus. *Mon. Wea. Rev.*, 5, 589-398.

Wurtele, M.G., 1957: The three dimensional lee wave. *Beiträge zur Physik der Atmosphäre*, 29, 242-252.

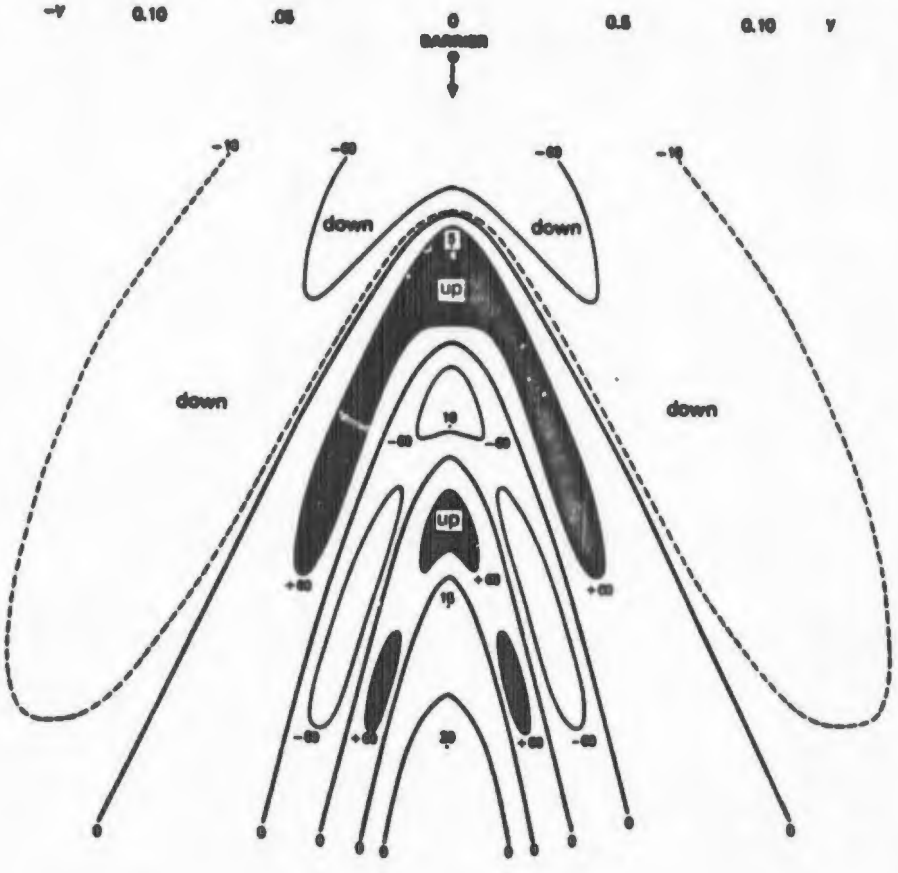

2C-4. Schematic of theoretical distribution of vertical motion (dimensionless units) in airflow past a barrier. 100 non-dimensional vertical velocity units are equal to 45.7 cm/sec. (After Wertele, 1957).

Fig. 2C-5 is a DMSP VHR enlargement showing pronounced clear areas on either side of Guadalupe Island that relates well to the suggested model (Fig. 2C-4). At 0000 GMT 16 June 1973, Guadalupe reported a surface wind from the north-northwest at 10 m sec^{-1} (20 kts). Again, secondary clear areas are not observed downstream; however, more complicated features of the low-level northerly flow are apparent resulting in the generation of a lee cloud plume and Kármán vortices downstream from the island barrier. The appearance of crescent-shaped clear areas, a cloud plume, and Kármán vortices, downstream from the island are useful indicators of the direction of the low-level flow past the island.

Important Conclusions

1. Strong low-level flow, under stable stratification, around an island barrier produces descending motion patterns giving rise to crescent-shaped clear areas downstream from the island.

2. The appearance of crescent-shaped clear areas in a cloudy region around an island can be used to deduce the direction of the low-level flow past the island.

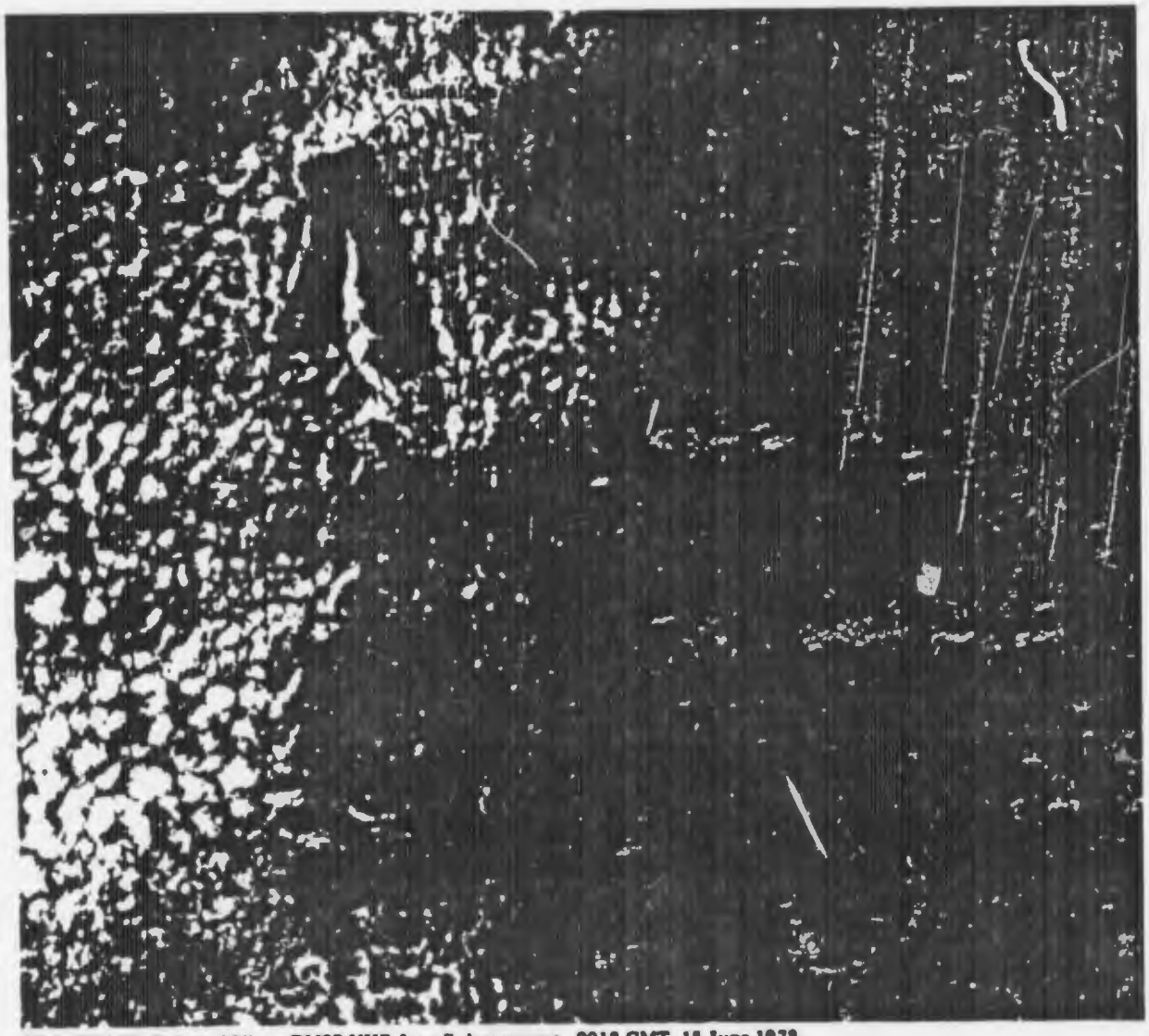

2C-5. FTV-28. Enlarged View. DMSP VHR Low Enhancement. 2018 GMT. 15 June 1973.

Case 3 Barrier Effects

Atmospheric gravity waves in a low-level temperature inversion layer

When the atmosphere at low levels does not possess continuous static stability, as described in the preceding case study (Section 2C, Case 2), but is characterized by stability aloft at a temperature inversion interface (Fig. 2C-6), Edinger and Wurtele (1972) suggest that a classical gravity wave (Kelvin ship wave) flow pattern should occur downstream from an island barrier.

The cloud pattern in the area outlined in Fig. 2C-7 is an excellent example of this type of gravity wave phenomena. The cloud pattern is located in the lee of the Faeroes Islands, about 300 km north-northwest of Scotland.

Fig. 2C-8 shows a schematic drawing of a theoretical configuration of the classical Kelvin ship wave. An enlargement of the DMSP imagery (Fig. 2C-9) reveals the close correspondence between the model and the atmospheric analogy. Some gravity wave interference patterns are observed along the southern branch due to the fact that, in this particular case, the gravity waves are produced by an island group (Faeroes) instead of a single island barrier.

References

Edinger, J.G., and M.G. Wurtele, 1972: Interpretation of some phenomena observed in Southern California stratus. *Mon. Wea. Rev.*, 5, 389-398.

Hogner, E., 1922: A contribution to the theory of ship waves. *Arkiv för Matematik, Astronomi och Fysik*, 17, 1-50.

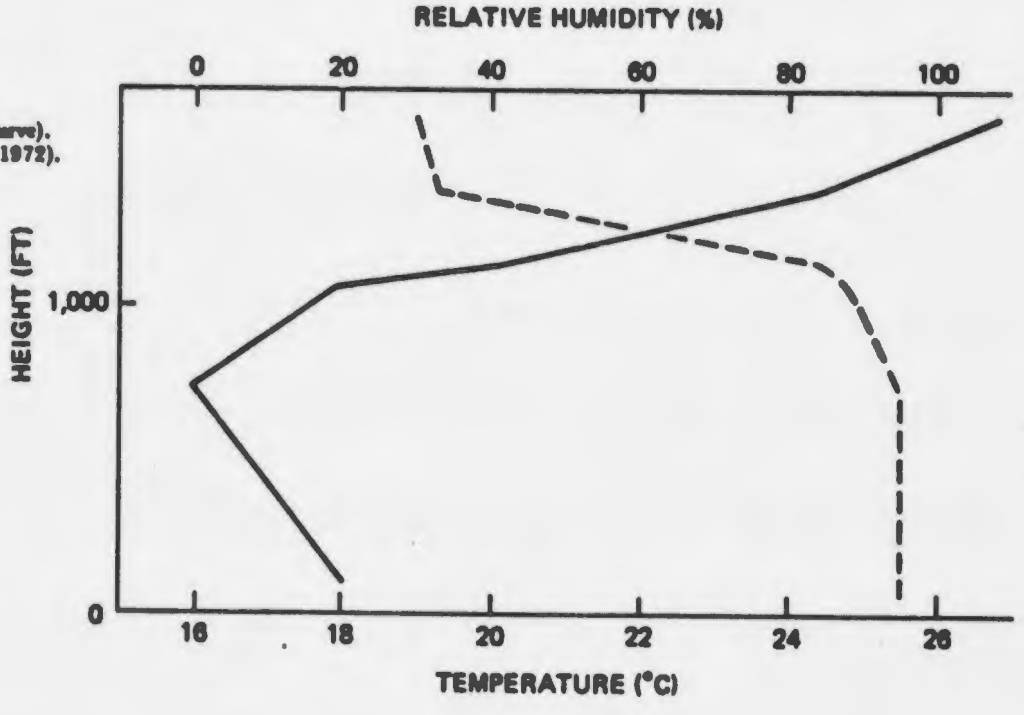

2C-6. Example of a temperature inversion profile conducive to gravity wave formation. Temperature (solid curve). Relative humidity (dashed curve). (After Edinger and Wertele, 1972).

Important Conclusions

1. In all cases of air flowing past islands under an inversion, downstream turbulent effects and effects due to upward and downward vertical motion are apparent.
2. Cloud plumes in the lee of islands appear to be logically associated with upward vertical motion and increased inversion heights. In the case of an extremely low inversion such vertical motion may produce a dry, lee plume through turbulent mixing.
3. Gravity waves indicate a very sharp inversion since such waves can only form under conditions of a density discontinuity at the inversion interface. This is analogous to ocean waves which form at the density discontinuity interface between the sea and atmosphere.

2C-7. FTV-29. DMSP VHR Low Enhancement. 0829 GMT. 23 June 1975.

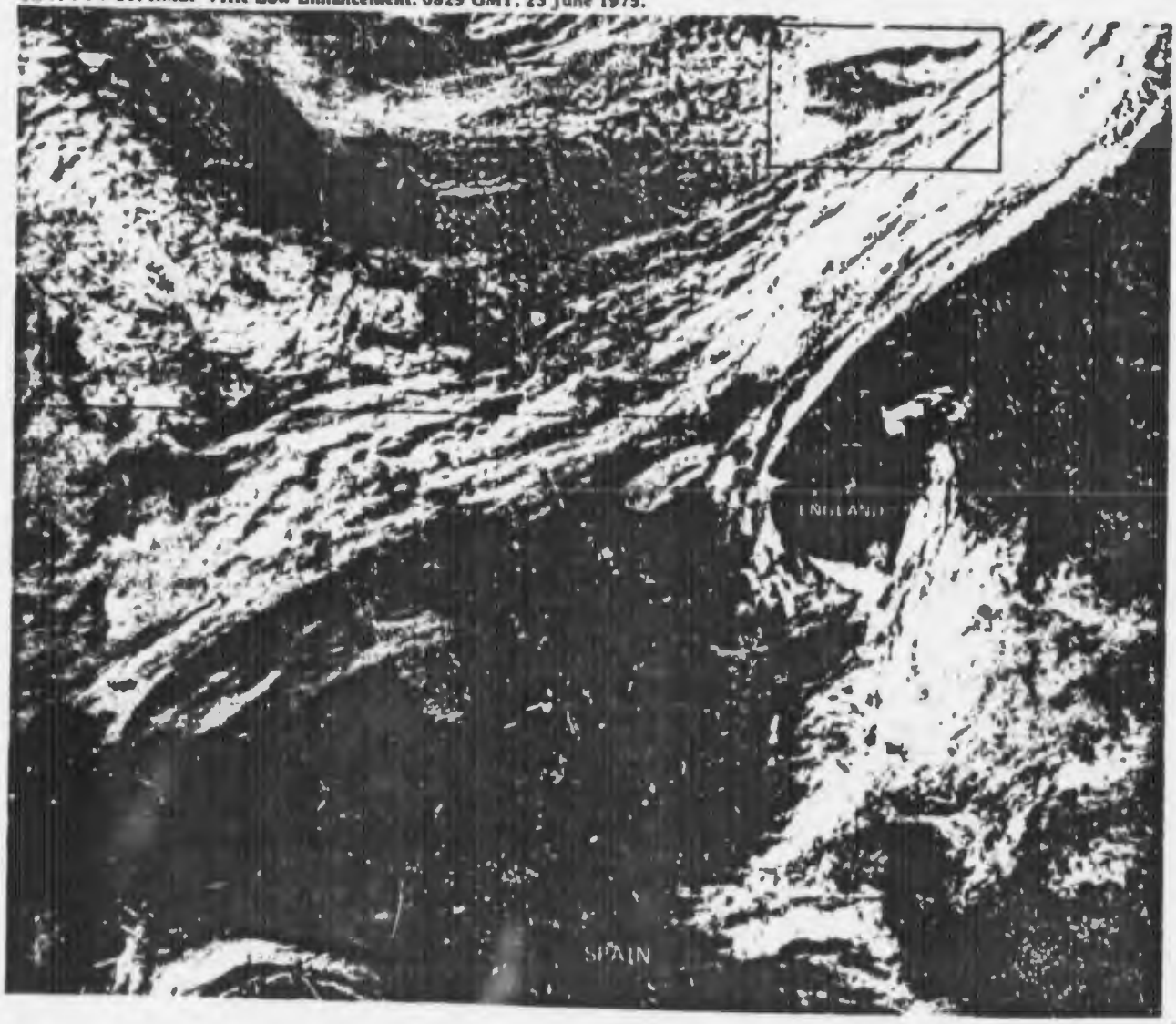

2C-8. Schematic of the Theoretical Ship Wave. Heavy lines denote crests of the wave system. (After Hogner, 1922).

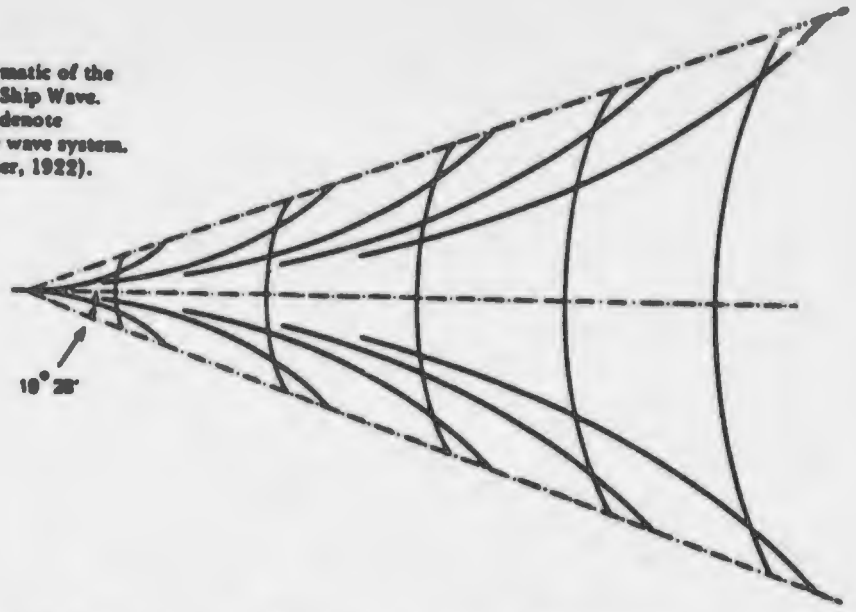

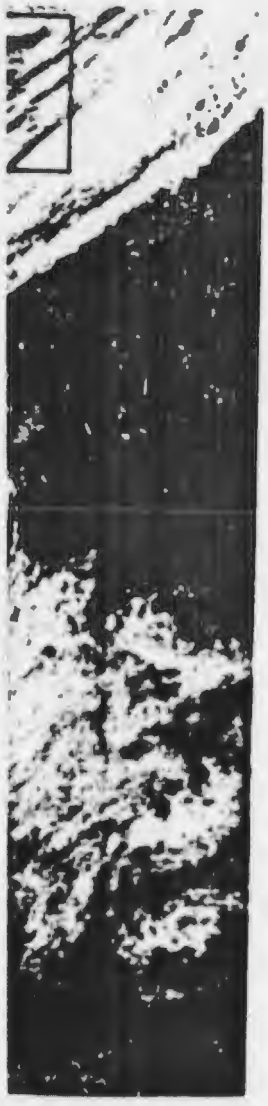

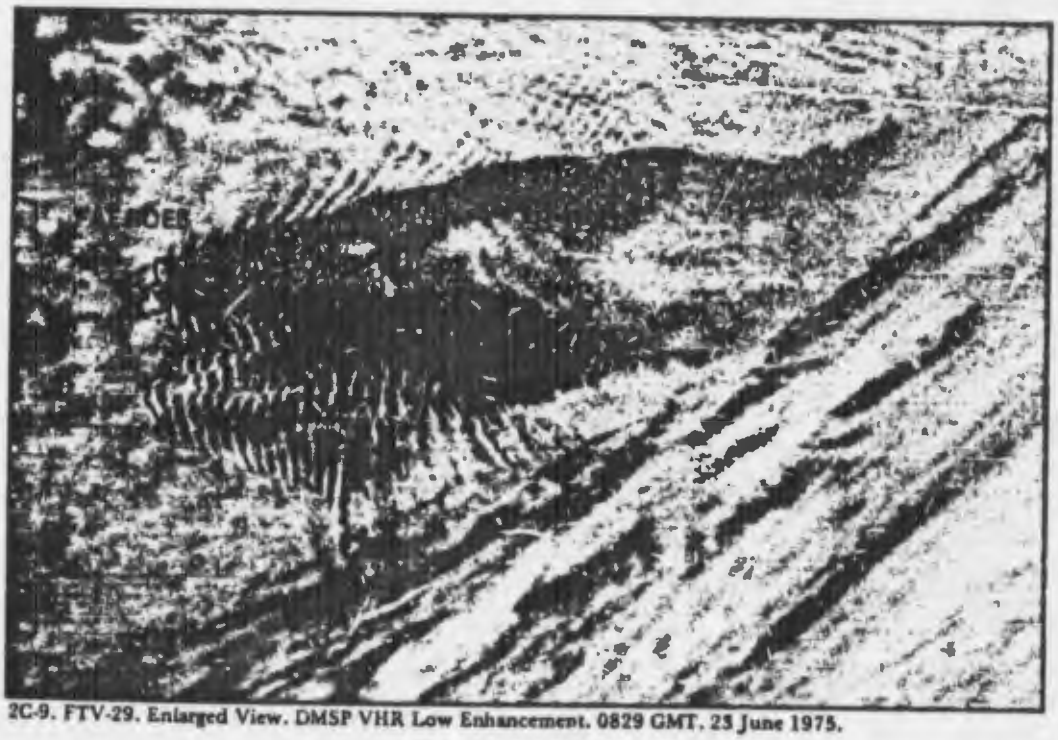

2C-9. FTV-29. Enlarged View. DMSP VHR Low Enhancement. 0829 GMT. 25 June 1975.

Case 4 Barrier Effects

Clear wake areas in downstream airflow around island barriers remote from sunglint

Clear wakes in the lee of isolated islands under conditions of a low-level inversion were the subject of a study by Lyons and Fujita (1968). They noted that such wakes could result from any of three mechanisms occurring singly or in combination: (1) Flow and low clouds could be diverted around the edge of the island leaving the lee area clear for a certain distance. (2) For air flowing over an island barrier, vertical mixing of low-level moist with dry air above the inversion could be induced by intense turbulent terrain effects. The modified drier air would be advected downstream producing a clear wake. (3) Air flowing over an island could also become dry due to evaporation of liquid water through heating, as a direct result of contact with the land surface.

Lee drying effects are very apparent in the DMSP VHR data. The appearance of such effects varies depending upon whether the area viewed is illuminated by sunglint or located in a region remote from sunglint.

Fig. 2C-10 is a DMSP VHR depiction of the eastern Pacific, in an area remote from sunglint, with a clear view of Guadalupe Island on 8 April 1974. The low-level wind flow on this day was from the northwest at about 7 to 12 m sec^{-1} (14-24 kts). A close examination of

2C-10. FTV-31.
DMSP VHR Low Enhancement.
1854 GMT. 8 April 1974.

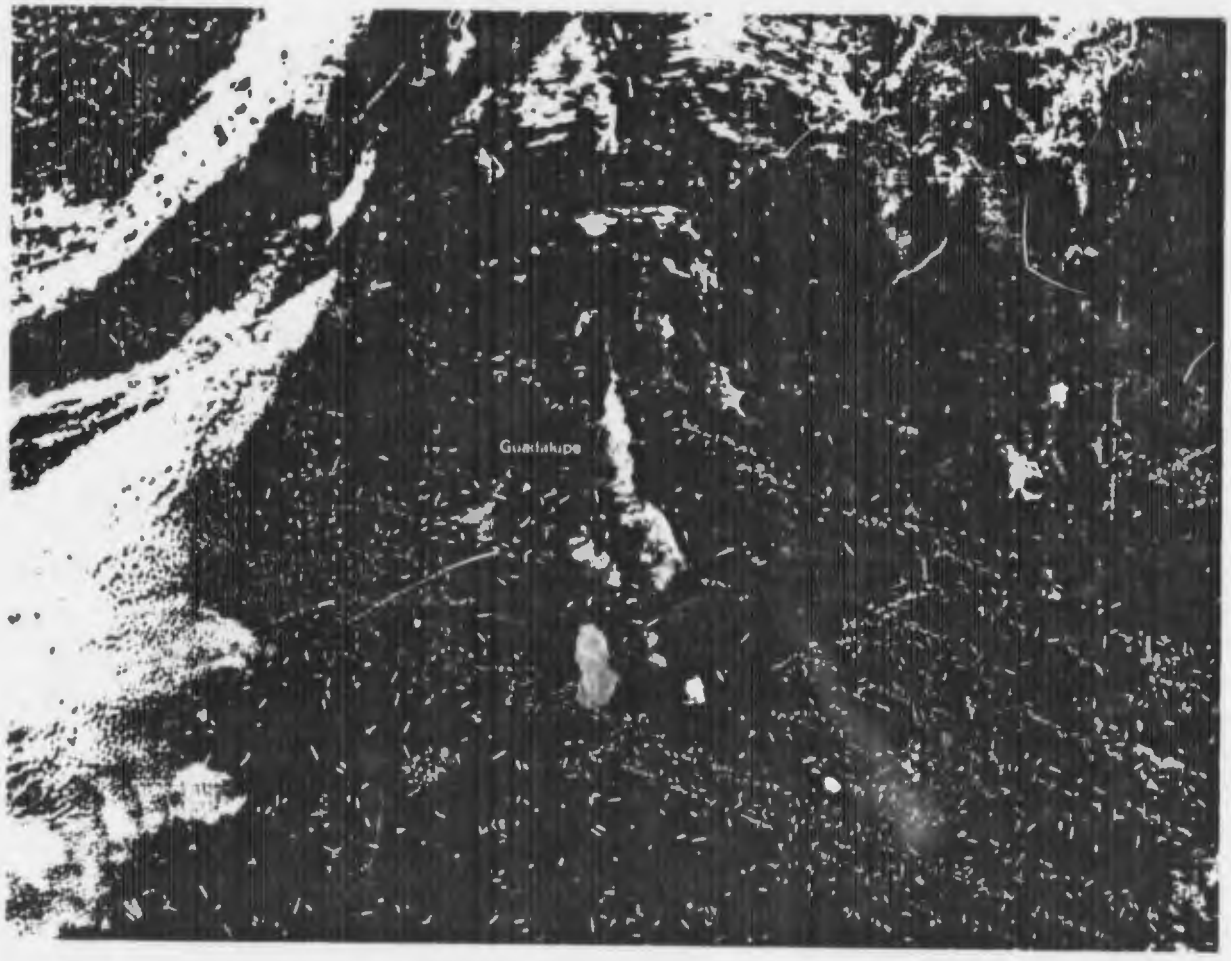

this area (Fig. 2C-11) reveals that a lee effect is distinctly apparent, consisting of a clear, dark, oval-shaped area outlined by a uniform shade of gray which merges into stratocumulus cloudiness. The lighter gray shades are interpreted to be low-level, high humidity areas due to the higher reflectivity expected from a heavy concentration of haze droplets. The oval-shaped dark tone is therefore interpreted to be a lee dry area where light-scattering effects are reduced and a minimum of light is reflected toward the spacecraft sensor.

Fig. 2C-12 provides important support for this hypothesis. In this figure, Guadalupe Island is seen on a different day (20 June 1973) under almost identical conditions of low-level wind flow and lack of illumination by sunglint. Again the oval-shaped dark area is visible, this time surrounded by a cloudy area indicative of moister atmospheric conditions than existed in the anomalous gray shade area of the previous example.

In Fig. 2C-13, a long cloud plume extends south from San Benedicto through a mixture of clouds and a heavy concentration of haze droplets, to an elliptically shaped dark area. This dark area has apparently been produced by a drying influence which extends downstream from Socorro Island. Note that the cloud plume from San Benedicto tends to dissipate over the dark area and appears to redevelop and merge with a trail of Kármán-type cloud vortices developing in the flow to the south of Socorro Island.

2C-11. FTV-31. Enlarged View.
DMSP VHR Low
Enhancement.
1854 GMT. 8 April 1974.

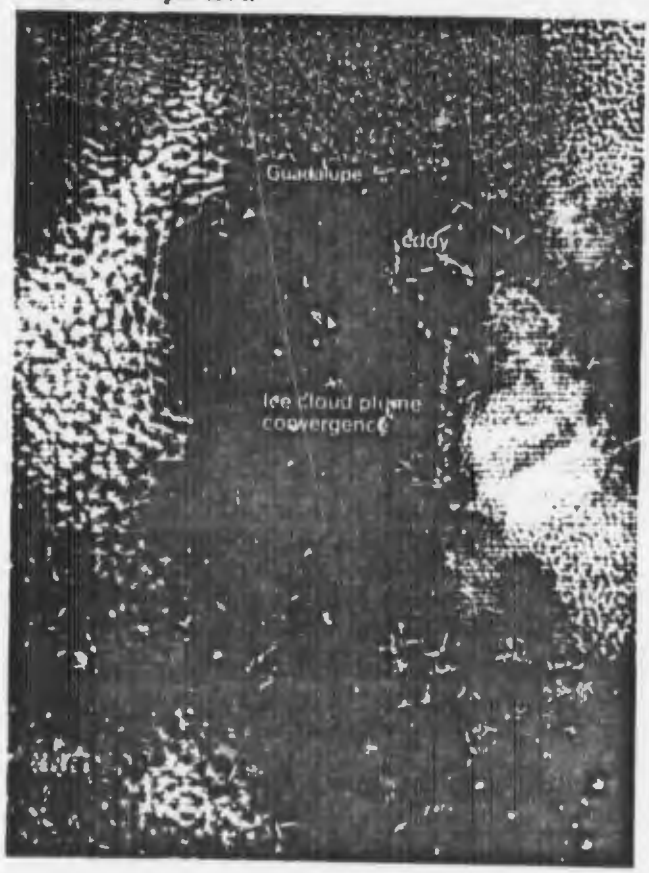

2C-12. FTV-28. Enlarged View.
DMSP VHR Low
Enhancement.
1905 GMT. 20 June 1973.

For Navy environmental forecasts, the light gray shades adjacent to the visible stratocumulus cloudiness imply areas of high, low-level humidity with attendant poor, low-level visibility. In addition increased low-level visibilities and lower moisture content can be presumed to exist in the dark areas over most of the eastern half of the imagery, and in a small area south of the island of Socorro.

Reference

Lyons, W.A., and T.T. Fujita, 1968: Mesoscale motions in oceanic stratus as revealed by satellite data. *Mon. Wea. Rev.*, 96, 304-314.

2C-13. FTV-31. Enlarged View. DMSP VHR Low Enhancement. 1758 GMT. 11 April 1974.

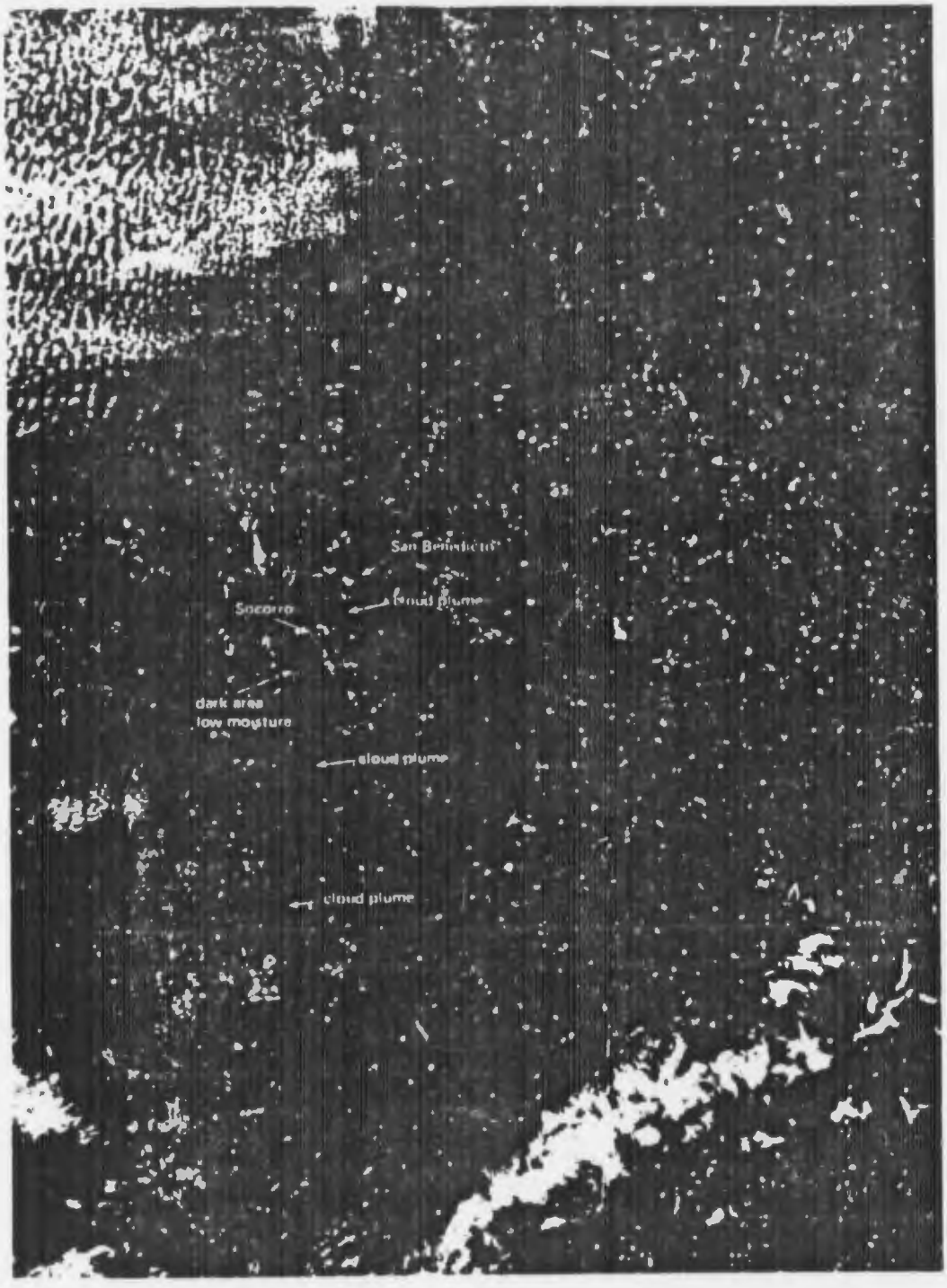

Case 5 Barrier Effects

Sunglint effects in areas downstream from islands

The reduced sea state in the lee of islands has an impact on the reflectivity measured by the DMSP VHR sensor in sunglint areas. Fig. 2C-14 displays island barrier effects in the lee of the Hawaiian Islands at 1017 GMT on 17 August 1972. In this example, Hurricane Celeste can be seen southeast of the islands. An enlarged view of the Hawaiian Island area(Fig. 2B-15) clearly shows the lee reflectance patterns.

In a sunglint area the sun's rays will reflect most brilliantly into the spacecraft sensor in areas where sea state is calm (referring primarily to short period wave and capillary action and neglecting long period swell). Reflectance will decrease as sea state (wave height) is increased. The lee drying effect in a sunglint area will, similarly, tend to increase reflectance because of reduced scattering and reduced absorption of solar rays by water vapor infrared wave lengths. The result of these combined effects are the turbulent wake patterns shown in Fig. 2C-15. Note the 15 knot wind reported by a ship in the lee of Oahu which was also reporting wave heights of 3 ft. This suggests that the lee drying effect accounts for a major portion of the reflectance pattern observed. Convergent airflow around the sides of the islands can be detected from cloud patterns forming at the termination of some of the reflective island wakes. (Note analogous formations in Fig. 2C-11 and 2C-12.)

2C-14. DMSP VHR Low Enhancement. 1017 GMT. 17 August 1972.

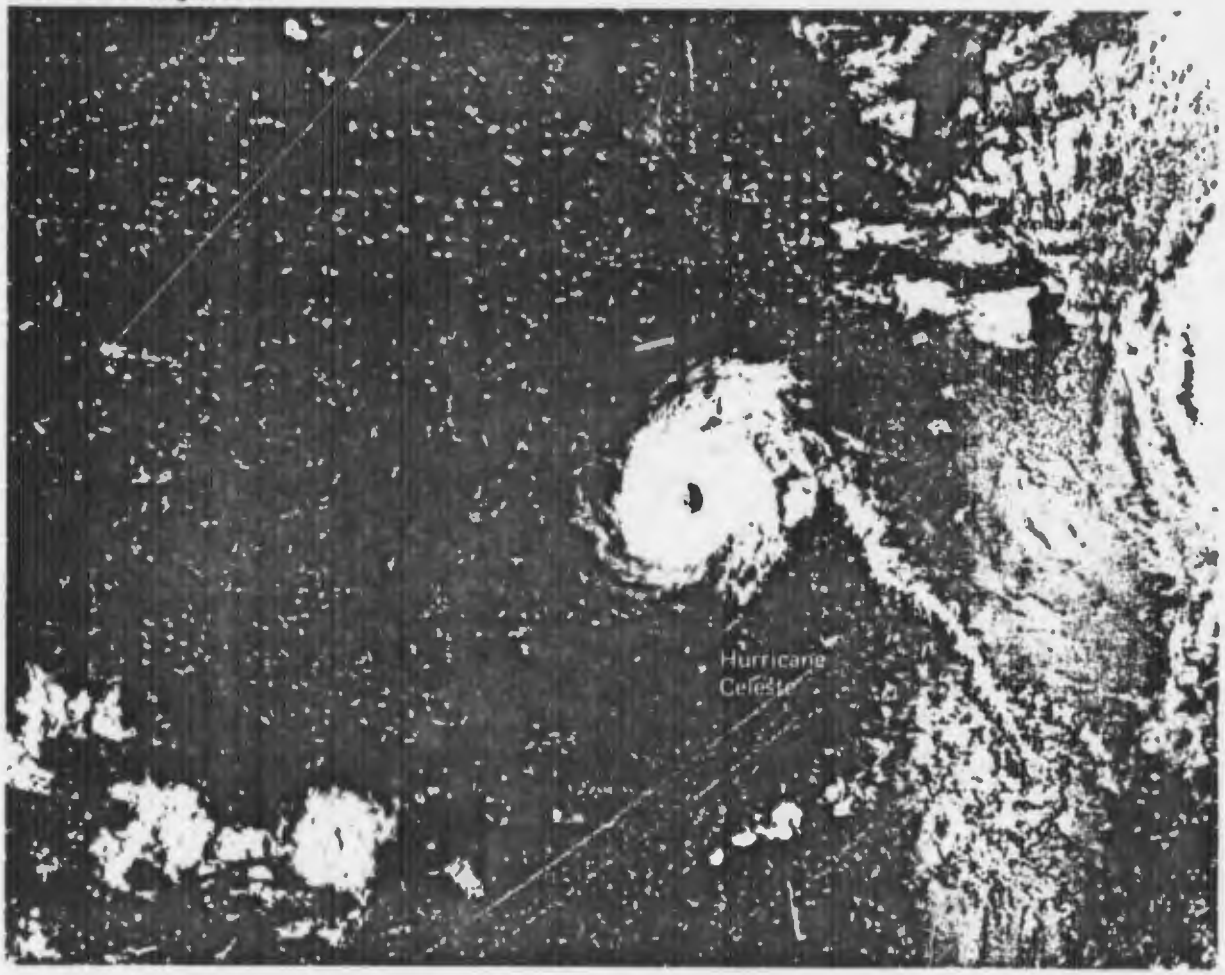

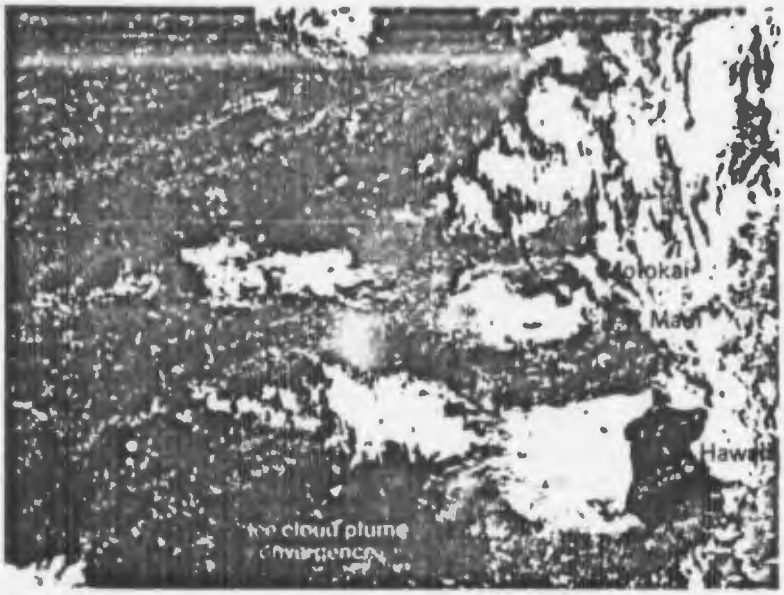

2C-15. Enlarged View. DMSP VHR Low Enhancement. 1017 GMT. 17 August 1972. Surface Wind Reports 1800 GMT. 17 August 1972.

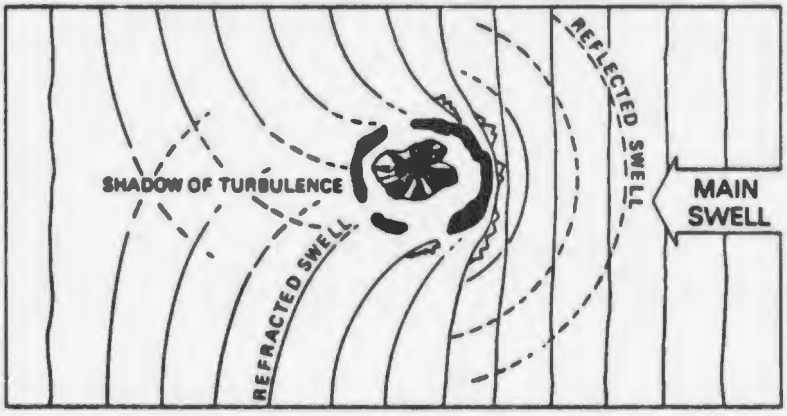

2C-16. Schematic of a typical wave refraction lee effect.

A schematic of a typical wave refraction lee effect is illustrated in Fig. 2C-16. The main effect to be noted is the refraction of swell on both sides of the island resulting in lee interference patterns called "shadow of turbulence". Some distance further to the lee (left side of the figure) undisturbed wave forms of the open sea again are dominant. A numerical model was applied at NEPRF to the task of predicting sea state in the lee of islands under varying wind conditions to gain an increased understanding of this topic (Fett and Rabe, 1975). Key results of this study show that, under all wind conditions, seas are essentially calm in the immediate lee of the island and that heights rapidly increase downstream attaining heights similar to that of the open sea at varying distances up to 200-300 km.

Note that the direction of low-level flow essentially parallels the direction of the lee reflectance patterns as shown in Fig. 2C-15. These patterns are useful in determining the direction of the low level flow and in resolving aberrant island wind reports, which may be responding strictly to local effects and not be giving a true indication of the general direction of the low level flow.

Reference

Fett., R.W., and K. Rabe, 1975: Island barrier effects on sea state and atmospheric moisture as detected by a numerical wave model and sensors of the Defense Meteorological Satellite Program (DMSP). NAVENVPREDRSCHFAC Tech. Paper No. 18-75. Naval Environmental Prediction Research Facility, Monterey, Calif., 67 pp.

Sunglint effects in areas between and downstream from island chains

Fig. 2C-17 is an example of drying effects in the lee of a mountain chain in the area of Borneo and Celebes. A large light-tone gray shade plume extends north from the Minahassa Peninsula. The primary specular point is located north of this area. Normally, increased reflectivity within a sunglint pattern some distance north or south of the primary specular point, and especially in the lee of an island or peninsula, is taken as an indication of reduced sea height in that area. As shown in the numerical model results of Fett and Rabi (1975), however, such reduction is primarily in the immediate lee of the barrier (see Section 2C, Case 5). Progressively higher seas are found further downstream.

In Fig. 2C-18, an enlarged view, it can be seen that the area of increased reflectivity extends well to the north of the Celebes barrier and does not diminish in reflectivity. It appears to be illogical, therefore, that sea height can be the only cause for this gray shade, and suggests that atmospheric moisture changes may be exerting a dominant influence. Southerly wind direction is readily inferred from the alignment of the plume and the observation that clouds have built up along the mountains on the southern coast of the peninsula. Mountain peaks on the peninsula extend to heights of about 2000 m so that air flowing over these mountains from the south would be subject to extreme turbulence effects that could, under inversion conditions, cause the air to be thoroughly mixed and "dried-out" in the process.

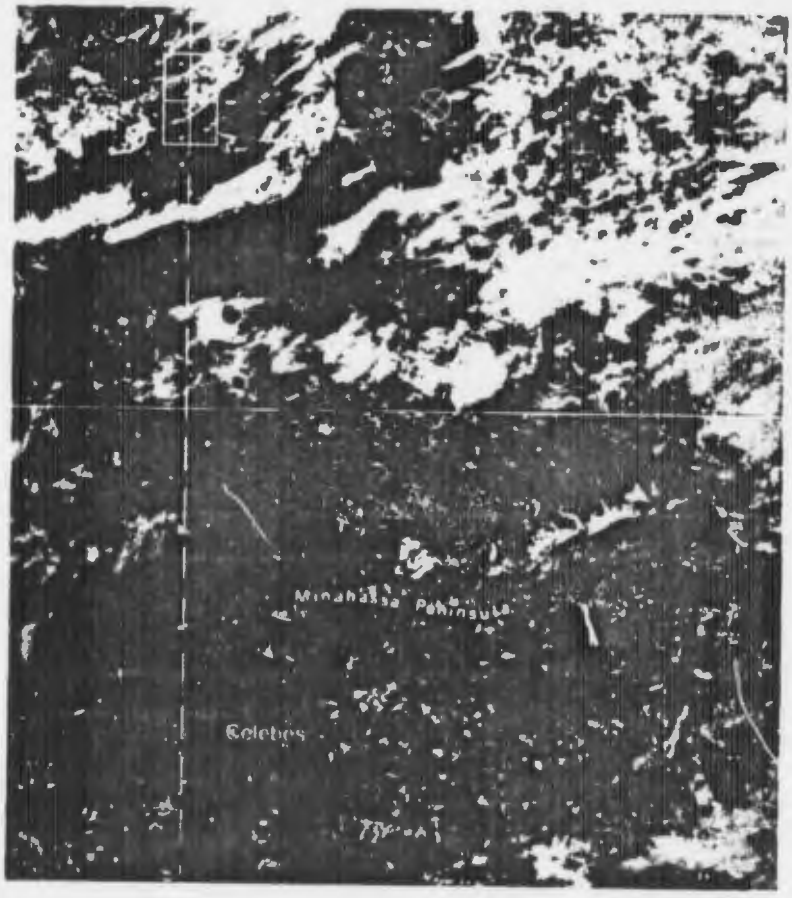

2C-17. FTV-29. DMSP VHR Low Enhancement. 0048 GMT. 14 August 1974.

Drier air in the central portion of the sunglint area scatters l[illegible] light and water vapor absorption is also reduced. Hence, the satellit[illegible]nsor receiving the reflected solar rays from this area records a [illegible]gher intensity as shown in this example.

The long, narrow dark-tone area adjacent to the light-tone area is in the lee of a major valley in the Minahassa Peninsula. Wind flowing through the valley between mountain ranges is often funneled in "Venturi" fashion, giving rise to much stronger southerly flow than in existence in the lee of the mountain range. Such a condition results in a roughening of the sea surface so that little solar reflection can be deflected toward the spacecraft sensor. Additionally, the valley air is not lifted to any appreciable extent so that little mixing occurs. Hence, atmospheric scattering and water vapor absorption become important factors in reducing transmittance. These factors are considered to be the cause of the long, narrow dark-tone area.

The island of Sangihe exhibits lee effects similar to that discussed in the Guadalupe Island example (see Section 2C, Case 4), however, with the gray shade tones reversed, due to a different satellite/sun geometry. In the Guadalupe example, the scanning radiometer was sensing reflectivity in a direction away from the sun and the oval-shaped lee areas appeared dark, because the sun's rays were deflected away from the satellite. In the case of Sangihe, as the scanning radiometer passed over the area, it was pointing towards the sun, resulting in a light gray shade depiction. In both instances we infer a lee of the island induced drying effect. Note that while Guadalupe produced a visible cloud eddy in its lee, Sangihe also produced a similarly shaped eddy which extends northward from the northern tip of the island as a darker shade of gray. The presence is most reasonably attributed, as in the former case, to haze droplets which in this case diminish the reflectivity of the area.

2C-18. FTV-29. Enlarged View. DMSP VHR Low Enhancement. 0048 GMT. 14 August 1974.

unt area scatters less lig
lence, the satellite sens
area records a high

the light-tone area is .
Peninsula. Wind flowin
es is often funneled in
r southerly flow than n
h a condition results in a
solar reflection can be
tionally, the valley air is
le mixing occurs. Hence,
ption become important
ors are considered to be

nilar to that discussed in
C, Case 4), however,
a different satellite/sun
anning radiometer was
rom the sun and the
e the sun's rays were
ase of Sangihe, as the
as pointing towards the
both instances we infer
e that while Guadalupe
ngihe also produced a
l from the northern tip
ence is most reasonably
plets which in this case

A similar valley wind depiction under slightly changed satellite versus sun angle configuration is shown in Fig. 2C-19, in the area of Celebes. Direction of the low-level wind flow can be determined by close examination of terrain induced blocking effects on cloud patterns and sea state. Southerly flow is implied by sunglint effects on the northern side of the Minaharsa Peninsula. Brilliant specular reflection implies calm seas in the lee of the mountains on the western portion of the peninsula while further east a dark plume indicates rougher seas in the lee of a major valley.

Near the edge of sunglint, calm areas appear as dark gray shade areas. Such indications may be used to deduce easterly flow blocked by a mountain near the southwestern extremity of Celebes. Such flow under stable conditions, below an inversion, is indicated by the wave clouds in that area oriented basically north-south, perpendicular to the flow. The diffluence implied by winds over the northwest portion of Celebes suggests subsidence and low-level divergence. In this respect, it is interesting to note that this area is remarkably cloud-free in comparison to other locations.

2C-19. FTV-29. Enlarged View. DMSP VHR Low Enhancement. 0052 GMT. 28 August 1973.

Appearance of moisture patterns delineating "corner effects" in airflow around islands

When a strong inversion, separating an upper dry layer from a lower moist layer, is very low so that an island projects well above the base of the inversion, airflow will tend to divert around the edges or corners of the island, rather than flow over the island. As indicated by Reiter (1975), under these conditions "stations on the windward and leeward sides of an island might experience lower wind speeds than stations on the two sides of the island around which the airflow is diverted. The venturi effect of this air can be expected to cause systematic mesoscale disturbances in the surface pressure distribution, with lower pressure likely to prevail on the high-wind sides of the island." In this manner "corner effects" are produced.

The DMSP VHR enlarged view (Fig. 2C-20) provides an example where corner effects rather than lee effects are illustrated. The figure shows lighter tone anomalous gray shades (against a dark background) extending east-west from the edge and, in a broken pattern, far to the lee of Socorro Island. A ship report just north of Socorro (21.2N, 111.1W) reported clear skies with a northerly wind and a 5 ft. swell from 360°. At 0000 GMT 6 November 1973, the Socorro surface report also indicated clear skies and a 15 kt wind from 010°. Note that the gray shade tonality in the lee of Socorro, excluding the lighter anomalous gray shades, is dark and of the same tonality as the rougher seas to the north in the area of the ship report.

Sunglint relationships for this example show the primary specular point to be located well to the south. Under these conditions, sunglint cannot be detected at Socorro. In other words, consistent with the above observations, calm seas cannot be differentiated from rough seas in the area of Socorro. Therefore, the anomalous gray shades shown in this case must represent an atmospheric rather than an oceanographic effect. Assuming conditions conducive to corner effects exist, the following hypothesis is suggested: Air, diverted in a quasi-horizontal fashion around the island, converges, with resultant uplifting and moisture condensation. This condensation is visible to the DMSP sensor through the process of atmospheric scattering and/or reflection. Under stable atmospheric conditions the formation of condensation particles in this manner is a continuous process causing them to spread out under the inversion and be advected long distances downstream.

2C-20. FTV-28. Enlarged View. DMSP VHR Low Enhancement. 1923 GMT. 5 November 1973.

In this manner, the broken gray shade pattern shown in Fig. 2C-20 could be produced. The moisture hypothesis in this example seems especially plausible since portions of the gray shade pattern merge with visible (white) cloudiness in small patches near the southern extremity. The close association of the gray shade with the visible cloudiness suggests that the gray shade is the precursor to the visible cloud formation, as has been shown in examples of anomalous gray shades (Section 2B). Variations of this effect could be expected to occur depending upon the precise height of the inversion, the strength of the wind flow, moisture content of the air, vertical wind shear, and other related atmospheric factors.

Reference

Reiter, E.R., 1975: Handbook for forecasters in the Mediterranean. NAVENVPREDRSCHFAC Tech. Paper 5-75, Naval Environmental Prediction Research Facility, Monterey, Calif., 374 pp.

Appearance of moisture produced anomalous gray shades in air flow around islands and sunglint in areas downstream from islands

Fig. 2C-21 is an example showing lee and corner effects in the same imagery, around the four islands: Santa Cruz, San Nicolas, San Clemente, and Cedros. These islands are in a sunglint area; however the primary specular point is out of the imagery area, south of Cedros island.

In Fig. 2C-22 and Fig. 2C-23 (enlarged views of Fig. 2C-21) notice the apparent corner effects visible as darker gray shades, extending left to right, from the sides of Santa Cruz, San Nicolas, San Clemente, and Cedros Islands. Also visible are lighter gray shade tones in the lee of these islands. The lee shades can be reasonably attributed to reduced seas and possibly decreased moisture resulting in increased reflectivity. The darker gray shades associated with the corner effects may be a combined effect. In Section 2C, Case 7, an example in an area remote from sunglint, a moisture hypothesis with sunglint scattering, or reflecting, off of condensation particles seemed most plausible. This produces a light-gray shade against a dark background. In this example, corner effects appear reversed in tonality as would be anticipated in a sunglint area. The cause could be threefold: (1) Increased winds along the edge of the island causes increased sea heights which reduces reflectivity. (2) Scattering of light by moisture particles reduces reflectance from the moist area in comparison to the background sunglint of calmer surrounding seas in drier air. (3) Increased water vapor absorption of light in moist areas causes reduced reflectivity.

2C-21. FTV-29. DMSP VHR Low Enhancement. 1632 GMT. 21 May 1974.

2C-22. FTV-29. Enlarged View. DMSP VHR Low Enhancement. 1632 GMT. 21 May 1974.

2C-23. FTV-29. Enlarged View. DMSP VHR Low Enhancement. 1632 GMT. 21 May 1974.

ous gray shades in ai
eas downstream from

rner effects in the same
uz, San Nicolas, San
nglint area; however the
' area, south of Cedros

n of Fig. 2C-21) notice
y shades, extending left
las, San Clemente, and
ade tones in the lee of
y attributed to reduced
n increased reflectivity.
rner effects may be a
mple in an area remote
sunglint scattering, or
d most plausible. This
round. In this example,
uld be anticipated in a
Increased winds along
heights which reduces
ture particles reduces
n to the background
r. (3) Increased water
luced reflectivity.

C-22. FTV-29.
nlarged View. DMSP VHR
ow Enhancement.
32 GMT. 21 May 1974.

-23. FTV-29.
larged View. DMSP VHR
w Enhancement.
32 GMT. 21 May 1974.

Fig. C-24 is a rare DMSP VHR example showing corner effects and lee effects in the Baja Peninsula area. The solar subpoint and the primary specular point are located south of the imagery limits. With the solar subpoint and the primary specular point in the Southern Hemisphere, sunglint effects from water surfaces cannot be detected at north latitudes. Thus, calm seas in these data should appear no different in reflectivity than rough seas, assuming identical moisture content above the two areas. Any barrier effects visible in these data then must, of necessity, be due to changes in atmospheric moisture (ruling out such causes as aerosol production, white-caps, and turbid or shallow water effects).

Two different effects are noted in Fig. 2C-24. Islands in the northern portion of the Gulf of California show lee effects, and corner effects are apparent around Guadalupe Island. (The step-like change in gray shade through the middle of the depiction is instrument induced.) The depiction was generated using the "Log" enhance mode of data production.

Dark gray shade tones extending south of Tiburon, San Esteban, and Angel de la Guarda Islands indicate northerly flow and are interpreted to represent dryness in the lee of the islands.

Corner effects (rather than lee drying effects) in the area of Guadalupe imply that most of the air is flowing around rather than over the island barrier. This implies a strong low-level inversion relative to the height of terrain on the island. The 1200 GMT RAOB for Guadalupe, about four hours prior to DMSP viewing time, verifies this condition. A pronounced inversion with very dry air above begins at about 200 meters, with terrain on the island projecting over 1000 meters above this level. Since oceanographic effects cannot be detected with this particular sun versus satellite geometry, the corner effects revealed are limited to those produced by increased atmospheric dryness. Increased moisture would cause the corner effects to become even more reflective than the environment, through enlargement of condensation particle diameters. Therefore increased dryness is implied, producing a dark gray shade similar to that found in the lee of islands in the Gulf of California. Such dryness, again, could be produced by mixing of lower moist with upper dry air above the inversion, as the air converges around the edges of the island.

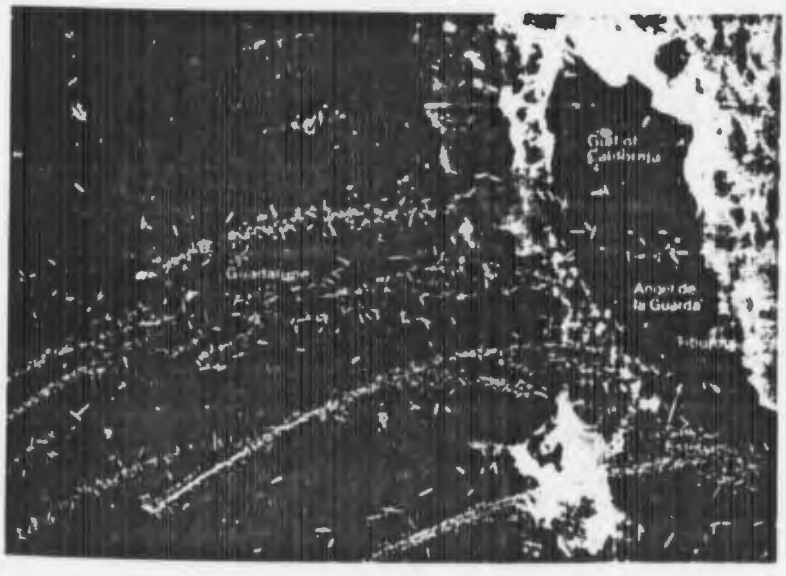

2C-24. FTV-29.
DMSP VHR
Low Enhancement.
1614 GMT.
25 October 1975.

Case 9 Barrier Effects

Shallow water areas around islands and island corner effects

The effect of sea state on reflectivity is shown in this enlarged DMSP VHR depiction off the west coast of the Baja Peninsula (Fig. 2C-25). Superimposed surface wind reports, and Guadalupe lee island effects, indicate northerly flow through the area and past Cedros Island. Note the dark gray shade indentation west of Cedros. Since the indentation is at the edge of the sunglint pattern, this suggests calmer seas in the area. Due to the northerly low-level flow in this area, however, the calmer seas would normally be expected south of the island instead of to the west, as implied by the dark gray shade indentation.

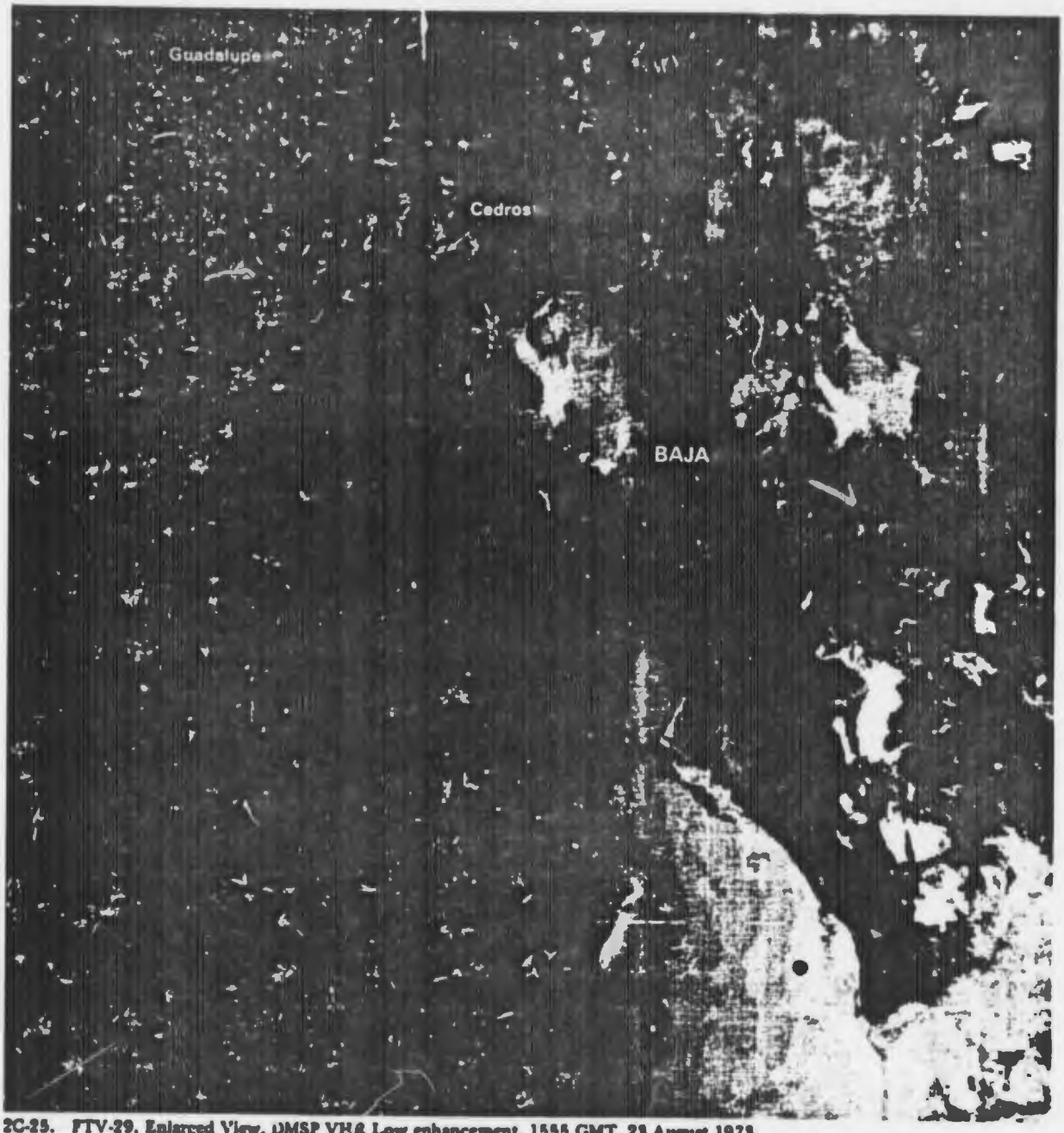

2C-25. FTV-29. Enlarged View. DMSP VHR Low enhancement. 1555 GMT. 23 August 1973. Surface Wind Reports. 1800 GMT. 23 August 1973.

A map of the region (Fig. 2C-26), reveals details which suggest a probable cause for this effect. Shallow water and a series of small islands are located in the area, immediately west of Cedros. Assuming a northerly swell, due to persistent northerly flow, the calmer seas (decreased reflectance) would occur because of the waves breaking in the shallower water areas. A wave dissipates its potential energy in the breaking process and reduced sea height results downstream.

Corner effects are apparent on the western side of Guadalupe Island, by the light gray shade tone. This gray shade, indicating increased reflectance, appears to be due to increased moisture in the form of haze droplets similar to Case 7 (Fig. 2C-20). Such an effect can be produced by air diverted around rather than over an island barrier.

2C-26. Map of Baja California with ocean depths.

Case 10 Barrier Effects

Large-scale, low-level flow patterns based on island barrier effects

Fig. 2C-27 is an enlarged DMSP VHR depiction of the Gulf of California area. Conventional surface isobaric analyses (not shown) indicated a basic northerly flow throughout the area. However, the DMSP data reveal that although the basic flow is northerly over the Pacific near Guadalupe and Cedros Islands, the flow is westerly or southeasterly over the Gulf of California. These data define a trough of major significance for short range forecasts of winds, sea state, and weather over the Gulf of California area. A streamline analysis based on the DMSP evidence is superimposed over Fig. 2C-27. The indications which provide the evidence for the streamline analysis are (1) the cloud patterns in the lee of Guadalupe Island and Cedros Island and (2) valley effects revealed by sunglint patterns and gray shade tones in the Gulf of California. Arrows point to the lee, valley, and corner effects.

Just north of La Paz, bright, cone-shaped sunglint patterns on the eastern side of two small islands relate to relatively calm seas.

Notice also that lighter gray shade and darker gray shade tones extend across the Gulf, well beyond the islands. The pattern is indicative of very stable conditions, with a pronounced low-level inversion. Under such circumstances flow tends to move quasi-horizontally around island barriers and corner effects are induced.

Some of the dark gray shade tones commence at the edge of the islands as a result of corner effects. The gray shade between the islands north of La Paz is of special interest because the dark tone begins at the passage between the islands and extends all the way across the gulf (see enlarged section of Fig. 2C-27 below). The commencement of the gray shade tone at the passage is consistent with a convergence of air in that area, resulting in higher wind speeds and an immediate roughening of the sea surface. The fact that this dark gray shade first broadens, then narrows in the middle and broadens again, suggests that not only sea state but also moisture may be involved (see Section 2B, Cases 9 and 10).

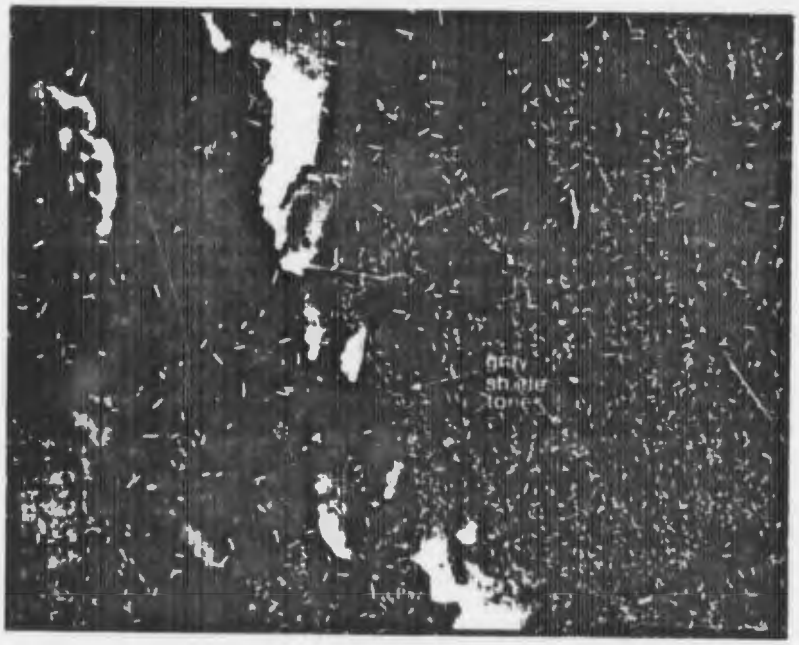

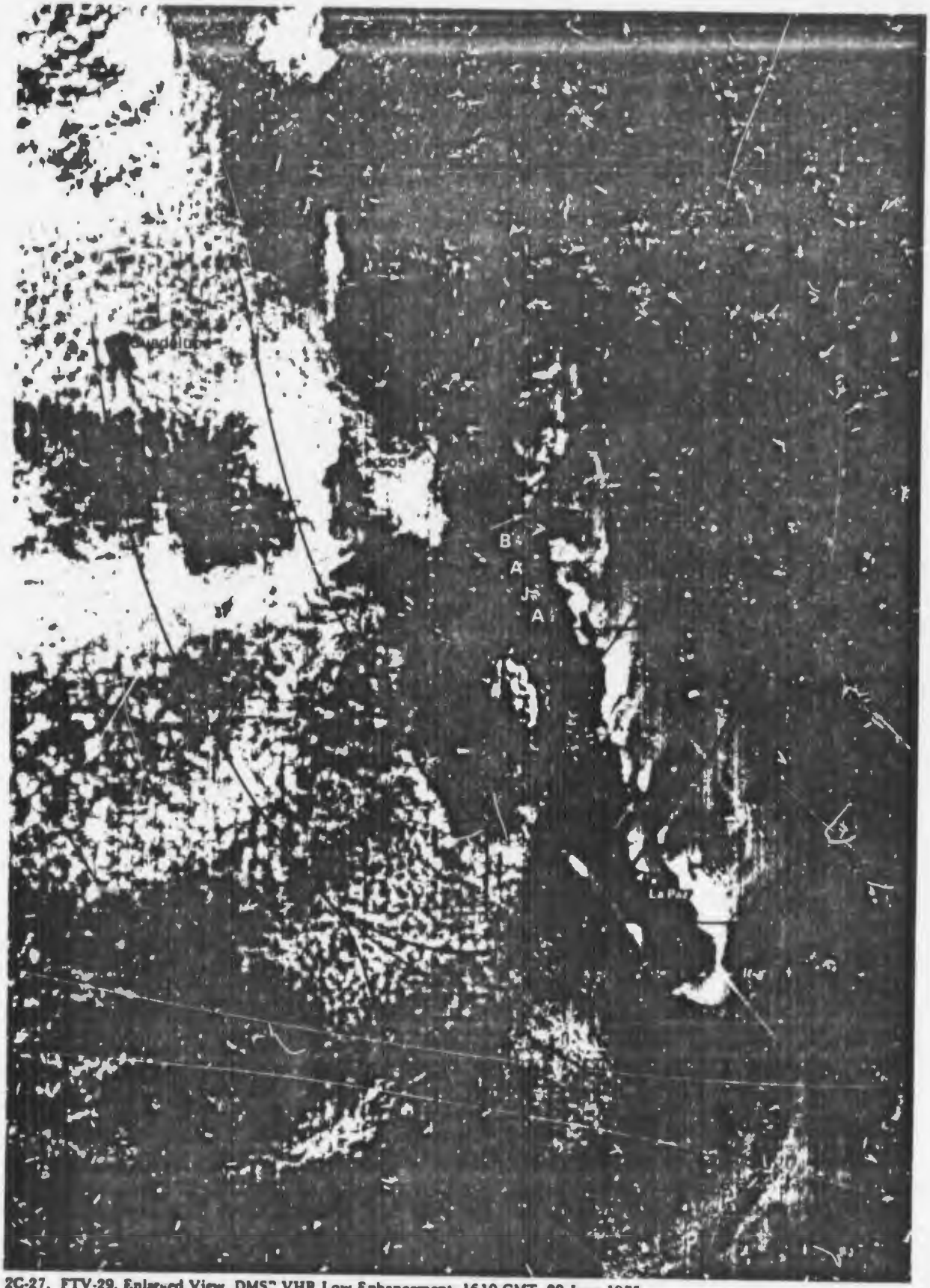

2C-27. FTV-29. Enlarged View. DMSP VHR Low Enhancement. 1610 GMT. 20 June 1975.
Streamline Analysis based on DMSP Imagery. Arrows point to the lee, valley, and corner effects.

Case 11 Barrier Effects

Variable sunglint effects in the lee of islands

In this DMSP VHR depiction (Fig. 2C-28) the satellite passed to the west of the Hawaiian Islands. The primary specular point is located north of the islands. Apparently the seas were not calm in this area otherwise brilliant reflection would be observed at the primary specular point. The Hawaiian Islands, however, do provide some blocking action to the prevailing northeasterly trades; and bright reflections, including calmer seas and possibly drier air, can be seen in the lee of Hawaii, Maui, and Molokai (Fig. 2C-29).

Oahu and Kauai are located on the western fringe of sunglint. Therefore calm, or reduced seas, in the lee of these islands should appear as a dark rather than a bright-tone gray shade. This is observed, particularly in the lee of Kauai, where a pronounced dark gray shade indentation into the sunglint pattern appears, differentiating this area from areas of rougher seas to the north and south.

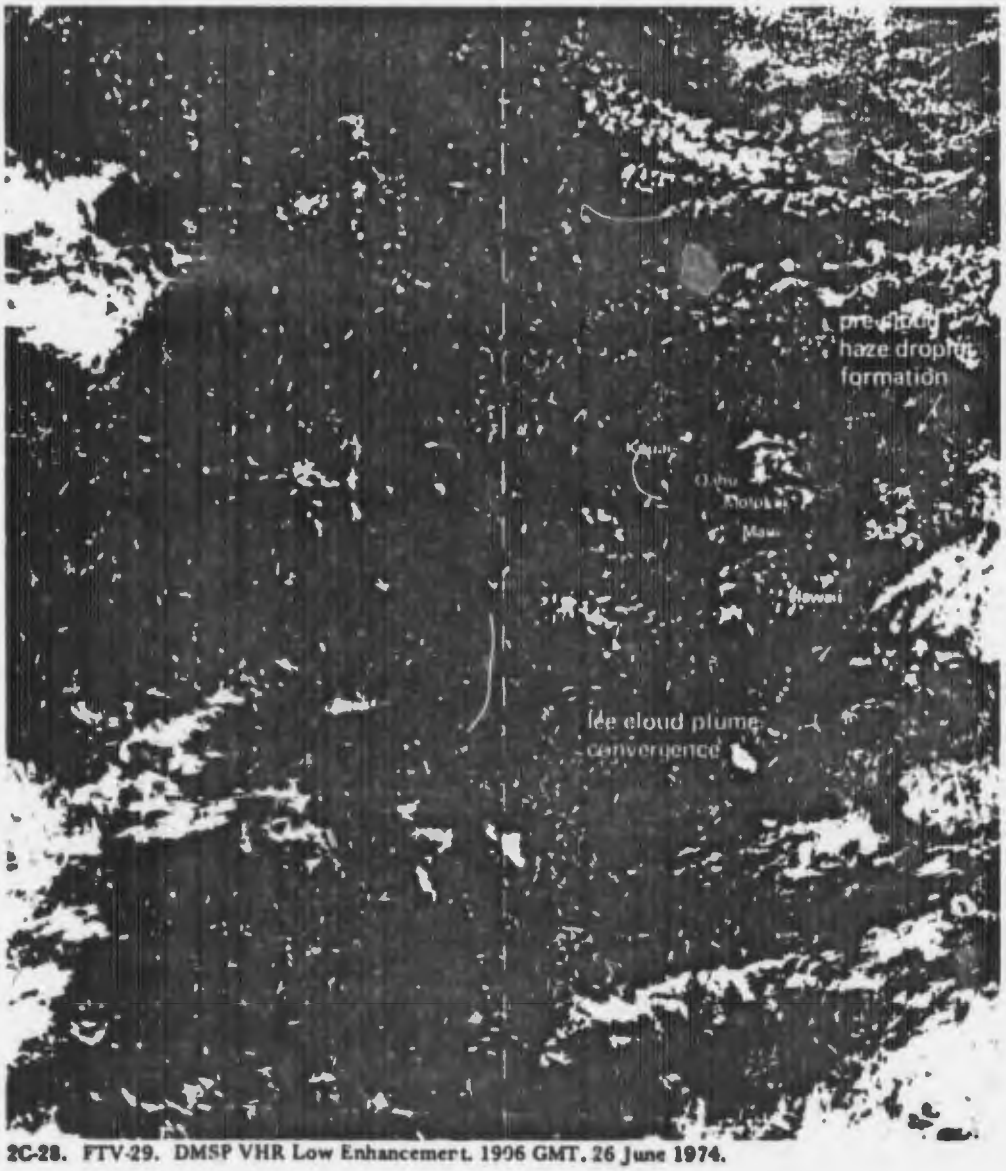

2C-28. FTV-29. DMSP VHR Low Enhancement. 1906 GMT. 26 June 1974.

In the sunglint region to the north and northeast of the islands (Fig. 2C-28), numerous middle-tone gray shade areas appear adjacent to cloud masses and in the areas between cloud groups. The fact that dark gray shades appear instead of visible clouds suggests pre-cloud or post-cloud conditions. Under these circumstances, large concentrations of condensation particles reduce transmittance in the DMSP visual mode data through diffuse reflection, scattering, and water vapor absorption. Note that the ability of the DMSP VHR sensor to detect such particles is a function of the background brightness and satellite/sun geometry. Depending upon sea state conditions and the satellite/sun geometry, these areas may appear indistinguishable, lighter, or darker than the underlying surface.

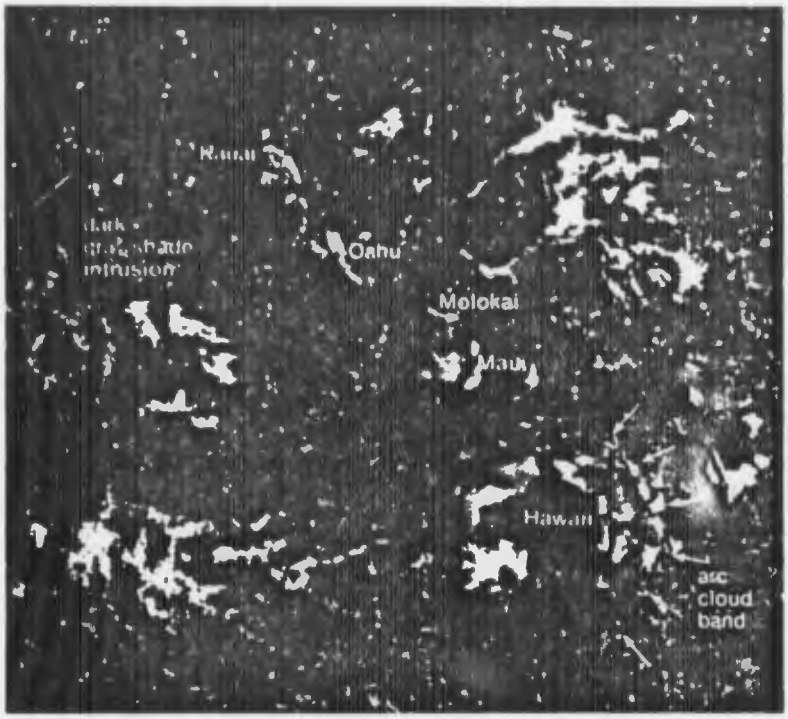

2C-29. FTV-29. Enlarged View. DMSP VHR Low Enhancement. 1906 GMT. 26 June 1974.

Note also the arc cloud band off the eastern shore of the island of Hawaii. This curved cloud band represents the convergence zone between a land breeze from Hawaii and the prevailing northeasterly trades. The time of the DMSP depiction is 0900 LST. Such convective bands are often observed until noon or later, even after the sea breeze has reversed the circulation. Fig. 2C-30 is a schematic illustrating the circulation features of this type of phenomena (Brandli, 1976). As described in the reference, the arc cloud band does not appear west of the island; as the land breeze in that area reinforces the tradewinds and no convergence zone develops.

The existence of such a cloud feature east of Hawaii indicates the tradewind flow was quite light, or its force would have overcome that of the land breeze and the mesoscale feature would not have appeared.

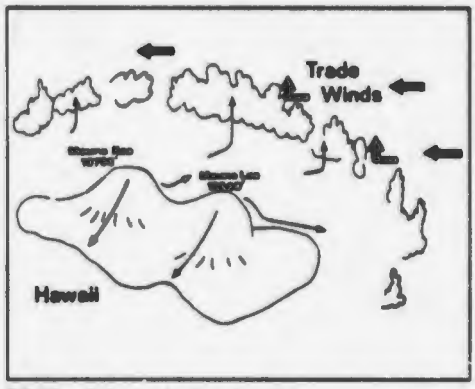

2C-30. Schematic showing the circulation features that formed the curved cloud band (arc cloud). (After Brandli, 1976).

Reference

Brandli, H.W., and J. W. Orndorff, 1976: Satellite-viewed cloud lines, anomalous or others. *Mon. Wea. Rev.*, 104, 210-213.

Synoptic analysis derived from barrier effects and interpretation of sunglint patterns

The area off the west coast of Mexico is generally a sparse data region, and preparing an accurate synoptic analysis is often difficult. This problem may be further complicated by unrepresentative surface reports. An example of this is the 1200 GMT NMC surface analysis for 23 May 1974 (Fig. 2C-31). This analysis shows a northerly divergent flow over the area. The ship report showing 65 kt winds is obviously discounted in the analysis; although this region is frequented by tropical cyclones and winds of such strength are not at all unknown to the area.

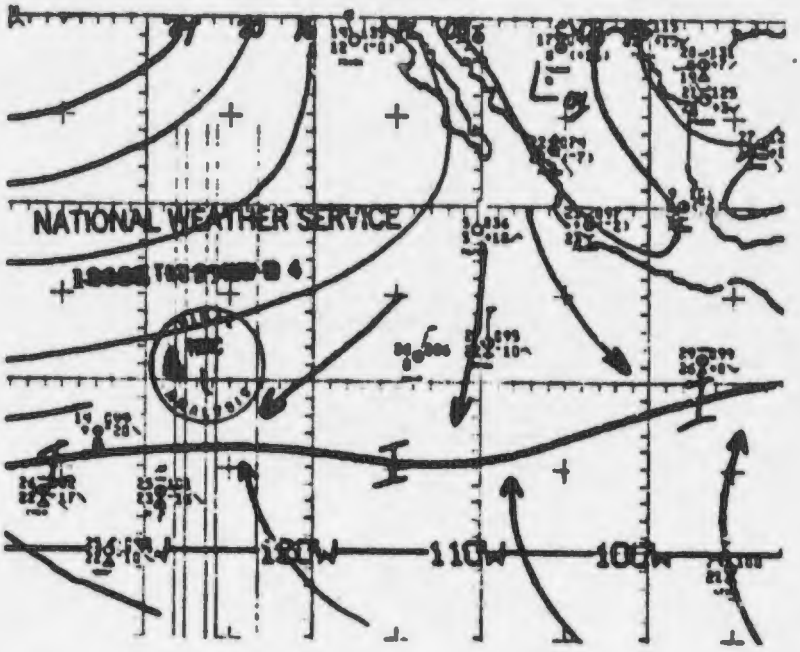

2C-31 NMC Surface Analysis, 1200 GMT. 23 May 1974.

Two successive DMSP VHR passes (Fig. 2C-32 and Fig. 2C-33) illustrate how low-level wind flow can be derived from: (1) lee clearing and cloud lines induced by island barriers, (2) changes in reflectivity induced by sea state variations in the lee of islands, and (3) changes in reflectivity induced by sea state variations in sunglint regions over the open ocean.

In Fig. 2C-32, the distinct crescent-shaped clear zones in the lee of Guadalupe and Cedros islands are obvious indicators of northerly low-level flow. Southwest of Baja, a curved north-south clear line (barrier effect) can be observed in the stratocumulus south of Clarion Island, indicating a northerly flow pattern. This is consistent with the NMC analysis over the area. This flow pattern is further substantiated on the following DMSP pass (Fig. 2C-33) with the persistence of the lee clear zones at Guadalupe and Cedros islands, and the development of a bright north-south cloud line south of Clarion.

In Fig. 2C-32, the islands of San Benedicto and Socorro have distinct gray shade areas extending east into the western edge of a sunglint pattern. These areas are reduced sea state zones in the lee of the islands produced by the blocking of the westerly low-level flow across the islands (see enlarged sections from Fig. 2C-32 and Fig. 2C-33 for a clearer view of these areas).

2C-32. FTV-29.
DMSP VHR Low Enhancement.
1555 GMT. 23 May 1974.

2C-33. FTV-31.
DMSP VHR Low Enhancement.
1831 GMT. 23 May 1974.

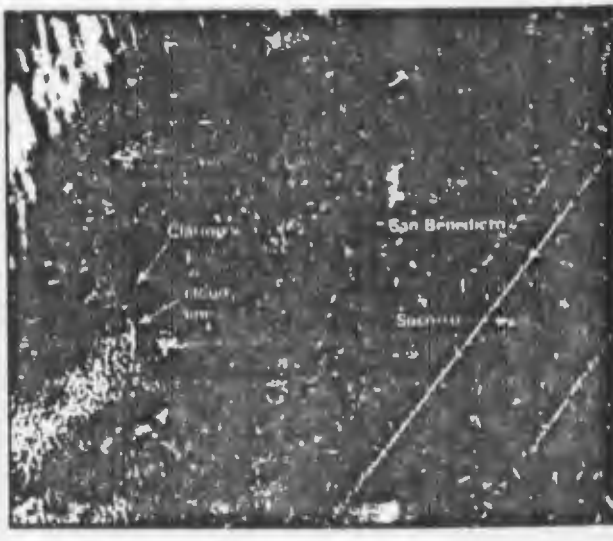

In the sunglint region observed in Fig. 2C-32, additional important details of the low-level flow pattern can be obtained. An enlarged view of this area (Fig. 2C-34) reveals that the bright, cone-shaped zones extending northeast from the Marias Islands are lee reflectivity patterns, indicating southwesterly flow in this area (as opposed to northerly flow implied by the 1200 GMT NMC analysis). To the north, southwesterly low-level flow is also suggested across the small islands along the southeastern coast of Baja by the bright reflective areas, in the sunglint region, extending northeast from the islands.

To the south, the typical sunglint pattern, indicative of a ridge-line axis, is revealed in the area of brilliant sunglint with dark zones extending east and west (Fig. 2C-32 and Fig. 2C-33).

Fig. 2C-34 also shows a bright reflective area within the sunglint region off the southeast coast of Baja, indicating calm seas. Approximately 3 hours later (Fig. 2C-35), a dark-tone on the edge of the sunglint region confirms the calm seas in this area. Note also the dark-tone patches in Fig. 2C-34 which become light-tone patches in Fig. 2C-35. These areas are heavy concentrations of cloud particles and haze droplets in a calm zone near the central portion of a sunglint region in the first DMSP pass, and at the edge of the sunglint region in the second DMSP pass. In addition, notice that the gradient of sunglint contours (Fig. 2C-32) is much stronger on the west side of the sunglint pattern than on the east side. This is also consistent with a more abrupt transition into rougher seas. This strong sunglint gradient is not as evident on the next DMSP pass (Fig. 2C-33) since the sunglint maximum is shifted eastward, highlighting instead the calmer areas.

Utilizing the barrier effects, sunglint patterns, and available wind reports, a revised streamline analysis is shown in Fig. 2C-37.

2C-34. FTV-29. Enlarged View.
DMSP VHR Low Enhancement.
1555 GMT. 23 May 1974.

2C-35. FTV-31. Enlarged View.
DMSP VHR Low Enhancement.
1831 GMT. 23 May 1974.

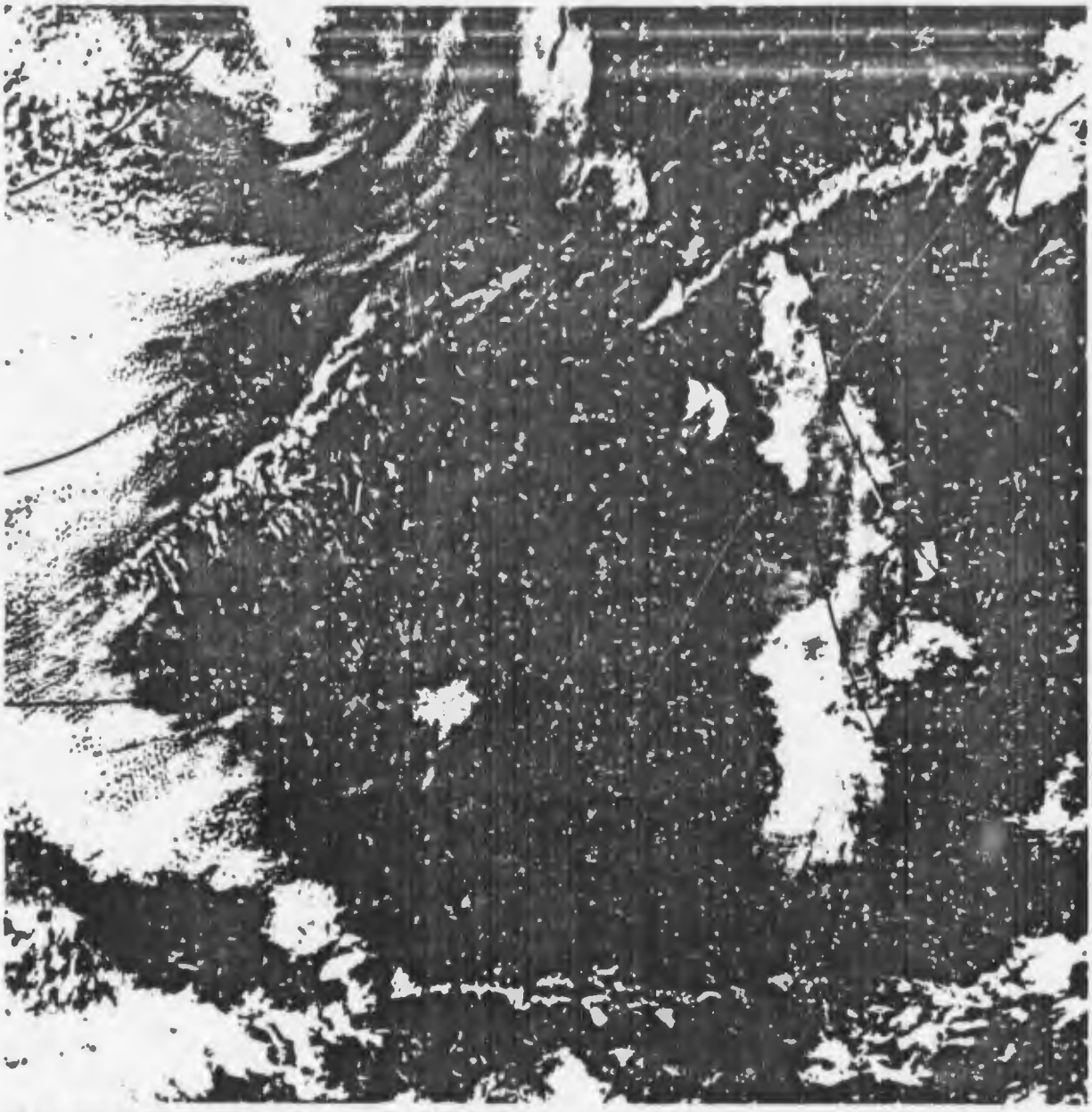

2C-36. FTV-29. DMSP VHR Low Enhancement. 1555 GMT. 23 May 1974.
NMC Surface Analysis. 1200 GMT. 23 May 1974. (Translated to DMSP Imagery).

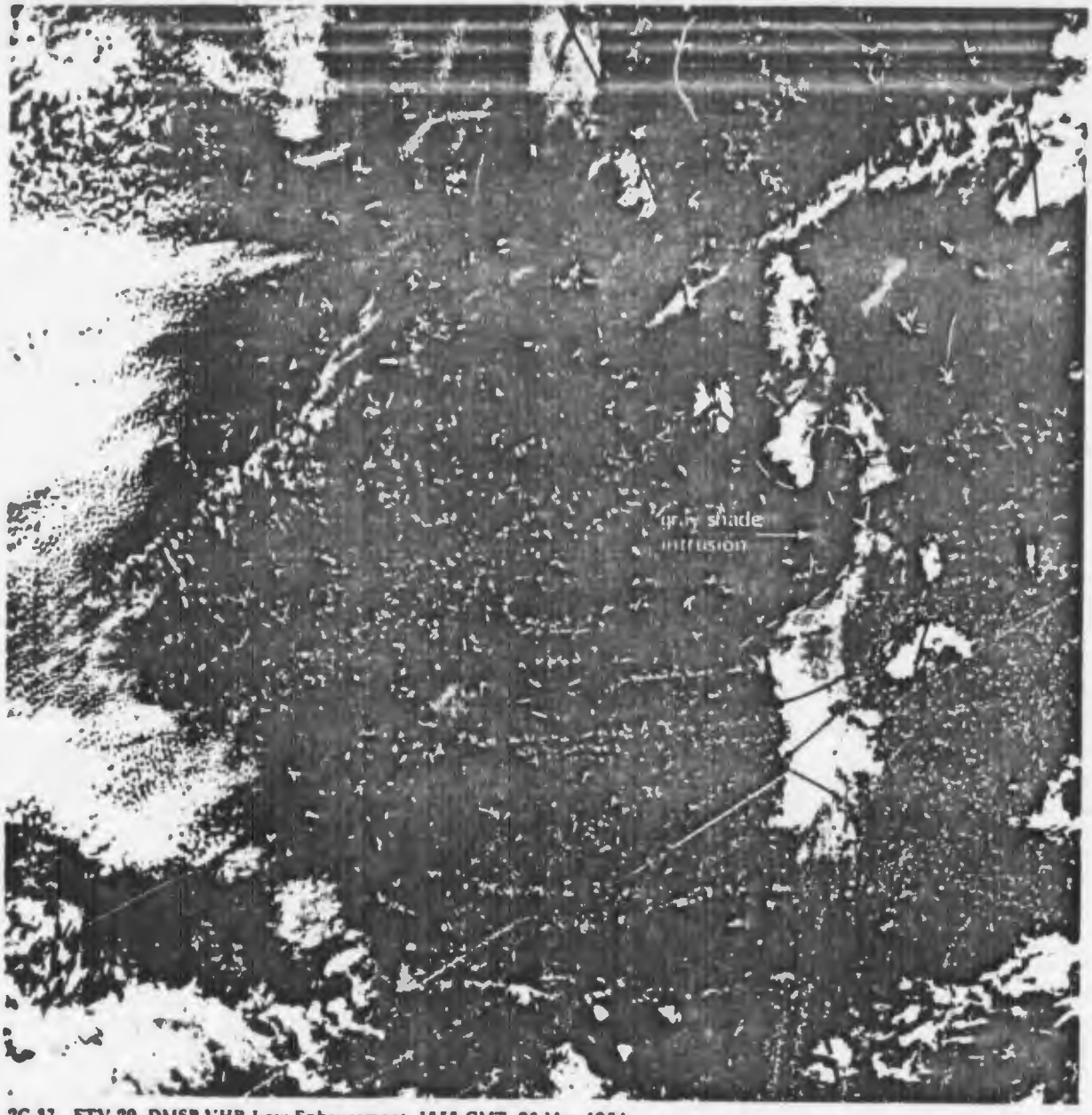

2C-37. FTV-29. DMSP VHR Low Enhancement. 1555 GMT. 23 May 1974. Revised Surface Streamline Analysis. 1200 GMT. 23 May 1974.

The analysis reveals a trough over the Gulf of California, with a ridge-line to the south, in contrast to the surface analysis prepared by NMC based on conventional reports only (Fig. 2C-36) which shows essentially, straight northerly flow over the entire area. In addition, note how well the dark gray shade intrusion into the sunglint pattern south of Baja relates to the turning of the winds in the area. This suggests that rougher seas were generated in the area, with a westerly or southwesterly direction rather than a northerly one as implied by the NMC analysis. This example illustrates: (1) that mesoscale details of wind flow and sea state can be derived from DMSP barrier effects, anomalous gray shades, and sunglint patterns; (2) the results applied in adjusting a surface analysis; and (3) the importance of image analysis for fleet tactical operations.

Synoptic analysis derived from barrier effects and interpretation of sunglint patterns

Where winds are quite light, errors in wind estimation or non-representative observations may be obtained. DMSP VHR data showing sunglint over the region in question can be useful in resolving ambiguities.

Fig. 2C-38 shows a DMSP VHR view of the west coast of the United States, Mexico, and the Gulf of California. The NMC surface analysis suggests that northerly winds are flowing over the Baja Peninsula. Surface reports appear to be ambiguous; since one ship reports a southerly wind, and a second ship, a light northwesterly wind. A closer view of the southern tip of the Baja Peninsula (Fig. 2C-39) reveals sunglint patterns which contain evidence that southwesterly winds occur over the area.

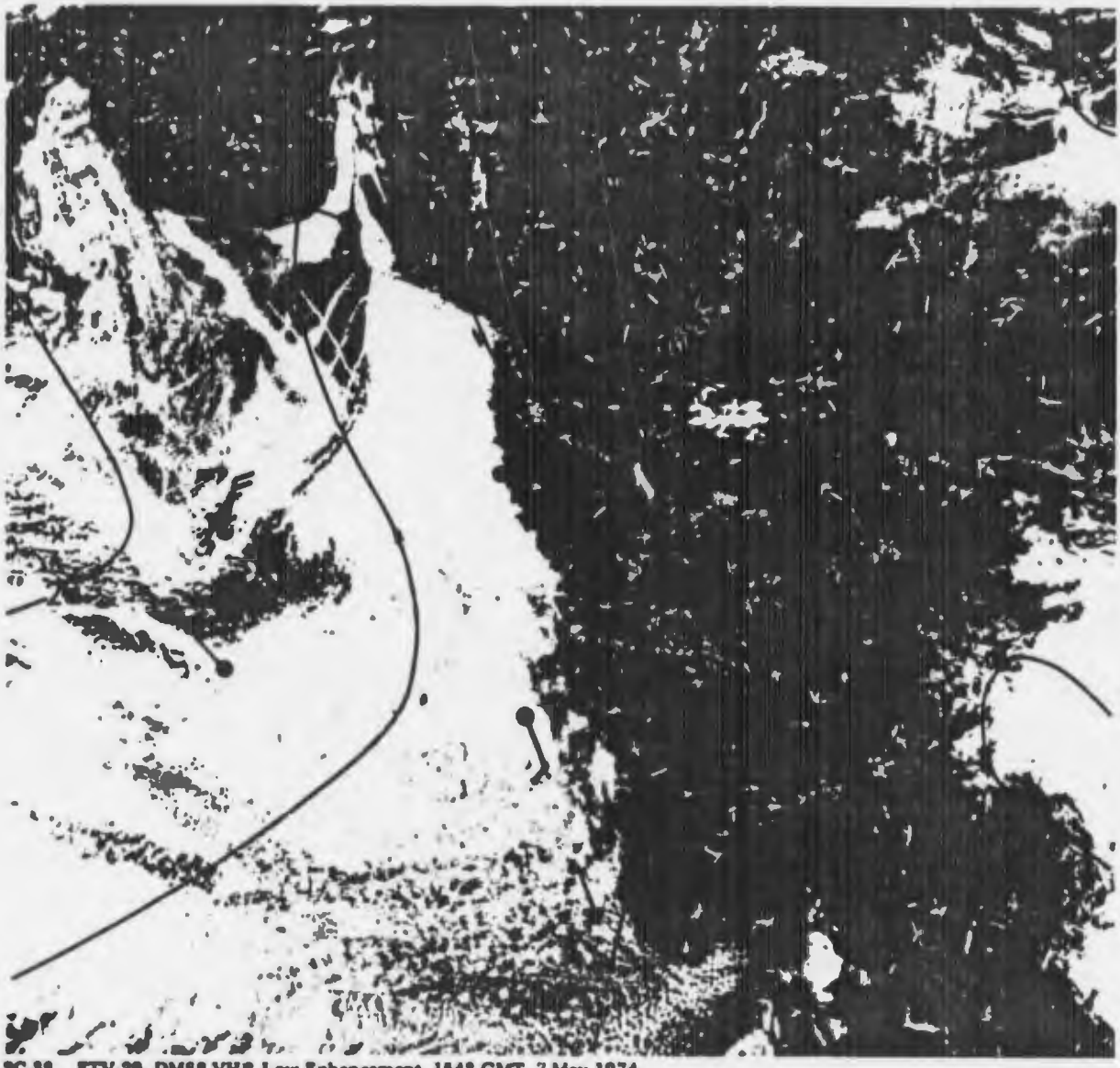

2C-38. FTV-29. DMSP VHR Low Enhancement. 1543 GMT. 7 May 1974.
NMC Surface Analysis. 1200 GMT. 7 May 1974.

The Marias Islands show lee sunglint patterns on the northeast side of the islands as a result of a southwesterly flow. The southwesterly flow apparently extends north to the southern tip of Baja, where a cloud line is oriented in the same direction.

In addition, the diverging light-tone gray shade pattern extending northeast from La Paz (Fig. 2C-40) is most reasonably explained as southwesterly wind-induced. A topographic map of this area is shown in Fig. 2C-41. Note that mountain barriers north and south of La Paz, and on the nearby islands, effectively block or restrict the southwesterly flow. There is no blockage, however, southwest of La Paz, so that southwesterly winds have an open channel through this area. The roughened sea surface, shown by the light gray shades, reflects more light to the spacecraft sensor in comparison to the adjacent calmer areas, and thereby reveals the direction of the wind. Note that these gray shade values would have been reversed had the area of specular reflection been close to La Paz; i.e., the calmer seas would have appeared bright (as over the Marias Islands) and the roughened seas dark.

Important Conclusions

1. A close examination of sunglint patterns in the lee of islands and coastal areas often reveals the direction of low-level flow because of terrain-induced blocking effects which cause changes in sea state.

2. Satellite imagery-derived direction of low-level flow in light wind areas are generally more accurate and representative than conventional observations.

2C-40. FTV-29.
Enlarged View.
DMSP VHR Low Enhancement.
1543 GMT. 7 May 1974.

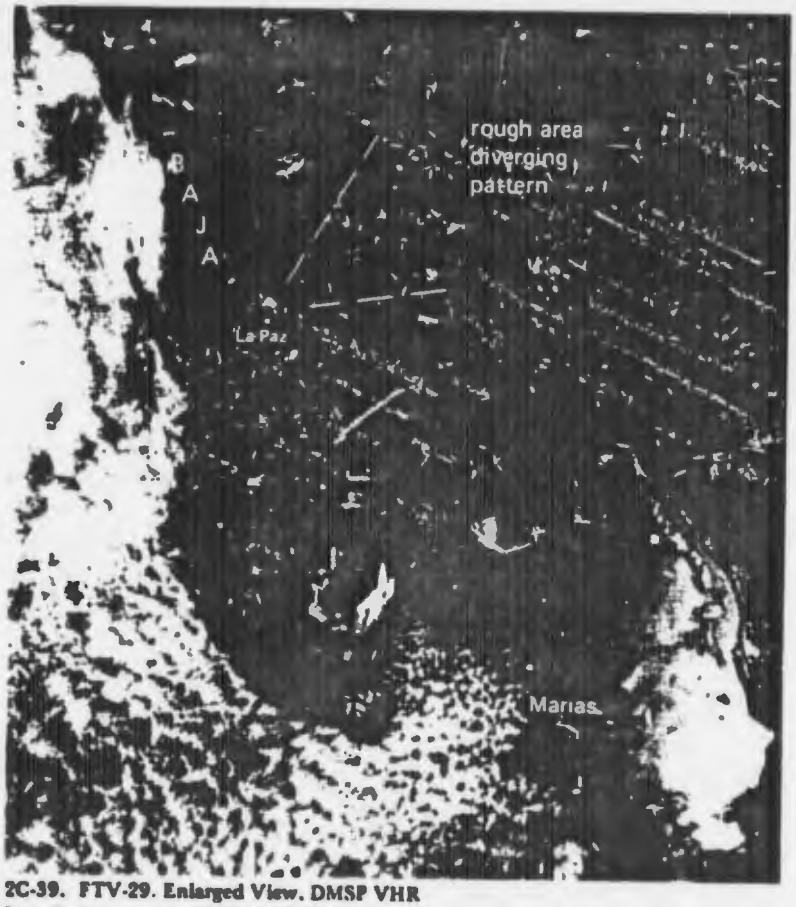

2C-39. FTV-29. Enlarged View. DMSP VHR
Low Enhancement. 1543 GMT. 7 May 1974.

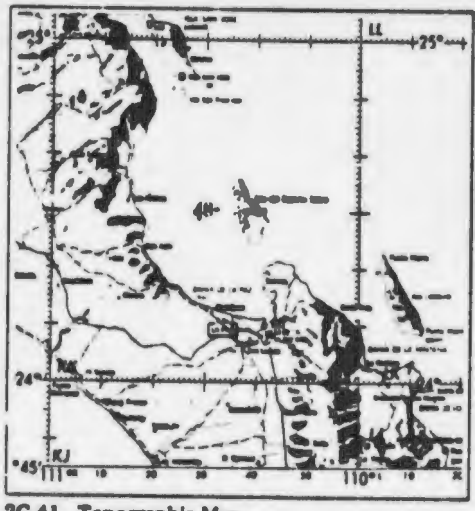

2C-41. Topographic Map.
La Paz, Baja.

Synoptic analysis derived from barrier effects and interpretation of sunglint patterns

Fig. 2C-42 is a Landsat image of the Marias Islands off the west coast of Mexico at 1702 GMT 19 June 1973, which reveals sunglint effects in the 0.5-0.6μm wavelength region (Channel 5). Surface wind reports indicate light southwesterly flow near the islands. Dark tones in the lee of the islands are interpreted to be calm areas due to the mid-morning (0902 LST) sun angle, which diverts light reflections in this area away from the Landsat sensor. The resolution of Landsat is about 100 m, so that some details of lee wave refraction and ocean eddy formation are visible. At least three distinct ocean eddies are delineated by slicks in the sunglint pattern.

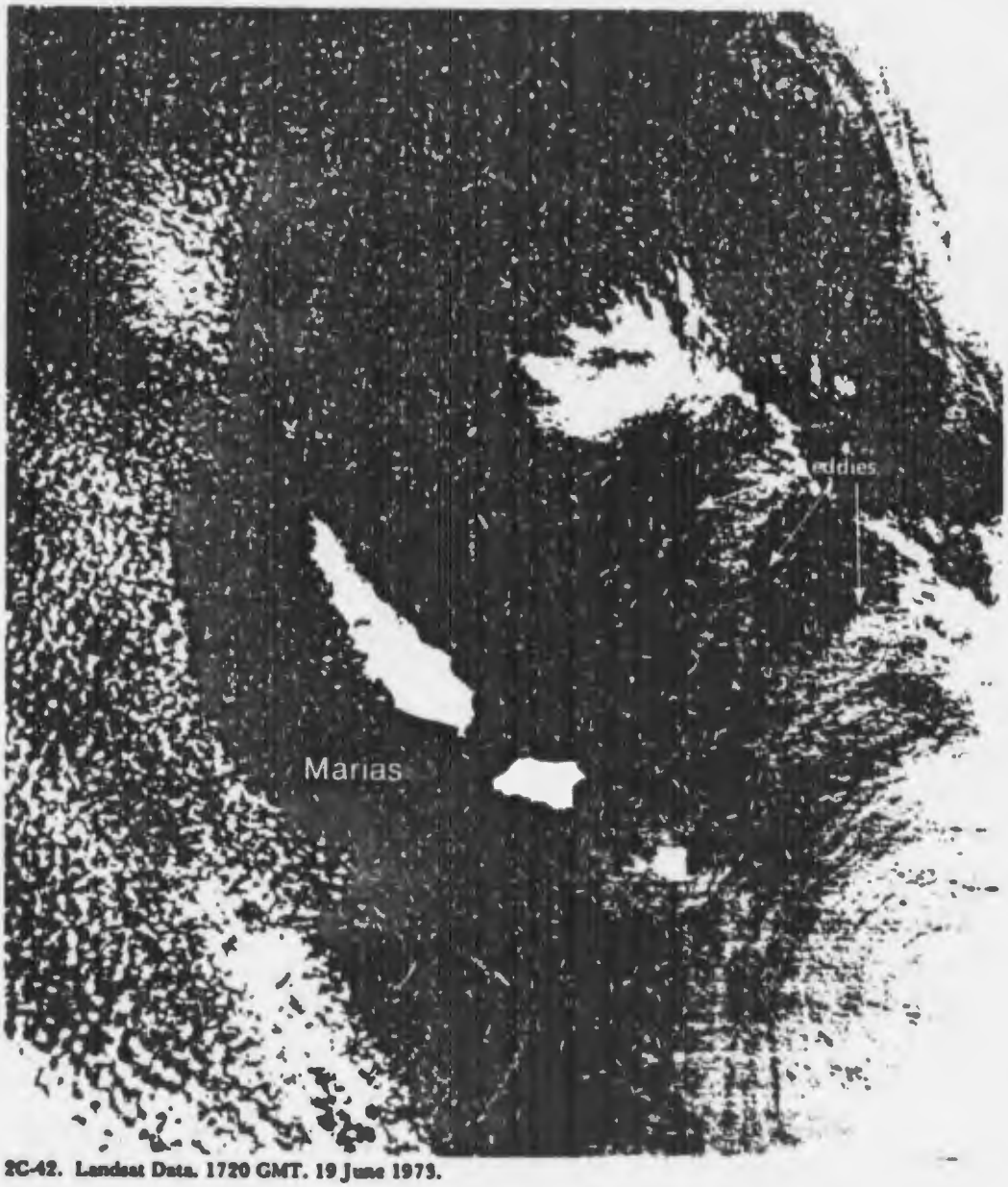

2C-42. Landsat Data. 1720 GMT. 19 June 1973.

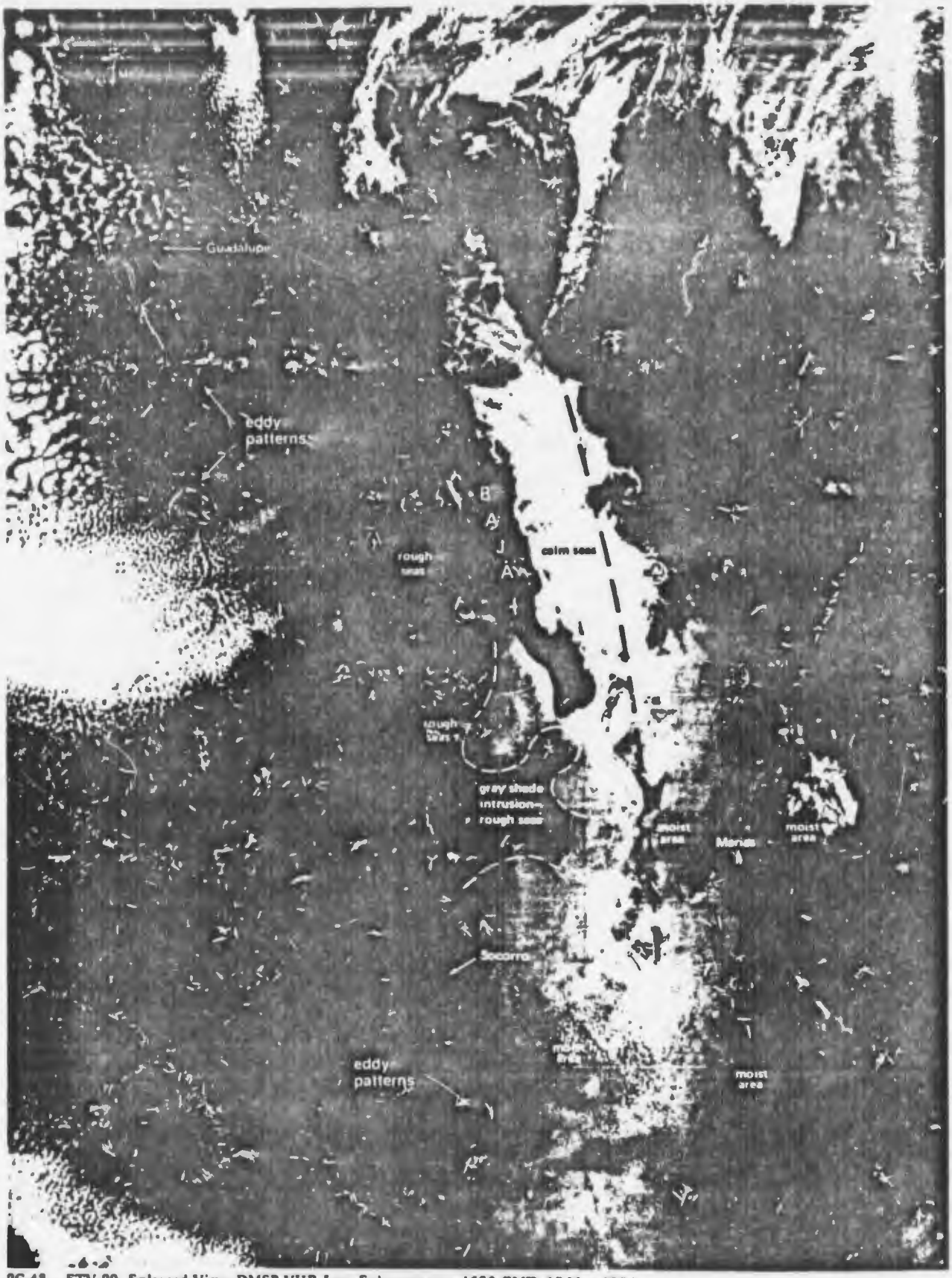

2C-43. FTV-29. Enlarged View. DMSP VHR Low Enhancement. 1630 GMT. 17 May 1974. Surface Wind Reports. 1800 GMT. 17 May 1974.

Fig. 2B-93 is an enlarged DMSP VHR depiction showing an intense sunglint pattern in the Gulf of California and south of Baja. Again, note the dark gray shade tones extending northeast of the Marias Islands. Since these islands are located on the fringe of the sunglint pattern, such gray shade tones are consistent with calmer seas in the lee of the islands and thus are excellent indicators of low-level southwesterly flow in that area, similar to the preceding view, from Landsat imagery.

Northerly flow can be deduced from cloud eddies in the lee of Guadalupe and Socorro Islands, although Socorro shows a local variation to this basic northerly flow in its surface wind report of 240° at 10 kts. Coupling these indicators with available surface reports, it is apparent that a streamline trough exists over the area with a north-south axis through the Gulf of California. Conventional surface analyses at the time of these data, and for earlier and later times, indicated no such feature. Yet the pattern is obviously not small scale, and is of importance in predicting wind and sea state over the area.

Additional information on sea state can be gleaned from noting the sunglint contour gradient on the west side of the pattern. Rougher seas along the west coast of Baja have reduced reflectivity in that area, as opposed to further south near Socorro. Note also the dark gray shade intrusion into the sunglint pattern in the area just south of Baja. Seas of 8 ft. from 300° were reported off the west coast of Baja, changing direction to 270° with heights of 5 ft. in the darker gray shade intrusion. This is an apparent indication of rougher seas being advected into the center of the sunglint pattern, possibly as a result of wind flow action around the trough which seems to be a seasonal semi-permanent regional feature. (see Cases 10 and 12).

It should be emphasized that the barrier effect and sunglint pattern interpretations are most likely to be valid when all available observations are utilized. Ambiguities of interpretation are inherent because similar gray shade tones can have completely different causes. For example, the darker gray shades in the immediate lee of the Marias Islands appear to be due to calmer seas at the edge of a sunglint pattern. Probable moisture in the form of condensation particles in the area east of the Marias, and rough seas in the central portion of the sunglint pattern, produce similar gray shades. Note, however, that the dark gray shades of small, visible cloud elements have a mottled appearance which is distinctive (see also Section 2B, Case 10). The wind, sea state, and cloud observations are most helpful in resolving ambiguities; taking into consideration geometrical aspects of each specific problem area appearing in the DMSP data.

Mountain-gap wind effects revealed by sunglint pattern variations

This DMSP VHR depiction (Fig. 2C-44) shows sunglint effects east of the Strait of Gibraltar. The primary specular point is located well to the south over Africa during this pass. Had seas been calm east of the strait, lighter-tone gray shades would have appeared throughout the sunglint area.

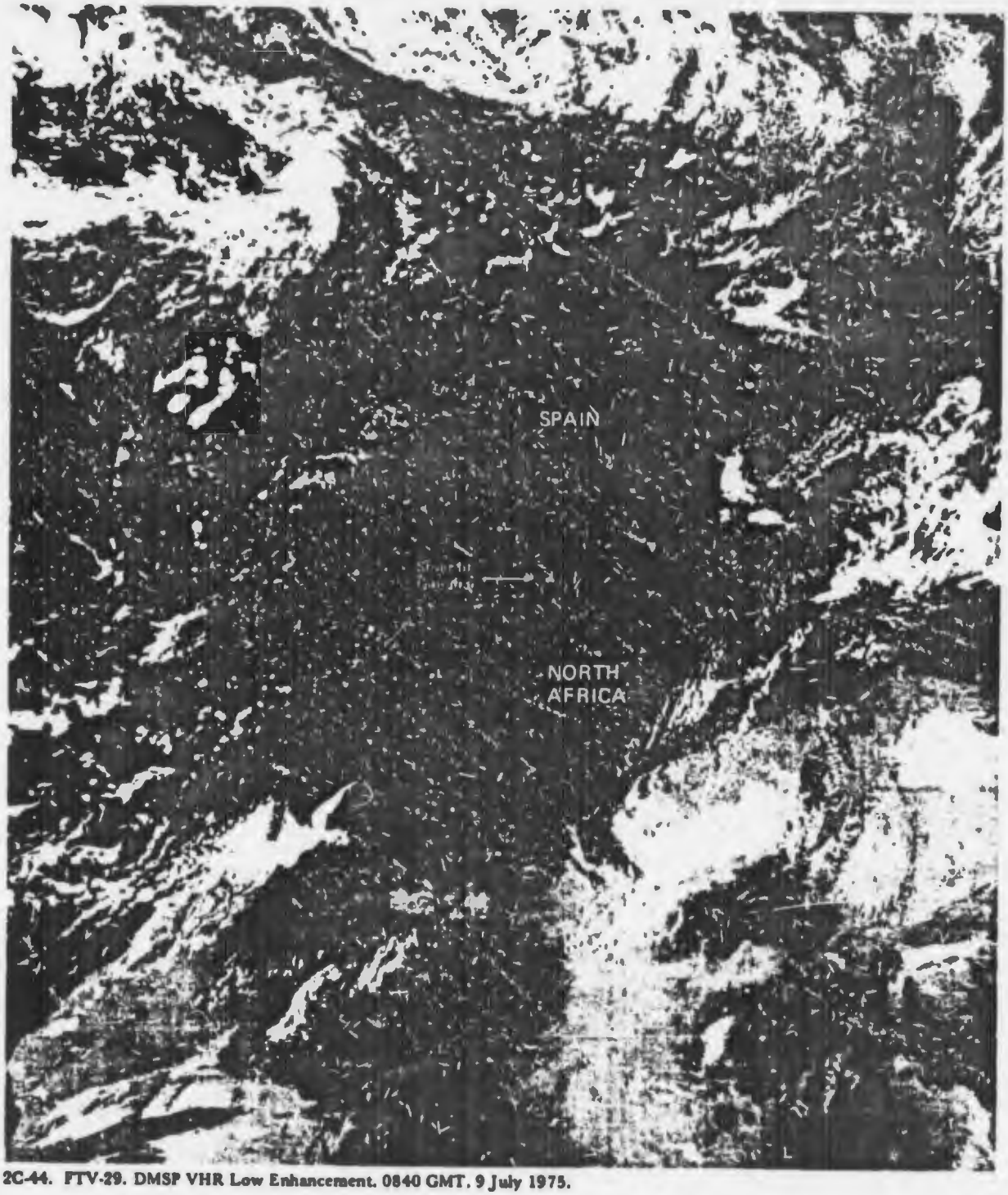

2C-44. FTV-29. DMSP VHR Low Enhancement. 0840 GMT. 9 July 1975.

In the enlarged view (Fig. 2C-45) of this area, the eastward bulge of darker gray shades east of the strait suggests a westerly mountain-gap wind effect. Such an effect would roughen the sea surface and disperse the sun glitter near the central portion of the sunglint pattern. Note that closer to the strait, at the outer fringe of the sunglint, a light gray shade tone bulges to the west. This is consistent with a roughening of the sea surface, extending the outer limits of diffuse reflection from the sun.

This figure also shows available surface wind reports. These reports verify generally light westerly flow through this portion of the Mediterranean. It is apparent that the mesoscale funneling effect, which should create stronger winds, is not reflected in these reports, although there is good agreement concerning implied direction. The sunglint contours clearly suggest stronger winds in the middle of the Mediterranean Sea between Spain and Africa, and it is quite possible that existing local reports were simply not dense enough to delineate this feature.

2C-45. FTV-29. Enlarged View. DMSP VHR Low Enhancement. 0840 GMT. 9 July 1975. Surface Wind Reports. 1200 GMT. 9 July 1975.

Wind flow analysis and mountain-gap wind effects based on interpretations of sunglint patterns

When a sunglint pattern is regular and symmetrical, a uniform sea state and atmospheric moisture condition is implied. Irregularities imply a non-uniformity of sea state, moisture, or both.

Fig. 2C-46 is a DMSP VHR depiction showing irregularities in sunglint patterns over the Ionian Sea and eastern Mediterranean. Scattered surface wind reports show light to moderate northwesterly flow (Fig. 2C-47). Such a flow is also implied by the lee reflective patterns visible southeast of Peloponnesus and southeast of Crete.

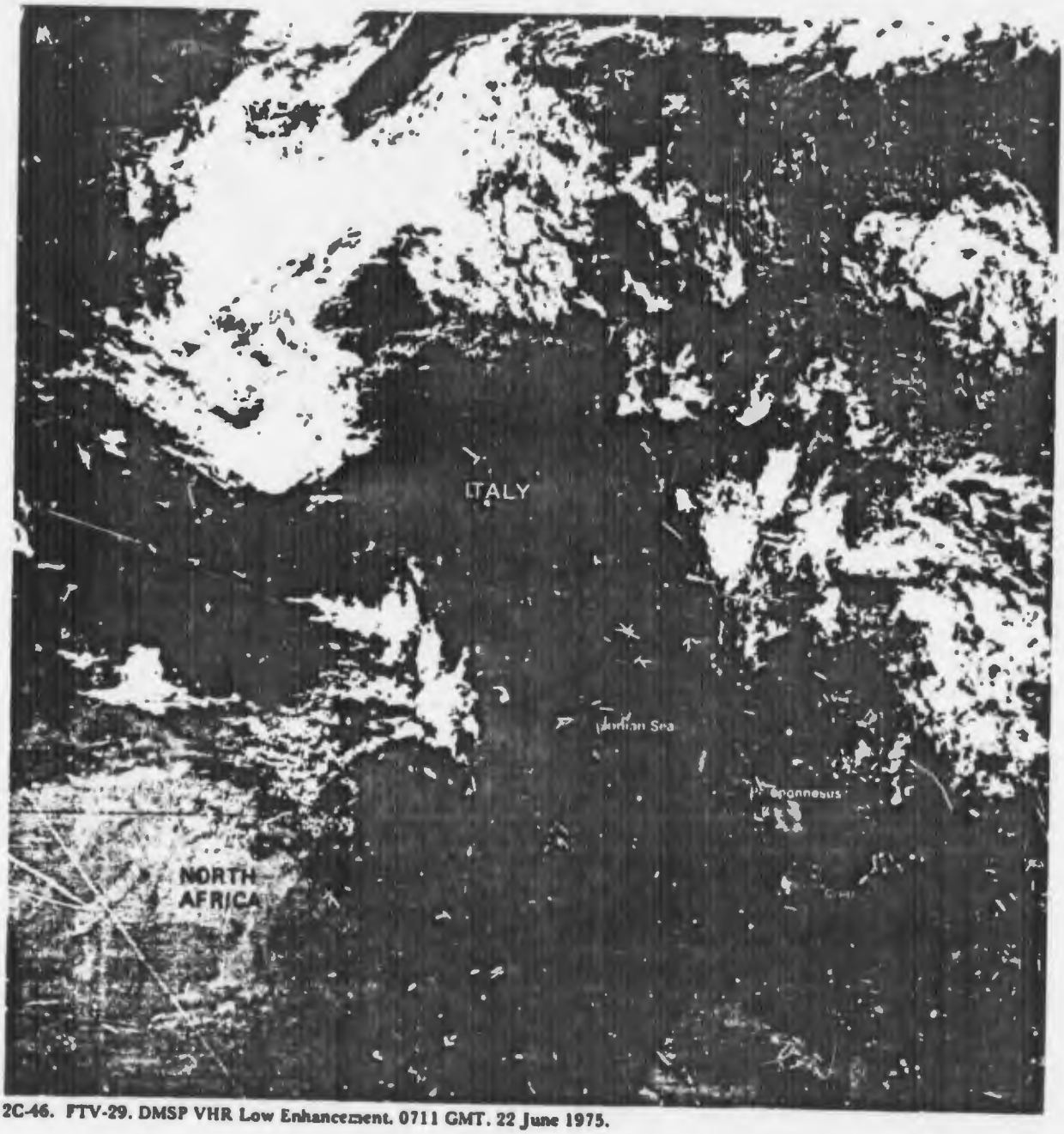

2C-46. FTV-29. DMSP VHR Low Enhancement. 0711 GMT. 22 June 1975.

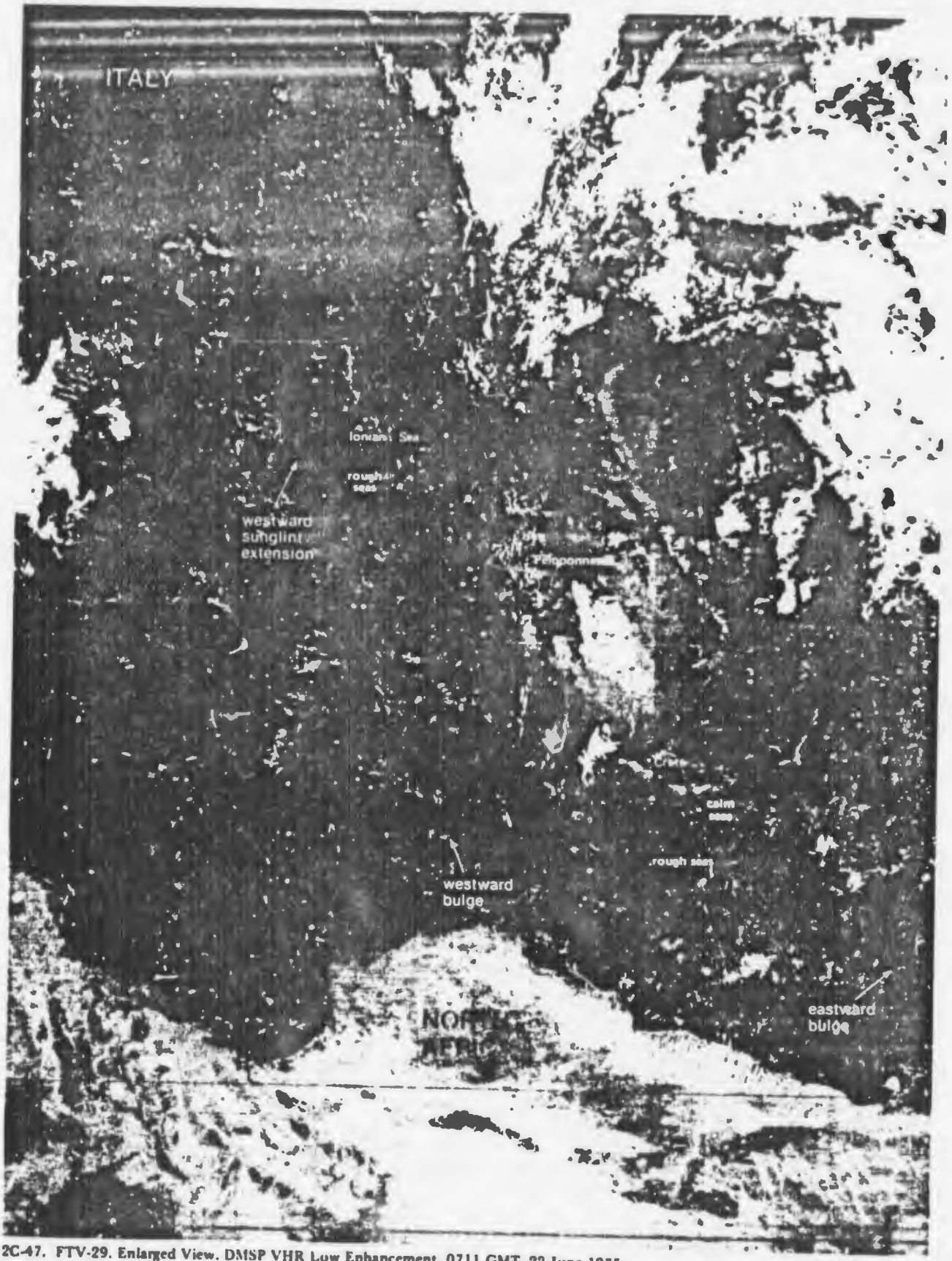

2C-47. FTV-29. Enlarged View. DMSP VHR Low Enhancement. 0711 GMT. 22 June 1975.
Surface Wind Reports. 1200 GMT. 22 June 1975.

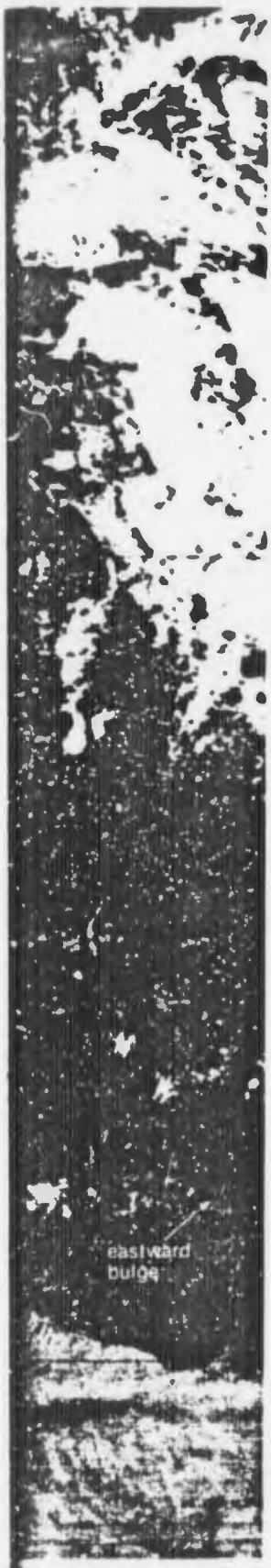

In Fig. 2C-47, note the east-west bulging of the gray shade pattern south of Crete. The axis of this pattern is parallel to the streamline flow suggested by the wind reports in the area. The intrusion of the darker gray shade tone into the central portion of the sunglint pattern, in conjunction with the available wind reports, suggests that rough seas are being advected into the area. Rough seas near the central portion of a sunglint pattern disperses the sunglint and diminishes reflectivity. The pattern is modified by barrier effects of the island of Crete and by moisture particles evident as visible clouds and gray shades extending northeast from the coast of North Africa.

Moisture particles will generally appear darker against areas of reduced sea state in sunglint. However, when sea state is increased, reflection from the sea surface is dispersed and reflection from moisture particles over the disturbed sea appears as a lighter shade of gray. It is often difficult, from DMSP VHR data alone, to separate the moisture effect from the sea state effect. In this case the westward bulge of the sunglint pattern off the North African coast, coincident with the eastward bulge, is most consistent with rough sea conditions. Rough seas at the edge of a sunglint pattern extends the limit of lighter gray shade patterns due to increased diffuse reflection.

Sunglint expansion due to rough seas at the edge of a sunglint pattern is also apparently shown in the area east of the southern tip of Italy. This particular sunglint expansion is in the lee of a valley area between mountain ranges. Winds through valley areas (mountain-gap winds) are often known to accelerate due to Venturi action. The resulting seas are much rougher in the lee of such valley areas in comparison to the areas protected by the blocking terrain. Horizontal and vertical wind shear in such areas may be severe and hazardous to low-level aircraft operations. Coastal water upwelling is commonly induced over such an area with attendant disruptions to the underwater propagation of sound. (See analogous sunglint extension through a valley in Baja California, Section 2C, Case 13.)

Important Conclusions

1. Irregularities in sunglint patterns are predominantly due to changes in sea state and/or atmospheric moisture.

2. Such irregularities are useful indicators of the low-level flow direction, associated sea state conditions, and low-level moisture distribution.

3. Winds blowing out to sea through valley areas often accelerate, producing localized lee patterns of increased sea state. Such patterns are revealed in DMSP data as light gray shade extensions of sunglint tones at the edge of a sunglint pattern.

Wind flow analysis and mountain-gap wind effects based on inter pretations of sunglint patterns

Fig. 2C-48 is a DMSP VHR depiction extending south across th South China Sea to Indonesia. Typhoon Ivy, intensity 90 kts, is locate near the China coast. This pass, acquired at 0902 LST, shows effects o sunglin. in the eastern portion. The primary specular point is located t the east of the typhoon. Applying general rules for sunglin

2C-48. FTV-29.
DMSP VHR Low Enhancement.
0102 GMT. 22 July 1974.
Surface Wind Reports.
0000 GMT. 22 July 1974.

2C-49. FTV-29.
Enlarged View.
DMSP VHR Low Enhancement.
0102 GMT. 22 July 1974.

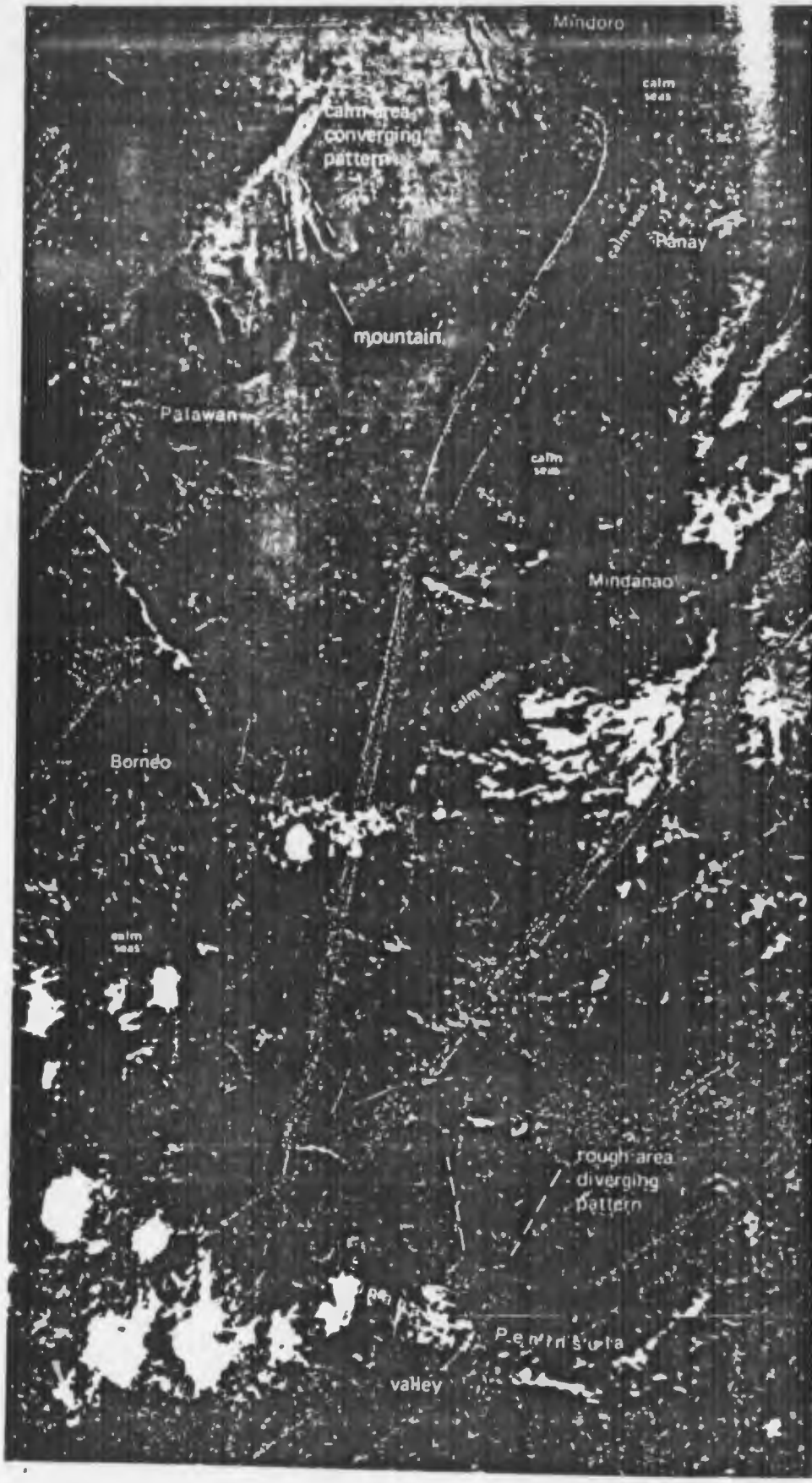

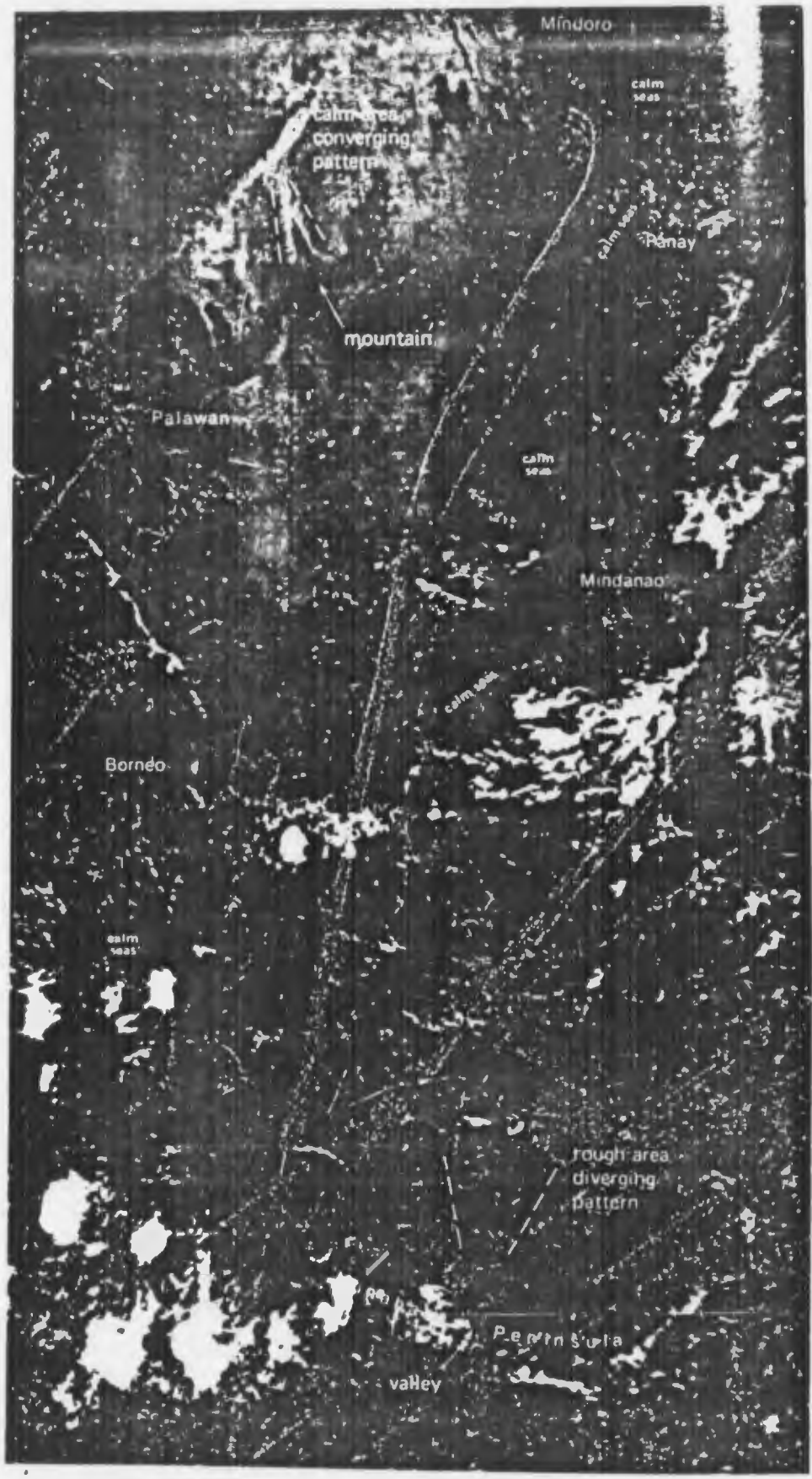

2C-49. FTV-29.
Enlarged View.
DMSP VHR Low Enhancement.
0102 GMT. 22 July 1974.

Case 18 Barrier Effects

Wind flow analysis and mountain-gap wind effects based on interpretations of sunglint patterns

This DMSP VHR depiction (Fig. 2C-51) of Southeast Asia shows sunglint effects extending south from Mindanao through the Celebes area to Timor. The primary specular point, in this early morning pass, is located on the western extremity of Mindanao.

Light southerly flow can be immediately deduced from the lee effects apparent on Timor, Celebes, Mindanao, and several smaller islands in the sunglint area, although sparse surface reports in the area indicate near calm conditions. Note the dark plume indicating rougher seas north of a major valley area on the Minahassa Peninsula. Brighter areas in the immediate lee of the Minahassa Peninsula correspond to calm areas in the lee of major mountains. To the south, at Kepulauan Sula and at Timor, tonality of calm areas changes from light to dark. This effect is due to increased distance from the primary specular point.

2C-51. FTV-29.
DMSP VHR Low Enhancement.
0500 GMT. 25 August 1974.

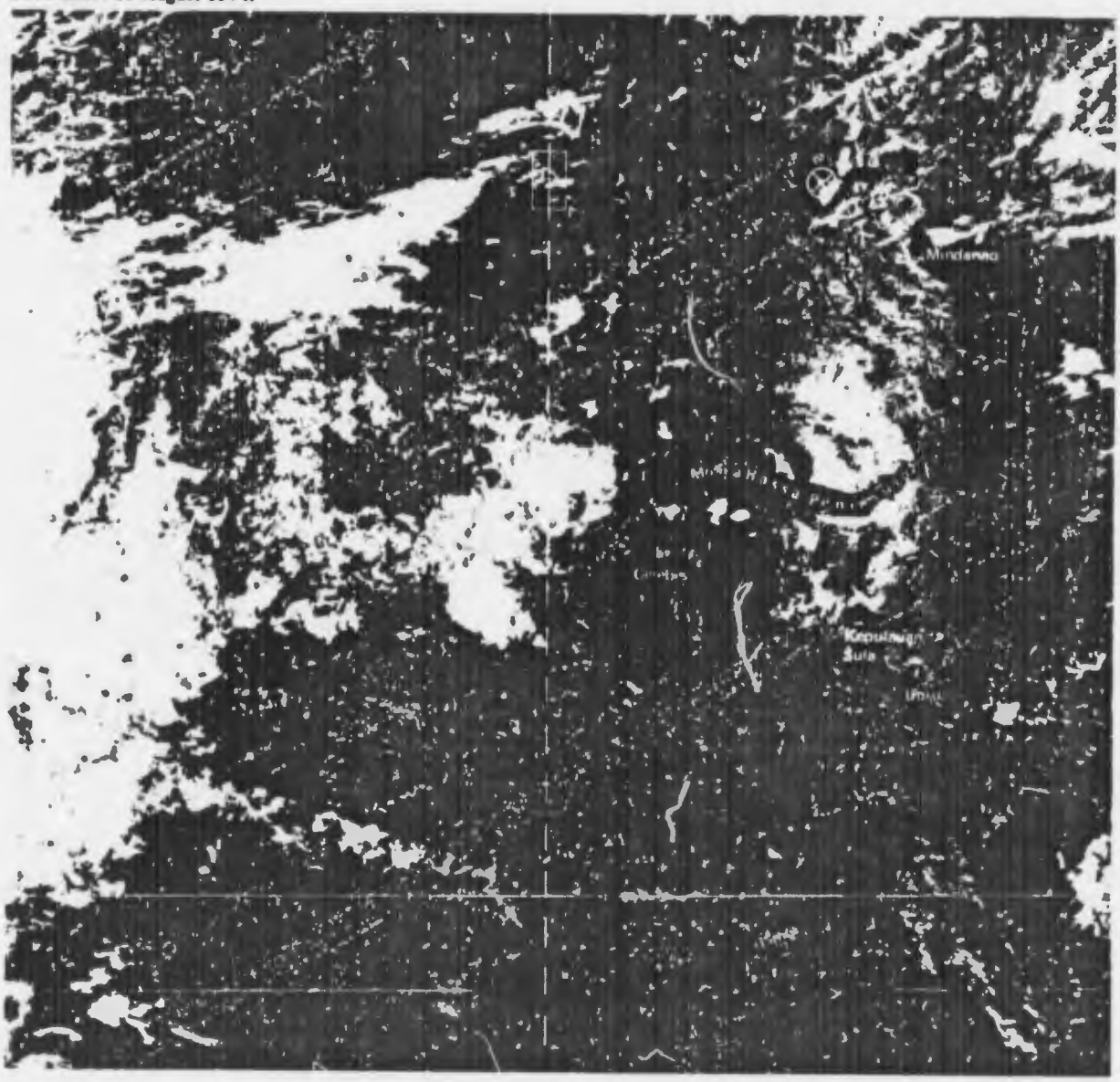

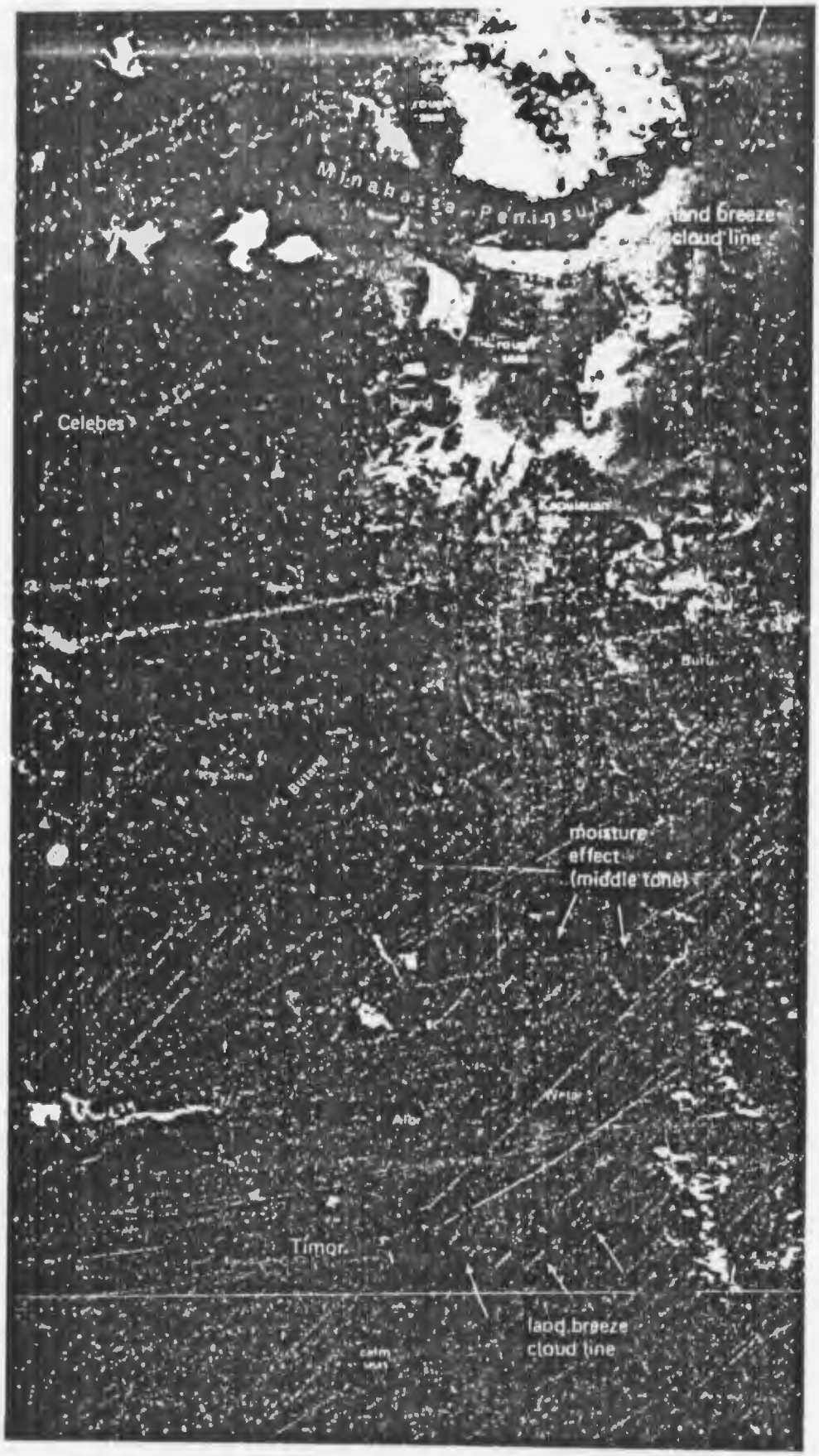

2C-52. FTV-29.
Enlarged View.
DMSP VHR Low Enhancement
0050 GMT. 25 August 1974.

observed south of the Minahassa Peninsula and Timor, the result of mesoscale effects of northerly flow from the islands converging with the prevailing southerly flow. These lines would not appear if the basic southerly flow was stronger. They are therefore very important indicators of basic current strength. Note also in this enlarged view that sea state between the land and the land-breeze convective cloud line differs from that of outlying seas, judging from the reflectivity of these seas. South of the Minahassa Peninsula, the convective cloud line separates a darker gray shade tone in the open water (indicative of rougher seas) from a lighter gray shade tone (indicative of calmer seas) in the narrow off-shore land breeze strip.

At Timor, however, the prevailing flow was apparently weaker since relatively rough seas are indicated by the lighter gray shade between the southern coast and the land-breeze convective cloud pattern. Further out to sea, the black tones indicate calm conditions over a small off-shore area. Note that this calm area is also contained on its southern extremity by another convective cloud line which separates the area from rougher seas to the south. This convective band is apparently another mesoscale effect of convergence. Such bands separating distinctive wind regimes would be expected to persist for several hours and therefore are valuable indicators for use in tactical wind and sea state forecasts.

It is important to emphasize that in the above analysis, the use of the term rough as opposed to calm, is strictly intended in a relative sense. A small increase in wind speed from calm conditions is sufficient to change the surface reflectivity of a given area.

C-52. FTV-29.
nlarged View.
MSP VHR Low Enhancement.
050 GMT. 25 August 1974.

Mountain-gap wind, sea state, and atmospheric moisture estimates from sunglint pattern analysis

The Cua Viet River forms a valley between mountains in Vietnam through which southwesterly winds frequently funnel (Fig. 2C-53). These winds, often called the "Winds of Laos", are accelerated in venturi fashion—at times reaching gale intensity (Brand and Lester, 1969). The winds cause heavy seas in a narrow strip as they move out over the South China Sea. In an opposing manner, mountain barriers of coastal Vietnam restrict the movement of such flow. Seas in the lee of the mountain barriers are relatively calm for a certain distance, depending mainly upon the strength of the flow, vertical and horizontal wind shear, and stability of the lower atmosphere. Quite frequently DMSP VHR data delineates the exact areas of rough and calm seas through sunglint effects.

In Fig. 2C-54, note that the primary specular point is inland, only a short distance from the South China Sea. Calm areas along the coast therefore reflect brilliantly in the form of cone-shaped regions. The rougher areas appear as darker shades of gray diverging outward from the coast, separating the brighter shades of gray in the calm areas. Note that in the enlarged view of this area (Fig. 2C-55), the Cua Viet Valley is precisely defined. On this date however, winds were not particularly strong, for sunglint would have been further disrupted due to high seas and, as a result, reflectance considerably more reduced.

Reference

Brand, S., and J. Lester, 1969: Wind conditions in the Cua Viet River area during the southwest monsoon. NAVWEARSCHFAC Tech. Paper No. 15-69, Naval Environmental Prediction Research Facility, Monterey, Calif., 22 pp.

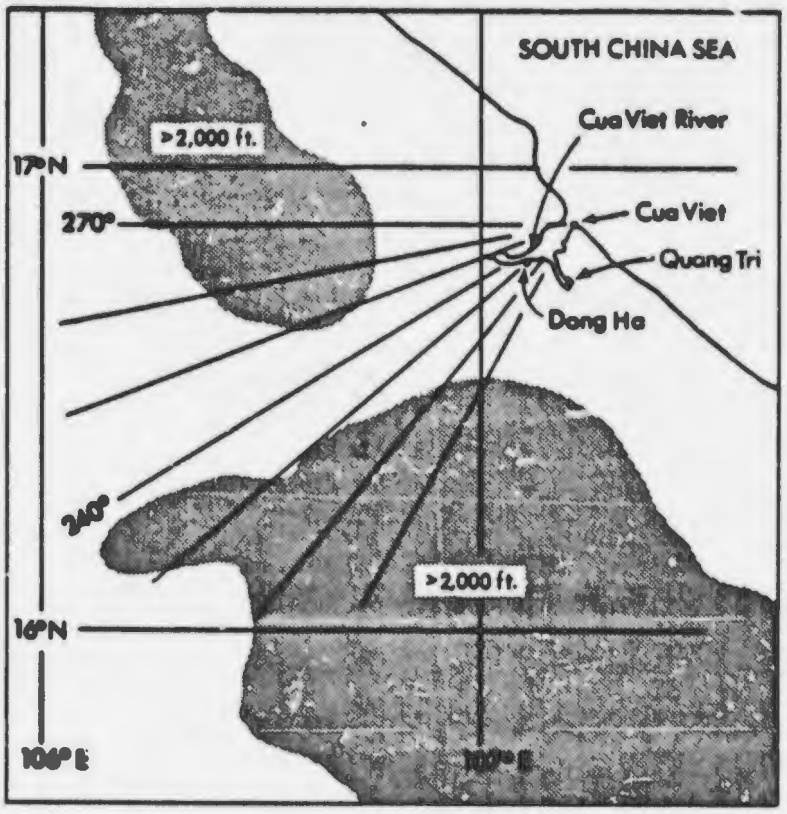

2C-53. Location Map for Cua Viet River. Valley. (Shaded region denotes terrain greater than 2000 feet). (After Brand and Lester, 1969).

Another example of the "Winds of Laos" blowing through the Cua Viet River area is shown in Fig. 2C-56. Note the darker gray shade in the lee of the valley on this date, indicative of rougher seas diffusing the sunglint to a greater extent. The protective areas have become narrower and more elongated, indicating a stable stratification of flow with little lateral mixing (Deardoff, 1976). The elongated pattern suggests weaker winds at the surface increasing rapidly with height i.e., strong vertical shear.

An important feature in the interpretation of these gray shades is that downslope motion from the Annam Mountains is producing a general drying effect on the lower atmosphere. Reduced humidity translates into increased transmittance for reflected solar rays due to decreased water vapor absorption in the near infrared, producing a light gray shade when the satellite sensor scans in the direction of the primary specular point. This effect is demonstrated in the DMSP VHR view (Fig. 2C-57) obtained on 10 August 1974. The rough coastal

2C-54. FTV-29.
DMSP VHR Low Enhancement.
0141 GMT. 31 July 1974.

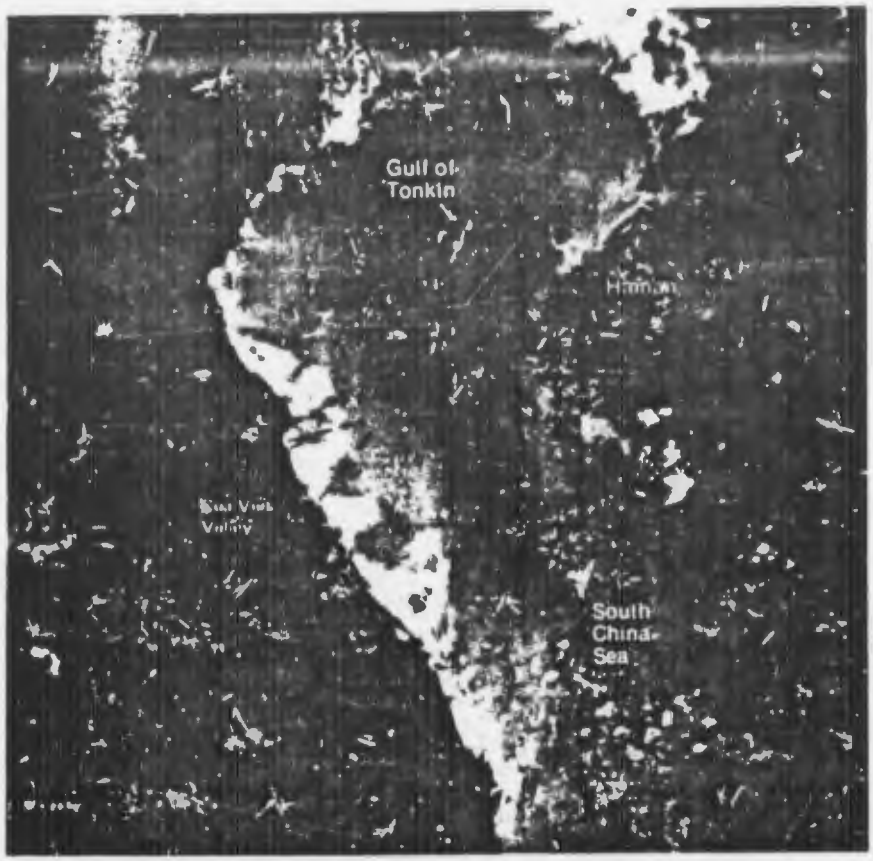

2C-55. FTV-29.
Enlarged View.
DMSP VHR
Low Enhancement.
0141 GMT.
31 July 1974.

Enhancement.
ly 1974.

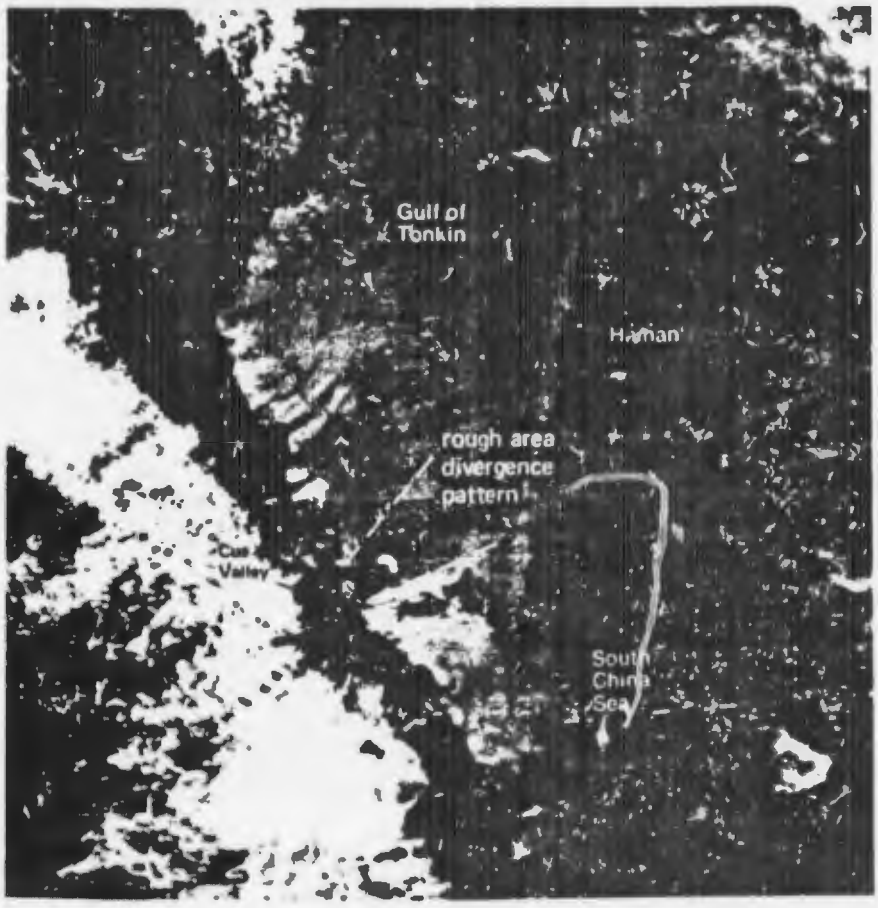

2C-56. FTV-29.
Enlarged View.
DMSP VHR
Low Enhancement.
0213 GMT.
22 August 1974.

oceanic strips in the lee of mountain gaps or river areas and the calm areas in the lee of mountains are not revealed through sunglint effects on this pass since the primary specular point is too far west (near the Gulf of Thailand). In other words, the coastal area is out of the sunglint pattern and sea state differences are not detectable. Nevertheless, a light gray shade tone extends over the South China Sea. Winds and relative humidities are shown in Fig. 2C-57. It will be noted that the driest air (78% Relative Humidity) is located in the light gray shade tone. A relative humidity of 100% is shown in the darker area immediately to the south.

Fig. 2C-58 demonstrates this effect under a different sun angle condition. In this case, the satellite track passed over the Gulf of Tonkin and the area was viewed at the edge of the sunglint pattern. The roughened sea effect to the lee of the Cua Viet Valley area is readily apparent due to increased reflectivity. (Rough seas at the edge of a sunglint pattern appears lighter.) Off-shore Vietnamese calm areas would appear black under conditions of this particular sun angle perspective. However, as has been shown in the preceding views, it is unlikely that calm seas predominate over the entire black tonal area shown in the depiction. These, again should be revealed, if present, as rather limited cone-shaped areas in the lee of the mountain barriers. Apparently, what is revealed is a combined effect of calmer seas (i.e., calmer than those in the lee of the Cua Viet Valley area) and drier air. The drier air would contribute to the dark gray shade tone through increasing transmittance of light away from the spacecraft sensor for the particular geometry of this pass.

Important Conclusions

1. Near the primary specular point, calm areas in the lee of mountain barriers appear as brilliant cone-shaped areas. Away from the primary specular point, near the center of a sunglint pattern or at the edge of sunglint, tonality of such areas reverses to dark or black gray shades.

2. Near the primary specular point, rougher seas appear as darker gray shade areas. In the lee of mountain-gaps such areas diverge in shape outward from the coastline. Away from the primary specular point, near the center of a sunglint pattern, rougher sea areas also appear darker than adjacent calmer areas. However, at the edge of sunglint, rougher sea areas appear lighter than adjacent calmer areas.

3. Dry areas near the primary specular point appear lighter in tonality. Moist areas near the primary specular point appear darker, assuming relatively slight sea state conditions contributing to a light background.

4. East of the primary specular point (for satellites with morning ascending nodes), dry areas appear as lighter tones in the direction of the sun, and as darker tones away from the sun.

5. In general, improved low-level visibilities can be anticipated in dry areas as compared to adjacent moist areas.

6. It is not always possible to ascertain the cause of a given anomalous gray shade. For example, near the primary specular point, rougher seas appear darker, but moister air also appears darker. These two aspects may act together or independently, depending upon the unique circumstances of the given event.

Reference

Deardoff, J.W., 1976: Island wind shadows observed by satellite and radar. *Bull. Amer. Meteor. Soc.*, 57, 1241-1242.

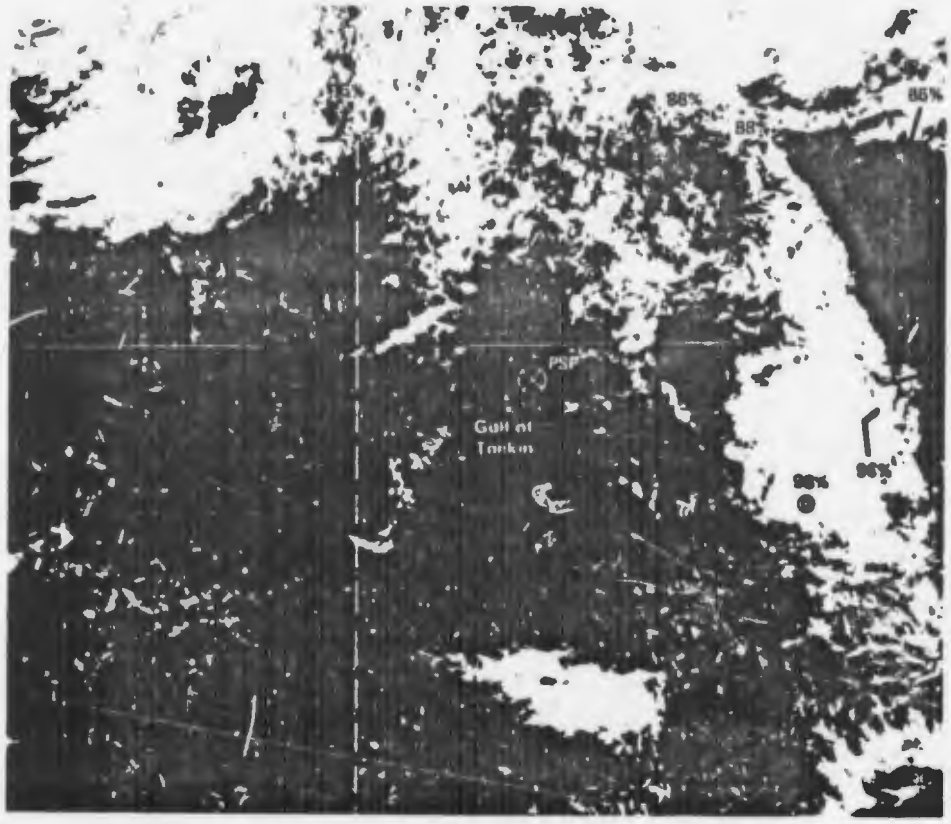

2C-57. FTV-29.
DMSP VHR Low Enhancement.
0201 GMT. 10 August 1974.

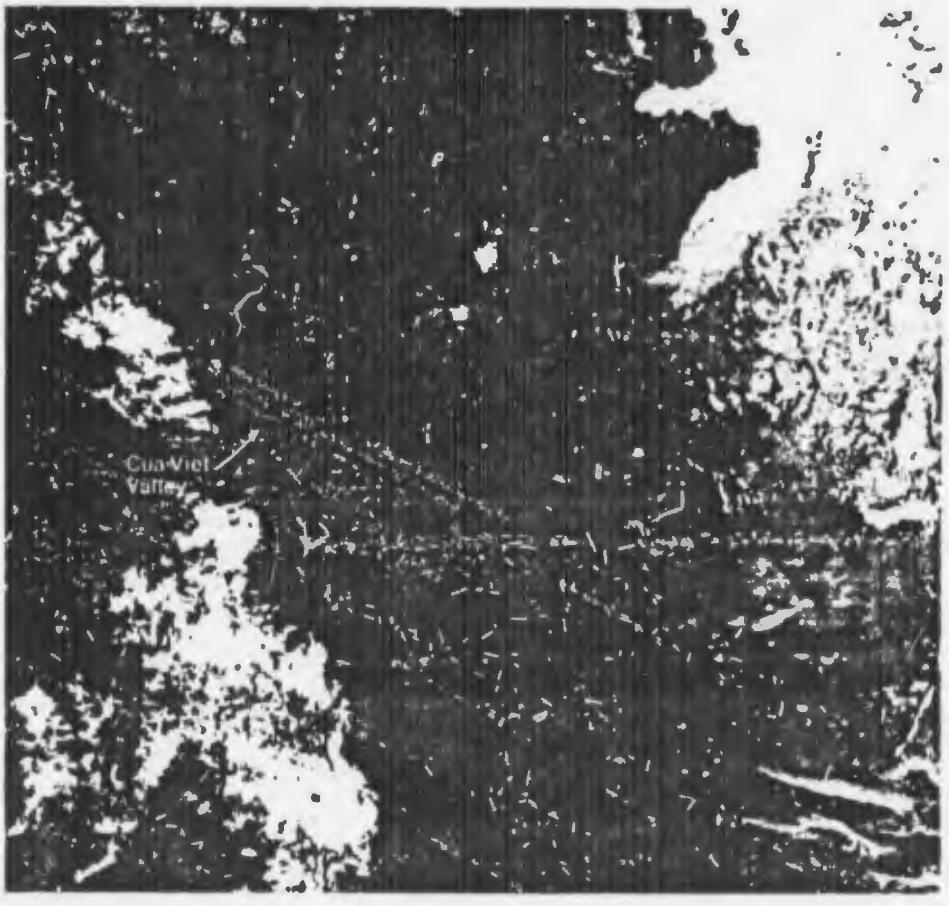

2C-58. FTV-29. Enlarged View.
DMSP VHR Low Enhancement.
0118 GMT. 10 July 1974.

aerosol/moisture effect—An optical effect of reflection, scattering, or diffraction caused by solid or solid/liquid particles suspended or dispersed within an air mass. When the particles are condensation nuclei they may occur in dry or moist form. In the latter form, as haze droplets, they are commonly observed in the DMSP visible data as anomalous gray shades.

albedo—The ratio of the amount of electromagnetic radiation reflected by a body to the amount incident upon it, commonly expressed as a percentage. Usage varies somewhat with regard to the exact wavelength interval implied in albedo figures; sometimes just the visible portion of the spectrum is considered, sometimes the totality of wavelengths in the solar spectrum. The albedo is to be distinguished from the reflectivity, which refers to one specific wavelength.[1] For the near-infrared wavelengths, in which the DMSP visible sensors have a peak response, the reflectivity from smooth ocean areas, with dry air above, is near zero. The effect serves to provide excellent contrast between these areas and adjacent moist atmospheric areas, revealed as lighter gray shade patterns due to scattering or other optical effects.

anomalous gray shade—Dark and/or light gray shade areas, patches, and streaks evident in DMSP visible data which are not identified as visible cloudiness, snow, or terrain features. Anomalous gray shades appearing in DMSP visible data can be observed in conjunction with:

a. Sunglint regions.
b. Low-level moisture fields (haze droplets, etc.).
c. Broken fields of small cumulus, stratocumulus, or alto/cirrocumulus cloud elements.
d. Cirrus cloudiness.
e. Contrails.
f. Dust storms, sand storms, smoke, and pollution.
g. Shallow ocean areas.
h. Moonglint regions.
i. Turbid or muddy water.

atmospheric scattering—The process by which incident solar radiation is deflected by small particles suspended in the atmosphere. The type of scattering is governed by the size or diameter (d) of the particle in relation to the wavelength (λ) of incident energy. Rayleigh scattering occurs when $d/\lambda < 1/10$. This type of scattering is effective for only short wavelengths since it is proportional to λ^{-4}.

The DMSP visible sensor is responsive to wavelengths extending from 0.4 to 1.1 micrometers (μm), and is responsive to Rayleigh scattering only at the low end of this spectral range. However, particle sizes necessary to provide the proper ratio of 0.1, indicated above, would have to be less than .04μm in diameter. This would imply very dry air and not the moist conditions necessary to produce anomalous gray shades as observed in DMSP visible data. Additionally, since the DMSP visible sensor has its peak response near 0.8μm, in the near IR, and responds only weakly at the low end of the spectrum (see Fig. 1A-4), it can be concluded that the DMSP visible sensor has only a very limited response to Rayleigh scattering effects.

Diffraction is a special case of scattering where the particle size (d) is on the same order of magnitude as the wavelength of incident radiation. Diffraction effects can, therefore, theoretically be observed in DMSP visible data through the complete range of particle sizes from 0.4 to 1.1μm. Diffraction effects are particularly observed in DMSP visible data in sunglint areas having heavy concentrations of haze droplets. In this case, all of the incoming sunglint is diffracted by the haze particles and none reflected back to the satellite, producing anomalous small, black gray shade areas.

For d/λ ratios greater than 1, but less than 10, Mie scattering occurs and for ratios greater than 10, ray reflection and geometric optical effects begin to occur. Moisture-produced anomalous gray shades appearing in DMSP visible data are believed to be predominantly an effect of Mie scattering and ray reflection. Mie scattering is generally concentrated in the forward direction with a minimum near 100° (as measured from the direction of the incident ray) and a secondary peak in the backward direction. Thus a moist, hazy atmosphere is generally detected as an anomalous gray shade pattern in DMSP visible data for spacecraft with morning or afternoon ascending nodes, in areas to the east and west of the satellite subpoint track. The area directly below the spacecraft with a morning or afternoon ascending node shows a minimal scattering effect and a reduced capability to produce the anomalous gray shade pattern. The schematic below illustrates this effect.

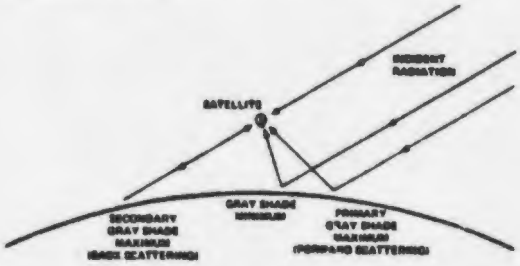

back scattering—The scattering of radiant energy into the hemisphere of space bounded by a plane normal to the direction of incident radiation and lying on the same side as the incident ray; the opposite of forward scattering.[1]

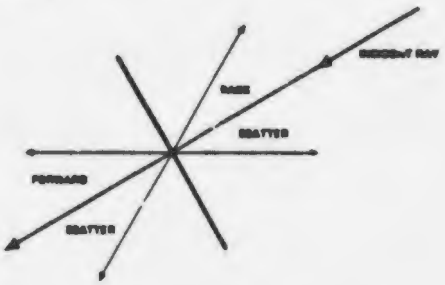

barrier effect—A blocking and turbulence-inducing effect of terrain on atmospheric flow and on ocean swell. This effect is particularly pronounced with stable atmospheric conditions under a pronounced low-level temperature inversion. In the case of a temperature inversion higher than the blocking terrain, air flowing over the terrain is subject to turbulent effects which are frequently severe enough in the case of islands, as an example, to cause downstream mixing of low-level moist air with drier air above the inversion. The drying effect downwind from the island caused by this action is frequently revealed by a distinct anomalous gray shade pattern in DMSP visible data. When the temperature inversion is pronounced and below the maximum elevation of the blocking terrain, the air flows around the barrier rather than over the barrier. In the case of

... increased pressure gradient along the sides of the island. Moisture distribution again can be affected, because of the convergent flow, producing anomalous gray shades. In addition, increased sea state, caused by the increased winds, may also influence the reflectivity near the sides of an island, resulting in the production of anomalous gray shades in the DMSP visible data.

blackbody—A hypothetical "body" which absorbs all of the electromagnetic radiation striking it; that is, one which neither reflects nor transmits any of the incident radiation. In accordance with Kirchoff's law, a black body not only absorbs all wavelengths, but emits at all wavelengths and does so with maximum possible intensity for any given temperature. Kirchoff's law shows "that if a body emits radiation of a given wavelength at a given temperature, it will absorb radiation of the same wavelength at that temperature."[2]

corner effect—See barrier effect.

drying effect—See barrier effect.

equatorial orbit—An orbit about the earth (or other planet) whose plane is coincident with the equatorial plane. The GOES spacecraft orbits in the equatorial plane but is launched at an altitude (with a corresponding period) such that it remains essentially stationary over a given geographical point above the equator—thus the term geo-(earth) stationary.

geostationary satellite—See equatorial orbit.

gnomonic projection—A map projection in which any straight line drawn connecting two points on the projection corresponds to a segment of a great circle arc on the earth's surface.

gravity wave—A wave disturbance in which buoyancy acts as the restoring force on parcels displaced from hydrostatic equilibrium. Gravity waves in DMSP data are frequently observed as wave-like cloud formations along vertical temperature inversion surfaces over oceanic regions.

great circle arc—A line segment formed by the intersection of the surface of the earth and a plane passing through the center of the earth.

HR—DMSP high resolution (2nm) visible data. Nighttime data can be acquired from the HR sensor under illuminations as low as 1/4 moon. When the lunar phase is 1/2 moon or greater, visible data have the same clarity as data obtained in sunglint.[3] There is one DMSP HR scan to every six DMSP VHR scans.

infrared data—DMSP data sensed in the 8-13 micrometer (μm) region of the electromagnetic spectrum.

infrared radiation/spectrum—Electromagnetic radiation in the wavelength interval from about 0.8 micrometers (μm) to an indefinite upper boundary sometimes arbitrarily set at 1000μm. There are two infrared "windows" in the atmosphere, that is wavelength bands where the atmosphere is nearly transparent to infrared radiation. These bands are centered at approximately 4 and 11μm. The DMSP IR sensor bridges the latter band in its extension from 8-13μm.

IR—Infrared (IR). See above.

Karman vortice—In the flow of wind past an island barrier, under conditions of a low-level inversion, cloud vortices are frequently generated to the lee of the island. vortices bear the name of the mathematician Von Karman, who first described their characteristics.

Landsat (ERTS)—A sun-synchronous polar orbiting satellite carrying two types of imaging sensors, the Multi-Spectral Scanner Subsystem (MSS) and the Return Beam Vidicon (RBV) cameras.

The Multi-Spectral Scanner (MSS) is a line-scanning device which uses an oscillating mirror to simultaneously scan the terrain passing beneath the spacecraft. The scanner produces four synchronous images, each at a different wave band. The wave length ranges of each band are:

Band 4 (green)	0.5 to 0.6μm
Band 5 (lower red)	0.6 to 0.7μm
Band 6 (upper red-lower infrared)	0.7 to 0.8μm
Band 7 (near infrared)	0.8 to 1.1μm

Band 4 sometimes discriminates, qualitatively, the depth and/or turbidity of standing bodies of water. Band 5 is best for showing topographic and cultural features, such as drainage patterns, roads, and cities. Band 6 also shows the best tonal contrasts that reflect various land use practices. It also gives maximum land-water contrast. Band 7 is the best for land-water discrimination.

The Return Beam Vidicon cameras are television camers mounted side by side in the spacecraft and bore-sighted to simultaneously photograph the earth beneath the spacecraft. The wave length ranges of each band are:

Band 1 (green)	.460 to .600 μm
Band 2 (red)	.569 to .680 μm
Band 3 (near infrared)	.650 to .820 μm

Landsat MSS data are of a much higher resolution than DMSP data (about 80m as opposed to 600m). For this reason, combined with the multi-spectral capability, comparisons of simultaneous Landsat/DMSP views are often useful in resolving ambiguities in DMSP data interpretation.

line-scan radiometer—The radiometer which senses reflected and emitted radiant energy from the earth and clouds along a line stretching from horizon to horizon perpendicular to the satellite subpoint track. The VHR/WHR line-scan radiometer of the DMSP system receives energy from a mirror mounted on a shaft oriented 45° to the direction of satellite motion. The shaft revolves at 534 Hertz (cycles per second). The mirror is double-faced so that two horizon to horizon scans are made for each shaft revolution of the earth scene. This scan rate, combined with a 0.766 milliradian field of view, gives a spatial resolution of 0.33 nm at subpoint.[3]

MI—The lower resolution infrared data obtained from the DMSP (Block 5C) system. The MI is the complementary system of the HR/MI scanner. This scanner is driven by a 3:1 reduction gear from the VHR/WHR shaft and revolves at 1.78 Hertz. Since this mirror is single-faced and rotates at one-third the speed of the VHR/WHR mirror, only one-sixth the number of scan lines are produced. This scan rate combined with a 4.56 milliradian field of view, provides 2.0 nm resolution visual data (HR) at subpoint. The MI detector has a 5.33 milliradian field of view which yields 2.4 nm resolution infrared data.[3]

nadir—The point on a given observer's celestial sphere diametrically opposite his zenith, that is, directly below him.[1] The nadir angle of the DMSP imaging system is essentially zero at satellite subpoint, meaning that there is no pitch error (nominally) to this system, and that the scanner continually scans across the

satellite subpoint as it progresses in its orbit. Important satellite viewing angle relationships are illustrated in the diagram below.

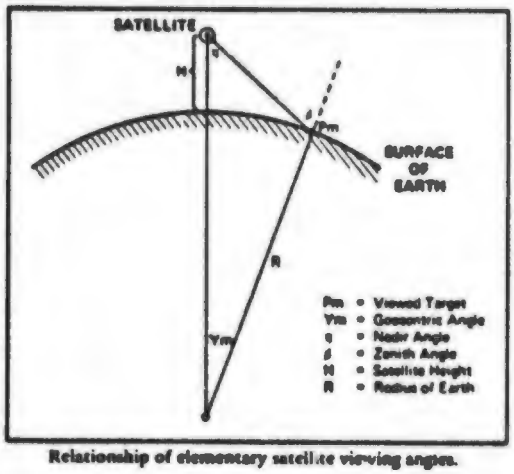

Relationship of elementary satellite viewing angles.

near infrared—That portion of the electromagnetic spectrum covering wavelengths from 0.7-1.5 micrometers (μm). The upper region of the DMSP visible sensor response extends into this range, which is beyond the response or sensitivity of the human eye.

node—One of the two points of intersection of the orbit of a satellite with the plane of the equator of the earth. In satellite meteorology, the ascending node of equator crossing refers to that point on the plane of the equator at which the satellite crosses from the Southern to the Northern Hemisphere. The descending node of equator crossing denotes that point at which the satellite crosses the plane of the equator from the Northern to the Southern Hemisphere.

non-specular light—Non-specular reflection is diffuse sunglint received at the satellite from wave facets of non-calm seas outside the primary specular point which provide the proper reflective geometry.

polar orbiting satellite—A satellite whose orbit lies in a plane passing through the center of the earth and is inclined to the equatorial plane so that the subpoint track traverses polar latitudes on every orbit. The DMSP satellite is a polar orbiting spacecraft in an orbit inclined to 98.7° to the equatorial plane where the spacecraft crosses the equator northbound (see diagram below).

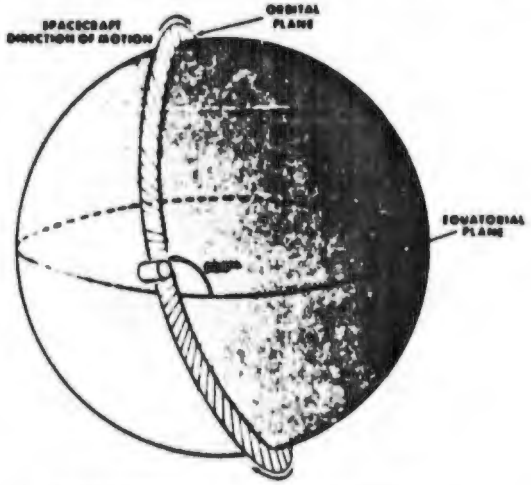

Nominal DMSP orbital inclination (after AWS [1]).

primary specular point (PSP)—The primary specular point (PSP) is that point on the great circle arc passing through the satellite subpoint and the solar subpoint where the angle of incidence of the sun's rays on a horizontal plane (measured from the local zenith) is equal to the angle of reflection of the sun's rays to the satellite in space (see Fig. 2A-4).

satellite subpoint—The point of zero nadir angle for a satellite in planetary orbit.

solar subpoint—The point on the earth's surface on the line connecting the center of the earth with the center of the sun.

specular reflection—Reflection in which the reflected radiation is not diffused; reflection as from a mirror. The angle between the normal to the surface and the incident beam is equal to the angle between the normal to the surface and the reflected beam.

summer solstice—The summer solstice is that time of year when the sun, with respect to the earth, is farthest north and occurs just a few days before aphelion (when the earth is closest to the sun). At that time the sun is directly overhead at noon at 23.5°N. The approximate date for summer solstice is June 22.[2]

sunglint—When the sun illuminates a water surface, a portion of this shortwave radiation is reflected to space. This reflected radiation is called sunglint.

sun-synchronous orbit satellite—An orbit which precesses 360° during the course of the year permitting the satellite, in this orbit, to obtain daylight views of the same geographical area, at the same local time each day. A depiction of a sun-synchronous polar orbit is illustrated below.

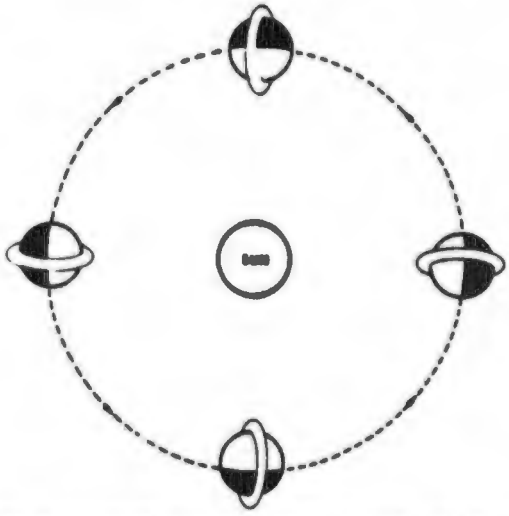

View of a sun-synchronous, local noon, near polar orbit from Polaris. Note precession of the orbital plane through 360° during the year (after AWS [1]).

terminator—The great circle of transition from daylight to darkness on the earth's surface (see Fig. 1A-8).

transverse mercator projection—A mercator projection is a cylindrical map projection centered on the equator. A transverse mercator is a similar projection centered on the satellite subpoint track.

VHR—DMSP Very High Resolution visible data. The 1/3 nm visible imagery derived from the DMSP VHR scanning radiometer.

visible spectrum—That portion of the electromagnetic spectrum to which the human eye is sensitive, having wavelengths extending approximately from 0.4 to 0.7 micrometers (μm).

WHR—The DMSP very high resolution infrared data having a resolution of approximately 1/3 nm at subpoint. The "W" distinguishes the very high resolution infrared data from the very high resolution visible or "V" data.

winter solstice—That time of year when the sun, with respect to the earth, is farthest south. This time occurs just a few days before perihelion (when the earth is nearest the sun). At that time the sun is directly overhead at noon in 23.5°S. The approximate date of winter solstice is 22 December.[2]

zenith—The point on a given observer's celestial sphere that lies directly above him. When the DMSP satellite passes directly overhead the zenith angle is zero.

References

1. Air Weather Service: *Defense Meteorological Satellite Program (DMSP) User's Guide*, AWS-TR-74-250, Scott AFB, 1974.
2. Byers, H.R., 1944: *General Meteorology*, New York, McGraw-Hill Book Co., Inc., pp. 645.
3. Huschke, R.E., 1959: *Glossary of Meteorology*, Boston, American Meteor. Soc., pp. 638.